

Development of Nanofiber-based Biosensors

Dissertation zur Erlangung des
Doktorgrades der Naturwissenschaften

(Dr. rer. nat.)

An der Fakultät Chemie und Pharmazie
der Universität Regensburg
Deutschland



Vorgelegt von

Antonia-Teodora Perju

Aus Heltau

im Jahr 2023

Development of Nanofiber-based Biosensors

Dissertation zur Erlangung des
Doktorgrades der Naturwissenschaften
(Dr. rer. nat.)

An der Fakultät Chemie und Pharmazie
der Universität Regensburg
Deutschland



Vorgelegt von
Antonia-Teodora Perju
Aus Heltau
im Jahr 2023

Die vorliegende Dissertation entstand in der Zeit von Dezember 2019 bis Januar 2023 am Institut für Analytische Chemie, Chemo- und Biosensorik der Universität Regensburg.

Die Arbeit wurde angeleitet von Prof. Dr. Antje J Bäumner and Dr. Nongnoot Wongkaew.

Promotionsgesuch eingerichtet am: 08.02.2023

Kolloquiumstermin: 21.04.2023

Prüfungsausschuss

Vorsitzenderin: Prof. Dr. Miriam Breunig

Erstgutachterin: Dr. Nongnoot Wongkaew

Zweitgutachterin: Prof. Dr. Antje J. Bäumner

Drittprüferin: Prof. Dr. Margaret Frey

Acknowledgments

First, I want to thank **Prof. Dr. Antje J. Baeumner** for accepting me in her research group as one of the first students from the nanoscience program belonging to the physics department, moving to the chemistry department. I appreciate her trust in allowing me to do my master's thesis and continue with my PhD thesis. I am very grateful for her support and for offering me opportunities to join the wonderful GRC community and to go abroad to Cornell University in the USA. I would also like to thank her for the scientific guidance offered during these years.

I would like to especially thank **Dr. Nongnoot Wongkaew** for her continuous help and guidance over the years, not only for scientific development but also for my personal development. I express my gratitude for her support and encouragement, which helped me to achieve this stage, and her constant motivation helped me pass through the challenges of my projects.

Further, I thank **Prof. Dr. Margaret Frey** for allowing me to visit her lab at Cornell University and conduct research there. I am thankful for her guidance during my stay there and her willingness to be part of my PhD committee.

I am thankful to **Prof. Dr. Miriam Breunig** for being willing to be the chairwoman in my doctoral examination.

I want to thank my colleagues Dr. Marcel Simsek and Arne Behrent for helping me with my experiments and offering their support through scientific discussions. I also want to thank Alissa Wieberneit, Florian Weinzierl, and Christoph Bruckschlegel for making the workplace pleasant.

Last but not least, I want to thank **Oleg Vrabie** for his immense emotional support, for listening to me every day talking about work, for feeding me appropriately when spending my weekends in the lab, and for waiting for me after staying late at work. I am very grateful to my family members: **Mioara, Ion,** and **Cipi**, for their constant emotional and financial support, and encouragement in difficult times. They constantly watered my motivation. I would also like to thank Lisa and Sandro Matejka for being my “adoptive” family in Germany and for their emotional support.

Declaration of Collaborations

This work was conducted in large degrees of experimental and theoretical work solely by the author. However, parts of the results were achieved in collaboration with other researchers, which are stated in this section in accordance with §8 Abs. 1 Satz 2 Punkt 7 of the “Ordnung zum Erwerb des akademischen Grades eines Doktors der Naturwissenschaften (Dr. rer. Nat.) an der Universität Regensburg vom 18. Juni 2009”.

Integrating high-performing electrochemical transducers in lateral flow assay (Chapter 1.4)

This chapter has been published. The author and Dr. Nongnoot Wongkaew contributed equally to literature search and manuscript preparation.

Freestanding 3D-interconnected carbon nanofibers as high-performance transducers in miniaturized electrochemical sensors (Chapter 3)

This chapter has been published. The author and Dr. Nongnoot Wongkaew contributed equally to designing and conducting experiments and evaluating the data. Prof. Dr. Antje J. Baeumner led the project administration and promoted manuscript preparation.

Laser-induced carbon nanofibers for redox cycling (Chapter 4)

This chapter will be submitted as an original research article. The author and Dr. Nongnoot Wongkaew contributed equally to designing the experiments. The author conducted the experiments. The author and Prof. Dr. Antje J. Baeumner contributed to evaluation of the data. The author and Dr. Nongnoot Wongkaew contributed equally to manuscript preparation. Prof. Dr. Antje J. Baeumner led the project administration and promoted manuscript preparation.

Flow-through Carbon Nanofiber-based Transducer for in-line Electrochemical Detection in Paper-based Analytical Devices

This chapter was submitted as an original research article. The author and Prof. Dr. Antje J. Baeumner contributed equally to designing the experiments. The author, together with Anna Maria Lauerer and Ferdinand Holzhausen (both supervised by the author) conducted the experiments. The author and Prof. Dr. Antje J. Baeumner contributed to evaluation of the data. The author and Dr. Nongnoot Wongkaew contributed equally to manuscript preparation. Prof. Dr. Antje J. Baeumner led the project administration and promoted manuscript preparation.

Table of Contents

List of Used Symbols and Abbreviations	I
I.Introduction.....	1
1.1. Nanofibers: General introduction.....	1
1.2. Carbon nanofibers	4
1.3. Point-of-care devices with integrated electrochemical (bio)sensors	7
1.4. Integrating high-performing electrochemical transducers in lateral flow assay.....	9
1.4.1 Abstract	9
1.4.2 Author contributions.....	10
1.4.3 Introduction	10
1.4.4 Integrating electrochemical transducers into LFAs.....	21
1.4.5 Conclusions and future perspectives	27
II.Motivation and structure of the thesis.....	29
III.Freestanding 3D-interconnected carbon nanofibers as high-performance transducers in miniaturized electrochemical sensors.....	32
3.1. Abstract	32
3.2. Author contributions.....	33
3.3. Introduction	34
3.4. Experimental	37
3.4.1 Chemicals and reagents	37
3.4.2 Fabrication of PI nanofibers via electrospinning.....	37
3.4.3 Laser-induced carbonization of electrospun PI nanofibers	38
3.4.4 Electrochemical characterization.....	38
3.4.5 Morphological and mechanical stability characterization	39
3.5. Results and discussion.....	40
3.5.1 Fabrications of freestanding LCNFs and their characterizations	40
3.5.2 Anodic stripping analysis of silver ions using a three-electrode system.....	42
3.5.3 Assembly of freestanding LCNF electrodes into microfluidic systems	45
3.5.4 Electrochemical characterization.....	46
3.5.5 Investigation of the reliability and stability of LCNFs as a pseudo-reference electrode.....	48

IV

3.5.6	Analytical performance for dopamine sensing	49
3.6.	Conclusion.....	53
3.7.	Supplementary Information.....	54
3.8.	Storage of LCNF electrodes	64
3.9.	Open circuit potentiometry	70
IV.	Laser-induced carbon nanofibers for redox cycling.....	73
4.1	Abstract	73
4.2	Author contributions.....	74
4.3	Introduction	75
4.4	Material and Methods.....	78
4.4.1	Fabrication of LCNF electrodes	78
4.4.2	Electrochemical characterization.....	78
4.4.3	Morphology characterization.....	78
4.5	Results and Discussions	80
4.5.1	Interdigitated electrodes fabrication	80
4.5.2	Characterization of IDE.....	83
4.5.3	Stacked electrodes	86
4.6	Conclusion.....	89
4.7	Supplementary Information.....	90
4.8	Interdigitated electrodes for point-of-care.....	98
V...	Flow-through Carbon Nanofiber-based Transducer for in-line Electrochemical Detection in Paper-based Analytical Devices	104
5.1	Abstract	104
5.2	Author contributions.....	105
5.3	Introduction	106
5.4	Materials and Methods	108
5.4.1	Chemicals and Reagents.....	108
5.4.2	Fabrication of f-LCNFs	108
5.4.3	Assembly of LFA strip and modification with biotinylated DNA capture probes	109
5.4.4	Synthesis of liposomes	109

5.4.5	DNA sandwich hybridization assay	110
5.4.6	Electrochemical measurements	110
5.4.7	Characterizations	110
5.5	Results and discussions	111
5.5.1	Development of the EC-LFA assembly.....	111
5.5.2	Development of a proof-of-principle EC-LFA.....	116
5.5.3	Detection of pathogenic target DNA using the EC-LFA.....	117
5.6	Conclusion.....	120
5.7	Supplementary information	121
VI.	Conclusion and Future Perspectives	128
	Summary	133
	Zusammenfassung	134
	References	136
	Curriculum Vitae.....	145
	Personal Data.....	145
	Professional experience	145
	Education.....	145
	Scholarships and international research stays	146
	Poster and oral presentations:.....	146
	Publications (peer-reviewed).....	147
	Awards	147
	Publications	1
	Presentations.....	2
	Oral presentations.....	2
	Poster presentations.....	2
	Eidesstattliche Erklärung.....	3

List of Used Symbols and Abbreviations

In the following, all used symbols and abbreviations, besides common abbreviations, are explained. The page number corresponds to the first appearance of the respective word.

Abbreviation	Meaning	Page
μ PAD	microfluidic paper-based analytical devices	7
μ -TAS	micro total analysis systems	76
A	electroactive surface area (cm ²)	40
AA	ascorbic acid	31
Ab	antibody	14
AChE	acetylcholinesterase	2
AE	auxiliary electrode	5
AF	amplification factor	83
AFP	alpha-fetoprotein	23
AgNO ₃	silver nitrate	39
AgNP	silver nanoparticles	54
ASV	anodic stripping voltammetry	40
AuNp	gold nanoparticles	10
BSA	bovine serum albumin	106
C	concentration of the analyte in the bulk solution (M)	40
<i>C. parvum</i>	<i>Cryptosporidium parvum</i>	105
CA	chronoamperometry	18
CC	chronocoulometry	18
CCD	charged-coupled device	16
CE	collection efficiency	83
CL	chemiluminescent	16
CNF	carbon nanofibers	3
CNP	carbon nanoparticles	16
CNT	carbon nanotubes	3
CTAB	cetrimonium bromide	106
CV	cyclic voltammetry	18
CVD	chemical vapor deposition	1
<i>D</i>	diffusion coefficient (cm ² /s)	40
DA	dopamine	31
DLS	dynamic light scattering	108
DMAc	N,N-Dimethylacetamide	39
DPI	dots per inch	40
DPPC	1,2-Dipalmitoyl-sn-glycero-3-phosphocholine	106
DPPG	1,2-dipalmitoyl-sn-glycero-3-phospho-(1'-rac-glycerol) sodium salt	106
DPV	differential pulse voltammetry	18
EC-LFA	electrochemical lateral flow assay	9
eCNF	electrospun carbon nanofibers	36
EDS	energy-dispersive spectroscopy	130
EDTA	disodium ethylenediaminetetraacetic acid	106
EIS	electrochemical impedance spectroscopy	5

II

ESA	electroactive surface area	30
Fe(acac) ₃	iron (III) acetylacetonate	39
f-LCNF	freestanding LCNF	37
FTIR	Fourier-transform infrared spectroscopy	3
GCE	glassy carbon electrodes	7
GO _x	glucose oxidase	24
H ₂ SO ₄	sulfuric acid	39
hCG	human chorionic gonadotropin	11
HEPES	2-[4-(2-hydroxyethyl)piperazin-1-yl]ethanesulfonic acid	106
HIV	human immunodeficiency virus	13
HNO ₃	nitric acid	39
HRP	horseradish peroxidase	16
HSS	HEPES-saline-sucrose	106
ICP-OES	inductively coupled plasma - optical emission spectrometry	108
IDE	interdigitated electrode	31
IgG	immunoglobulin G	24
<i>I_p</i>	peak current (mA)	40
ITO	indium tin oxide	12
KCl	potassium chloride	79
KNO ₃	potassium nitrate	39
LAMP	loop-mediated isothermal amplification	15
LCNF	laser-induced carbon nanofibers	31
LFA	lateral flow assays	8
LFS	lateral flow strip	10
LIG	laser-induced graphene	3
LOD	limit of detection	1
LSG	laser scribed graphene	92
LSV	linear sweep voltammetry	40
MIP	molecularly imprinted polymers	2
MNP	magnetic nanoparticles	16
MPO	myeloperoxidase	26
n	the number of electrons transferred	40
NADH	Nicotinamide adenine dinucleotide	6
NADH	nucleic acid	14
NC	nitrocellulose	13
NF	nanofibers	1
NP	nanoparticles	3
NPV	normal pulse voltammetry	18
OCP	open-circuit potential	50
OG	Octyl-beta-Glucoside	106
OPD	O-phenylenediamin	23
PAD	paper-based analytical devices	46
PAN	polyacrylonitrile	3
PANI	polyaniline	3
PB	hexadimethrine bromide/polybrene	2
PBS	phosphate buffered saline	49
PDMS	polydimethylsiloxane	8

III

PEDOT	poly(3,4-ethylene dioxythiophene)	3
PEI	polyethyleneimine	3
PI	polyimide	3
PLA	polylactic acid	2
PMA	poly(methyl vinyl ether-alt-maleic anhydride)	2
PMG	personal glucometer	25
PNA	peptide nucleic acid	15
POC	point-of-care	3
POCT	point-of-care testing	46
PPI	pixels per inch	40
PPy	polypyrrole	3
PSA	prostate specific antigen	22
pStAv	polystreptavidin	106
PTFE	polytetrafluoroethylene	39
PVA	poly (vinyl alcohol)	2
QCM	quartz crystal microbalance	3
QD	quantum dots	3
RE	reference electrode	5
RF	roughness factor	82
RPA	recombinase polymerase amplification	15
RuHex	ruthenium hexamine	37
SDS	sodium dodecyl sulfat	106
SEM	scanning electron microscopy	43
SERS	surface-enhanced Raman spectroscopy	16
SHE	standard hydrogen electrode	71
SPCE	screen- printed carbon electrodes	20
SPE	screen-printed electrodes	12
SPGE	screen- printed gold electrodes	20
SRB	sulforhodamine B	46
STDV	standard deviation	51
SWASV	square wave anodic stripping voltammetry	20
SWV	square wave voltammetry	18
tDNA	target DNA	108
tL	total lipid	108
TMB	3,3',5,5'-tetramethylbenzidine	16
UA	uric acid	31
UCNP	upconverting nanoparticles	17
w_{b0}	wax barrier	46
w_{c0}	channel width	46
WE	working electrode	5
W_f	real finger size	82
W_{f0}	designed finger width	82
W_g	real gap size	82
W_{g0}	designed gap size	82
ΔE_p	peak-to-peak separation	48
v	scan rate (V/s)	40

I. Introduction

The idea of nanotechnology was first presented during the American Physical Society's annual meeting in 1959 by physicist Richard Feynman by pointing out the possibilities of exploiting materials at their atomic and molecular levels.^[1] *Nanomaterials* are broadly defined as materials with at least one dimension in the nanometer (10^{-9} m) range. Even though that is below our visual capabilities, a way to imagine one nanometer is to think about ten hydrogen atoms lined up.^[1] The constant interest in nanomaterials is motivated by their potential quantum effects. Moreover, they offer an enhancement in the surface-to-volume ratio, increasing the number of binding sites for biorecognition molecules and enhancing the mass transfer rates.^[2] Nanomaterials can have different geometries such as nanowires, nanofibers, nanofilms, and the most popular being nanoparticles.

A *biosensor* is defined as a device detecting an analyte of interest that consists of a biological or bioinspired receptor and a transducer. The transducers should efficiently translate the interaction between the analyte and the biological recognition event. The resulting signal can be electrochemical, electrochemiluminescent, magnetic, gravimetric, or optical. Nanomaterials are used for transduction to improve the sensitivity of biosensors, decreasing the limit of detection (LOD).^[3] The decrease in the LOD is realized through increased binding sites that increase the number of biorecognition molecules, with more analytes being detected. Even though there are various immobilization strategies, such as non-covalent ones: electrostatic interaction, π - π stacking, entrapment, or covalent ones, the biggest challenge remains the efficient immobilization of bioreceptors on nanomaterials.^[3]

1.1. Nanofibers: General introduction

Nanofibers (NFs) are 1-D nanomaterials with a diameter in the nanometer range and varying lengths, depending on the fabrication processes.^[4] These represent a particular type of nanomaterial due to their versatility in fabrication possibilities and material choices, such as metal, metal oxides, ceramics, polymers, and carbon. Moreover, essential functionalities can be determined by tailoring characteristics such as diameter, shape, or surface texture.^[5]

Available fabrication methods for nanofiber production can be categorized into physical vs. chemical processes and electrospinning vs. non-electrospinning. Non-electrospinning techniques include solution blowing, template or freeze/drying synthesis, drawing techniques, phase separation, or self-assembly. Physical fabrication techniques are represented mainly by top-down strategies, while chemical ones refer mostly to bottom-up. Physical vapor deposition is one of the main methods to create nanofibers, involving a process that converts a solid or liquid into the vapor phase for subsequent condensation into

various nanomaterials. However, they suffer from some disadvantages, namely inert gas and very low pressure are required for this. Another similar synthesis method is represented by chemical vapor deposition (CVD), which is often used to produce carbon or metal oxide nanofibers. Carbon nanotubes or nanofibers can be obtained by tailoring the catalyst precursor or growth conditions. Both strategies are complicated, require expensive equipment, and have yet to be demonstrated for mass production possibilities. Even though electrospinning can cause health risks due to the vapors of the used solvent emitted in the electrospinning process, it is still the most common used.^[5]

The electrospinning method is the most exploited for fabricating polymeric nanofibers due to its simplicity, flexibility, inexpensiveness, and mass-scale possibilities. This strategy allows for accessible tuning parameters such as nanofibers' porosity, size, and shape. The electrospinning setup consists of a spinneret, typically a syringe connected to a needle through which a pump drives a constant flow rate on the polymer solution. (Figure 1.1) Additionally, a voltage supply creates an electric field between the polymer solution at the needle and a collector. The high electrical applied voltage (tens of kVs) induces the polymer to overcome the surface tension creating the so-called Taylor cone. The polymer solution gets expelled and forms fibers, which by solvent evaporation result in solid fibers accumulating on the collector in non-woven mats. Such fibers can be dense, porous, hollow, aligned, or random. Depending on polymer concentration, applied electric voltage, and flow rate, the size of fibers can vary from nanometer to micro-sized fibers.^[5]

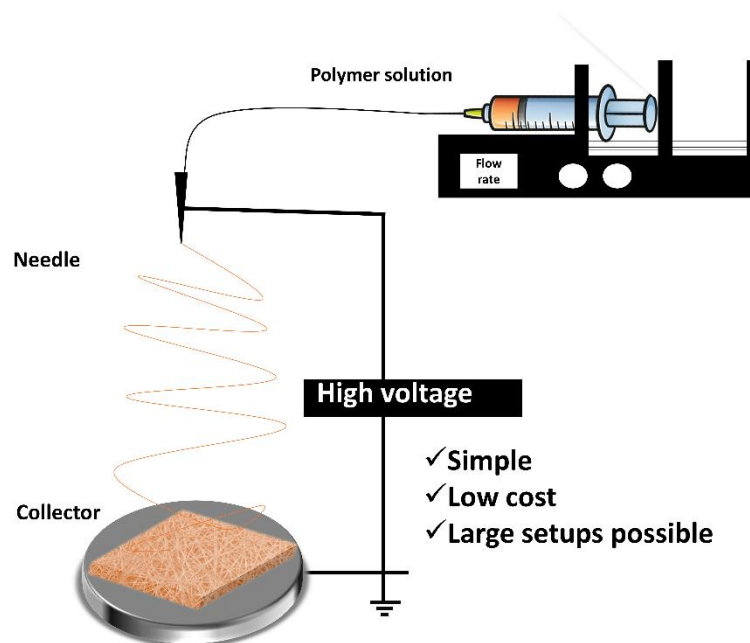


Figure 1.1. Scheme for a simple stationary electrospinning setup.

Even though nanofibers can be fabricated from a single polymer, it is common to design them with functionalities by incorporating different materials in the spinning dope or through modification after

spinning. A parameter that can be easily adjusted is the charge of the spun nanofibers. Positive and negative charged nanofibers were obtained by mixing the hydrophilic water-soluble polymer poly (vinyl alcohol) (PVA) with poly(methyl vinyl ether-alt-maleic anhydride) (PMA) or hexadimethrine bromide (polybrene, PB).^[6] Moreover, PVA was mixed with enzymes such as acetylcholinesterase (AChE)^[7] or glucose oxidase^[8], or molecularly imprinted polymers (MIPs)^[9]. Biodegradable and biocompatible nanofibers were electrospun from chitosan, additionally improving enzymes' immobilization efficiency.^[2] Polylactic acid (PLA) was also successfully spun together with biotin offering the possibility of specific binding with any streptavidin-modified biomolecules.^[10]

Conductive nanofibers are a particular class of nanofibers with high electrical conductivity, which can be obtained by doping with carbon nanotubes (CNT) or nanoparticles (NP)^[11], by electrospinning conductive polymers such as polyaniline (PANI), polypyrrole (PPy) or poly(3,4-ethylene dioxythiophene) (PEDOT)^[12] or by thermal treatment post-spinning. The most popular strategy is using polyacrylonitrile (PAN) for thermal treatment rendering carbon nanofibers (CNFs). PAN is electrospun and stabilized at 200-300°C and then carbonized, typically involving temperatures up to 1500°C resulting in graphite-like structures.^[13] Even though it is widely used, the high temperatures and the expensive equipment limit their mass production possibilities and their integration into point-of-care (POC) devices, which require cost-efficient fabrication for disposable devices. Another strategy for fabricating CNFs is electrospinning a polyimide (PI) precursor mixed with metal salt and carbonizing them in a patterned manner with a CO₂ laser.^[14] This strategy is commonly used with commercially available Kapton foil (polyimide) for writing graphene patterns by inducing the transformation of *sp*³ carbon atoms into *sp*² carbon lattice, yielding so-called laser-induced graphene (LIG).^[15]

As the catalog of nanofibers prepared by various fabrication methods and even more numerous materials is constantly increasing, their application field is very diverse. Their similarity with the extracellular matrix was studied for cell growth, migration, and infiltration used for wound healing.^[16] Biomimetic scaffolds were investigated for tissue engineering by exploiting the nanofibrous structure of non-woven mats.^[17] Developing biocompatible and biodegradable nanofibers demonstrated their use in the repair of skeletal, nervous, and cardiovascular systems in animal models.^[18] Nanofibers were also implemented as catalysts for increasing the reaction efficiencies in reactions such as decomposition, hydrolysis, hydrogenation, oxidation, or photocatalysis.^[19] In general, one of the popular applications for fibers is filtration and separation, where thin nanofibers offer higher porosity for higher filtration efficiency. Other applications involve chemical protection and decontamination, textiles and cosmetics, solar cells, energy storage, and sensors.^[20]

Nanofibers have been successfully implemented in analytical applications. One application for nanofiber-based sensors is in quartz crystal microbalance (QCM). Due to the need for improved sensor sensitivity and selectivity for chemical analytes, nanofibers were exploited as coatings on QCM. Especially polyethyleneimine (PEI) was investigated for the detection of formaldehyde.^[21] Moreover,

nanofibers have been extensively used as optical sensors, either with FTIR, fluorescence, or colorimetric sensors. Colorimetric nanofibers can be obtained by doping the polymer solution, spinning functionalized polymers, or surface functionalization of the spun nanofibers.^[22] Fluorescent nanofibers are fabricated with quantum dots (QDs), bio-chromophores, or even conjugated polymers, to detect metal ions, explosive compounds, or biosensors for glucose, urea, or protein detection.^[23] Furthermore, nanofibers are applied in gas sensing, exploiting ionosorption and oxygen vacancy mechanisms.^[24] A different class is represented by immunosensors, which use the nanofibers to immobilize biorecognition elements for malaria, cancer, or pathogenic bacteria detection.^[25]

1.2. Carbon nanofibers

Carbon nanofibers are conductive nanofibers, considered a one-dimensional form of graphite, with different characteristics than carbon nanotubes.^[26] CNFs have hollow structures due to their cylindrical geometries consisting of graphene layers.^[2] The angle between graphene layers is important for classifying different CNFs into herringbone or fishbone, platelet, and parallel nanofibers. Characteristics such as low thermal expansion, lightweight, high tensile strength, chemical resistance, stiffness, excellent thermal conductivity, and high-temperature tolerance represent this type of nanomaterial. Moreover, CNFs consist of sp^2 – discontinuous linear filaments with enormous surface area to volume ratio, having an aspect ratio greater than 100:1.^[27]

Carbon nanocomposites like CNTs and CNFs have excellent electrical conductivity but CNFs have increased edge planes and graphite planes, available as functionalizing surface areas beneficial for immobilizing biomolecules.^[2] The way of stacking graphene sheets influences electron transfer for electroactive analytes.^[28] Furthermore, CNFs can be easily treated, either chemically or physically, to enhance their specific surface area and surface oxygen moieties.^[27] The two most used methods for the fabrication of CNFs are chemical vapor deposition and electrospinning with thermal treatment. Even though the first method can produce high-quality CNFs, electrospinning is more advantageous.^[29]

The advancements in the production and functional tailoring of CNFs have enlarged their applications in supercapacitors, batteries, solar and fuel cells, clean energy production, tissue engineering, antibacterial materials, environmental science, and shape memory materials.^[30] Between the most obvious implementation of CNFs into supercapacitors or batteries, due to their high specific area, good electrical conductivity, and high chemical stability and less popular applications such as drug delivery and environmental purposes, the achievements of CNFs as sensing strategies remain the most widespread ones. CNFs are sensitive to gas exposure, so multiple studies show the advantage of using CNFs for various gas such as H_2 , NO_2 , H_2S , or NH_3 .^[30] Due to their excellent electrical conductivity,

high surface area, and chemical functionalities, CNFs have been extensively used for electrochemical sensors.

Electrochemical sensors typically consist of the recognition element and the signal transducer, which converts the recognition of an analyte at the electrode into a detectable quantifiable signal.^[31] The basic principles of electrochemistry rely on the transfer of charge, which results from a chemical reaction between the electrode and the solution.^[32] Electrochemical sensors are classified into potentiometric, voltammetric, impedance-based, and conductometric techniques. Electrochemical systems traditionally consist of three electrodes: working (WE), auxiliary (AE), and reference electrodes (RE). While the potential is maintained between the working and the reference electrode, the current flow is measured between the AE and the WE.^[4] The RE is an electrode whose potential needs to remain constant independently of the WE or the measured solution. Standard RE are Ag/AgCl or Hg/HgO electrodes.^[33] However, a lot of efforts are being made to develop REs suitable for miniaturized systems, such as screen-printing Ag/AgCl.^[34]

The amperometric sensors measure a signal due to the oxidation or reduction of a chemical species at the electrodes, so electrons are transferred between the analyte and the WE. The direction of the flow of electrons is controlled by the electric potential applied to the WE.^[32] While for potentiometry, a difference in potential between two electrodes is measured, the variation of conductance is monitored for conductometry. Furthermore, electrochemical impedance spectroscopy (EIS) has gained popularity, being able to monitor binding events at the transducer surface by linking the change in impedance (frequency-dependent resistance) with the electrochemical reaction.^[4] Nevertheless, voltammetric sensors are prevalent due to their simple implementation possibilities and the different possibilities to apply the potential to enhance the sensitivity. Additionally, the current intensities can be enhanced by redox cycling which regenerates the oxidized or reduced species at the electrodes.^[35]

Electrochemical sensors are equipped with proper selectivity by combining them with a biorecognition element. Sensors that employ biorecognition molecules are called *biosensors* and can be identified as affinity-based or catalytic biosensors. While an affinity biosensor typically involves antibody-antigen binding, nucleic acid-probe with a complementary nucleic acid, or aptamers, the catalytic ones are based on enzymes, cells, or DNazymes.^[35] The biorecognition element can be in close proximity to the transducer or within other areas of the sensor, immobilized via adsorption, covalent binding, entrapment, or embedment. Moreover, two different strategies exist, one which uses a so-called label that provides the source for the electrochemical signal or a label-free variant that can monitor either binding events of biomolecules (EIS or potentiometric) or measure intrinsically electroactive molecules. Typical electrochemical (bio)sensor implementations are in health care, food analysis, food safety, and environmental monitoring.^[4] The essential characteristics of such sensors are sensitivity, specificity, and selectivity. While the selectivity is highly dependent on the chosen (bio)recognition element, the sensitivity can be tailored by using nanomaterials as transducer elements.^[31]

Carbon nanofibers have been extensively used in electrochemical sensing. The advantages of electrochemical sensors, such as fast response time, high affordability, and the possibility to miniaturize and, therefore, portability, can be further enriched with nanomaterials. Mainly, CNFs can be used to modify electrochemical transducers for sensitivity improvement. Electrochemical sensors can be classified into enzyme-based and non-enzymatic sensors. While enzyme-based sensors have become one of the most popular ones with the commercialization of glucometers, the non-enzymatic counterparts use electrocatalytic reactions.

The presence of defects in the carbon lattice or the addition of metallic composites influences the electrocatalytic activity of electrochemical sensors. A technique is adding a metal salt precursor into the polymer solution before electrospinning. After the carbonization, the metal particles are made available on the surface of the nanofibers. This method improved the fiber formation and increased the homogeneity of the nanofiber mat by an increase of the ionic conductivity of the polymer solution. It is observed that the nanoparticles are embedded inside the nanofiber matrix.^[29] Palladium-loaded CNFs were demonstrated by electrospinning PAN with Palladium acetate and carbonized by thermal treatment to have high electrocatalytic activity for the oxidation of NADH and reduction of H_2O_2 .^[36] By a similar method, nickel acetylacetonate was incorporated into PAN nanofibers and rendered CNFs containing nickel nanoparticles demonstrating good catalytic activity for glucose sensing.^[37] A novel study using the same principle demonstrated the mechanism of gold nanoparticles migrating to the surface of the CNFs by variation of temperature and heating rate during carbonization and also showed good catalytic activity towards H_2O_2 detection.^[38] A different strategy is to carbonize the nanofibers under heteroatom-containing atmospheres, such as N content in polymers (PAN and PPy).^[29]

CNFs offer great immobilization sites for biomolecules due to the high number and types of functional groups. These particular advantages are exploited in enzyme-based sensors. Enzymes convert a substrate into a product, which the electrode can monitor. This was demonstrated by comparing different types of CNFs with CNTs and graphite powder for immobilizing glucose oxidase, which proved the superiority of CNFs.^[39] An ethanol sensor was fabricated by immobilizing alcohol dehydrogenase via a simple drop-casting strategy on CNF-based electrodes.^[40] AChE was immobilized onto CNFs and modified with silica grown around the enzyme for stability improvement and demonstrated good sensitivity for acetylthiocholine.^[41] Even though excellent selectivity and sensitivity can be achieved with enzymes, they need improvement in stability, cost fabrication, and conditions needed for storage.

Most studies exploiting CNFs for electrochemical sensing rely on glassy carbon electrodes (GCE) or carbon paste electrodes to support the CNFs. Moreover, the conventional strategies used for CNFs hybrids have multiple and significant disadvantages. These include complicated and expensive electrode preparation, non-malleable electrode design, and loss of beneficial features after processing.^[29] Due to their cost and multiple complicated steps during fabrication, their mass-production possibility is limited. In contrast, electrospinning combined with laser-induced carbonization is a promising technique to

overcome the mentioned drawbacks. Nonetheless, their electrocatalytic activity was demonstrated by incorporating iron into the spinning solution towards NADH and hydrazine detection^[14] or for glucose sensing by the presence of nickel nanoparticles^[42].

1.3. Point-of-care devices with integrated electrochemical (bio)sensors

Biosensors have been implemented in food quality control, environmental monitoring, clinical diagnostics, and *point-of-care* (POC) devices. A POC device is a miniaturized portable system that can perform sample pretreatment, detection, and readout in the field. The motivation for developing POC devices lies in replacing the time-consuming laboratory experiments performed by trained professionals with having a simple device handled by the patient to detect or monitor a biomarker of interest. Electrochemical detection strategies are advantageous to be implemented into POC because of their high sensitivity, portability, low cost, simple instrumentation, and ease of operation.^[43] Moreover, due to the miniaturization of electronics, small and portable potentiostats are available for monitoring electrochemical reactions. One of the best examples of an electrochemical POC device is the glucometer, which consists of a screen-printed electrode on which glucose oxidase or dehydrogenase is immobilized and coupled to an amperometric transducer.

POC devices commonly imply the use of microfluidics, which solves the problem of a multistep assay, including fluid handling, sample processing, signal amplification, washing, and detection on a single platform. Microfluidic-based POC can be classified by their fabrication material: paper, polymer, silicon, or glass. Paper is flexible, low-cost, lightweight, recyclable, biocompatible, and best suited for POC devices. Moreover, it eliminates the need for external pumps or power supplies since the capillary force controls the flow.^[44]

Microfluidic paper-based analytical devices (μ PADs) are widely used in POC technologies. Microfluidic strategies aim to integrate functions such as injection, reaction, separation, and detection by having hydrophilic and hydrophobic channels. These paper-based systems have advantages like low production cost, simplicity, easy processing, good biocompatibility, and small reagent consumption. Moreover, all necessary steps for POC testing, including sample pretreatment, reagent transportation, mixing, separation, and detection, can be done on the same platform.^[45] Their production can be done by polydimethylsiloxane (PDMS) plotting, inkjet etching, plasma etching, cutting, and wax printing.^[46]

Among the most famous examples of paper-based POC devices, *lateral flow assays* (LFAs) have been extensively researched during the Covid19 pandemic. These consist of different membranes from fibers, such as cotton, glass, or cellulose. The sample is added to the first membrane and moves across different membranes due to the capillary force. The following chapter describes possibilities for developing LFAs with different biorecognition elements, labels, and various detection strategies. Electrochemical LFAs

are emphasized, and the advantages and drawbacks of existing techniques for implementing electrochemical sensing in LFAs are discussed.

1.4. Integrating high-performing electrochemical transducers in lateral flow assay

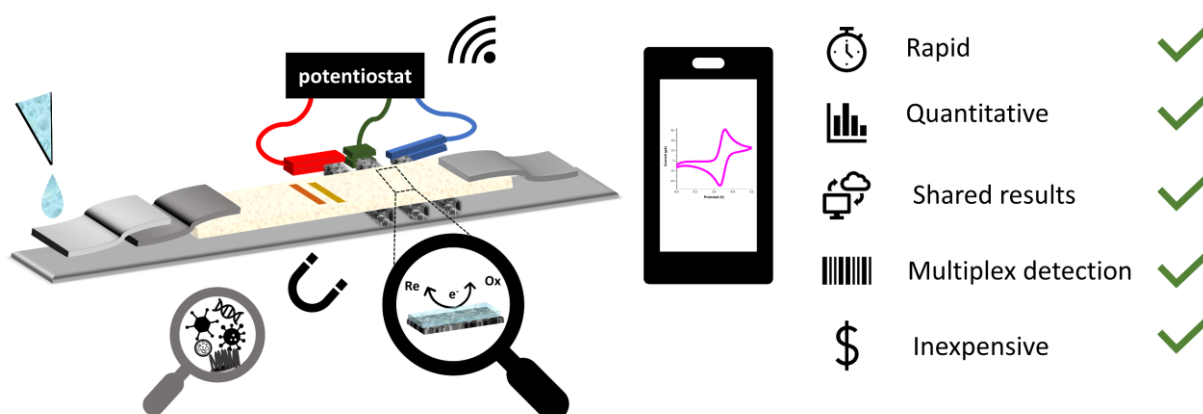


Figure 1.2. Scheme of an LFAs containing carbon-based electrodes under the nitrocellulose membrane connected to a minipotentiostat with a possible Bluetooth connection to a smartphone and the advantages of such a development.

1.4.1 Abstract

Lateral flow assays (LFAs) are the best-performing and best-known point-of-care tests worldwide. Over the last decade, they have experienced an increasing interest by researchers towards improving their analytical performance while maintaining their robust assay platform. Commercially, visual and optical detection strategies dominate, but it is especially the research on integrating electrochemical (EC) approaches that may have a chance to significantly improve an LFA's performance that is needed in order to detect analytes reliably at lower concentrations than currently possible. In fact, EC-LFAs offer advantages in terms of quantitative determination, low-cost, high sensitivity, and even simple, label-free strategies. Here, the various configurations of EC-LFAs published are summarized and critically evaluated. In short, most of them rely on applying conventional transducers, e.g., screen-printed electrode, to ensure reliability of the assay, and additional advances are afforded by the beneficial features of nanomaterials. It is predicted that these will be further implemented in EC-LFAs as high-performance transducers. Considering the low cost of point-of-care devices, it becomes even more important to also identify strategies that efficiently integrate nanomaterials into EC-LFAs in a high-throughput manner while maintaining their favorable analytical performance.

This chapter has been published and formatted to fit this thesis:

Perju A, Wongkaew N. Integrating high-performing electrochemical transducers in lateral flow assay. *Anal Bioanal Chem.* 2021 Sep;413(22):5535-5549. doi: 10.1007/s00216-021-03301-y

1.4.2 Author contributions

The author and Dr. Nongnoot Wongkaew contributed equally to literature search and manuscript preparation.

1.4.3 Introduction

Lateral flow assays (LFAs) are the most well-known point-of-care (POC) devices that enable rapid detection of relevant bio- or chemical markers in a simple and low-cost manner by non-specialized users. Additional advantages of the LFA include the facile fabrication process and the inexpensive material used in the device preparation. Only a small volume of sample is needed, typically in the microliter range, and the sample does not require special pretreatment, allowing a feasible sample-to-answer process. LFA usage was primarily aimed towards medical diagnostics as home-based testing devices, or used in clinical laboratories, but their applicability has later extended to agriculture, food safety, and environmental monitoring^[47]. It dates back to 1969 when Margaret Crane first patented a diagnostic test device concept applicable for home testing of pregnancy^[48]. This seminal work led to further developments in various versions prior to the commercial home pregnancy test based on LFAs as can be seen in Figure 1.2. Lateral flow strips (LFSs) have found rapid successful commercialization due to the following attractive characteristics: **A**ffordable, **S**ensitive, **S**pecific, **U**ser-friendly, **R**obust & **R**apid, **E**quipment-free and **D**eliverable (ASSURED), that meet the demands of a POC device. As can be seen in Figure 1 the principle has actually emerged a long time ago and set the foundation for a number of interesting subsequent developments. Nowadays, utilizing gold nanoparticles (AuNPs) as a signal tracer remains a gold standard in LFA that allows detection of the color change by naked eyes. Despite the simplicity and rapid signal generation of AuNPs, many attempts have been made towards improving detection sensitivity as the target analytes found in body fluids are normally present at low concentrations that may lead to false-negative prediction or detection^[49]. More importantly, LFAs that can quantify analyte concentrations will be desirable to serve in a wide range of applications.

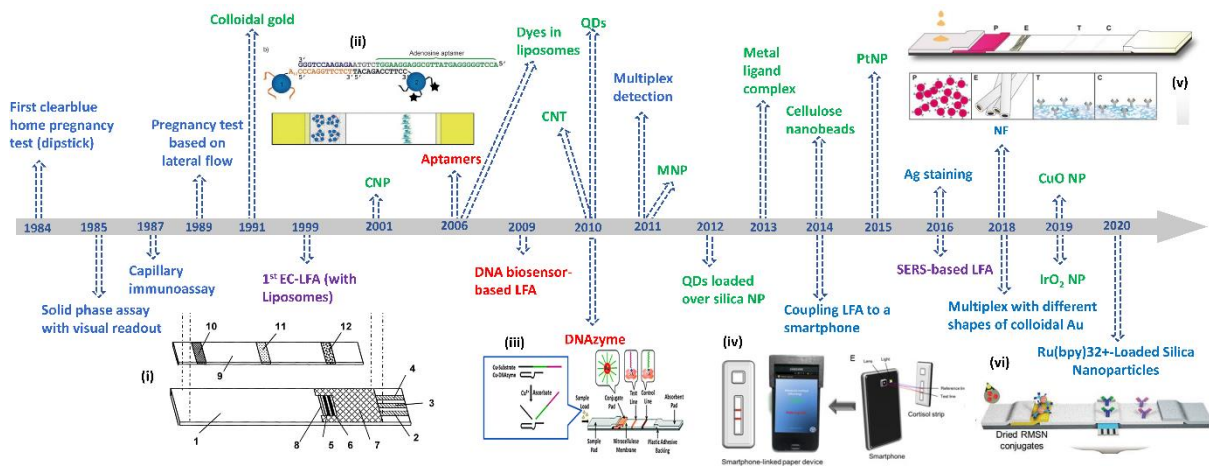


Figure 1.3. Timeline of the exemplary developments of LFA starting in 1984 with the first clearblue home pregnancy test (clearblue.com), which continued with two important patents: solid phase assay with visual readout^[50] and capillary immunoassay^[51], then the first pregnancy test based on a lateral flow test (clearblue.com), leading to the first patent on LFA using colloidal gold^[52]. The development continued with the first EC-LFA and first use of liposomes^[53], followed by first use of carbon nanoparticles (CNP)^[54], then liposomes entrapping dyes^[55] and use of aptamers in LFA^[56]. Further research led to DNA hybridization detection based LFA using enzyme as a tracer^[57], implementation of DNAzyme for metal ion detection^[58] use of CNT^[59], QDs^[60], and MNP^[61], achieving multiplex detection^[62]. Further improvements focused on tracer strategies, like metal ligand complexes^[63], cellulose nanobeads^[64] and the coupling to a smartphone^[65]. In the past few years the research has been focused on further developing labels like Pt-nanoparticles (PtNP)^[66], the use of Ag staining for amplification^[67], combining LFA with SERS^[68], implementing nanofibers (NF)^[69], using different shapes of colloidal gold^[70], using different nanoparticles (NP) like IrO₂^[71] or CuO^[72] and integrating electrodes for electrochemiluminescence (ECL)^[73]. The texts shown in blue, green, purple, and red represent the development focusing on assay format, signal tracer, detection technique, and recognition element, respectively. Figures reprinted from (i)^[53], (iv)^[65], (v)^[69] with permission from Elsevier. Figures reprinted from (ii)^[56] and (vi)^[73] with permission from John Wiley and Sons. Figure (iii) reprinted from^[58] with permission from Royal Society of Chemistry.

In order to improve the sensitivity of LFAs many attempts have targeted detection techniques, using new transducer materials, and enhancing signal through effective amplification strategies and the use of nanomaterials. Another important aspect is to develop LFAs with a quantitative readout which plays an important role in medicine, agriculture, food safety, and environmental monitoring. Especially in the medical area, the specific pathogen concentrations or level of clinical relevant markers^[74] will determine the proper treatment. Qualitative LFAs may be sufficient for some applications such as the detection of human chorionic gonadotropin (hCG) in a pregnancy test. However, for some diseases, e.g., diabetes, knowing the concentration of an analyte is crucial to make further treatment decisions. Other analytes whose concentration levels are highly relevant are metabolites, hormones, and blood-borne chemicals^[75]. The metabolites which are targeted by most POC devices are cholesterol, triglycerides, creatinine, lactate, ammonia, and urea. For example, creatinine is used for the assessment of renal function; lactate for tissue perfusion and presence of ischemia or hypoxia; urea and ammonia levels help diagnosing renal disfunction, liver disease or asthma. Moreover, the focuses of POC diagnostics lie also on metabolites of regulated or illegal drugs, such as cocaine, opiates and cannabis^[75].

Strategies using electrochemical detection offer attractive features such as high sensitivity, selectivity, low instrumentation cost, and inherent miniaturization ability with improved analytical performance. So far the developments of LFA based electrochemical detection have utilized disposable transducers such as screen-printed electrodes (SPE), disposable gold electrodes built from recordable compact discs or indium tin oxide (ITO)^[76], which are well suited for single use in an LFA. Moreover, the development of nanomaterials offers the possibility to enhance the performance of the transducers, e.g. by increasing their conductivity, enabling electrocatalytic effect, enhancing electron transfer rate and increasing the surface area of the electrodes^[76]. The nanomaterials with various dimensions (0D- 3D) have been successfully implemented to miniaturized analytical systems as shown in many studies ^[77]. Electrochemical transducers of 3D-architecture are more attractive for use in LFAs than those of other dimensions as sample liquid can pass through the transducer, promoting efficient interactions between analyte and transducer surface. In addition, the increased electroactive surface area could possibly extend the dynamic range of the sensor.

With LFAs being widely studied, there are many reviews available in the past and present. This indicates that the developments of LFAs are still very active and in focus by many researchers around the world. An interesting review focusing on recent developments towards quantitative LFAs highlighted that the majority of devices reaching commercialization are based either on colorimetry or on fluorimetry. They address a number of advantages for developing quantitative LFAs^[74]. A more recent review focused on detection strategies available for LFAs has also been published by Nguyen et al^[78]. Moreover, there have been many reviews^[47,49,79–83] on LFAs with foci on different aspects of LFA, for example, directed flow on LFAs in the form of microfluidic paper-based analytical devices ^[80], or on nanoparticles used in LFAs^[84]. To the best of our knowledge, despite their many beneficial features mentioned above, less attention has been paid to LFAs operating with electrochemical detection which could likely be because the integration of electrochemical transducers to LFSs requires complicated fabrication methods. However, non-obvious fascinating analytical performance is possible in this format, especially in comparison to optical based detection techniques. Furthermore, with ongoing progresses in material science with respect to facile fabrications strategies available, it could be seen in the future that LFA based electrochemical detection is one of the most interesting areas to put research efforts on. Therefore, in this trend article, we want to emphasize the benefits of integrating electrochemical transducers onto LFSs for achieving quantitative results, by merging the advantages of a POC device with those of electrochemical detection. At the beginning, we describe recent developments of recognition strategies and signal tracers. Then, the common techniques used in LFAs are described. We further take into consideration all the advances that have been made in the last years to fabricate electrochemical LFAs and we propose how recently developed transducers could be integrated into LFS. At last, a future perspective is intended to highlight the possibilities and advantages of electrochemical LFA. The overall purpose of this trend article is to propose beneficial integration strategies for high performing electrochemical transducers onto LFSs.

Principle of LFAs

The LFA requires low sample volumes to apply on a porous membrane, flowing further along the entire strip that consists of different connected zones with specific functions (Figure 1.4). As illustrated in Figure 1.4, a sample pad is the zone located at the beginning of the strip where fluid sample is applied. This zone typically contains pre-dried buffering salts and surfactants to pretreat the sample, if necessary. The reagents become rehydrated when the sample passes through. The sample solution from the sample pad is further delivered to a conjugated pad positioned underneath an overlapping nitrocellulose (NC) membrane. Here, (bio)-recognition elements anchored with signal labelling are stored at the conjugated pad. The target analyte bound to the conjugated receptors further travels along the NC membrane where a detection zone is located. In general, the detection zone consists of two lines namely test- and control lines. In the test line, a recognition element complementary to the analyte is immobilized and responsible for capturing the analyte complex. In the control line, the recognition elements anchored with signal labelling will be trapped to confirm a proper functioning of the strip^[81]. The last part of the LFS is called a waste pad which is overlapping with the NC membrane. This part is responsible for promoting the flow and preventing the back flow of the sample solution. It is important to note that all pads must slightly overlap when assembled on the backing substrate, to ensure a proper fluidic contact between zones that allows the solution to be driven by the capillary forces smoothly till the end of the strip.

In general, the LFSs applied to immunoassay can be performed into two formats, namely direct- and competitive assay. The direct assay is typically performed via a sandwich format, where the antigen (analyte) binds first to the specific primary antibody present in the conjugate pad and is then captured by the secondary antibody on the test line. Therefore, the presence of signal in the test line indicates a positive result. This format is suitable for analytes of relatively large size which have multiple binding sites, e.g., p24 antigen used for HIV detection and hCG used in the home-based pregnancy test. In a competitive assay, antigen (analyte) is immobilized in the test zone, therefore, the labeled receptor can be captured, generating the signal when the target analyte is absent. On the other hand, the presence of analyte in a sample will hinder the binding event of labeled receptor, thus hampering the signal generation in the test line. Therefore, a lack of signal or reduction in signal intensity at the test line indicates a positive result^[81]. Similar to the direct-assay format, antibodies specific to labeled receptor is immobilized at the control line to confirm proper functionality of the system. The competitive assay is more flexible as it can be applied to any analyte of interest without the restrictions of available binding sites and sizes. The construction concept shown in Figure 1.4 and the two assay formats remain the standard configuration for LFA development nowadays.

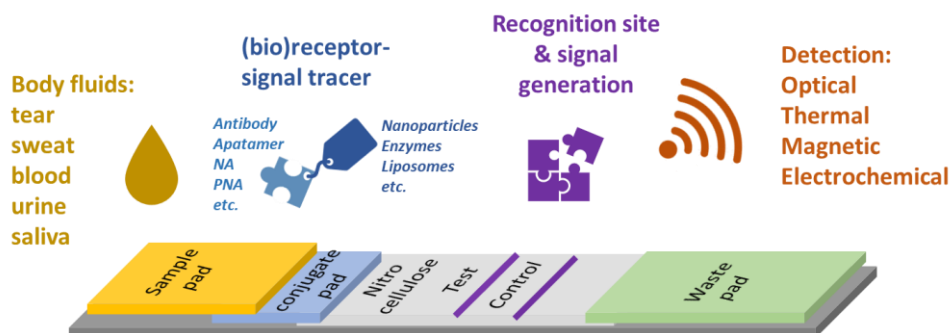


Figure 1.4. Scheme illustrating components of an LFA

Current developments of LFAs

This section aims to provide readers with a broad overview on what has been done so far to improve performance of LFAs, especially in terms of selectivity and sensitivity, for nonelectrochemical readings. The developments of novel recognition probes can be definitely implemented to electrochemical-LFAs to promote high selectivity and stability. The developments of signal tracers for other detection techniques can be promising for electrochemical readings as some of them are inherently electroactive.

Recognition strategies

Recognition elements are a crucial part in LFAs as they determine specific reactivity to target analytes. Ideally, real sample solution is expected to be directly applied to LFA without any pre-treatments. Therefore, recognition elements should be highly stable in the sample solution of interest. Binding between biorecognition elements and analytes should be fast as no pre-incubation is present in ideal LFAs. The most common biorecognition elements present at a conjugate pad and test zone (test and control line) are antibodies (Abs) as they are very well-established, especially in terms of immunoreactivity, production, and commercial availability. However, they still suffer from drawbacks, such as long production time, poor stability, strict storage conditions required and batch-to-batch variation^[85]. As a solution to these problems, aptamers have nowadays gained more attention as counterparts to Abs in LFAs, as they are stable, simpler to use and have lower costs than Abs^[86]. Aptamers, also known as chemical Abs, are made from nucleic acid (NA) in which their complex folding into 2D or 3D structure allows them to bind selectively to corresponding analytes with high affinity^[87]. The change of their conformation upon binding to analytes is also highly suitable for label-free assays, in particular for small molecule detection^[88]. Aptamers have been successfully implemented to LFAs with good detection sensitivity and specificity not only for clean samples such as sweat^[86] and saliva^[89] but also for challenging samples such as the avian influenza H5N2 virus particle spiked in solution containing duck's feces^[90]. With their attractive features and progresses in terms of production and a vast variety of available NA sequences for specific analytes, aptamers possess a great potential to substitute the use of Abs in LFA in the coming future.

Oligonucleotide sequences have been commonly used for detection of their complementary target sequences. However, most detection techniques in LFA are not sensitive enough to enable direct detection after NA isolation and purification. Therefore, NA targets are commonly pre-amplified, then termed DNA amplicons, prior to the detection on LFA^[91]. The amplification can be performed either off- or on LFS^[92]. The resultant double stranded DNA amplicons (such as from loop-mediated isothermal amplification (LAMP)) typically require denaturation into single stranded DNA prior to introducing into LFS for the hybridization assay^[93]. However, Jauset-Rubio et al. demonstrated the possibility to detect double stranded DNA amplified by recombinase polymerase amplification (RPA)^[94]. Herein, the use of tailed primers in RPA provides DNA amplicons with duplex flanked by two single stranded DNA tails. Therefore, direct hybridization to immobilized capture probes and labelled reporter probes are feasible.

Molecular beacons are short single stranded DNA sequences that can form a hair pin loop structure with a 15-30 base pair long region complementary to the target sequence and 4-6 base pairs that form the stem^[82]. Molecular beacons are suitable for detection of short NA sequences without the need of a second reporter probe, thus lowering the assay cost. A labeling molecule is anchored at the end of the molecular beacon probe. Upon binding to complementary target NA, the stretching of the probe alters the signal transduction property of the labeling molecule, thus enabling detection of the binding event.

Peptide nucleic acids (PNAs), are DNA mimics with neutral polyamide backbone, have gained a lot of attention as alternatives to DNA probes, in particular for short NA sequences such as micro-RNAs (20–22 mers) that are unlikely to be effectively amplified^[95]. Here, the polyamide backbone in PNA probes enables the formation of a PNA-RNA duplex with higher binding strength than those of RNA-RNA or DNA-RNA. The neutral backbone of PNA contributes to the highly strong binding of NA as electrostatic repulsion between the two hybridized strands is eliminated. In addition, background signal in electrochemical detection is considerably lower due to the uncharged backbone. Thus, monitoring the hybridization event of PNA with DNA or RNA based on electrochemical label-free techniques is feasible as demonstrated in previous studies where charge of the probe plays an important role for signal generation^[94,96,97]. LFA combined with PNA probes has been successfully implemented to determine microRNA-150 in plasma samples for preterm birth screening test^[98].

Nucleic acids with catalytic cleavage reactions, e.g., DNazymes, are an interesting recognition element for metal ion detection in LFAs^[99]. In principle, the DNzyme sensor for metal ion detection consists of substrate and enzyme strands^[100]. Here, metal ions serve as a cofactor of the DNzyme complex and induce cleavage of the substrate strand. The cleaved substrate strand can then be detected by various techniques^[101].

Moreover, peptides that consist of short amino acid chains can be an attractive candidate for biorecognition elements^[102]. Specific peptide sequences can recognize various kinds of analyte molecules including proteins, metal ions, and NAs. Some peptide sequences can act as a substrate that

can be cleaved by proteases^[103]. Therefore, peptides can be used as a recognition probe for determining protease activity which is an important biomarker in many diseases, for example matrix metalloproteinase-9 (MMP-9) is a well-known protease for cancer diagnosis as it plays a crucial role in the cell invasion and tumor metastasis^[104].

Signal tracers and nonelectrochemical readings

Recent developments have proposed the use of advanced labels based on naked-eye detection, fluorescent or chemiluminescent reading, and surface-enhanced Raman spectroscopy (SERS). Alternative to these optical readings, measurements of physical properties such as magnetic strength and generated heat have been exploited in LFAs but are not as popular as the optical methods^[105]. In this section, we therefore focus mainly on optical based detection strategies.

Naked-eye detection remains the most popular choice over the other options due to instrument-free readout. Gold nanoparticles (AuNPs) are the most popular signal tracer in LFAs because they deliver a strong signal that is visible to the naked eye and moreover are easy to synthesize, stable and uncomplicated in handling^[84]. However, to improve their detection sensitivity and to develop the LFA strategy towards a semi- or fully quantitative detection, many research efforts have been focused on other nanomaterial tracers. For example, to increase signal intensity via naked-eye detection, nanoparticles that allow more intense color than AuNPs or high contrast signal over the white background of the LFA membrane have been proposed. These included nanoparticles based on Prussian blue^[106], carbon nanoparticles (CNPs)^[107], and magnetic nanoparticles (MNPs)^[108]. Enhancement of colorimetric signal of AuNPs before or after capturing at the detection zone is an alternative strategy^[109]. This could be carried out by i) increasing the density of AuNP tracers, e.g., using AuNP aggregates, ii) increasing particle size through silver or gold deposition, and iii) decorating AuNPs with catalysts, e.g., enzyme or metal, that enables greater signal generation than obtained from AuNPs alone.

Apart from inorganic nanomaterials, enzymes have also been used as a signal tracer for optical detection in LFAs^[110]. Here, substrate reagent is needed to generate detectable products which introduces one more step in the detection. Horseradish peroxidase (HRP) is the most common enzyme applied to LFAs. Its chromogenic substrate, 3,3',5,5'-tetramethylbenzidine (TMB) is being oxidized by HRP in presence of H₂O₂, resulting in a product that is visualized on the LFSs^[110]. Apart from detecting colored product, a chemiluminescent (CL) signal can be obtained from the catalytic reaction of luminol with H₂O₂ via HRP, that can be detected by a charged-coupled device (CCD) camera or other analyzer system^[111,112]. The high sensitivity and high signal-to-noise ratio using simple optical readout systems make CL more attractive than other optical readout methods.

The signal enhancement of the LFAs based on optical detection has been also achieved by using fluorescent dyes instead of the metallic NP, resulting in a higher signal-to-noise ratio, which increases the sensitivities and thus lowers the detection limit^[78]. The fluorescent tracers such as quantum dots

(QDs) are also very popular to implement in LFAs by taking advantage of good sensitivity and high stability of generated signals. QDs can provide a strong photoluminescent signal upon excitation by UV light. The signals can be detected at long wavelengths in which the emission peaks are dependent on size and composition of QDs. Therefore, QDs are suitable for multi-analyte detection in LFA [113,114]. Alternative to QDs, upconverting nanoparticles (UCNPs) have become more attractive as the excitation wavelength in the near IR region can reduce the tendency of auto-fluorescence of the membrane, unlike when using UV light, and produce a strong signal in the visible region which is more sensitive than that provided by QDs.

Loading the signal tracers into micro- or nanocarriers, e.g., liposomes^[53], polystyrene beads^[115], MNPs, and cellulose nanobeads^[64] has shown to be an effective strategy to dramatically improve detection sensitivity of LFAs for various kinds of signal tracers mentioned above.

Even though the developed detection strategies mentioned above have shown desirable performance when applied to LFAs, the difficulty in commercialization remains a major obstacle as either LFA fabrication, or the necessary instrumentation for readout is expensive. Even so, the ones that are available on the market only offer mostly qualitative or semi-quantitative detection. As mentioned at the beginning, this is sufficient for some diagnostics, but there are a wide variety of analytes that need to be quantitatively determined, as their concentration greatly affects the decision taken for subsequent actions. The visual colorimetric detection often suffers from poor sensitivity and lack of reproducibility. Moreover, subjective visual comparisons of color may still be suitable for qualitative results, but reliable quantitative measurements require objective data interpretation [80]. Even for the fabrication of new nanoparticles, which can offer a great improvement of the sensitivity, the surface properties have to be carefully controlled, to allow an efficient bioreceptor conjugation, low non-specific binding and smooth migration across the membrane^[109]. Although, technologies have evolved and higher sensitivity is possible to achieve, in most cases simplicity is compromised by involving multiple steps or even complicated procedures. For example, for quantification of visual signals, optical or fluorescent readers or a camera could be employed. However, these require a complicated software for measuring and analyzing the intensity of the signal. Even if there is an enormous advantage to use the smartphone for both imaging and analyzing, the data has to be normalized to the specific characteristics of the camera used for data acquisition and a consistent lighting has to be ensured, in order to yield reliable results.

Electrochemical lateral flow assay (EC-LFA)

Electrochemical transduction is attractive to be integrated into LFAs due to its simplicity, high sensitivity, fast signal generation, and cost-effectiveness. Moreover, EC-LFAs benefit from large detection range, high reproducibility, and possibility for real-time measurements. The miniaturization together with high analytical performance can be easily achieved not only in the fabrication of the electrodes, but also for the necessary instrumentation, all at a relatively low cost. The advantages of micro- or even nano-sized electrodes promote the use of very small sample volumes and improve the

sensing performance, unlike optical based detection where miniaturized system can lead to poorer sensitivity. Another very important characteristic of electrochemical detection is its low level of interferences from complex sample matrices, such as in clinical or food samples, which is a great advantage over the optical detection techniques^[116]. Additionally, the development and continuous improvement of the screen-printing technique and ink material formulation facilitate their facile integration into electrochemical biosensors. One of the most desirable characteristics is their cost effectiveness and mass production possibilities of such systems^[78]. The materials used for this technique are also disposable, simple, have low power requirements, quick response, high sensitivity and the ability to operate at room temperature^[117]. Moreover, the electrochemical performance can be further improved through developing of signal tracer in similar manners achievable for naked-eye detection, fluorescent or chemiluminescent readings, i.e., incorporating a large number of signal tracer in a single label. Another interesting advantage of electrochemical detection that is the feasibility of label-free detection.

Modes of signal generation in EC-LFA.

The most popular techniques for signal generation in EC-LFAs are voltammetry, amperometry, and impedimetry as can be seen in Table 1. While for voltammetry the current is measured at a potential varying over time, amperometric current is measured at a constant potential. Voltammetry and amperometry based techniques typically require a redox indicator to detect a signal. A well-known and most used method for investigating electrochemical reaction at an electrode is cyclic voltammetry (CV). The potential is applied as a triangular waveform, generating current vs potential in a cyclic wave form. Normal pulse voltammetry (NPV), differential pulse voltammetry (DPV), and square wave voltammetry (SWV) are voltammetric methods in which the potential follows more complicated patterns. Alternative to DC potential, electrochemical impedance spectroscopy (EIS), which measures the impedance in dependence of the frequency of the applied AC potential, has been applied to LFA ^[118]. The electrochemical techniques can be label-based (enzyme, nanoparticles, etc.) or label-free platform. As shown in Table 1, EC-LFAs utilizing SWV^[119–124], chronoamperometry (CA)^[125–128], chronocoulometry (CC)^[129], EIS^[118,130–132], stripping voltammetry^[122,133] and CV^[134,135], have been demonstrated with low detection limits and wide linear ranges. SWV is the most advanced form of voltammetry, which uses a staircase potential function in combination with potential pulses of constant amplitude^[136] to diminish the charging current, present in CV, also enabling a fast measurement and high sensitivity. A simple technique based on CA with good signal-to-noise ratio, still enabling sensitive detection and real-time measurement, is also popular. Stripping voltammetry is considered a very sensitive technique for quantitative determination of small molecules. A pre-deposition step prior to detection allows the intimate contact between the analyte of interest and electrode surface. In LFAs, metallic or ionic signal tracers, e.g., QD containing cadmium^[133] and bismuth ions^[122] have been used. The acid induced release of cations from the nanoparticles is initially performed prior to electro-deposition onto electrodes. Multiplex detection is feasible when various signal tracers are used.

Enzyme generated electroactive products have been widely studied^[119,120,124,127–129,132,134,137] to increase the sensitivity and selectivity of the system. However, the immobilization and stabilization of the enzyme can be complicated, which could also increase the cost of the sensor and affect the overall stability of the system. Moreover, in case the enzyme reaction takes place at the test zone where the electrode and capture probes are located, fast reaction and efficient electron transfer between the enzyme and the electrode is required. However, it is more favorable to place electrodes downstream after the capturing zone.

In contrast to other techniques, electrochemical detection in LFAs can be performed without tracer. For direct assay formats, after analyte has bound to the biorecognition element immobilized on the electrode, an increase in impedance at the electrode electrolyte interface can be monitored. For the competitive format, on the other hand, the impedance is theoretically decreased when analyte is present^[118]. In addition to EIS, direct oxidation or reduction of electroactive analyte after binding to biorecognition element immobilized on an electrode can be monitored by CA^[125]. The label-free LFAs could be advantageous due to the reduction of assay cost. However, it should be noted that electrode materials must be very sensitive and facilitate efficient electron transfer in order to detect small changes and enable electrochemical reactions, respectively. Therefore, microelectrodes or nanomaterials have been used for this purpose.

Table 1.1 LFAs based electrochemical detection with their analytical performance

Analytes	Electrode type	Method	Signal tracer	Electrode assemble Strategy	LOD	Linear range	Reference
Clenbuterol	PANI@GO /ITO	EIS	-	Strip between the electrodes	0.12 ppb	0.12–58 ppb	[118]
Organophosphorus pesticide	SPE	SWV	acetylcholine esterase	Test zone cut with cutter embedded in plastic case	0.02 nM	0.05-10 nM	[119]
Alpha-fetoprotein	SPE	SWV	HRP	Electrode under test zone	0.5 ng/mL	1-100 ng/mL	[120]

PSA	SPE	SWV	CdSe@ZnS QD	Electrode under test zone	0.02 ng/mL	0.05-4 ng/mL	[121]
hCG	SPE	SWASV	Bi ³⁺	Electrode under test zone	1 mIU	0-70 mIU	[122]
Lead and Cadmium	SPCE	SWV	-	Electrode over the test zone	7 and 11 ppb	10 to 100 ppb	[123]
Trichloropyridi nol	SPCE	SWV	HRP	Test zone cut with cutter embedded in plastic case	0.1 ng/ml	0.1–100 ng/mL	[124]
8-OHdG	CNT paper	CA	-	Electrode over the test zone	3.11 ng/ mL	0–150 ng/mL	[125]
Myeloperoxida se	SPE	CA	MBs (separation) and HRP	SPE printed on the membrane	0.18 ng/mL	0.25-8 ng/mL	[126]
Testosterone	Gold electrodes made by lithography	CA	HRP	Test zone cut	1 ng/mL	1–625 ng/mL	[127]
Troponin I	ITO	CC	Gal and An- GP	Electrode over the test zone	0.1 pg/mL	0.1 pg/mL – 100 ng/mL	[129]
PSA	Interdigitate d-SCPE	capacitan ce	urease	Electrode over the test zone	1 ng/mL	0-30 ng/mL	[132]

Cardiac Troponin T	SPE	CV	HRP	Electrode under test zone	0.15 ng/ml	0-700 ng/mL	[134]
Dengue NS1 protein	SPGE	CV	TEMPO tagged AuNP	Electrode under test zone	50 ng/mL	0–1000 ng/mL	[135]
8-OHdG and PSA	-	Glucose meter	Invertase	Test and control zone cut	0.23 and 1.26 ng/mL	0.1-100 and 1-100 ng/mL	[137]
Hg(II) ions	SPE	SWV	HRP	Test zone cut	30 pg/mL	0.1-200 ng/mL	[138]

Abbreviations: magnetic beads (MBs), galactosidase (Gal), 4-amino-1-naphthyl β -D-galactopyranoside (AN-GP), 4-amino-1-naphthol (AN), polyaniline@graphene oxide/indium tin oxide (PANI@GO/ITO), 8-hydroxy-2'-deoxyguanosine (8-OHdG), prostate-specific antigen (PSA), and square wave anodic stripping voltammetry (SWASV)

1.4.4 Integrating electrochemical transducers into LFAs

The concept of an LFA coupled with an electrochemical transducer is highly promising as discussed in the previous section. However, fabrication and integration of electrochemical transducers into LFAs are crucial to their successful translation into commercial products. In this section, we aim to give an overview on how electrochemical transducers can be fabricated and integrated into LFAs and discuss the pros and cons of each method.

External electrodes

Screen printed electrodes (SPEs) are well-established disposable transducers that have been widely combined with LFAs (see also Table 1). Although SPEs have been already employed in LFS for more than two decades^[53,139], the principle in their fabrication technology has basically remained the same. Different integration strategies that have been employed in the past years are summarized in Figure 1.5. The external electrode can be mounted either underneath (Figure 1.5A) or above (Figure 1.5B) the NC

membrane at or after the test zone. For the detection of prostate specific antigen (PSA) Fernandez-Sanchez et al made use of screen- printed carbon electrodes (SPCEs) coupled together with an LFA. In this case, the SPCE with an interdigitated electrode configuration was turned upside down and positioned over the Ab capture line of the LFS. Here, they used urease as a signal tracer which can catalyze hydrolysis of urea substrate into ammonia. The increase of pH due to ammonia thus resulted in degradation of the polymer layer coated on the electrode in which a change in the capacitance was monitored^[132]. It should be noted that even though the authors achieved a satisfying detection limit for determination of free- and total PSA levels, the response time was relatively long especially at low PSA concentrations (> 700 s). This could be attributed to the complex signal attainment, i.e., hydrolysis to generate an intermediate to subsequently trigger polymer degradation, which is highly dependent on diffusion of urea and ammonia. The poor contact between electrodes and the Ab capture line could result in low sensitivity, long response time and poor reproducibility of the assay.

In a similar integration approach, Lu et al combined SPE with an immunochromatographic strip and used it together with a coupling strategy of bismuth ions to the antibody. Here, the electrodes were placed underneath the strip directly at the test zone. The bismuth ions were released by addition of 1 M HCl and then detected via square wave anodic stripping voltammetry (SWASV) in order to quantify the target analyte^[122]. Furthermore, QDs were also implemented in such types of LFS, where the Cd present in the QD was also detected via SWASV. This strategy proved to be highly sensitive and an LOD of 20 pg/mL of PSA was achieved for QDs either made from CdS@ZnS or CdSe@ZnS^[121,133]. The stripping analysis-based approach is highly advantageous to the sensitivity of EC-LFA, in particular with an external electrode, as an efficient recruitment of signal tracer to the electrode surface could be achieved. The contact between electrodes and LFS may be less prone to affect the sensitivity and reproducibility in comparison to the work shown by Fernandez-Sanchez et al^[132]. However, when SPCEs are used, pre-treatment is necessary to ensure sufficient hydrophilicity and surface homogeneity as they are of importance in attaining greater electrodeposition of metal ion tracers. Further research attempt in this area should focus on developing environmentally friendly metal nanoparticle tracers, e.g. AuNPs, and stripping analysis without using mercury.

A similar integration system was implemented for detection of Alpha-Fetoprotein (AFP) in human serum samples. The sandwich type immunoassay contained HRP and anti-AFP antibody co-immobilized on AuNPs. HRP induces catalytic oxidation of O-Phenylenediamin (OPD) in the presence of H₂O₂ that can be detected by SWV^[120]. It should be noted that the electrochemical measurement in a stagnant condition, especially in voltammetry-based techniques, requires a confined detection area. In order to do this, the authors simply created two lines as a hydrophobic barrier on the LFS, where the test line was located in between, by using a liquid blocker pen mini super pap. This technique has been also implemented with stripping analysis after formation of immunocomplex on LFS^[121,133].

Sinawang et al used screen- printed gold electrodes (SPGEs) to immobilize capture antibodies against NS1 protein directly on the electrodes, thus forming a sandwich immunoassay with the detection antibodies and ferrocene molecules attached to AuNPs. The SPGE was placed at the end of the cellulosic LFS (Figure 1.5A-ii) where the detection was performed by CV^[131]. The work highlighted the ability to integrate the modified SPGEs into a compact cassette that further assists a precise alignment of lateral flow on electrode surface as well as a tight contact between electrodes and LFS, thus minimizing variation between devices.

In addition to placing a whole electrode piece on top, at bottom, and at the end (Figure 1.5A and B), the NC membrane can be sandwiched in between two electrode pieces which serve as a working and a counter/reference electrode as illustrated in Figure 1.5C^[125,140]. This electrode assembling configuration is highly attractive for implementation with reversible redox markers as the distance between the two electrodes defined by the thickness of thin layer paper could be sufficiently small for redox cycling^[141].

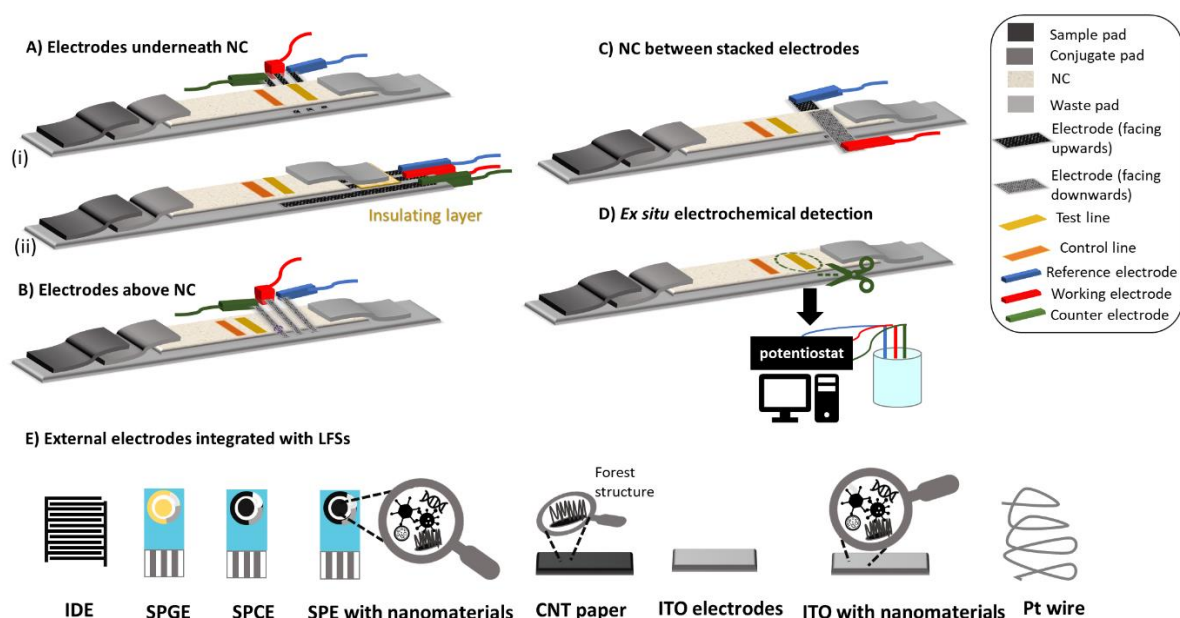


Figure 1.5. Scheme of existing principles to integrate electrodes into LFS: A) electrodes underneath NC with the different electrode orientations (i and ii), B) electrodes placed above the NC with the electroactive surface facing downwards, C) NC membrane positioned in between the stacked electrodes in a two-electrode configuration, D) cutting of the test zone and performing electrochemical measurement off-strip, and E) types of electrodes and modifications which were demonstrated in developing of EC-LFA.

A wide variety of electrodes other than SPEs, e.g., indium tin oxide (ITO) or electrodes made from carbon nanotube (CNT) paper, have been implemented in EC-LFS (Figure 1.5E). ITO was coated on a glass substrate as a three-electrode setup via photolithography, placed in contact with the NC membrane and clamped before the absorbent pad where the working electrode (WE) was positioned at the test zone (Figure 1.6A)^[129]. In addition, electrodes made from Toray paper coated with Pt/C and AuC acting as cathode and anode, respectively, of a microfluidic fuel cell assembling in the EC-sandwiched LFS format (Figure 1.5C) could serve as a good candidate for electrochemical sensing in LFAs^[140]. A

colorimetric and electrochemical detection was combined on an LFS containing a paper electrode for the detection of a DNA oxidative damage biomarker (8-OHdG) (Figure 1.6B). A conductive CNT paper strip was used as a WE, being placed on the control line whereas a copper paper painted with Ag/AgCl ink was implemented as a reference electrode (RE). The detection limits achieved via CA and colorimetric detection were found to be very similar in the range of 5-8 ng/mL^[125].

Apart from flat electrodes, Pt wire has been also employed as a WE in an LFS that consisted of two NC membranes set in contact at the conjugate pad (Figure 1.6C). In this work, acrylic substrates were used to seal the membranes together with the Pt wire (WE) and Ag wire (RE) with screws. The enzyme labeling strategy utilized IgG antibody and glucose oxidase (GOx), to detect mouse IgG via CA^[128]. This design permits the quantitative electrochemical detection in a single step as all necessary reagents are accommodated within the LFS.

In fact, using external electrodes in LFS could minimize electrode fouling from complex sample matrices because binding between bio-receptors and analytes can take place only on the LSF prior to integrating to an electrode. By far, external electrodes produced by screen-printing technology are more attractive and promise simpler integration into LFS than the others, e.g., CNT paper and Pt wire. The current screen-printing technology commonly provides SPEs with high reproducibility from electrode-to-electrode and batch-to-batch. However, after their integration into LFSs, good reproducibility is often hard to achieve which is mainly attributed to variation of contact strength between electrodes and LFS. This problem has been overcome by using a cassette^[131] or lamination^[125].

Ex situ electrochemical detection

A different strategy for electrochemical detection developed in combination with an LFA involves cutting the test line after the assay is performed. For example, in order to detect testosterone, Inoue et al formed the immunocomplex as normally conducted in LFAs but the test line was later cut and transferred to an external electrochemical cell to determine the activity of the HRP that labeled testosterone Ab. The quantification was performed in ferrocene methanol and H₂O₂ via CA^[127]. Similarly, Wang et al. developed a system by coupling AuNPs with HRP and antibody against Hg (II) ions. The test zone was cut and added into an electrochemical cell containing the substrate solution. The quantitative detection was achieved by SWV based on the HRP reaction catalyzed by the oxidation of OPD in the presence of H₂O₂^[138].

Manually cutting a test zone for further electrochemical measurement may cause variation between assays. This problem could be overcome by assembling LFS in a housing device with an integrated cutter that is located over the test zone as shown by Du et al (Figure 1.6D). Herein, after precise cutting, the test zone was dropped directly into the microelectrochemical cell located underneath^[119]. Followed by addition of reaction reagent, e.g., substrate for enzyme, detergent for liposome, or acid solution for

QD tracer, to the microelectrochemical cell, the electrochemical measurements can be performed in a more reproducible manner.

To achieve the measurement by affordable home-based electrochemical devices such as a personal glucose meter (PMG), some studies have demonstrated assay platforms that can produce glucose as a signal generation molecule. For example, Zhu et al employed invertase/Ab-AuNP as a signal tracer in LFA for a sensitive quantification of 8-OHdG and PSA. The immunocomplex was initially performed on a traditional LFS where the test and control lines were cut and immersed into sucrose solution. The invertase can convert sucrose into glucose which can be subsequently measured by a PGM^[137]. The use of PGM was also established for quantification of phosphor-p53¹⁵ (a biomarker for gamma radiation exposure). Instead of an enzyme, liposomes encapsulating glucose were used as a signal tracer. The cut test line was transferred in a detergent solution to release glucose prior to measuring by PMG^[142].

Performing electrochemical detection off-LFS is actually similar to the case of external electrodes. Nevertheless, *ex situ* electrochemical detection may provide better sensitivity and reproducibility as the available electrode surface is not hindered or interfered by NC membrane laid on top or underneath. Among all examples described above, the signal transduction strategy based on glucose detection is the most attractive manner to implement in real-world applications owing to the well-established technology of PGM. However, it should be noted that all strategies based on *ex situ* detection still introduce inconvenience to users.

Internal electrodes

With the progress in screen-printing technology and other electrode fabrication techniques, it becomes feasible to generate electrodes onto or into LFSs. As shown in Figure 1.6E, a three-electrode system can be screen-printed directly on the LFS. The fabricated EC-LFA device was applied for the quantification of myeloperoxidase (MPO) in human serum^[126]. Here, the sandwiched immunomagnetic complex was initially formed off-strip prior to transferring the solution to LFS for separation purpose. The complex was trapped over the electrode by a magnet placed underneath. Nevertheless, the proposed work encountered some shortcomings with respect to the retention of immunomagnetic complex over the specified electrode area during washing on LFS. Here, while large solution volume assists the flow, the confinement of the immunomagnetic complex was troublesome. Additionally, employing a large and strong magnet could induce clustered immunomagnetic complexes and interfere the subsequent electrochemical signal.

Human cardiac troponin T was also detected using an internal SPE underlying a lateral flow membrane. Unlike the previous study^[126], the capture antibodies (anti-cardiac troponin T) were modified onto the electrode and the sandwich assay was conducted together with the enzyme HRP labeled antibodies^[134]. With respect to the handling, the strategy is more user-friendly than immunomagnetic separation.

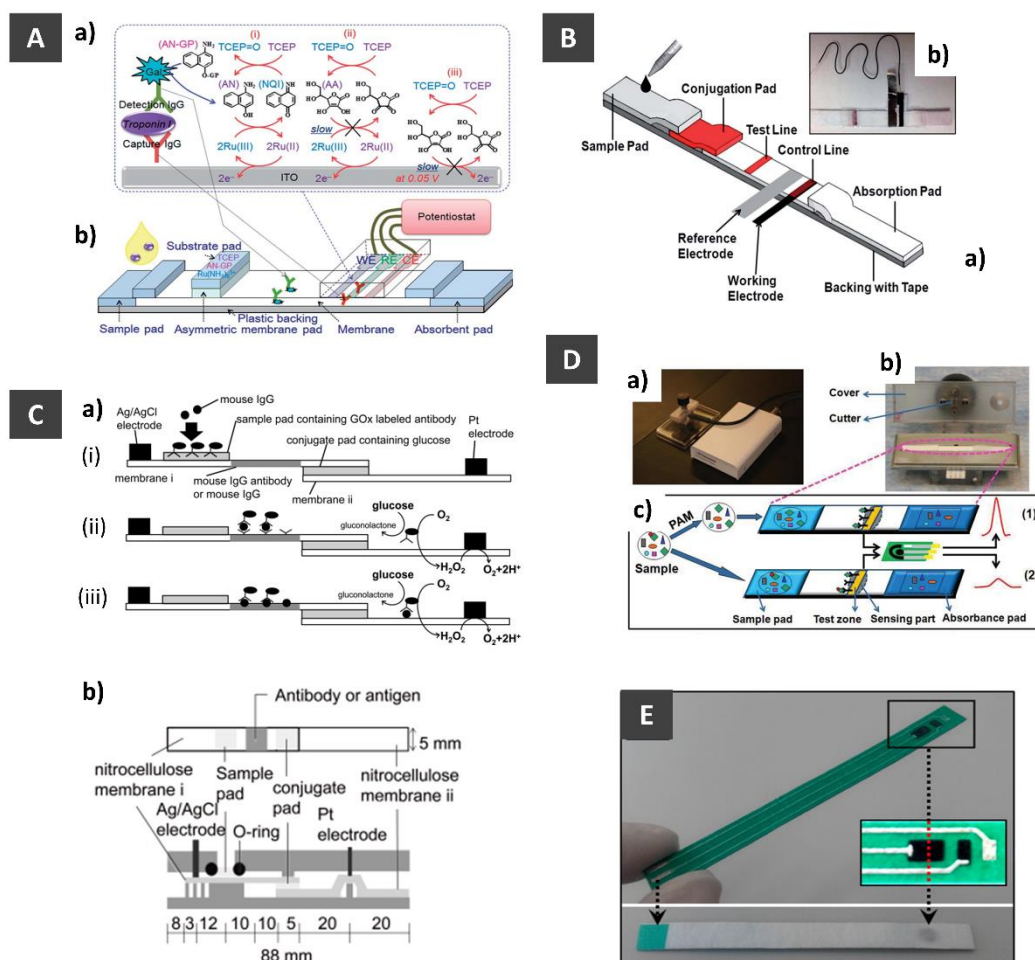


Figure 1.6. Representative exemplary EC-LFAs with various electrode configuration integrated into LFS as well as assay platforms. A) ITO electrode-coated glass plates assembled onto LFS (b) and detection principle (a), reprinted from ^[129] with permission from Royal Society of Chemistry, B) scheme of CNT conductive paper integrated immunostrip (a) and photograph of actual device adapted from ^[125] with permission from Royal Society of Chemistry, C) scheme of single-step quantitative EC-LFS using glucose oxidase (GOx) as signal tracer (a), and components of LFS at the top and side view (b) adapted with permission from ^[128]. Copyright (2017) Japan Society for Analytical Chemistry, D) Integrating cutter into an LFS holder for precisely cutting the test line adapted from ^[119] with permission from American Chemical Society, and E) internal screen-printed electrodes on LFS reprinted from ^[126] with permission from John Wiley and Sons.

Overall, the strategies mentioned above possess their own pros and cons. Placing commercially available SPE or other electrodes above, underneath, or at the end of an LFS is a straightforward manner which combines existing LFA technology with a well-established and reliable electrochemical transducer. However, intimate contact between electrode surface and LFS has to be established to ensure the desired detection sensitivity. Moreover, too tight or too loose contact may lead to poor reproducibility between LFS devices. Therefore, chip holders that can specify the exact location and provide consistent contact between LFS and electrode should be developed in this case. Similar to on-LFS detection, the strategy based on cutting the test line and performing electrochemical measurement *ex situ* benefits from the well-established technologies that render reliable results of the measurement. In addition, neither

intimate contact nor specific electrode location has to be concerned. However, the strategy may suffer from poor reproducibility due to improper handling by end-users. A cutter built into the LFS holder demonstrated by Du et al could be a good solution^[119]. However, creating electrodes directly on the LFSs is more attractive than the aforementioned strategies. Despite holding a great potential to enable robust EC-LFA, LFAs with internal electrodes have been so far scarcely explored which requires more research attention in the future.

1.4.5 Conclusions and future perspectives

A lot of effort focused on the improvement of the sensitivity of lateral flow assays over the last decades, yet it is still a long way to move this technology toward truly challenging applications. This includes not surprisingly the need to detect a variety of target analytes at low concentrations in a rapid manner while maintaining the key platform features of portability, low cost and easy adaptation to use in areas with limited resources. In our opinion, the integration of electrochemical detection into a lateral flow assay is highly desirable, enabling quantitative detection with high sensitivity for precise diagnostics that should come into focus in the future. Missing so far are studies to better understand the influence of flow rates on the electrochemical performance and how this can be engineered to favor a better performance. Electrochemical transducers have the potential to easily be further extended to multiplex testing, for example using nanoparticles made from different encoding metals, that can be detected simultaneously by stripping voltammetry on a single electrode. Furthermore, their simple fabrication can be easily extended to array production, allowing modifications with different immobilized receptors for a broad range of analytes. Potential interferences from sample matrices can be avoided by dilution of the sample or via magnetic separation. The former strategy obviously requires high-performing electrochemical transducers. The latter could be beneficial in case the electrochemical transducer is not sensitive enough, as the use of magnetic beads allows the complex to be entrapped on the electrodes, promoting the tracer in close contact to the electrode surface.

In addition, current electrochemical-lateral flow assays (EC-LFAs) rely mostly on well-established commercially available electrodes such as SPEs. The proposed integration strategies into LFS are however not yet robust as they require some extra efforts in terms of instrumentation and human inputs. It would be therefore more favorable to develop LFS with self-contained internal electrochemical transducers, but this has been rarely demonstrated so far. The development would make EC-LFAs highly competitive to widely used optical-based detection but with rather relatively low-cost and high sensitivity. In order to robustly integrate electrodes into LFSs, screen-printing electrode materials onto nitrocellulose membrane could be a promising strategy. However, the limited active surface area may result in poor assay sensitivity. Therefore, it is much more desirable to generate electrodes with an elevated electroactive surface area for EC-LFA.

Furthermore, electrochemical transducers allow their versatile tuning by modification with nanomaterials. Nanomaterials like nanofibers can easily be modified to bear different functionalities not only as part of the transducer but also for sample preparation, such as trapping interfering molecules prior to reaching the transducers.

Considering that strategies for sensitive and fast detection are available, have been well-studied and rather well-understood as described in this article, efforts should now be oriented towards innovation needed for their commercialization as POC devices. The simplicity of the assay itself will need much attention as successful EC- LFAs must avoid additional steps. Inherently, electrochemical transducers benefit from inexpensive fabrication techniques, important for single-use devices. Sustainable production and disposal must be studied and may be not too challenging for carbon-based transducer materials.

Nowadays it is obvious how bulky, expensive lab-equipment can be replaced by small, handheld, useful gadgets. An important example is the potentiostat, which was miniaturized and can now easily be plugged into a smartphone and used for measurement. Unique features make the implementation of high-performance sensors thus adaptable to everyday life. With a simple Bluetooth connection, the potentiostat can be connected to the smartphone, which already accounts for high computing power similar with bench computers. This enables not only the possibility of home testing, but also an easy display of the results, which can be automatically saved into a shared cloud or transferred immediately to doctors or data scientists. Additionally, in a suited application software machine learning can be encoded, which can make data analysis more accurate and can easily identify possible problems. Considering the great impact electrochemical transducers had on the point-of-care market such as in the glucose sensors, EC-LFAs will be able to harness all of the associated advancements and hence significantly improve the traditional lateral-flow-assay and hence further their success in point-of-care applications.

II. Motivation and structure of the thesis

Electrochemical sensors based on nanomaterials have been researched for a long time, with significant improvements in sensitivity, selectivity, and simplification of fabrication techniques. An interplay between electrochemistry, biosensors, and microfluidics is beneficial for implementing electrochemical transducers into POC devices. Microfluidics aims to integrate different laboratory processes into one platform. Electrochemical sensors are attractive to be merged with microfluidic channels due to their possible simple integration. A typical way to achieve this is to pattern electrodes by inkjet printing onto a flat substrate (glass or silicon) and fabricating another substrate incorporating a microchannel. The electrode position and flow rate significantly influence the performance of the electrode. The main advantage of such a system is that the electroactive species are confined near the electrodes, which can significantly improve sensitivity.^[35] However, the flat electrodes have limited electroactive surface area (ESA) and limited contact with the electroactive species in the solution. Moreover, the rigidity and substrate of the electrodes can limit their miniaturization and integration into microfluidic devices. Therefore, porous, and freestanding nanofiber-based transducers are proposed to address these challenges.

Chapter 1 discusses nanofibers in general: definition, different fabrication possibilities, and the various types of nanofibers. As the interest for this work lies in the development of electrochemical sensors, carbon nanofibers are of particular interest and were discussed in the following subchapter. Carbon nanofibers are described related to their structure and general properties. In the following, applications of CNFs in electrochemical sensing are reviewed. As a possible application of CNFs, POC devices are defined and described. Lastly, LFAs are reviewed, and their versatility is discussed. The highlights lie in the integration examples of electrochemical transducers in LFAs. Concluding the discussed examples, there is a lack of porous substrate-free transducers with flow-through possibilities, which could offer benefits when integrated into an LFA.

It is crucial to develop a freestanding material that could enable very efficient interaction between redox species and an electrochemical transducer for possible integration into a microfluidic system. As mentioned, there is a strong link between electrochemistry and microfluidics to address current challenges. Therefore, three-dimensional (3D) porous electrochemical transducers can tackle the small ESA and the efficiency in the interaction between the analyte and the electrode. Additionally, a substrate-free porous electrode could be easily implemented into a microfluidic channel. However, current fabrication techniques of 3D porous electrochemical transducers are laborious, complicated, and require expensive equipment.

Our research group developed a new technique for creating porous electrodes. The fabrication strategy exploited the benefits of electrospun nanofibers from a polyimide precursor mixed with metal salts such

as iron^[14] or nickel^[42]. First, the polyimide solution was electrospun into nanofibers collected on an indium-thin oxide (ITO) substrate for 15 minutes. The carbonization is achieved with a CO₂ laser in a simple and patternable manner rendering so-called laser-induced carbon nanofibers (LCNFs). Even though this strategy has many advantages, such as simplicity, versatility, and robustness, the electrodes are firmly attached to the substrate (ITO), which can hinder a simple integration into a microfluidic channel. Furthermore, the ITO substrate is conductive, which hinders the fabrication of a complete electrochemical cell consisting of WE, CE, and RE. The current flow on the conductive substrate would lead to short-circuit between the three electrodes limiting their use in real applications.

Therefore, much effort was put into developing a porous substrate-free electrochemical transducer. The investigations leading to a porous freestanding CNF-based electrode system were conducted in a project related to this thesis beforehand. The successful fabrication of LCNF on an insulating substrate was achieved by using filter paper as a substrate. Furthermore, by increasing the collection time of the nanofibers, thick and homogenous mats were achieved, which enabled the elimination of the filter paper rendering freestanding nanofibers. The obtained nanofibers and their carbon counterparts were investigated with different redox mediators, which showed a superior ESA compared to the LCNF on ITO. The LCNF exhibited an excellent response toward dopamine sensing, which was investigated in more detail. These studies will be presented in **Chapter 3**. Even though they were part of the Master thesis related to this PhD thesis, they represent important information for the story's completion.

At the beginning of this thesis, the selectivity of the electrochemical sensor toward dopamine detection was investigated. As mentioned in the introduction, an essential characteristic of a sensor is selectivity. This is mainly achieved through biorecognition elements in biosensors, but selectivity can also be achieved through other means. **Chapter 3** presents studies showing the successful hindrance of the interfering molecules (uric acid and ascorbic acid) achieved by applying Nafion. Numerous experiments have been conducted at this stage to show the stability and reliability of the three-electrode setup made just from LCNF. **Chapter 3** comprises not only the developing procedure for freestanding LCNF-based electrodes but their implementation into a microfluidic channel and their application for the detection of the neurotransmitter dopamine in a mixture containing common interfering species.

Voltammetry is the most popular strategy implemented in electrochemical sensors. Among its advantages, merging it with redox cycling as an amplification can be advantageous for improving the sensitivity of electrochemical sensors. **Chapter 4** investigates two different LCNF electrodes strategies for redox cycling. Redox cycling is achieved only for small electrodes in such proximity that their diffusion layers overlap. Therefore, different sizes were implemented for the finger-like electrodes in an interdigitated electrode (IDE) array. Their fabrication was studied concerning finger and gap size. A direct correlation was found between the collection time and the ESA of the array. The fabricated IDEs were successfully implemented for redox cycling. Since the advantage of the flow-through can be exploited in a horizontal and vertical flow, the freestanding LCNF-based electrodes were stacked upon

each other with a non-carbonized nanofiber mat in between. In this regard, different strategies were studied, first electrospinning directly onto the electrodes and the second transferring a nanofiber mat onto electrodes. Both strategies showed the possibility of generating regeneration of the redox molecule. Lastly, it is discussed how these two systems can be further integrated into microfluidic platforms for POC applications.

The introduction presents the current status of LFAs and the possible advantages of having such strips incorporating electrodes towards the quantification of analytes. As mentioned, planar electrodes have shown limited sensitivity in such electrochemical LFA. In **chapter 5**, LCNF will be investigated towards their integration in electrochemical LFA. Different electrode setups are studied to maintain the proper functioning of the electrochemical transduction but to simplify the system used until the current stage. Moreover, the strip is optimized with respect to width and components, such as the waste pad and plastic foil, for sealing the electrodes. After the proper functioning is demonstrated, liposomes are exploited as labeling strategies. For proper lysis, different surfactants and their implications are considered. For a proof-of-concept, biotinylated liposomes are employed to a lateral flow strip modified with polystreptavidin. The subsequent detection of the encapsulated redox molecules demonstrates an efficient binding of the liposomes on the strip. In the last part of **chapter 5**, a nucleic acid detection is realized for a waterborne pathogen. In this regard, reporter probes for *Cryptosporidium parvum* are immobilized onto the surface of the liposomes. A successful detection was demonstrated with a low detection limit for the target DNA of the pathogen.

To conclude this work, **chapter 6** summarizes the results obtained for the freestanding LCNF-electrodes for their different applications. The key findings concerning material characterization, electrochemical performance, and general accomplishments are highlighted. Moreover, problems of current design and challenges will be addressed. Lastly, future perspectives are discussed, and possible applications are elaborated.

III. Freestanding 3D-interconnected carbon nanofibers as high-performance transducers in miniaturized electrochemical sensors

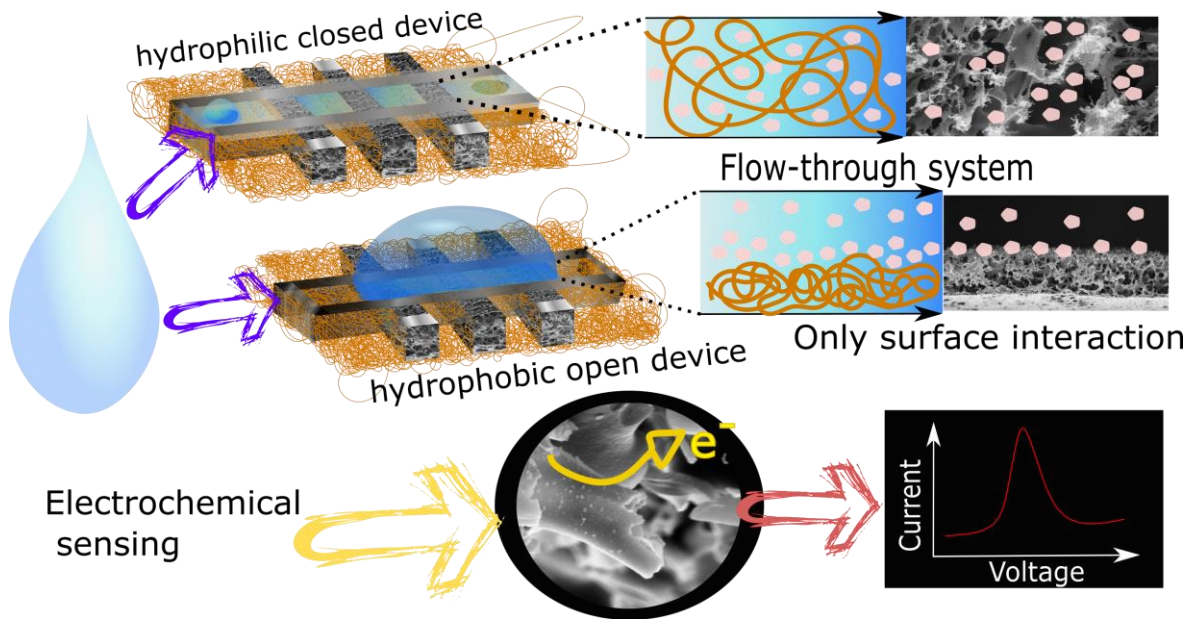


Figure 3.1. Three-electrode setup made from LCNF electrodes in a closed configuration with hydrophilic electrodes surface, where the analytes interact with the hole 3D surface of the CNFs. The second configuration consists of three hydrophobic electrodes, where the solution only lies on the surface of the electrodes.

3.1. Abstract

3D-carbon nanomaterials have proven to be high-performance transducers in electrochemical sensors but their integration into miniaturized devices is challenging. Herein, we develop printable freestanding laser-induced carbon nanofibers (f-LCNFs) with outstanding analytical performance that furthermore can easily allow such miniaturization through a paper-based microfluidic strategy. The f-LCNF electrodes were generated from electrospun polyimide nanofibers and one-step laser carbonization. A three-electrode system made of f-LCNFs exhibited a limit of detection (LOD) as low as 1 nM (S/N = 8) for anodic stripping analysis of silver ions, exhibiting the peak at ca. 100 mV vs f-LCNFs RE, without the need of stirring. The as-described system was implemented in miniaturized devices via wax-based printing, in which their electroanalytical performance was characterized for both outer- and inner-sphere redox markers and then applied for the detection of dopamine (the peak appeared at ca. 200 mV vs f-LCNFs RE) with a remarkable LOD of 55 pM. When modified with Nafion, the f-LCNFs were highly

selective to dopamine even against high concentrations of uric and ascorbic acids. Especially the integration into closed microfluidic systems highlights the strength 3D porous structures can bring to bear providing excellent analytical performance and paving the way for their translation to affordable lab-on-a-chip devices where mass-production capability, unsophisticated fabrication techniques, transfer-free, and customized electrode designs can be realized.

This chapter has been published and formatted to fit his thesis:

Perju, A., Baeumner, A.J. & Wongkaew, N. Freestanding 3D-interconnected carbon nanofibers as high-performance transducers in miniaturized electrochemical sensors. *Microchim Acta* **189**, 424 (2022). <https://doi.org/10.1007/s00604-022-05492-2>

3.2. Author contributions

The author and Dr. Nongnoot Wongkaew contributed equally to designing and conducting the experiments and evaluating the data. The author and Dr. Nongnoot Wongkaew wrote the manuscript draft. Prof. Dr. Antje J. Baeumner led the project administration and promoted manuscript preparation.

3.3. Introduction

Three-dimension (3D) carbon nanomaterials, e.g. graphene foam and carbon nanofibers, possess intrinsic beneficial architectures, besides their favorable electrical conductivity and low material costs, that enable their potential use as a high-performance transducer in miniaturized electrochemical sensors ^[143]. In comparison to 2D-based graphene, the 3D architecture not only prevents the agglomeration of graphene sheets but also promotes greater interaction between analytes and the sensing interface. Additionally, chemical- or bio-functionalities, e.g., metal nanocatalysts or bioreceptors, respectively, can be facilely and uniformly incorporated into the material, promoting their applicability in chemo- and biosensors based electrochemical detection methods.

Various approaches have been reported for the fabrication of 3D graphene composites. Template-based methods are known as an effective strategy to generate 3D graphene with well-controlled morphologies. However, the methods suffer from high production cost and inherent complexity, in particular the need for template removal. Template-free based strategies such as hydrothermal technique ^[144], freeze-drying ^[145], and electrochemical deposition ^[146] are much simpler and less expensive, but the integration of the as-fabricated 3D graphene to the miniaturized electrochemical sensor is still an issue, in particular, in terms of mass-production feasibility. Even though 3D-printing of carbon materials promises high throughput manufacturing of electrochemical transducers with convenience, fast and customizable shapes, and designs, the dimensions of electrodes are typically limited to the millimeter range unless sophisticated instrumentation is applied. In addition, surface activation with harsh conditions is needed as the carbon materials contain insulating polymers, e.g. conductive graphene-doped polylactic acid filaments ^[147].

Despite their high-performance capability, 3D-carbon nanomaterials suffer from difficulties in integrating into microfluidic analytical systems due to their irregular shape, high thickness (in micrometers to millimeters range), and rough surface. A few studies attempted such integration, for example, graphene foam was manually inserted into a polydimethylsiloxane (PDMS) microfluidic channel ^[148]. Ali et al. filled photopolymers into graphene foam, and later selectively polymerized channel barriers prior to removing unpolymerized polymer with solvent ^[149]. Alternatively, a gel was filled into the 3D-PDMS porous scaffold before assembly and later removed by hot water ^[150]. The aforementioned methods are laborious, incompatible for mass-production, and prone to having poor batch-to-batch reproducibility.

Electrospun carbon nanofibers (eCNFs) make up their 3D structure via fibers with diameters in the range of a few hundreds of nanometers. Such eCNFs possess disordered graphitic structures exposing a number of edge sites that promote efficient electron transfer of electroactive species ^[28]. Nanofiber precursors are typically electrospun and heat-treated in a strictly controlled condition. Apart from tunable morphological/chemical characteristics of electrospun fiber precursors prior to carbonization,

the production is scalable and cost-effective. Previous studies in our group demonstrated the successful generation of eCNF electrodes from electrospun polyimide (PI) nanofibers through CO₂ laser pyrolysis, namely laser-induced carbon nanofibers (LCNFs), with great flexibility in shapes and designs. Excellent electroanalytical performances were achieved apart from fulfilling all requirements stated above. *In situ* generation of metal oxide decorated LCNFs was recently demonstrated with highly competitive performance for glucose sensing ^[42]. However, in those cases indium tin oxide (ITO) was used as a base substrate, hindering the generation of complete 2- or 3-electrode system configurations due to short circuits via conductive film (or other conducting collectors). Even though peeling of fiber mats from the surface of the conductive collector is feasible the resulting fiber mat's fluffiness and uneven mat thickness make reliable laser-carbonization impossible.

In this study, we, therefore, developed freestanding LCNFs (f-LCNFs) by a one-step laser exposure as well as a robust strategy to implement them into the miniaturized electrochemical device with an integrated microfluidic channel (figure 3.2). Herein, instead of collecting PI nanofibers on an ITO sheet, a non-conductive porous filter paper was used. The conditions in electrospinning and lasing process that render f-LCNFs with favorable morphologies were initially investigated. To demonstrate the analytical performance, the 3-electrode system made of f-LCNFs without assembly into the microfluidic devices was used for anodic stripping analysis of silver. Further integration into a microfluidic analytical system was realized through the transferred wax barriers. The electroanalytical performance of the f-LCNFs-integrated miniaturized system was assessed and compared with unenclosed devices through common redox markers, e.g., ruthenium hexamine (RuHex), ferri/ferrocyanide, and dopamine. Furthermore, a highly sensitive and selective f-LCNF device for dopamine detection realized from the as-developed device was demonstrated.

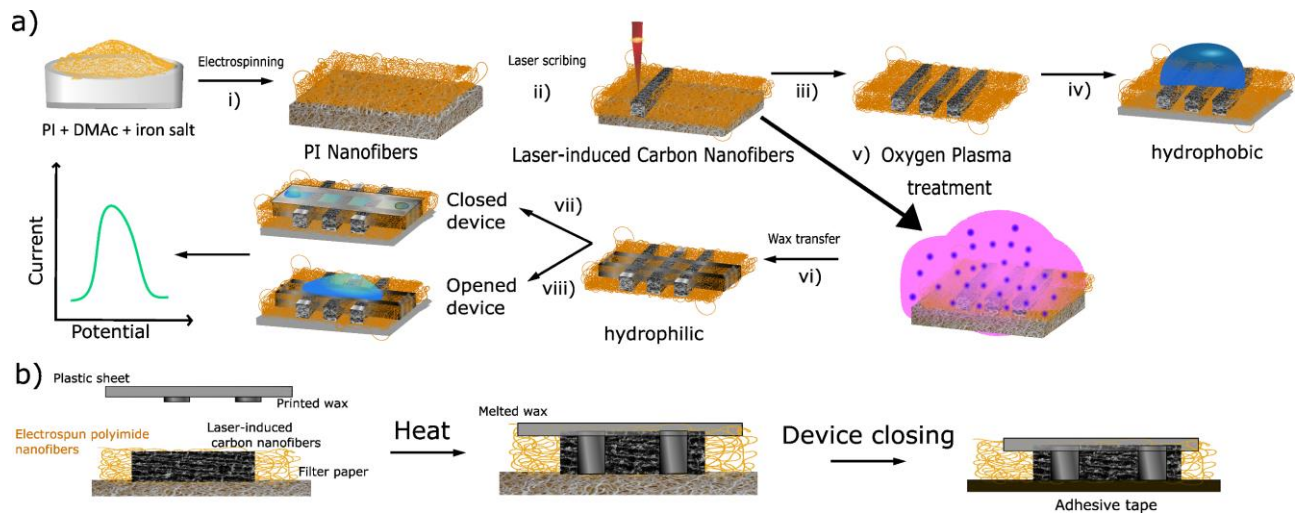


Figure 3.2. a) Fabrication of 3D-freestanding LCNF electrodes and their integration into a device. i) electrospinning of PI solution into precursor nanofibers collected on an oxygen plasma treated filter paper, ii) carbonizing PI nanofiber substrate, iii) releasing LCNF electrodes from the filter paper, iv) the device without any further treatment (hydrophobic-open device), v) increasing the wettability of the device via plasma treatment, vi) creating channel wax barrier and device assembling, vii) the device with plastic cover consisting of the wax channel (hydrophilic - closed device), and viii) the device after the removal of the plastic cover (hydrophilic - open device). b) Transferring of printed wax (step vi) onto the PI carried LCNF nanofiber substrate. The whole substrate piece and printed wax were sandwiched between two glass slides and placed on a heat plate (100 °C) until the wax is completely melted (~ 60s). The filter paper was afterwards removed before closing the channel with double-sided adhesive tape (step vii). A plastic sheet can be also added to another side of the tape, enabling a robust device and ease of handling. The plastic cover will be removed in case of opened device (step viii).

3.4. Experimental

3.4.1 Chemicals and reagents

A solvent-soluble polyimide (Matrimid 5218) was purchased from Huntsman Advanced Materials (Europe) BVBA Belgium. Iron (III) acetylacetonate ($\text{Fe}(\text{acac})_3$), nitric acid ($\geq 65\%$) (HNO_3), dopamine hydrochloride, hexaamineruthenium (III) chloride (RuHex), potassium ferricyanide ($\text{K}_3[\text{Fe}(\text{CN})_6]$), potassium ferrocyanide ($\text{K}_4[\text{Fe}(\text{CN})_6]$) were purchased from Sigma Aldrich, Germany. N, N-Dimethylacetamide (DMAc), and potassium nitrate (KNO_3) were purchased from Merck KGaA Darmstadt, Germany. Silver nitrate (AgNO_3) was purchased from Carl Roth GmbH Karlsruhe, Germany. Silver paint was purchased from Busch GmbH & Co. KG Viernheim, Germany. Filter paper MN616 with 90 mm in diameter and 200 μm in thickness (Ref. 432009) was purchased from Machery-Nagel Düren, Germany. Double-sided adhesive tape was purchased from tesa. Plastic sheets in A4-size were purchased from Exponent as Laser Films. Dropsens electrodes were purchased from Metrohm, Germany.

3.4.2 Fabrication of PI nanofibers via electrospinning

The PI nanofibers were fabricated by electrospinning the solution containing 15% (w/v) Matrimid 5218 (750 mg) and 5% $\text{Fe}(\text{acac})_3$ (37.5 mg) (unless stated otherwise) in 5 mL DMAc. In order to obtain a homogenous mixture, the solution is sonicated for 30 minutes prior to stirring overnight at room temperature. The solution could be used one to five days after the preparation without significant changes in nanofiber properties.

An electrospinning device (Spraybase®) connected to a syringe pump was used to generate PI nanofibers. Here, the solution was injected into the system by a 5 mL-glass syringe connected to a polytetrafluoroethylene (PTFE) tubing where a metal needle (inner diameter of 1.2 mm) was placed at the end. The distance between the collector and the needle was set to 15 cm. The flowing rate was chosen at 10 $\mu\text{L}/\text{min}$. Environmental conditions such as humidity and temperature play an important role in the electrospinning process. Therefore, the applied voltage, between the needle and the collector, has to be adjusted according to the two parameters. This can be usually changed from 13 to 17 kV. However, the optimum conditions for spinning the nanofiber were found to be at 20° C and around 40% relative humidity where the optimum applied voltage was ca. 16 kV.

The nanofibers were deposited on a filter paper (9 cm in diameter with a collecting area of 6 cm \times 6.5 cm) that was fixed on a metal collector. Prior to collecting the fibers, the filter paper was treated with O_2 plasma at 100 W (unless stated otherwise) to promote strong adhesion between the nanofibers and the paper's surface.

3.4.3 Laser-induced carbonization of electrospun PI nanofibers

A CO₂ laser with 10.6 μm wavelength from Universal Laser Systems, Polytech System GmbH was used to carbonize the nanofiber substrate. Its maximum power is 30 W, and its maximum speed is 1270 mm/s. The laser process was always set to 1000 DPI and 500 PPI. For the carbonization of the nanofibers, the 2-inch lens is used. The design of the electrodes was created using CorelDRAW. The nanofiber mat is first fixed in place with tape in the laser chamber to prevent the uncontrolled movement of the mat during the scribing process. The laser conditions were varied concerning laser power and speed. The optimum conditions were found to be 4% power and 80 % speed for the chosen fiber collection time. If the fiber collection time is varied the laser parameters must be adjusted accordingly. Each electrode is scribed separately.

3.4.4 Electrochemical characterization

The potentiostat PalmSens4 (The Netherlands) was employed for the electrochemical measurements. One electrochemical cell is fabricated containing a three-electrode setup, all of them are made from LCNFs. For detecting silver, anodic stripping voltammetry (ASV) was used. ASV consists of two main steps, including a deposition step and a stripping step. In the first step, silver is cathodically electrodeposited onto the surface of the working electrode by applying a constant negative potential. Then using linear sweep voltammetry (LSV) silver is stripped away from the surface by re-oxidation in the second step. Electroactive surface area (ESA) is estimated by the Randles-Sevcik equation shown below at the scan rate of 25 mV/s to 250 mV/s.

$$I_p = (2.69 \times 10^5) n^3 A C D^{\frac{1}{2}} v^{\frac{1}{2}}$$

where I_p is the peak current (mA), A is the ESA of the electrode investigated (cm²), D is the diffusion coefficient of ferricyanide (7×10^{-6} cm²/s), RuHex (9.1×10^{-6} cm²/s), and of dopamine (6.74×10^{-6} cm²/s) [151], n is the number of electrons transferred in the redox reaction, C is the concentration of the analyte in the bulk solution (M), and v is the scan rate (V/s). The value for the ESA is calculated from the slope of the I_p versus $v^{1/2}$ linear regression equation. Dopamine was detected via LSV. The resistance was measured with a four-point probe, containing a current source, Keithley 6430 SUB-FEMTOAMP REMOTE SourceMeter, and a Keithley Multimeter 2000 to measure the voltage between the inner two probes.

For open devices without plasma treatment a larger volume (approx. 50 μL) of solution is required to cover the three electrode strips while 10-30 μL is sufficient for the open and closed devices with plasma treatment in which 10 μL was used for these cases especially when f-LCNFs were employed as a reference electrode (RE). However, in case of using an Ag/AgCl external RE, 30 μL of sample was dropped on the plasma treated electrodes where the tip of RE can be inserted to the drop.

3.4.5 Morphological and mechanical stability characterization

The morphology of the nanofibers was characterized using a scanning electron microscope (Zeiss/LEO 1530 Germany) at 5.0 kV. Prior to imaging, the samples have been sputtered with gold for 30 s, which should create a layer of ≈ 7 nm. The confocal microscope Olympus LEXT 3D Measuring Laser Microscope OLS4000, Germany was used to determining the thickness of the mat and the side view of the device with and without wax. Images for optical measurements were taken with a light microscope (KERN optics).

Tensile strength measurements were performed using Instron 5566 testing machine. The nanofibers were electrospun for 90 minutes without any further modification. The filter paper was peeled off, so both PI nanofibers and PI carrying LCNFs were tested in a freestanding form.

3.5. Results and discussion

3.5.1 Fabrications of freestanding LCNFs and their characterizations

The collection of fiber precursors is generally performed on a conductive substrate, e.g. indium tin oxide (ITO) ^[14] to provide a uniform electric field during electrospinning. However, this underlying surface will interfere with electroanalytical applications resulting in mixed signals from nanofiber and underlying electrodes. Research was thus performed creating a strategy for the fabrication of freestanding fibers with uniform mat thickness. A non-conductive porous substrate such as a filter paper was chosen as a sacrificial layer, since it allowed for unhindered penetration of the electric field and generated a homogeneous fiber mat thickness (Figure 3.3a-i) and uniform nanofiber diameters (Figure 3.3a-ii). In the end, after laser exposure, by removing the filter paper highly porous freestanding laser-induced carbon nanofibers (f-LCNF) 3D mats with pore sizes in a few micrometer ranges were obtained (Figure 3.3a-iii and 1a-iv). Due to the roughness of the filter paper support, the f-LCNFs could easily be peeled off the support as well.

To achieve a suitable nanofiber substrate for f-LCNF generation various parameters were studied. The effect of iron content and lasing condition was initially assessed suggesting optimal concentrations between 5% and 7% iron (Fig. S3.1). Furthermore, it was found that thick and dense fiber mats are needed for reliable laser-induced pyrolysis (Figure 3.3b) in contrast to LCNFs made on ITO previously, which needed only 15 minutes collection times ^[42]. This implies that a conductive substrate assists with heat distribution during the laser carbonization process whereas the non-conductive substrate relies on the highly interconnected fiber network. In the end, an electrospinning time of 90 minutes was chosen as the electrical conductivity (156 S/m) and reproducibility of f-LCNF mats were best (Figure 3.3c).

After the collection of a homogenous nanofiber mat, the pattern of the electrodes was carbonized into the mat, as shown in Figure 3.2 step ii, obtaining ready to use electrodes (Figure S3.2a and S3.2b). The fabrication strategy is not only fast (3 minutes for each set of electrodes (Figure 3.3d) at the optimum laser speed) but also highly affordable considering the material costs of 0.01 €/electrode set (Table S3.1). Our current electrospinning setup allowed the fabrication of a 6.5 cm × 6 cm substrate accommodating 12 sets of three-electrode systems (Figure S3.2b). A higher number of electrode sets is feasible with larger collectors or smaller electrode sizes.

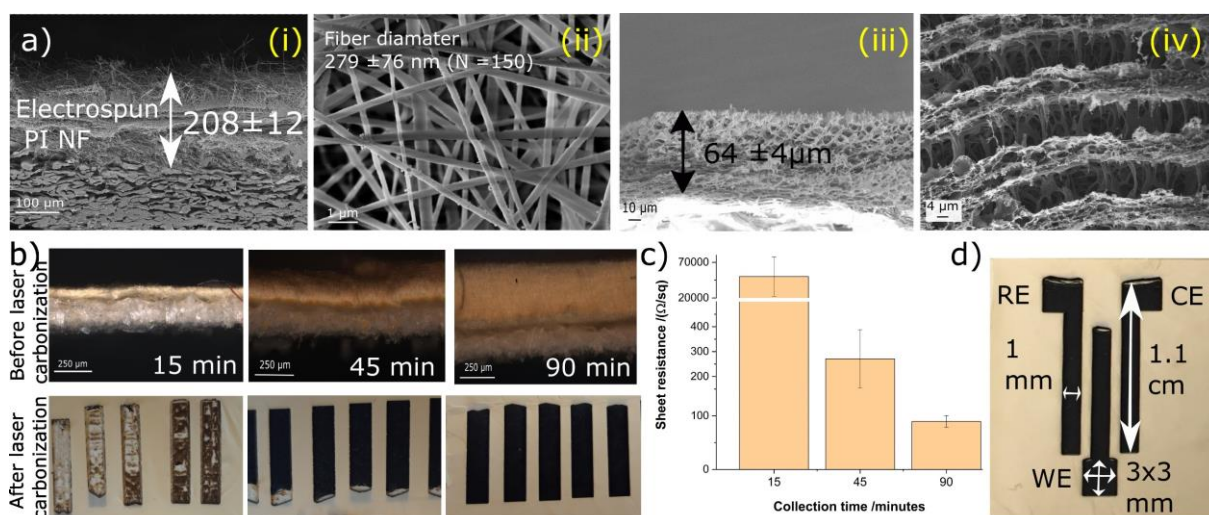


Figure 3.3. Laser-induced free-standing CNFs from electrospun PI nanofibers. a) SEM of electrospun nanofibers/filter paper substrate (i), PI nanofibers (ii), side view of LCNFs on paper (iii), and higher magnification of LCNFs on the top view (iv). b) Effect of electrospinning time on LCNF features, and c) sheet resistance of the as-generated LCNFs. d) Dimensions of working (WE), counter (CE), and reference (RE) electrodes.

Proper adhesion between electrospun nanofibers and the filter paper was studied as poor adhesion promoted bending and loose nanofibers which in turn led to unreliable surfaces for the lasing process (Figures S3.3a-i to S3.3a-iii). Oxygen plasma treatment of the filter paper prior to fiber collection was identified as a key parameter. Calvimontes et al. demonstrated that such treatment increases surface roughness and the number of oxygenated groups of the filter paper^[152], which we assume in turn assists in the attraction of fiber mat to the surface of filter paper (Figure S3.3b). Finally, it was found that drops formed during electrospinning lead to defects. The agglomeration of iron in these spots could lead to substrate burning due to dramatic heat collection (Figure S3.3c).

Characterizing the mechanical properties of the LCNFs, their tensile strength was measured (Figure S3.4). For this purpose, nanofibers are electrospun for 90 minutes on filter paper, which is removed afterwards. The freestanding PI nanofibers proved to have a Young's modulus of 20 MPa (Figure S3.4d), being comparable to other reports found in literature^[153]. After carbonization, the LCNF electrodes were tested again without any modification (Figure S3.4b) resulting in a decreased Young's modulus (Figure S3.4d), probably caused by a more brittle nature of the laser-induced carbon. Furthermore, it was found that their obtained elasticity is similar to the skin (~100 kPa), suggesting the PI nanofiber carried LCNFs are suitable for developing wearables sensors in medical applications^[154].

3.5.2 Anodic stripping analysis of silver ions using a three-electrode system

To assess the electroanalytical performance of the f-LCNFs, a three-electrode system (open hydrophobic device – Figure 3.2-iv and S3.2c) was used and employed for anodic stripping voltammetry (ASV) of silver ions. Linear sweep voltammetry (LSV) scanned from -200 mV to -800 mV (*vs* f-LCNFs RE) was performed to determine the proper reduction potential of silver ions with respect to an LCNF pseudo-RE (Figure 3.4a-i), suggesting -600 mV (*vs* f-LCNFs RE) for electrodeposition of silver ions (Figure 3.4a-ii). The subsequent re-oxidation by LSV scanned from -200 mV to 400 mV (*vs* f-LCNFs RE) generated an anodic peak corresponding to silver at ca. 100 mV (*vs* f-LCNFs RE) (Figure 3.4a-iii). These settings are similar to those published by others where Ag/AgCl and saturated calomel electrodes are used as a RE (Table 3.1) [155]. ASV signals increased proportionally to the silver concentration ranging from 0.001 – 1 μ M (Figure 3.4b). At higher concentrations, the signal drop-off is likely caused by competitive electrodeposition on the rough surface resulting in loosely bound silver grains detaching from the LCNF surface [156]. The peak shifts of the measurements seen in Figure 3.4b-ii is likely due to the variation from device-to-device. Effective climate control during electrospinning as well as rotating collector could potentially reduce such variations as uniform fibers and mat thickness play a crucial role in electrode reproducibility.

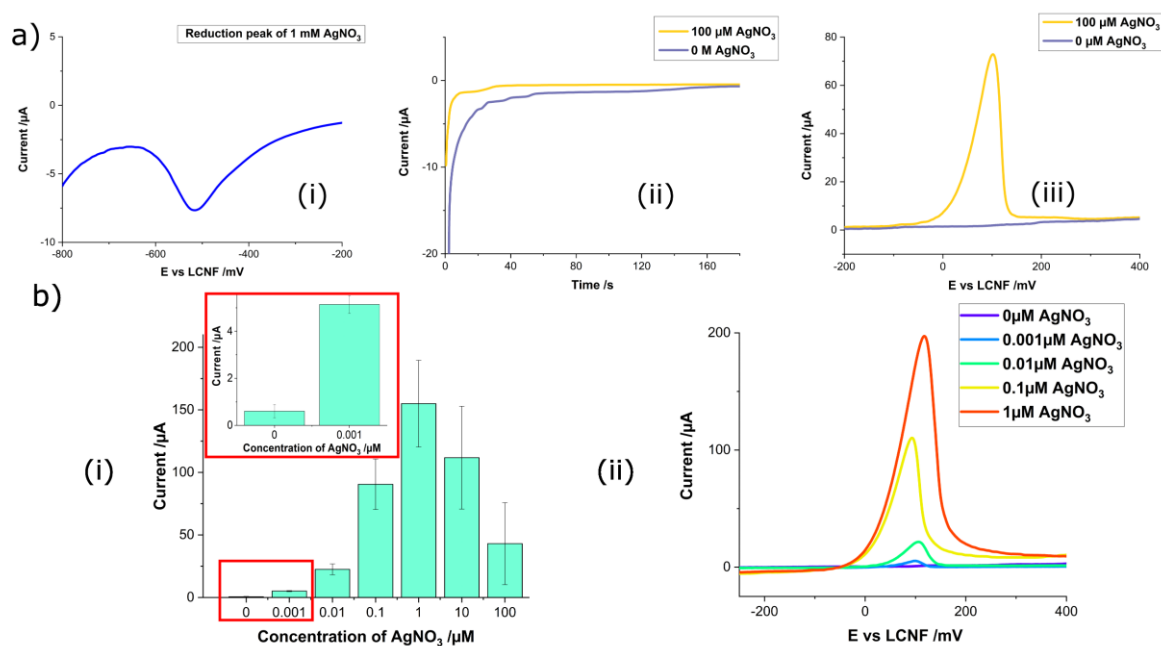


Figure 3.4. Three-electrode system of LCNFs for anodic stripping voltammetry of silver ions. a) Cathodic peak of 1 mM silver ions (i), chronoamperograms during electrodeposition at -600 mV (ii), and linear stripping responses in the presence and absence of silver ions (iii) with a scan rate of 50 mV/s. Silver ions were dissolved in 0.1 M HNO₃ containing 0.1 M KNO₃. b) Current intensities of various silver ion concentrations (all measurements were performed in triplicate from different devices) (i), and linear sweep voltammograms of silvers in the dynamic range (ii).

In the end, a three-electrode f-LCNF compares favourably to other high-performance electrochemical transducers (Table 3.1) without the need for stirred conditions to enhance mass transport via convection^[157]. The increase of mass transport can be attributed to better mixing in which chaotic nanofibrous structures of LCNFs could potentially promote efficient collisions between the analyte solution and LCNF surface. This hypothesis has been proven by our group in which PVA nanofibers possess mixing capability^[158].

Table 3.1 Comparison of electroanalytical performance of stripping analysis of silver of f-LCNF-based device to other types of carbon electrodes

Working electrode (WE)	Deposition potential vs Reference electrode (RE)	Counter electrode (CE)	Conditions			Anodic peak of deposited silver (mV)	LOD (nM)	Ref.
			Static/ stirred	Deposition time (min)	Stripping technique			
Glassy carbon electrode (GCE)	-500 mV vs Saturated calomel electrode	Platinum	Stirred	10	LSV	400	5	[159]
Carbon fiber ultramicroelectrode	-500 mV vs Ag/AgCl	Platinum	Static	2.5	LSV	350	1	[160]
Graphite felt (edge plane pyrolytic graphite)	-600 mV vs Hg/Hg ₂ SO ₄	Platinum	Static	2	LSV	-100	10	[161]
<i>p</i> -isopropylcalix[6]arene modified carbon paste electrode	-250 mV vs Ag/AgCl	Platinum	Stirred	3	DPV	50	48	[162]
Carbon paste electrode modified with multi-walled carbon nanotubes	-700 mV vs Ag/AgCl	Platinum	Stirred	0.33	DPV	100	0.74	[163]
Sulfur (S)-doped graphene (S-Gr) and a 3,3',5,5'-tetramethylbenzidine (TMB) composite (S-Gr-TMB) modified	-100 mV vs Ag/AgCl	Platinum	Stirred	5	DPV	300	2150	[164]

glassy carbon (GCE)									
LCNFs	-600 mV vs LCNFs	LCNFs	Static	3	LSV	100	1	This work	

3.5.3 Assembly of freestanding LCNF electrodes into microfluidic systems

The porosity, fluffiness, and electrostatics of the f-LCNFs make their assembly into microfluidic systems challenging. Here, a simple wax barrier was hence applied similar to strategies of paper-based analytical devices (PADs) [165]. Since direct printing onto the nanofiber mats was not feasible with the wax printer available, wax channels were printed onto a plastic film prior to transferring onto the LCNFs/fiber mat (Figure 3.2b). After printing the wax channels holes of 3mm were punched into the plastic cover sheet to obtain an inlet and outlet. The wax barriers are transferred by simply putting the plastic cover sheet together with the electrodes on a heat plate, this allows the wax to melt and penetrate into the pores of the nanofibers/electrodes (Figure 3.2-vi and 1b). Optimizing this process, the fiber mat thickness was investigated through fiber collection time concurrent to the variation of line width of the wax barrier (w_{b0}) and resulting channel width (w_{c0}) (Figure S3.5a-i). Lower density mats (15 minutes collection time) exhibited larger wax expansion (Figure S3.5a-ii), whereas denser fiber mats (≥ 30 minutes collection time) enabled the expansion within only 20% for all investigated w_{b0} . The results are attributed to the amount of fiber material and void space. Consequently, a reduction by approximately 50 – 60% of the resultant channel was observed for the w_{b0} of 0.8, 1, and 1.6 mm (Figure S3.5a-iii). The widest w_{b0} designed at 2.1 mm enabled a minimum reduction of channel width (ca. 30%) regardless of fiber density. Fluid flow and hence functionality of the resulting channels was done using sulforhodamine B (SRB) dissolved in ethanol. It was found that high-density fiber mats require a minimum amount of wax ink (determined by the designed width of the wax barrier) to completely form a hydrophobic barrier (Figure 3.5a and S3.5a-iv).

Since aqueous solutions need to be transported within the channel system for applications in point-of-care testing (POCT), the hydrophobic LCNFs/PI nanofibers were treated with oxygen plasma (Figure 3.2-v) prior to transferring the printed wax barrier (Figure 3.2-vi and 2.2b). Such treatment dramatically changes the wettability of LCNFs and PI nanofibers (Figure S3.5b-i) and can be optimized with respect to plasma power and exposure time depending on fiber mat density and thickness (Figure S3.5b-ii). Accommodating f-LCNFs within the device further promotes the flow of aqueous solutions due to their inherent hydrophilicity (Figure 3.5a).

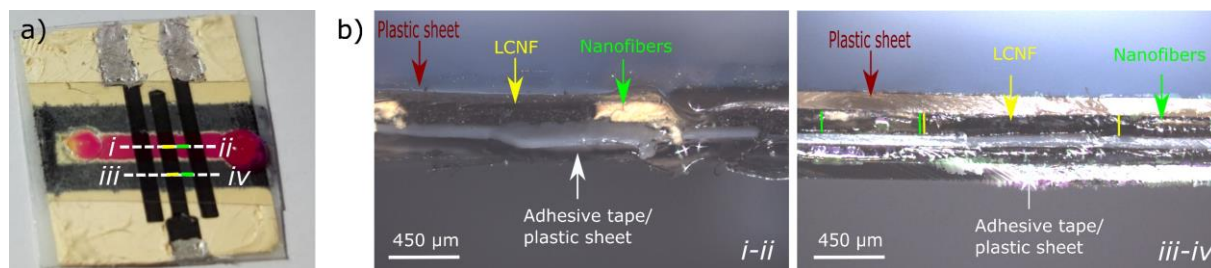


Figure 3.5. Integration of f-LCNFs in miniaturized devices. a) Picture of one closed device with a sulforhodamine B dye in water. b) Confocal microscope images of the side view of the device corresponded to the cross-sections shown in a) where the left and right picture depict the cross-sections located in the channel and at the wax barrier, respectively.

Further imaging the cross-section of the assembled device revealed that the proposed fabrication strategy is highly robust, resulting in intact freestanding LCNFs and PI nanofibers (Figure 3.5b-left and Figure S3.6a to S3.6c) with a tightly sealing hydrophobic barrier (Figure 3.5b-right and Figure S3.6d). The available porous structures of LCNFs and PI nanofibers therefore should be ready to promote efficient mixing and overcome diffusion limitations and ultimately enhance the electroanalytical performance of the devices.

The proposed integration strategy is by far superior to other traditional sealing methods such as bonding of channels engraved in plastic sheets or using doublesided adhesive tape to create a channel barrier and later closing the channel. The irregular structure as well as the high thickness of 3D-porous carbon electrodes, including LIG, make the traditional sealing methods challenging. For example, the high thickness leads to incomplete sealing between channel and electrode pieces. Moreover, pressing the channel piece over the delicate and brittle graphene flakes increases the chance of breaking the connection of working area and electrical contact pad.

3.5.4 Electrochemical characterization

Three sensor configurations were generated to investigate the analytical performance of the electrochemical devices (Figure 3.6a). Open devices enabled electrochemical reactions taking place at their surface. Here, the exposed active surface area of the f-LCNF electrodes was different for (i) untreated- and (ii and iii) plasma-treated devices. Furthermore, closing the channel with a plastic sheet diffusion of analytes within the plasma treated porous LCNFs electrode could be achieved (iii). Outer-sphere (ruthenium hexamine (RuHex)) and inner-sphere redox systems (ferri/ferrocyanide and dopamine) ^[166] were investigated towards their electrochemical behaviours using cyclic voltammetry (CV) in all three set-ups (Figure 3.6b). It was found that plasma treatment promoted proper flow inside the device and significantly increased the electroactive surface area (ESA) for all investigated redox markers in comparison to the pristine LCNFs (Figures 3.6b and 3.6c). It should be noted that the

Randles-Sevcik equation cannot accurately determine the actual ESA as it is established for electrodes with non-nanomaterials or flat surfaces ^[167]. Since no electrochemical strategies is currently available that would allow such determination, we used the equation to merely compare active surface area resulted from different electrode treatments and device configurations. Hence, the data of ESA in this work only reflect the changing of wettability of LCNFs which subsequently affects the obtained current intensity. We do not intend to report the actual ESA gained from the as-scribed LCNFs in the present work.

RuHex as an outer-sphere redox marker is insensitive to functional groups present at carbon electrode surfaces ^[168]. Consequently, plasma activation did not dramatically affect the generated peak potentials and peak-to-peak separation (ΔE_p) (Figures 3.6b-i and 3.6c-i) when compared to pristine f- LCNFs. Nevertheless, the significant increase in current intensities (Figure 3.6b-i) and ESA (Figure 3.6c-i) of RuHex for both open and closed devices suggest that the plasma treatment only enhances the electrode's hydrophilicity but not the electron transfer capability between RuHex and the LCNF surface. The closed channel devices do not result in a change of an electrochemical behaviour of RuHex when compared to the open device configuration, emphasizing the characteristic of an outer-sphere redox marker.

Since the inner-sphere ferri/ferrocyanide is not affected by oxide and adsorption ^[168] treating the devices with oxygen plasma only elevated ESA but did not facilitate greater electron transfer kinetic as indicated by the comparable peak potentials and ΔE_p related to the pristine devices (Figure 3.6b-ii and 3.6c). Interestingly, closing the channel resulted in a remarkable signal enhancement. We assume this is due to more efficient collisions at the interface compared to the open system, since the solution within the closed channel is confined inside the pores of the electrodes and thus the analyte is forced to interact with the electrode interface. The high capacitive current of the closed devices' CV (Figure 3.6b-ii) supports this assumption. As a side note, the anodic shifts of the reduction and oxidation peaks observed are likely caused by the change of LCNF pseudo-RE affected by the inner-sphere redox marker, even though it is insensitive to oxide and adsorption, which requires further investigations for elaborating such characteristic.

In the case of the inner-sphere redox marker dopamine, it can be seen that the required adsorption prior to undergoing redox reactions ^[168] is notably enhanced through available oxygenated groups from plasma treatment. Here, protonated dopamine (at pH 7.0) can be electrostatically adsorbed onto the LCNFs' surface (Fig. 4b-iii and 4c-i). As the adsorption mainly contributes to the electron transfer kinetics of dopamine, no obvious change in peak potentials was observed in the closed system.

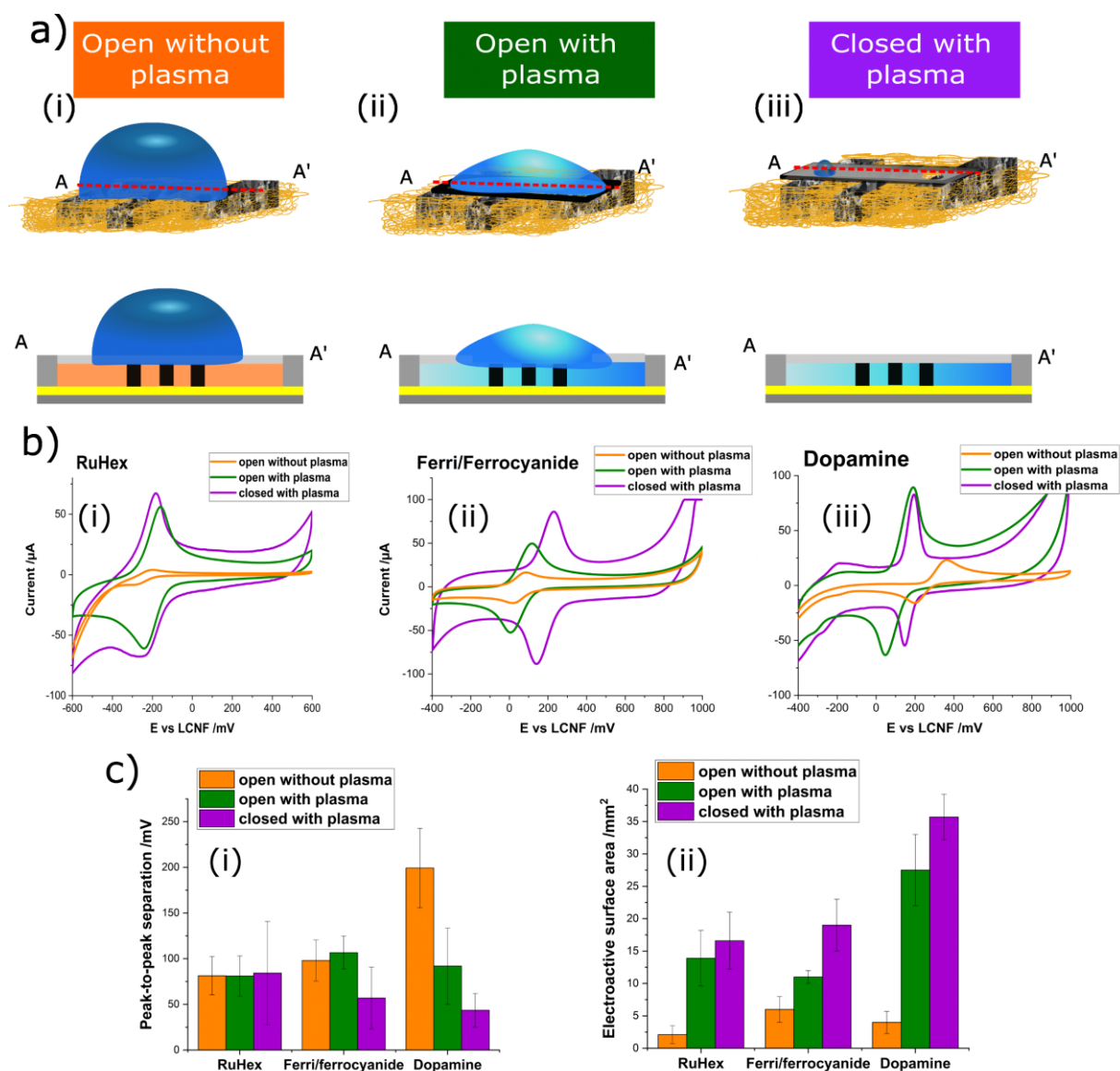


Figure 3.6. Comparison of electrochemical performance. a) Schematic illustration of the top view and side view of an open device without oxygen plasma treatment (i), an open device with oxygen plasma treatment (ii), and a closed device with oxygen plasma treatment (iii). b) CV's curves of the three different configurations in presence of 1 mM RuHex (i), 1 mM ferric/ferrocyanide (ii), and 1 mM dopamine (DA) (iii) in PBS (pH 7). Scan rate: 250 mV/s. c) Evaluation of electroanalytical performance by determining the peak-to-peak separation of CVs from 1 mM redox markers at a scan rate of 250 mV/s (i) and calculating ESA (ii) of the three configurations. All measurements were repeated using $N \geq 3$ devices.

3.5.5 Investigation of the reliability and stability of LCNFs as a pseudo-reference electrode

To assess the reliability of the LCNFs as an internal pseudo-reference electrode (RE), their cyclic voltammetric responses obtained for common redox markers were compared to that of an external RE (standard Ag/AgCl electrode). As shown in Figure S3.7a, to use LCNFs as a RE results in a cathodic shift for ferro/ferricyanide, approx. 200 mV, in comparison to the CV obtained from Ag/AgCl RE which

is similar to using microband carbon strip as a RE reported by Escarpa's group ^[169]. However, when measuring dopamine solution, the peak potentials obtained from LCNF RE exhibited only a slight deviation in comparison to using Ag/AgCl RE (Figure S3.7b). It is therefore suggested that analyte characteristics can influence the potential controlled at the working electrode which is a common behaviour of pseudo-reference electrode ^[170]. However, considering the insignificant difference in current intensities and ΔE_p in comparison to the standard Ag/AgCl RE, LCNFs can be used as a sufficiently reliable pseudo-RE.

Further studies regarding the reliability and stability of LCNF REs over a long measuring period were conducted by determining the open-circuit potential (OCP) using standard Ag/AgCl as RE of the system, and comparing to other, commonly used REs, e.g., Ag/AgCl film of Dropsens and laser-induced graphene (LIG). As can be seen in Figure S3.8, the potential controlled at the LCNFs was quite stable over the period of 3000s similar to that of LIG and highly comparable to the pseudo Ag/AgCl on screen-printed electrode from Dropsens.

Furthermore, the stability of the three-electrode system made of LCNFs was evaluated with closed devices ($N = 3$ devices), which were cycled 30 times in 1 mM of ferri/ferrocyanide or dopamine, respectively (Figure S3.9). The systems remain stable after 30 cycles for both analytes, confirming the robustness of the device. For ferri/ferrocyanide with continuous cycling the intensity of the current is enhancing slightly due to an increase in the wettability of the electrode material. The peak couple at ca. -250 mV and -300 mV (*vs* f-LCNFs RE), is probably due to the redox reaction of dopamine derivative, which is commonly formed when dopamine is electrochemically measured in neutral pH ^[171]. Oxidation of dopamine is in this case a quasi-reversible process. Interestingly, the LCNF systems behave similarly to the gold electrodes used in ^[171] regarding dopamine oxidation pathways.

It can be concluded that the stability of the potential over the investigated time period is sufficient for measurements in single use point-of-care devices. Furthermore, such carbon-based, binder-free pseudo REs open up the possibility to measure analytes dissolved in strong acidic medium such as HNO₃ in which Ag/AgCl may encounter instability problem, i.e., the acid could dissolve the pseudo Ag/AgCl film.

3.5.6 Analytical performance for dopamine sensing

Dopamine (DA) is an important neurotransmitter involved in several neurological disorders, which requires a highly sensitive transducer to detect the alteration from normal levels (10 to 480 pM in blood) ^[172]. Considering the significant difference in the mechanisms supported by open and closed devices of f-LCNFs, studies were performed in both set-ups. No difference in electrochemical behaviour for dopamine sensing was observed with open and closed devices at high dopamine concentrations (1 mM) (Figure 3.6b-iii), however, the closed system was by far superior at low concentrations, i.e., 1 nM. We

suggest that interactions between the analyte and interface are forced within the channel of the closed system as opposed to the open system (Figure 3.7a). After modification of the electrodes with sulfuric acid (Figure 3.7b), dose-response curves with high linearity over a low nM range were obtained (Figure 3.7c). It should be noted that the maximum current that we could obtain from the close devices is approx. 80 μA (see also the CV of 1 mM DA in Figure 3.6b-iii). This implies the maximum availability of LCNFs is reached and higher DA concentrations of 1 mM and 500 μM DA do not result in a greater current magnitude. This might be the reason why the current intensities of DA in Figure 3.7a and Figure 3.7b were similar even their concentrations are significantly different. The limit of detection (LOD) down to 55 pM was achieved (LOD was calculated based on $3 \times \text{STDV}_{\text{blank}}/\text{slope}$), which renders this simple electrochemical transducer highly potent for on-site POCT dopamine detection. The calculated LOD compares favourably to similarly developed detection strategies (Table 3.2).

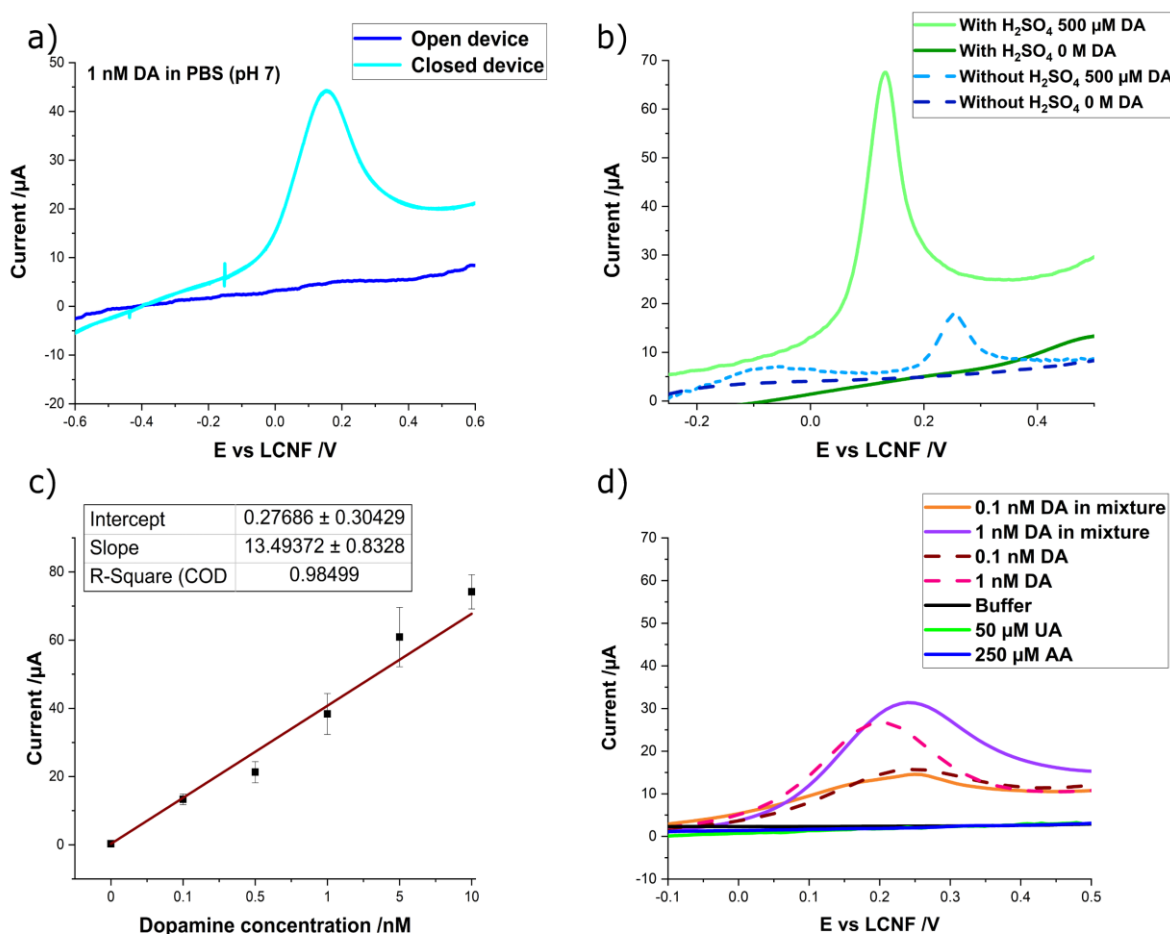


Figure 3.7. Electrochemical detection of dopamine (DA). a) Effect of device configuration on the sensitivity of DA detection. Both devices were treated with oxygen plasma and H_2SO_4 . b) Sensitivity enhancement by treating the closed devices with H_2SO_4 . c) Calibration curve of dopamine generated from closed devices treated with H_2SO_4 . d) Suppression of signal interferences from uric acid (UA) and ascorbic acid (AA) by 1.25 wt% Nafion coating (closed devices with H_2SO_4). DA solution was prepared in PBS (pH7). All measurements were performed by LSV with a scan rate of 100 mV/s ($N \geq 3$ devices)

A strong non-specific signal by uric (UA) and ascorbic acid (AA), common interferences for dopamine detection ^[173] (Figures S3.10a and S3.10b) could be avoided by applying Nafion as a well-known cation exchanger that possesses permeability to cations ^[174]. Specifically, its inherent negative charge from sulfonate groups in the structure can suppress anion interferences, e.g. UA and AA, as successfully demonstrated previously ^[173]. At the same time, its hydrophobic molecular backbone limits its useful concentration range, i.e., Nafion coating of an f-LCNF WE with high concentration solution, e.g., 5 wt%, leads to poor wettability of the device. In the end, we found that 1.25 wt% Nafion and plasma treatment at 200 W (instead of 100 W) was optimal to facilitate proper device assembling and solution flow (Figure S3.8c and d). The finally established fabrication process of f-LCNFs for dopamine detection entails (i) Nafion application (only at WE), (ii) plasma treatment, and (iii) gNincubation, the latter being performed after device assembly. As expected, the LCNFs modified with Nafion were able to suppress any signal interferences from UA and AA even at concentrations several times higher than dopamine (more than 10,000-fold the dopamine concentration) (Figure 3.7d).

Table 3.2 Comparison of the analytical performance of most recent reports on dopamine sensing, especially focusing on using 3D carbon nanomaterial

Materials	Linear range	Sensitivity	LOD (nM)	Ref.
CVD 3D graphene foam	0-25000 nM	619.6 $\mu\text{A mM}^{-1} \text{cm}^{-2}$	25 (S/N = 5.6)	[175]
Carbon-Black modified GCE	0.1-40 μM	0.61 $\mu\text{A } \mu\text{M}^{-1}$	13	[176]
Gold nanobipyramid/multi-walled carbon nanotube hybrids	50 nM – 2.7 mM	-	15 (S/N=3)	[177]
SU-8 photoresist based pyrolytic carbon (PyC)/PyC-O ₂	50 nM-1 μM	1.2 A M ⁻¹ cm ² /2.7 A M ⁻¹ cm ²	40 /20	[178]
Molybdenum (IV) disulfide nanosheets deposited on carbon nanofibers (CNFs)	0-60 μM	6.24 $\mu\text{A } \mu\text{M}^{-1} \text{cm}^{-2}$	36 (S/N=3)	[179]
3,4,9,10-perylene tetracarboxylic acid functionalized graphene–multiwalled carbon nanotube–gold nanoparticle nanocomposite modified glassy carbon electrode (PTCA-RGO-MWCNTs-Au NPs/GCE)	1-100 μM	0.124 $\mu\text{A mM}^{-1}$	70 (S/N=3)	[180]
3D GF/ITO	0-60 μM	1.88 $\mu\text{A } \mu\text{M}^{-1} \text{cm}^2$ (0-5 μM) and 1.44 $\mu\text{A } \mu\text{M}^{-1} \text{cm}^{-2}$ (5–60 μM)	100	[181]
ZnO nanosheet balls (ZnO NSBs) on three-dimensional graphene foam	1–80 μM	0.99 $\mu\text{A } \mu\text{M}^{-1}$	10 (S/N=3)	[182]

Au nanoparticles-ZnO nanocone arrays/graphene foam	0-80 μM	$4.36 \mu\text{A } \mu\text{M}^{-1}$	40 (S/N = 3)	[183]
Freestanding graphene foam-carbon nanotube composite coupled with gold nanoparticles	0.10– 48 μM	$12.72 \mu\text{A } \mu\text{M}^{-1} \text{ cm}^{-2}$	1.36 (S/N = 3)	[184]
LCNF electrodes (miniaturized systems)	0 – 10 nM	$13.9 \mu\text{A nM}^{-1}$	0.055 (S/N = 3)	This work

3.6. Conclusion

Herein we present laser-induced carbon nanofibers as freestanding electrodes that can be easily integrated into miniaturized devices. Ultralow detection limits for silver ions via stripping voltammetry suggest their applicability toward the detection of AgNPs use as signal generating label in (bio)sensors^[185,186], especially as analyses do not require stirring conditions due to the immense porosity of the f-LCNFs. Also, the results indicate that further modification with electrodeposited metal nanocatalysts may be of great interest in future studies especially at low metal salt concentrations. Overall, the presented strategy is robust, easy to perform and generates electrodes at <0.02 € per electrode. The comparison between open and closed devices supports well the beneficial feature realized by integrating 3D porous electrodes in microfluidic analytical systems. The tremendous enhancement offered by the 3D structure of the electrode has been proven in the detection of dopamine down to the pM range. Furthermore, the proposed assembling method is highly attractive for producing POC devices as it requires < 10 min (without the electrospinning) for each device and costs < 1€/device (Table S2). This will enable flow-through applications, where the reaction takes place inside the pores of the electrodes in contrast to other microfluidic systems, where the reaction is limited to the 2D interface between the electrodes and the channel. In the end, we suggest that devices based on f-LCNF integrated into a flow system are highly advantageous for point-of-care devices as their fabrication suits the ASSURED criteria well including mass production possibilities. Furthermore, we predict that f-LCNFs can revolutionize paper-based and wearable devices in which not only surface-bound signals (such as in optical systems and current electrochemical strategies), but 3D signals can be generated. Through the integration of selectivity agents such as aptamers, antibodies or chemical recognition molecules, the high specificity needed for real sample analysis will be enabled just like with other electrochemical systems.

3.7. Supplementary Information

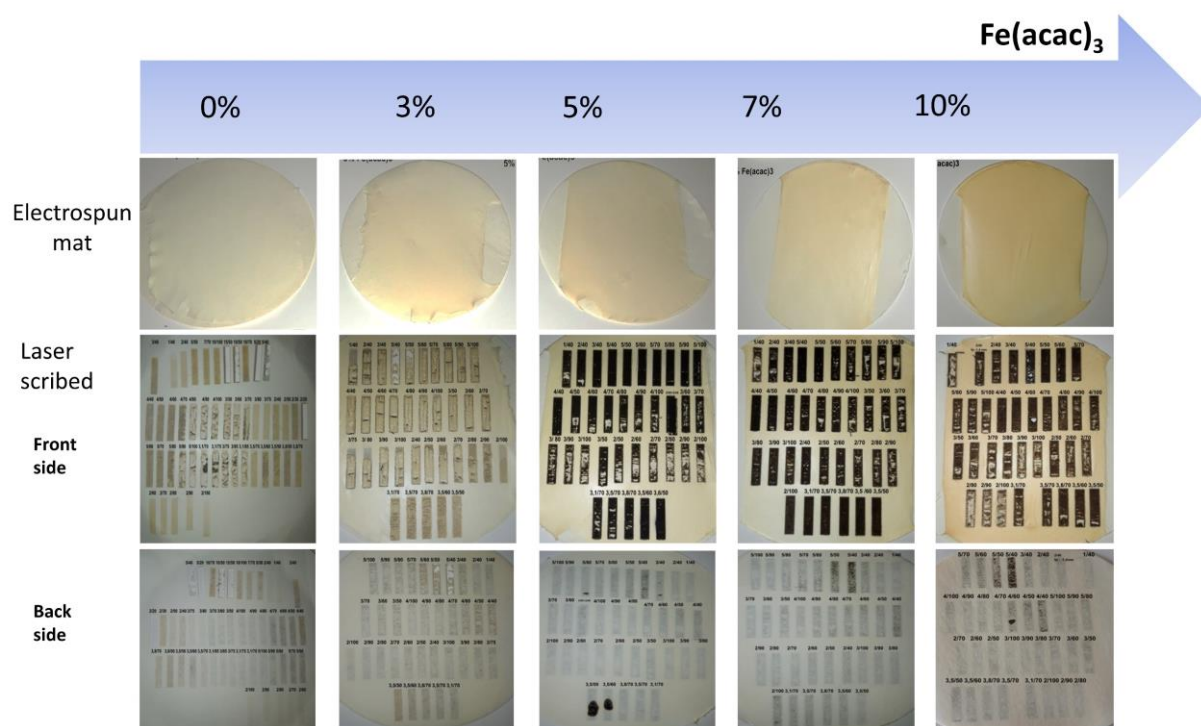


Figure S3.1 Effect of iron content and lasing conditions. Polymer solutions were prepared by dissolving 15% (w/v) polyimide (750 mg) and different $\text{Fe}(\text{acac})_3$ contents, i.e., 0%, 3% (22.5 mg), 5% (37.5 mg), 7% (52.5 mg), and 10% (75.0 mg) in 5 mL DMAc. The electrospun nanofibers were collected for 15 minutes on filter paper. Different laser settings (% of power/% of speed) were used to carbonize the nanofibers.

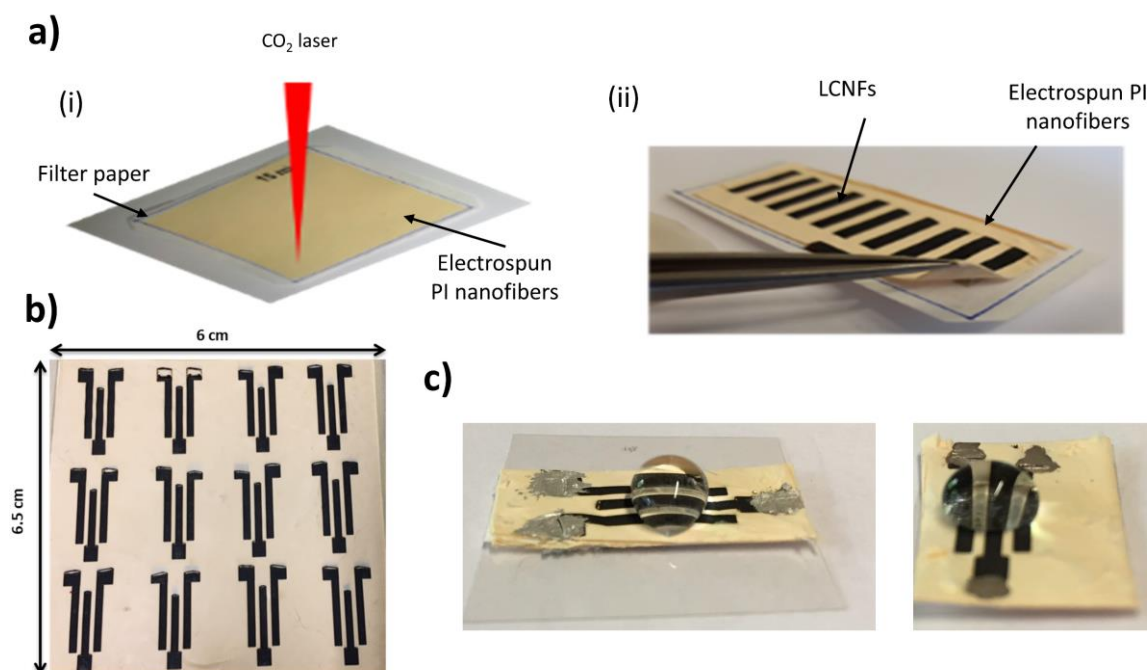
The iron content in the polyimide (PI) solution was varied from 0- to 10 % (rel. to the mass of PI). The same lasing conditions were tested on all mats. As it can be observed, especially on the front side of the scribed mats, the nanofibers were burned when the iron content was absent or present in a relatively low amount, while for 5% and 7% the mats were carbonized more homogenously. This proves that the iron present in the nanofibers facilitates heat dissipation during carbonization similar to the previous work [14].

Table S3.1 Cost estimation of electrode materials used for preparing electrospun nanofibers on filter paper substrate

List of material	Price per unit	Amount used for each fiber mat	Price per mat	Price per each electrode set (one mat contained 10 sets of electrodes)
Matrimid 5218	0.059 €/g	0.1875 g	0.01 €	0.001 €
Dimethylacetamide (DMAc)	0.0037 €/mL	1.25 mL	0.005 €	0.0005 €
$\text{Fe}(\text{acac})_3$	0.15 €/g	0.0094 g	0.0014 €	0.00014 €
Filter paper	0.079 €/piece	1 piece	0.079 €	0.0079 €
Total price per each electrode set (three-electrode system)				0.01 €

Table S3.2 Cost estimation of materials used for device assembly

List of material	Price per unit	Amount used for each device	Price per device
Double-sided adhesive tape	0.00238 €/cm ²	6.25 cm ² (for device of 2.5 cm × 2.5 cm)	0.015 €
Plastic sheet for wax printing	0.0045 €/cm ²	6.25 cm ² (for device of 2.5 cm × 2.5 cm)	0.028 €
Wax ink	2.2×10 ⁻⁵ €/cm ²	0.88 cm ² (for rectangle channel barrier with dimension of 0.7 cm × 1.9 cm, width of barrier (w_{bo}) of 0.2 cm)	2.5×10 ⁻⁵ €
Silver paint	0.024 €/μL	5 μL	0.12 €
LCNF electrode set (Table S1)	0.01 €/piece	1 piece	0.01 €
Total price per each device			0.17 €

**Figure S3.2 Production of laser-induced carbon nanofibers (LCNFs) using filter paper as an initial support.**

a) PI nanofiber collected on filter paper as a substrate for laser carbonization (i), and releasing PI nanofiber mat carried LCNFs from the filter paper. b) LCNF electrodes on the substrate. c) An LCNF device after transferring to a plastic sheet. The electrical contact pads were painted with silver paste. The nanofibers were collected for 90 minutes on the filter paper.

After the nanofibers are electrospun, the mat is fixed onto the laser support and carbonized (Figure S3.2a-i). After the carbonization, the nanofibers together with the LCNFs can be easily peeled off from the substrate, as seen in Figure S3.2a-ii. A mat has the size of 6 x 6.5 cm as shown in Figure S3.2b,

which can accommodate 12 sets of three-electrode systems for the present electrode design. Afterward, the devices can be cut using a normal scissor and put on a plastic sheet with double-sided adhesive tape to ensure robustness and stability. Without any treatment the electrodes and PI nanofibers are hydrophobic, but a small volume (50 μL) can be added as shown in Figure S3.2c and used for the measurements in this work.

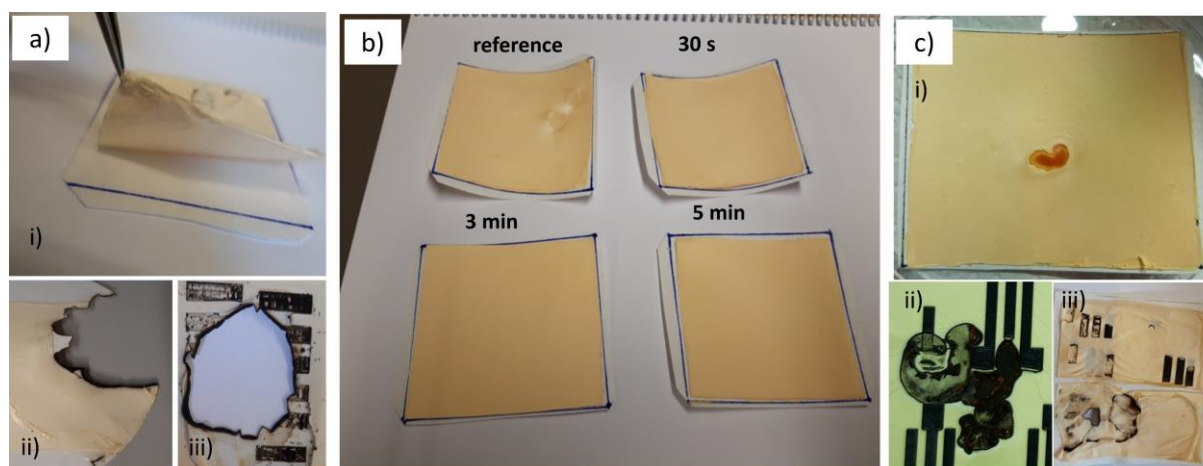


Figure S3.3 Effects of plasma-treated filter paper and defects on the production of LCNF electrode. a) Electrospun nanofiber mat collected on a filter paper without plasma treatment (i), and the burned fiber mat after exposure to the CO_2 laser (ii & iii). b) Electrospun nanofiber mat collected on a filter paper treated at various plasma exposure time and their comparison with the mat collected on an untreated filter paper. c) Dripping of the spinning solution on the nanofiber mat (i), causing iron aggregation and thus burning of nanofibers. Nanofibers containing 15 (w/v)% PI and 5% (rel. to the mass of PI) $\text{Fe}(\text{acac})$.

Adhesion of the nanofibers to the substrate plays an important role as can be seen in Figure S3.3ai-iii. If the nanofibers did not adhere well, during scribing they tend to burn, deteriorating the mat and the filter paper (Figure S3.3aii-iii). This is likely due to a gap of air in between the fibers and the substrate. To facilitate the adhesion of the nanofibers to the substrate, oxygen plasma was used. Prior to collecting the nanofibers, the filter paper was treated with oxygen plasma (100 W, 100% O_2) (Figure S3.3b). Without plasma treatment (denoted as reference) or with the short treatment time, e.g., 30s, the nanofibers/filter paper bends up, implying connections between fibers are stronger than fibers to the filter paper surface. When such substrate was fixed prior to laser scribing, a gap between fibers and filter paper may be created, which probably hinders the uniform heat dissipation during scribing. In contrast to the longer exposure time, e.g., 3 and 5 minutes, the substrates are flatter. The nanofibers, therefore, resulted in greater LCNF features (data not shown) where 5 minutes of plasma treatment was further used. Finally, if during the electrospinning process spinning solution has dropped on the mat (Figure S3.3c-i) this causes a defect in the mat in which an agglomeration of the iron is formed. When the laser beam reaches the iron aggregate, it will also carbonize the surrounding zone uncontrollably (Figure S3.3c-ii). Alternatively, it can just burn the mat similar to no adhesion of the nanofibers, shown in Figure

S3.3c-iii. The result also suggests that uniform heat dissipation during laser carbonization crucially requires homogeneous distribution of iron along the as-spun nanofibers.

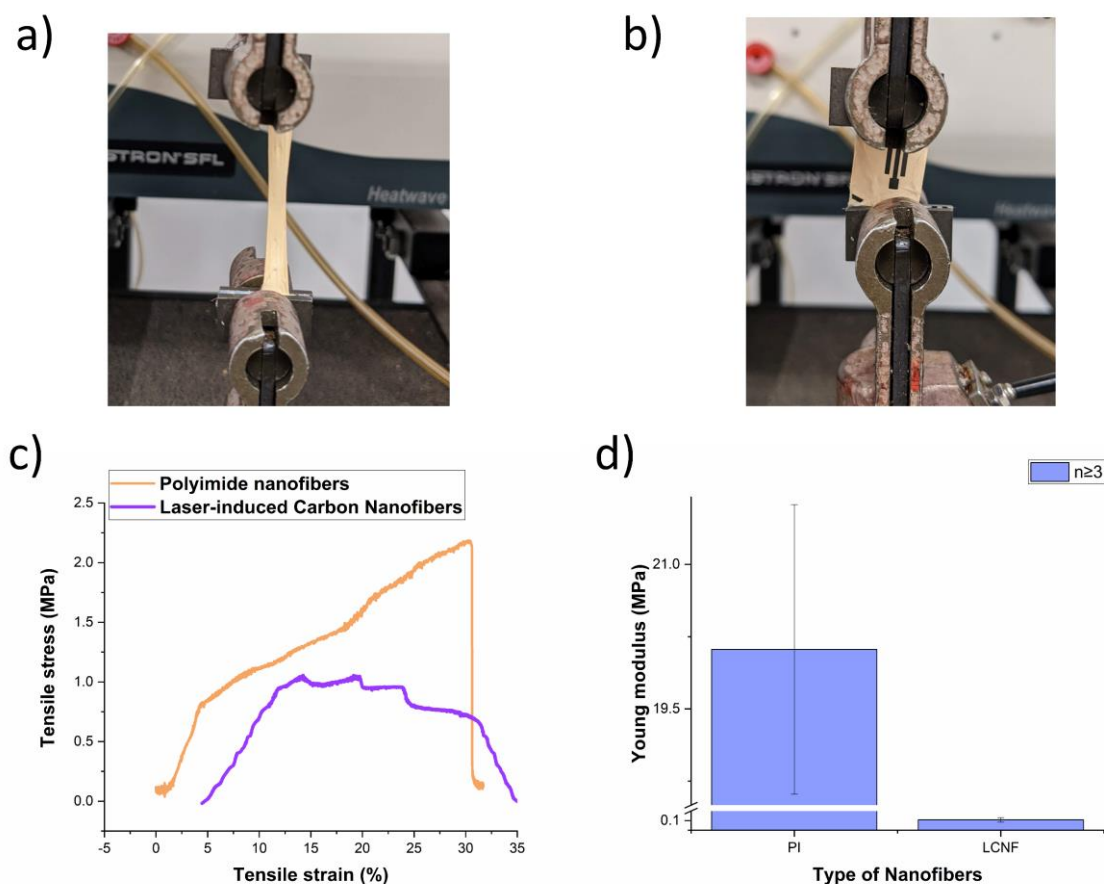


Figure S3.4 Study on mechanical stability. a) The measurement setup for PI nanofiber mat (PI NFs). The mats were cut into 45 mm long and 10 mm wide strips. The filter paper was peeled off and one strip was attached to the holders on the device. The measurements were performed in triplicate. b) The PI nanofiber carried LCNFs (PI-LCNFs) were cut into 20 mm long and 15 mm wide pieces. The filter paper was peeled off and they were set up vertically in the direction of electrode strips as shown in the photograph. The measurements were performed in quadruplicate. c) The tensile stress *vs* strain curves of PI nanofiber mat and PI-LCNFs. d) Young's modulus obtained from c). The raw data of the tensile strength were plotted in Origin and the data points outside the linear range corresponding to the elastic deformation were masked out for both PI nanofiber mat and PI-LCNFs. Young's modulus was determined by fitting linearly the slope in the elastic region (sharp increase) in the tensile stress *vs* strain curve.

As can be seen in Figure S3.4c, the PI nanofiber mats exhibit one point of fracture at the end which is a typical behavior for nanofiber mats ^[187,188], while for the PI-LCNFs four different points of fracture can be observed, corresponding to the three LCNF electrode strips and nanofiber mats at last fracture point.

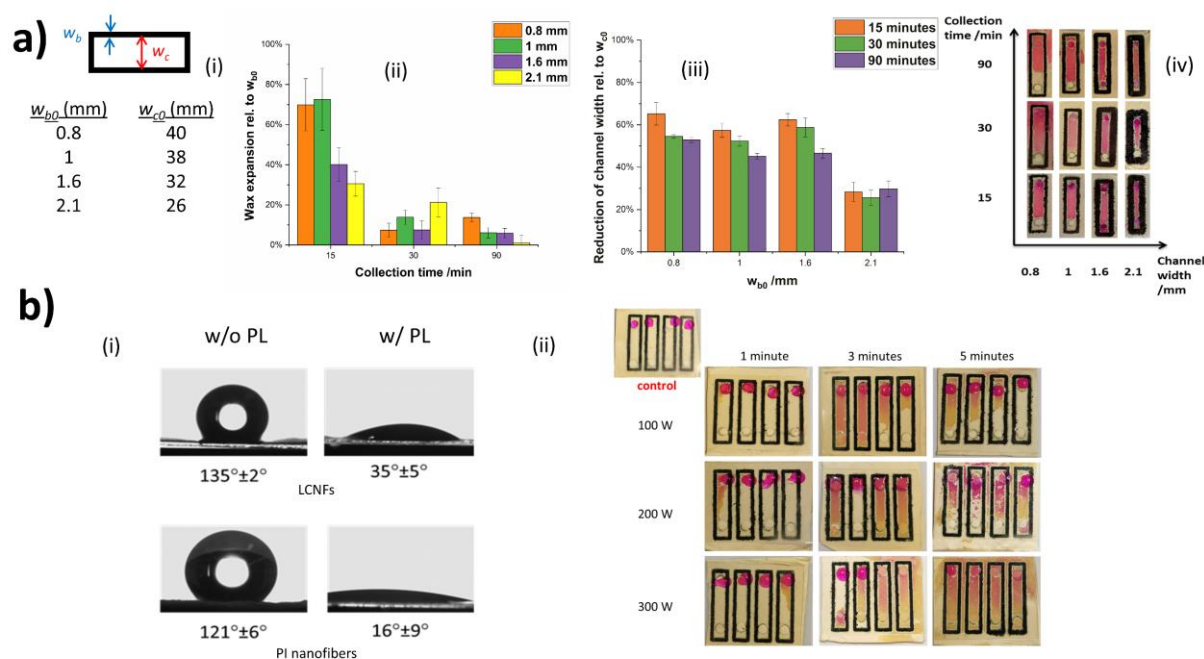


Figure S3.5 The fabrication of a microfluidic device containing PI nanofibers. a) Influence of channel designs and fiber collection time. Channel design with various line thicknesses of wax barrier (w_{b0}) and corresponding width of channel (w_{c0}) (i), effect of fiber collection time on percentage of wax expansion ($\frac{w_b - w_{b0}}{w_{b0}} \times 100$, w_b indicates the line width after wax melting) (ii), effect of w_{c0} on percentage of channel width reduction ($\frac{w_{c0} - w_c}{w_{c0}} \times 100$, w_c refers to the width of channel after wax melting) (iii), study of solution flow within assembled device at various fiber collection time and w_{b0} where w_{c0} of 20 mm was designed for the study (iv). The wax channels were created by heating the devices for 1 min at 100°C. Leaking test was performed by flowing 10 μ L of solution containing sulforhodamine B (SRB) dissolved ethanol into the devices. b) Increasing wettability of LCNFs and PI nanofibers by oxygen plasma treatment. Water contact angle of LCNFs and PI nanofibers after oxygen plasma treatment for 3 min (i), and optimization of the oxygen plasma treatment regarding power and treatment time (ii). Here, SRB dissolved in water was used for leaking test.

The widths of the barriers w_{b0} and w_{c0} of the channels for the studied systems are displayed in Figure S3.5a-i. The wax expansion was investigated with respect to different collection times and different barrier widths (Figure S3.5a-ii). This has a great influence on the performance of the device since the size of the channel correlated directly to the surface of the electrode used in the detection reaction. For fiber collecting time of 90 mins, the least wax expansion was observed for the thicker barrier, implying that the wax melts and diffuses vertically filling the pores of the nanofibers mat through the whole thickness of the mat. Furthermore, the direct correlation of the wax expansion is the reduction of the channel width (Figure S3.5b-iii). The thickest barrier preserves the best integrity of the channel. In order to ensure that there is no leaking the mats collected for different times were tested with the different barriers as can be seen in Figure S3.5a-iv. For the narrow barrier, the solution leaks outside, while the thicker barrier seals the channel regardless of the mat thickness. Pristine PI nanofibers and LCNFs are hydrophobic (Figure S3.5b-i). Therefore, to increase hydrophilicity of the materials enabled the flow of aqueous solution, both PI nanofibers and LCNF are treated with oxygen plasma. The dramatic decrease in contact angles proves that the oxygen plasma effectively renders both PI nanofibers and LCNFs with

great wettability. To ensure proper flowing of aqueous solution inside the channel different powers and different exposure times were investigated for the plasma treatment (Figure S3.5b-ii). In order to avoid leaking the best conditions were chosen to be 200W and 3 minutes.

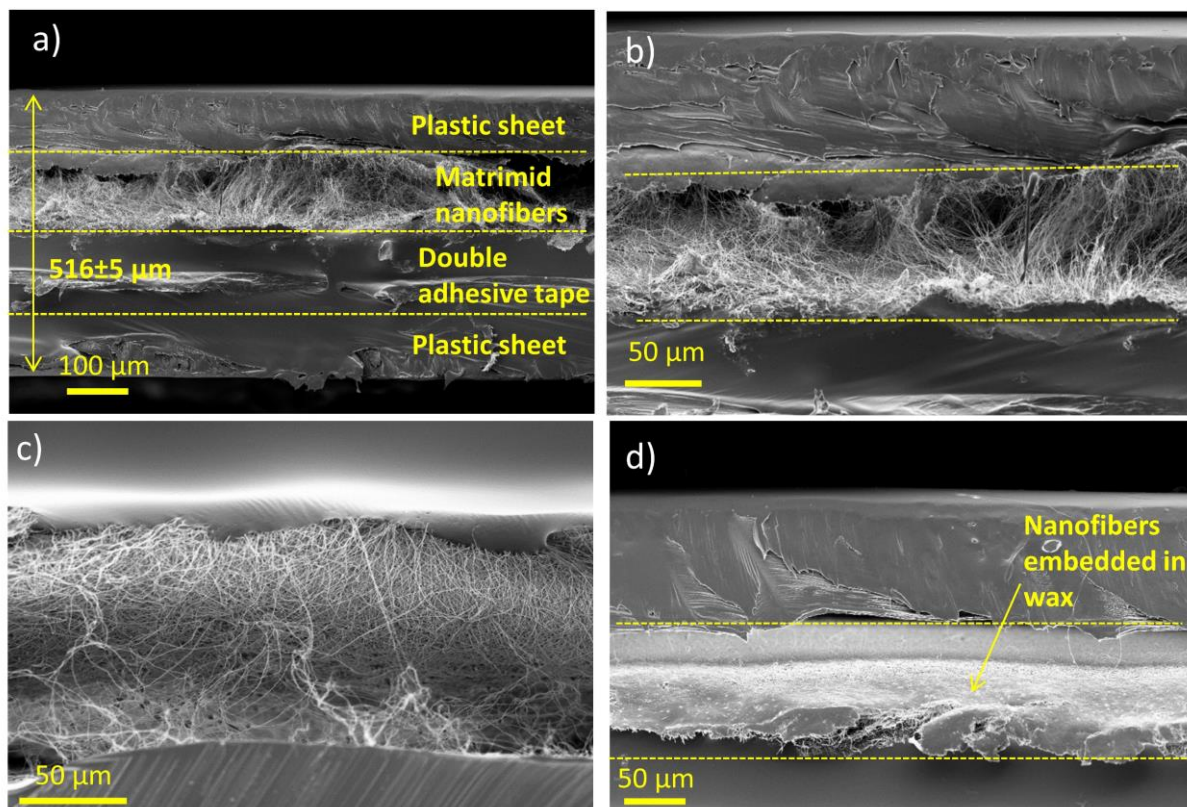


Figure S3.6 SEM images inside the microfluidic device. a) Side view of the device showing its components at the area contained nanofibers which is located in the middle. b) and c) the side view shown in a) with higher magnification. d) Side view at the area where wax barrier is located.

As shown in Fig. S6a, the whole device has a thickness of approx. 0.5 mm. It can be observed how the plastic sheets completely seal the device. On the plastic sheet underneath the device also with glue can be observed, which is a defect caused by the preparation of the sample for SEM. In Figure S3.6b and S3.6c, the nanofibers fill the channel inside the device, creating a mesh, through which the solution can flow through. This is contrast to the area where the wax barrier is located (Figure S3.6d). The mesh structure of nanofibers is filled with melted wax, therefore confining the area of the channel possible, and thus preventing the solution leaking. SEM images of LCNF embedded within the channel are not shown here because the structure was often destroyed during sample preparation for imaging.

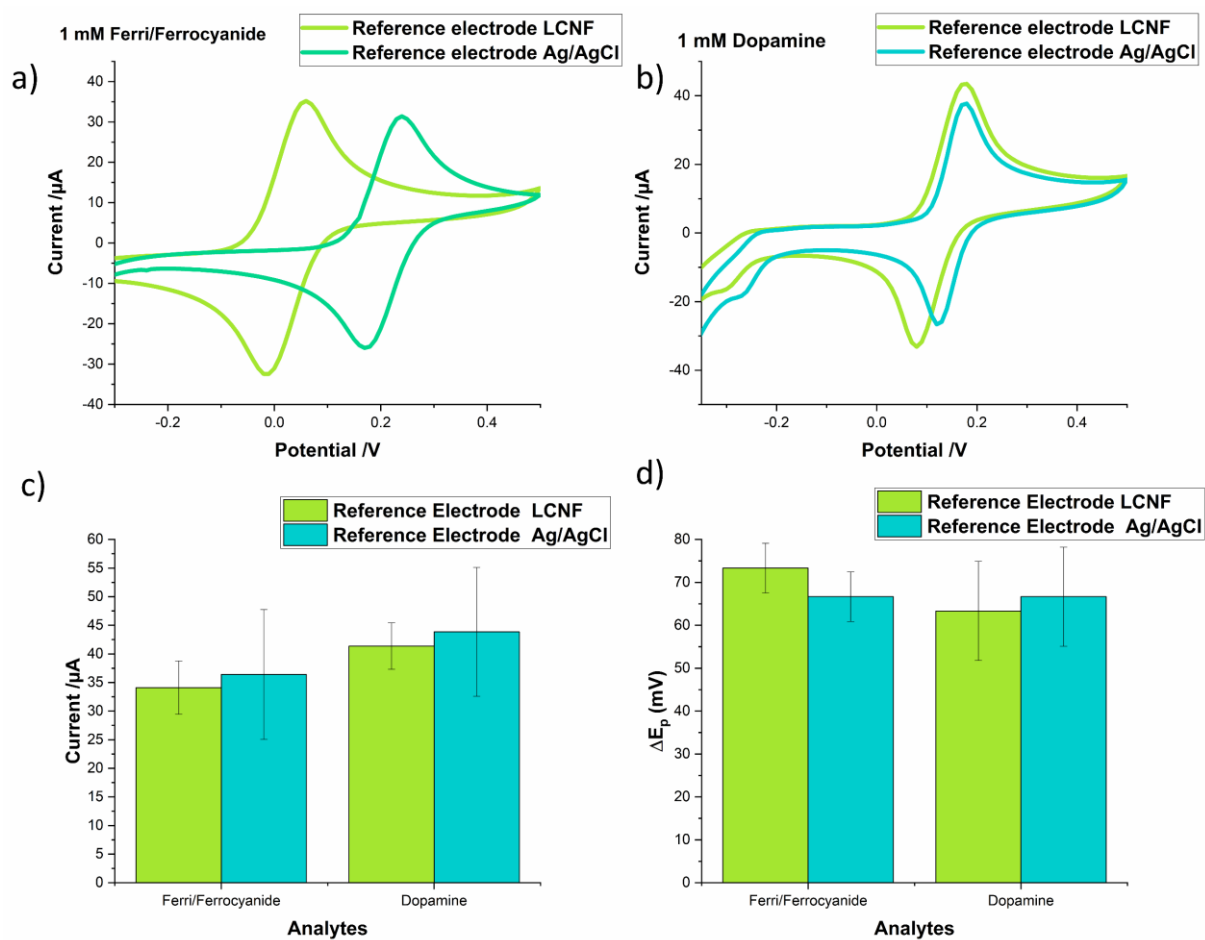


Figure S3.7 Comparison of analytical performance between using LCNF and Ag/AgCl as a reference electrode (RE). a) Cyclic voltammograms of 1 mM Ferri/Ferrocyanide on open device using LCNF as RE and using an external Ag/AgCl RE. b) Cyclic voltammograms of 1 mM dopamine on open device using LCNF as RE and using an external Ag/AgCl RE. c) The peak intensity was determined from the oxidation peaks of the respective voltammograms shown in a) and b). d) Peak-to-peak separation was determined from the cyclic voltammograms in a) and b). All LCNF devices were treated with oxygen plasma to increase the wettability and wax channels were applied to confine the area of the solutions. The plastic cover was removed to render open device configuration for the accessibility to an external Ag/AgCl RE. In case of using an external Ag/AgCl RE, internal LCNF electrodes were used as a counter electrode. A 10 μ L drop was added on top of the devices and in the case of the external RE, the electrode was immersed in the drop. The scan rate was 100 mV/s. All measurements were performed in triplicate.

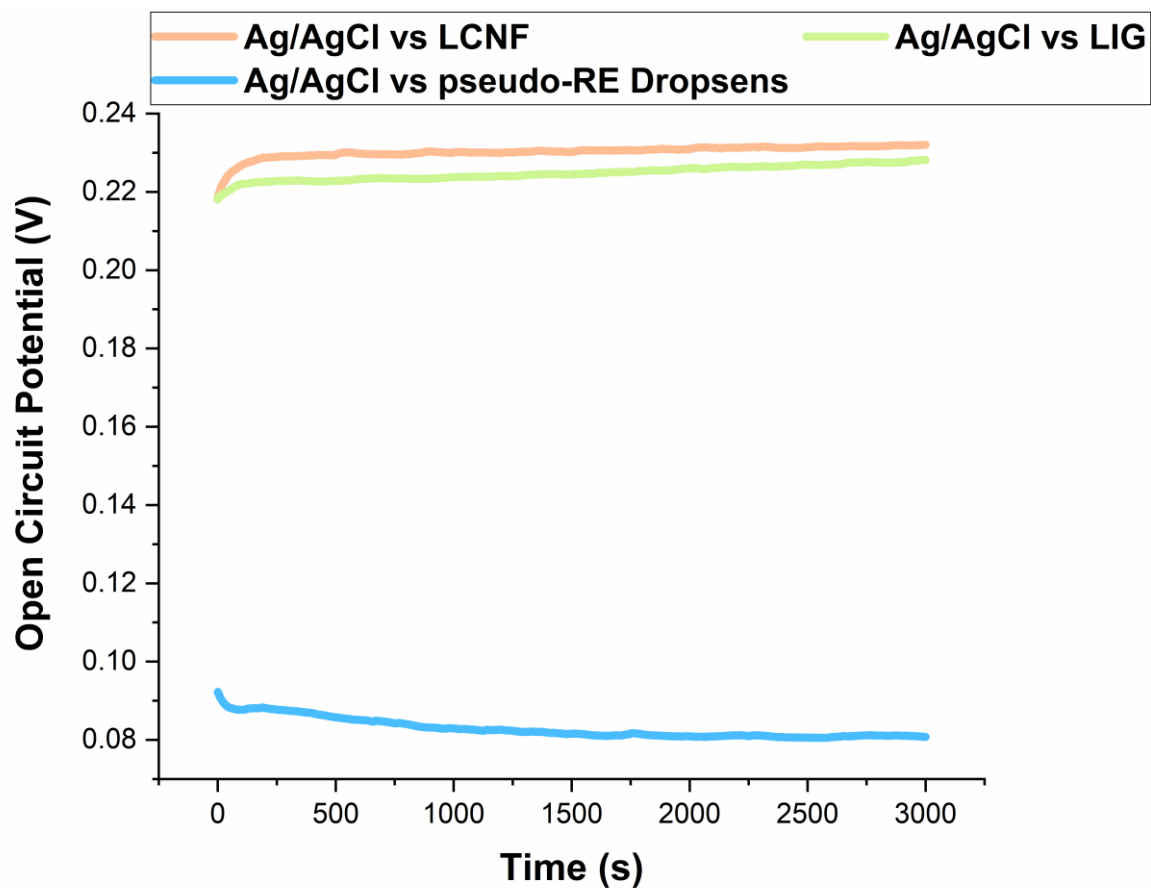


Figure S3.8 Investigating stability of LCNFs being used as a reference electrode (RE) and the comparison to other referencing electrode systems. The open circuit potentials of various electrode materials against a standard Ag/AgCl RE were measured in 1 mM ferri/ferrohexacyanide solution (PBS, pH 7.0 with 0.1 M KCl). A commercially available screen- printed Ag/AgCl film of Dropsens electrode (Metrohm) was also investigated for comparison.

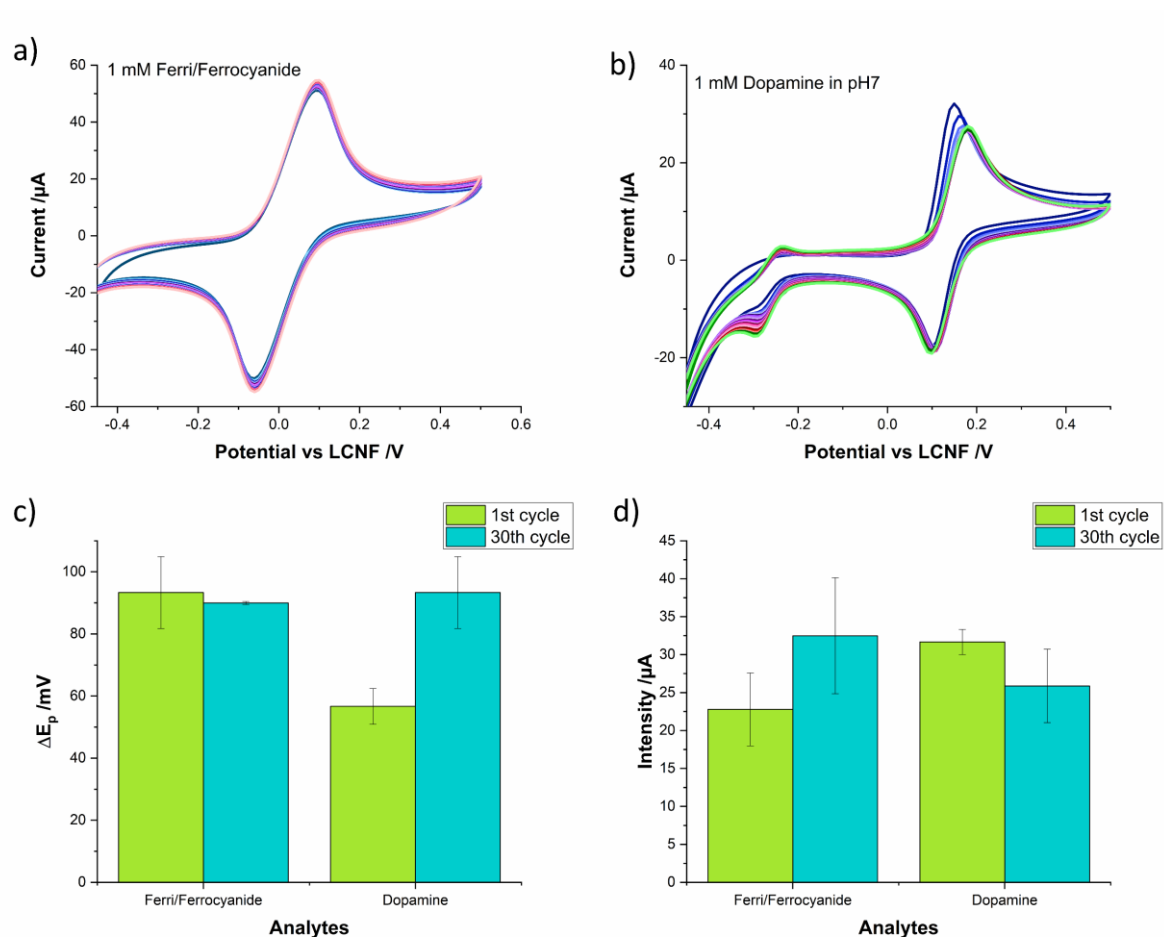


Figure S3.9 Stability of the three-electrode system in the closed device. a) and b) Cyclic voltammograms of 1 mM Ferri/Ferrocyanide, and 1 mM dopamine, respectively, running consecutively for 30 cycles. c) Peak-to-peak separation evaluated from the first and last cycle of the voltammograms. d) Intensity of the oxidation potential for the first and last cycle. The sample volume used was 10 μL . The scan rate is 100 mv/s. The measurements were repeated on fresh electrodes. $N = 3$

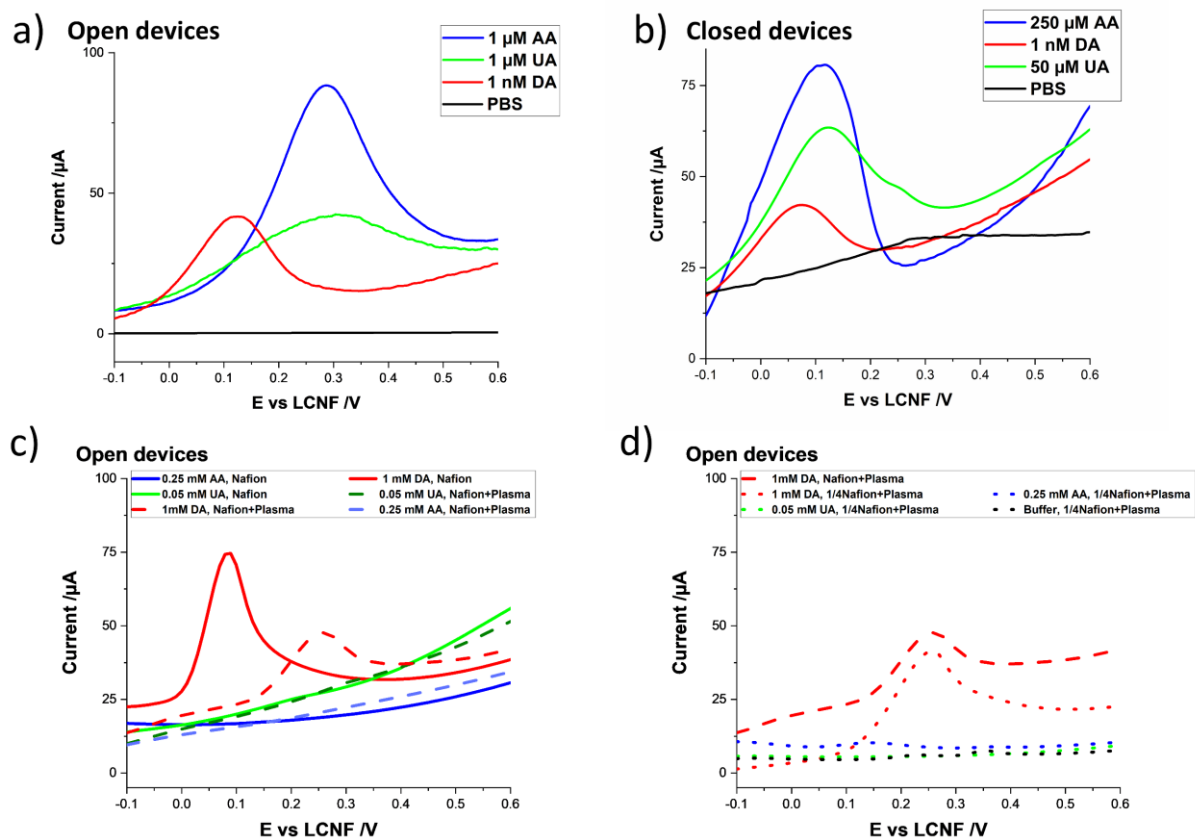


Figure S3.10 Interference caused by uric acid (UA) and ascorbic acid (AA). a) and b) Linear sweep voltammogram (LSV) of dopamine compared with those obtained from uric and ascorbic acids in open and closed devices, respectively. c) Eliminating interferent signals from UA and AA by drop-drying 1 μ L of undiluted Nafion (5 % (w/v)) on the WE as well as the post-plasma treatment. d) Effect of Nafion dilution on LSV signals. The sample volume used was 10 μ L. The scan rate is 100 mv/s.

In the open device the peak potential of uric acid (UA) and ascorbic acid (AA) is very close to the one of dopamine. Even if it is not at the same potential, it could potentially interfere with the signal of dopamine (Figure S3.10a). However, for the closed device, the peaks of UA and AA slightly shift to a more negative potential, overlapping the peak of dopamine, as shown in Figure S3.10b. After the addition of Nafion the signal of the two interfering species have been obviously eliminated (Figure S3.10c). To study if the oxygen plasma treatment affects the effect of Nafion, the same concentrations of analytes were tested on devices treated with Nafion and afterwards with plasma. Figure S3.10c proves that Nafion is still able to inhibit the signal of the interference, even after oxygen plasma treatment. Because Nafion creates a very hydrophobic layer, it has to be diluted to allow the penetration of the solution inside the electrodes. As can be seen in Figure S3.10d, dilution of Nafion results in greater accessibility to porous LCNF electrode indicated by the higher magnitude of the signal in comparison to undiluted Nafion solution. Moreover, even if Nafion is diluted and plasma treated, its function in preventing signal interference from UA and AA remains the same.

3.8. Storage of LCNF electrodes

This chapter has not been published. All experiments were performed by the author.

Storage is critical to determine the possible shelf life of a product. Products that are commercialized have to be stable over an extended period. The signal response should be maintained over time to have the sensor properly function for a longer time. Even though carbon is more inert than metal, changes upon exposure to humidity and actual environmental conditions might still have an impact.

In order to study how the LCNFs change over time, all three developed configurations were tested, namely open without plasma, open with plasma, and closed with plasma. For these studies, multiple spinning days were necessary (three different days by five mats/day). The mats were scribed after the spinning. All configurations were sealed into petri dishes with silica bags inside metal bags. Metal bags (Micro-Tec ziplock barrier foil storage bags) were purchased from micro to nano company. They are ideal for storing and protecting samples because they hinder moisture, light, oxygen, and dust from entering the bag. All configurations contained the same wax channels, to confine the same area of the electrodes.

The open devices without plasma were sealed right after the scribing process. The electrodes used as open devices with plasma, were freshly treated with oxygen plasma after scribing, and sealed. The LCNF electrodes were treated with oxygen plasma, for the closed devices, and wax was applied and sealed afterwards. Moreover, after all electrodes and devices are sealed into metal bags, they are kept in a desiccator with silica, and the air is removed by nitrogen flow. The measurements are represented by cyclic voltammograms measured with 1 mM Ferri/Ferrocyanide and 100 mV/s scan rate.

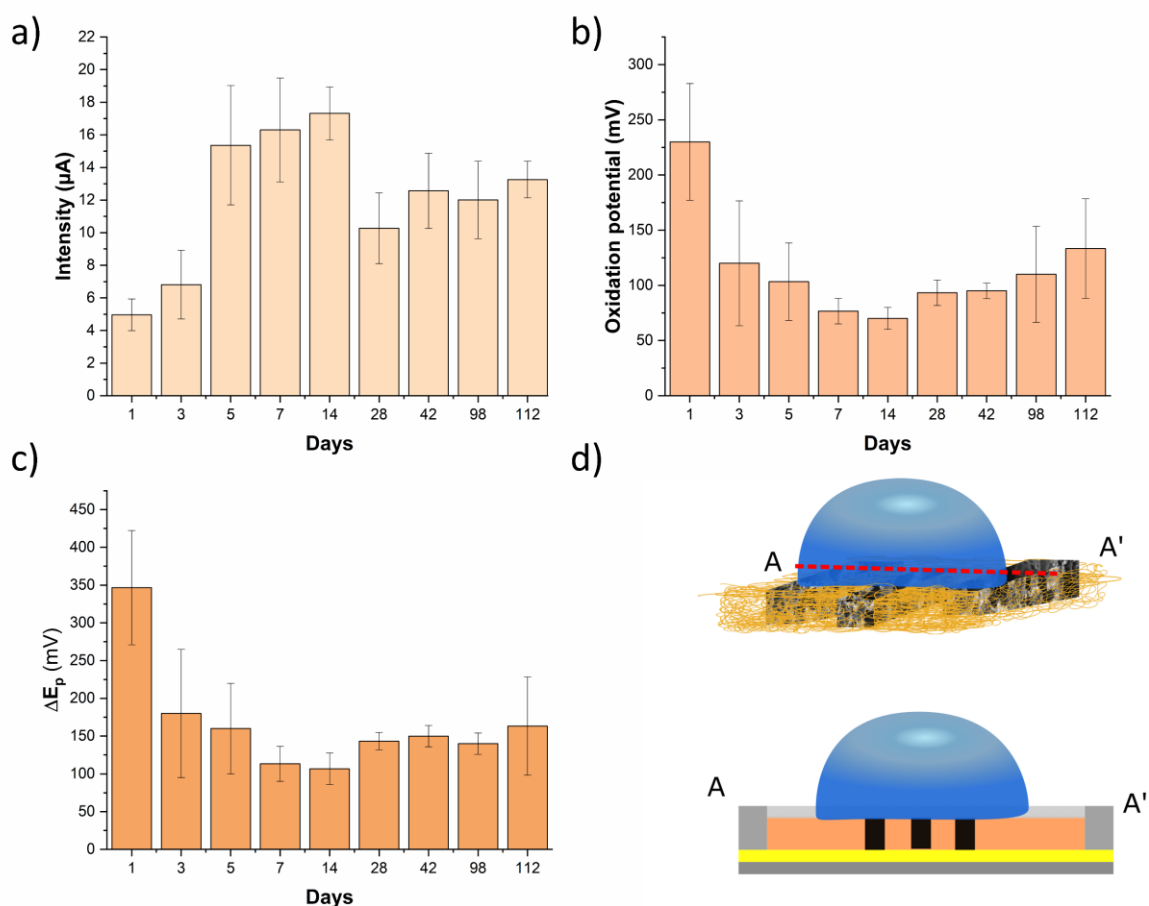


Figure 3.8. a) Intensity of the peak for the oxidation of Ferricyanide for 112 days. b) Oxidation potential of the peak variation for 112 days. c) The peak-to-peak separation between the oxidation and reduction peaks potentials. d) Schematics of the open configuration without plasma. $n \geq 2$ devices

The electrodes are very hydrophobic after scribing; therefore, the solution wets the superficial part of the electrodes correlating with the small peak intensity (Figure 3.8a). Moreover, the solution does not penetrate the pores, so only the upper surface of the electrodes interacts with the analyte (Figure 3.8d). After three days, the peak intensity increases (Figure 3.8a) and electron transfer improves as seen in the peak separation (Figure 3.8c), possibly due to an increased hydrophilicity caused by the moisture present in the bags. After two weeks, the intensity stabilizes and remains constant for up to 4 months. The change in hydrophilicity can also be observed for the oxidation potential and the peak-to-peak separation (Figure 3.8b). The electrodes undergo some interaction with the environmental components but stabilize between 1-2 weeks. The ΔE_p is about 150 mV after four months, showing a faster electron transfer than the freshly scribed electrodes (~350 mV) (Figure 3.8c).

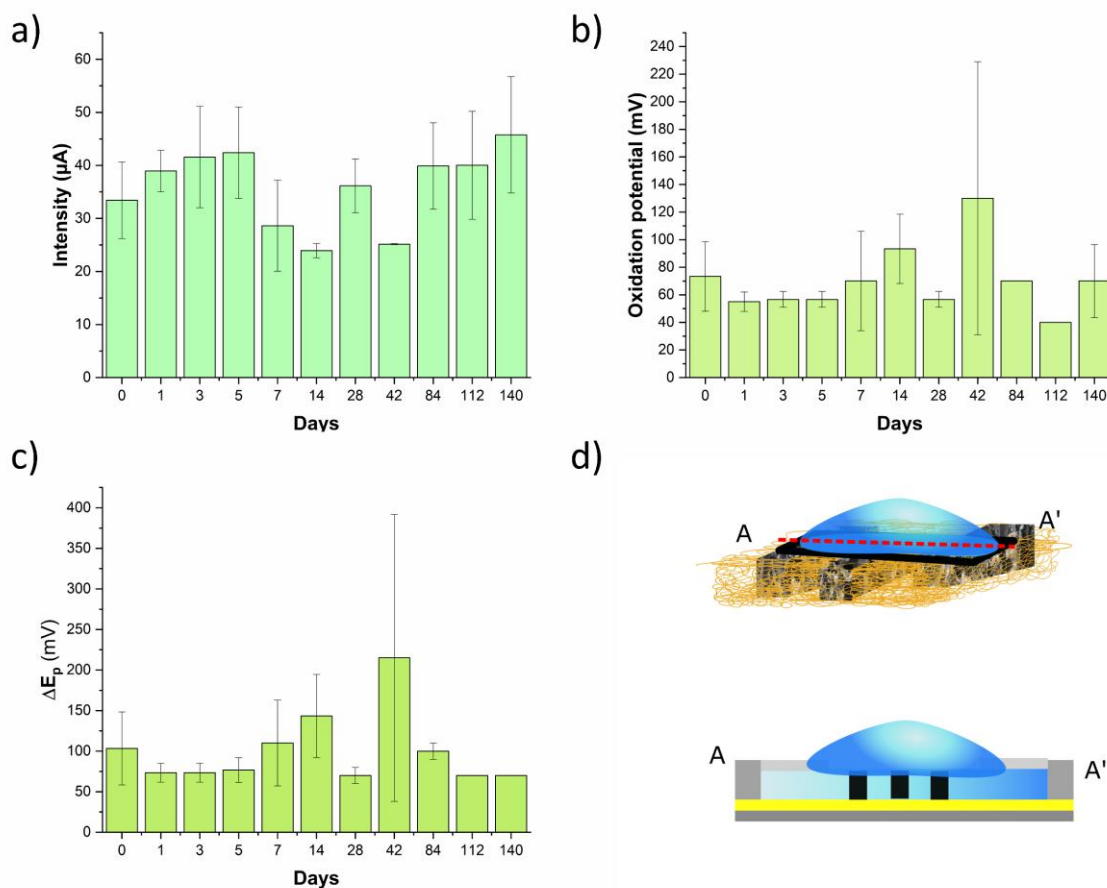


Figure 3.9. a) Intensity of the peak for the oxidation of Ferricyanide for 112 days. b) Oxidation potential of the peak variation for 112 days. c) The peak-to-peak separation between the oxidation and reduction peaks potentials. d) Schematics of the open configuration with plasma. $n \geq 2$ devices

The intensity of the plasma-treated open devices seems to remain stable even after ~ 5 months (Figure 3.9a). An inconsistency of the mats causes variations for day 7 to day 42. As already mentioned, multiple mats have been electrospun on different days. Changes in the environmental conditions (temperature and humidity) could have led to thinner mats and less robust electrodes. Not only a decrease in intensity can be seen for these periods, but also an increase in the standard deviation of the oxidation potential (Figure 3.9b) and peak separation (Figure 3.9c). This indicates that the mats for these electrodes have been from different days. However, the oxidation potential (Figure 3.9b) and the peak separation (Figure 3.9c) also have very similar values for the five-month-old electrodes compared to the fresh ones. The peak separation is 70 mV for the five-month-old electrodes and has a standard deviation equal to 0 for $n=3$ devices (Figure 3.9c). These results indicate that this system is stable for five months with relatively good oxidation peak intensity and fast electron transfer.

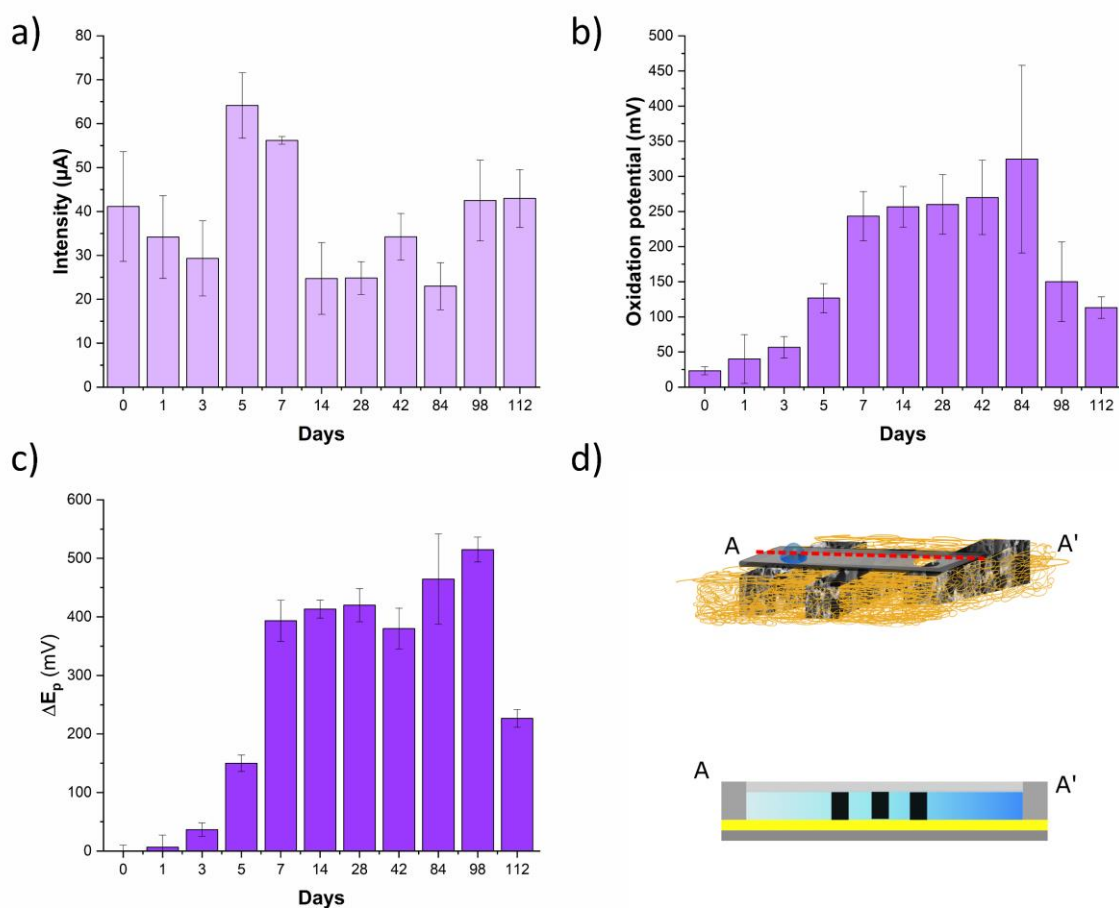


Figure 3.10. a) Intensity of the peak for the oxidation of Ferricyanide for 112 days. b) Oxidation potential of the peak variation for 112 days. c) The peak-to-peak separation between the oxidation and reduction peaks potentials. d) Schematics of the open configuration with plasma. $n \geq 2$ devices

The intensity for the hydrophilic enclosed electrodes stays nearly the same over four months (Figure 3.10a). Similar to the previous case, there are some outliers, probably due to a thicker mat for days five and seven compared to the others. There is a slight decrease in the intensity, but it is probably due to less solution coming in contact with the electrodes. The oxidation potential shows how the potential changes when the electrode's hydrophilicity decreases with time (Figure 3.10b). Even though the decrease is not substantial, as suggested by the peak intensities, the electrodes become more hydrophobic. Due to the change also being present at the reference electrode, a significant change in the oxidation potential was monitored (Figure 3.10b). The same trend can also be seen for the peak separation (Figure 3.10c); after five days, the electrodes become hydrophobic and show a slower electron kinetic. The change in the peak separation is enormous, with a 400 mV difference. The enclosed electrodes show excellent electron transfer only for 4-5 days (Figure 3.10c). The decay in the electron transport is probably due to the sealing of the electrodes between the plastic sheet and double adhesive tape (Figure 3.10d), which hinders airflow or moisture penetration. Moreover, it was observed that the

solution would not flow after 3.5 months. The hydrophobicity can also be seen in the significant drop in the peak separation for the four-month-old electrodes (Figure 3.10c).

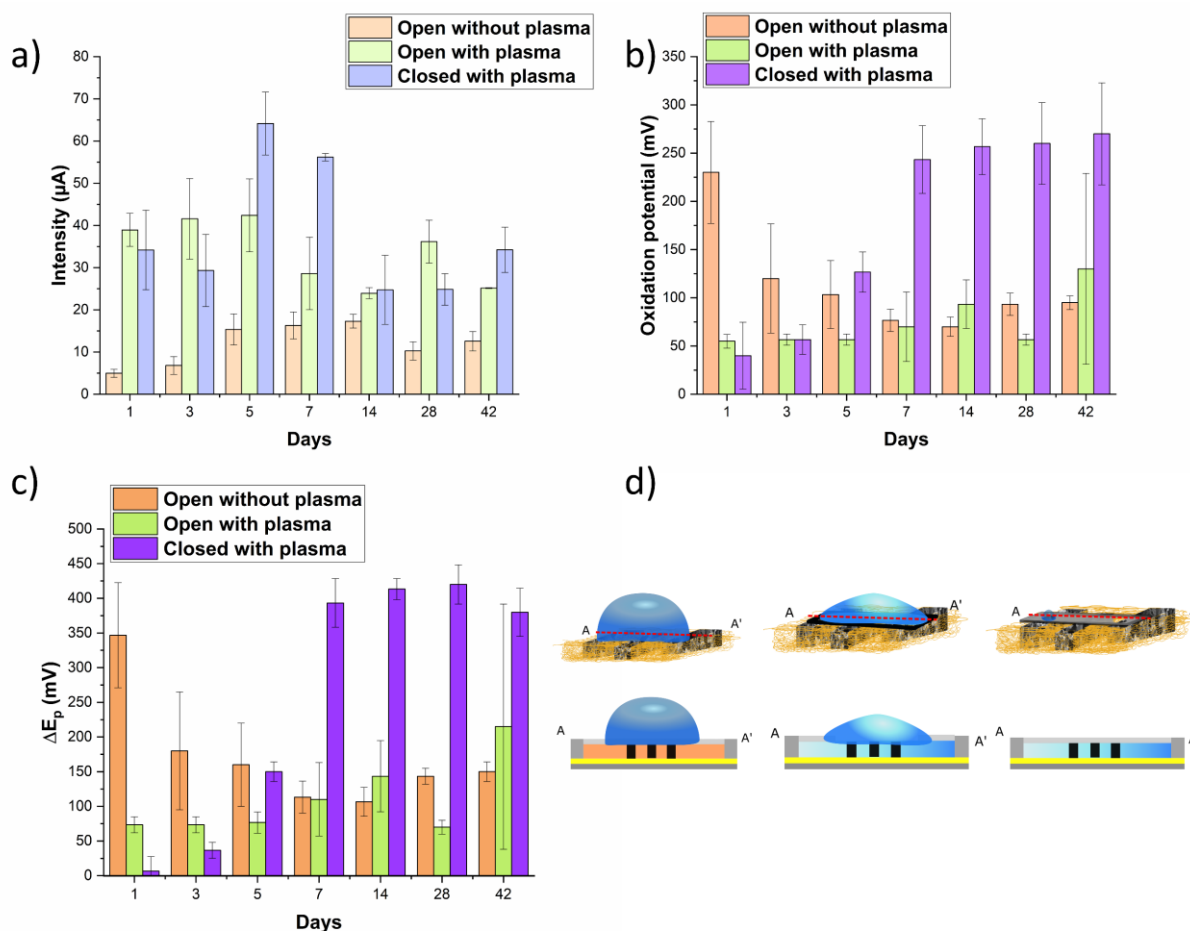


Figure 3.11. a) Comparison between the three configurations over 42 days for the oxidation peaks. b) Oxidation potential comparison between configurations for 42 days. c) Peak separation between oxidation and reduction potentials for the three configurations. d) Schematics for the three configurations.

The intensity is increased for the hydrophilic electrodes and only decreases slightly after one month and a half (Figure 3.11a). For both the open and closed devices with plasma, the intensity is higher after 42 days. While the oxidation potential decreases for the open hydrophobic configuration, as it gets more hydrophilic, for the closed hydrophilic configuration, it increases as the electrodes lose their hydrophilicity (Figure 3.11b). For the open device with plasma, the oxidation potential varies the least. The peak separation shows that with increasing hydrophilicity for the open without plasma configuration, the electron transfer improves after a couple of days, while for the other, it gets worse (Figure 3.11c). However, after one week the open device with plasma reaches nearly the same electron transfer as the closed configuration.

The closed configuration, which shows better performance overall, has to be used within one week for excellent response. Even though its electron transfer worsens over time, the intensity remains relatively

stable. The main problem with the closed device is that the hydrophobic nanofibers hinder the flow of the solution inside the microfluidic channel. The open device without plasma improves over time and stabilizes for five days but remains afterward constant for the tested time. However, it gets very brittle and hard to handle after four months resulting in destroyed electrodes. The described behavior allows the electrodes to be sealed after five days, maintaining their performance for up to 4 months. The open device with plasma has shown the best behavior regarding aging. It is the most stable system, where the electrodes have good performance overall due to the hydrophilicity, and the solution can still penetrate the whole surface of the electrodes even after a long time, which shows that the effect of plasma is somehow maintained for a longer time.

3.9. Open circuit potentiometry

This chapter has not been published. All experiments were performed by the author.

As mentioned in the introduction, many efforts are made to develop miniaturized reference electrodes with the possibility of being implemented into microfluidic devices. In order to use a fully built electrochemical cell made from LCNF, the stability of LCNF as a pseudo-reference electrode must be addressed. The stability must ensure that the electrode potential does not drift during the measurements and that the response analyte can be reliably correlated with the signal measured at the electrode.

Open circuit potentiometry (OCP) is a potentiometric method that enables the measurement of a potential when no current is flowing. OCP is the highest potential difference possible without applying a potential from the outside. There is no absolute potential, but it is agreed that the standard potential of the standard hydrogen electrode (SHE) is by convention 0. The difference between two reference electrodes must be as small as possible and stable over time.

In order to study the behavior of the LCNF electrode used as a RE, OCP was measured on different electrodes: Ag/AgCl as a standard electrode, LCNF, and LIG, which is a material similar to LCNF and is widely used and accepted as a RE by only applying silver paint, and a commercially available carbon electrode with a pseudo-reference electrode from Dropsens.

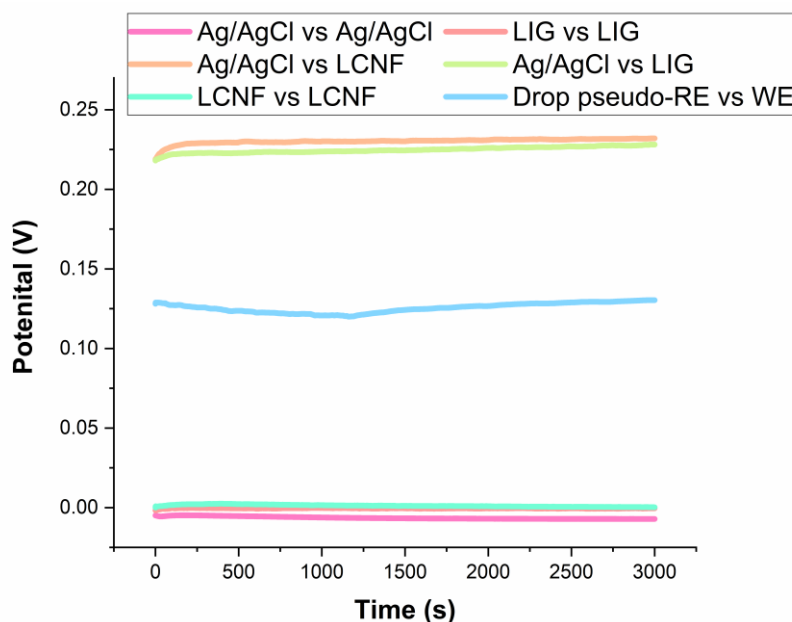


Figure 3.12. OCP measurements in 1 mM Ferri/Ferrohexacyanide between two different standard Ag/AgCl electrodes, between two LCNF electrodes, between two LIG electrodes, between LCNF and a standard Ag/AgCl electrode, between LIG and a standard Ag/AgCl electrode, and between the Dropsens pseudo RE and its WE.

The OCP shows that the potentials of the electrodes do not vary for the measured time, except for the Dropsens electrodes, where a small variation can be observed after 1000s (Figure 3.12). The constant

measured potential proves that there is no significant potential shift. For a proper comparison, these measurements were repeated with three different electrodes, and the potential difference (Figure 3.13), which is represented by the potential measured with OCP and the potential drift (Figure 3.14), which is the difference between the beginning and the end of the measurement were analyzed.

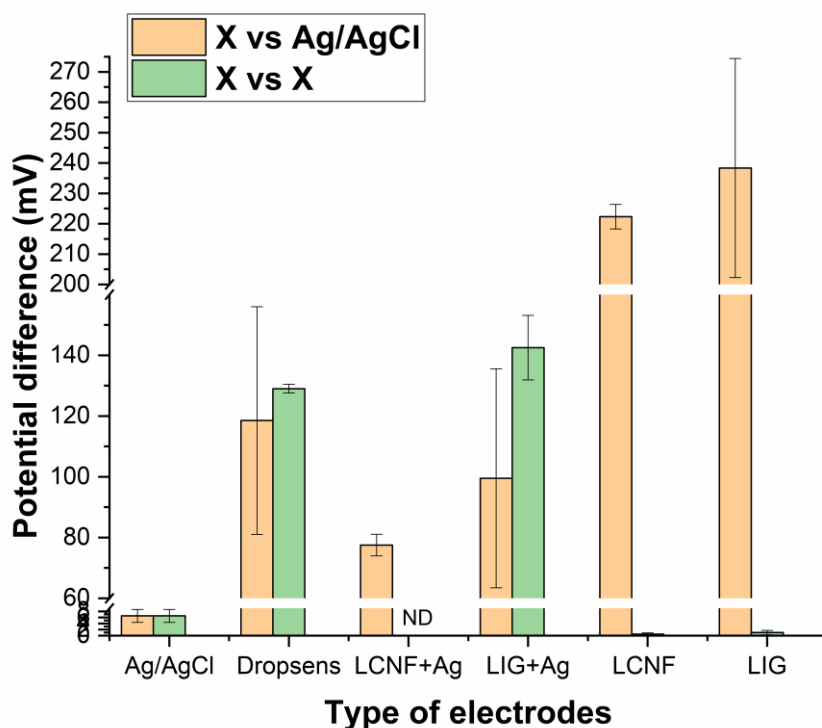


Figure 3.13. Potential difference measured in 1 mM Ferri/Ferrohexacyanide of different electrodes against each other (X vs X) and against the standard Ag/AgCl. LIG and LCNF electrodes were also painted with silver paint, labelled LCNF+Ag and LIG+Ag. $n \geq 2$

As expected, when measuring the potential difference between electrodes from similar materials, the difference is very low (X vs X): for Ag/AgCl is 6 ± 2 mV, for LIG is 1 ± 0.7 mV and for LCNF is 0.5 ± 0.5 mV (Figure 3.13). The low potential difference shows that electrodes have similar potentials when measured against the same material, like in the case of the three-electrode setup made from LCNF. To ensure the reliability of a pseudo-reference this should be measured against a standard reference electrode, here Ag/AgCl (X vs Ag/AgCl). When comparing LCNF and LIG to Ag/AgCl there is a potential difference of about 220 mV. This difference is probably due to the material difference between the two electrodes. However, the difference is acceptable. The widely known and used Dropsens electrode also has a potential difference of 118 ± 37 mV to the Ag/AgCl electrode, less than the carbon material, because its component is probably similar to silver paint. When applying silver paint to LIG and LCNF, the potential decreases significantly due to the less variation between the silver paint and

silver used in Ag/AgCl. The LCNF electrodes with silver paint had a difference of only 78 ± 4 to the standard electrode, which is remarkably good.

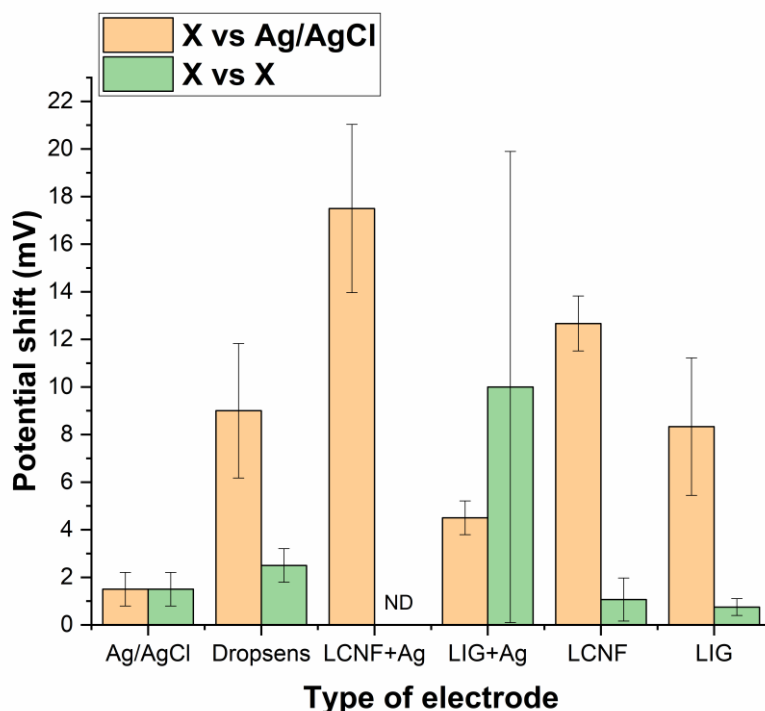


Figure 3.14. Potential shift calculated by the difference between the beginning potential difference and after 3000s. measured in 1 mM Ferri/Ferrohexacyanide of different electrodes against each other (X vs X) and against the standard Ag/AgCl. LIG and LCNF electrodes were also painted with silver paint, labelled LCNF+Ag and LIG+Ag

The potential shift is overall very stable for 3000s, as shown in Figure 3.14. As expected, the standard Ag/AgCl has the lowest drift of 2 mV. The Dropsens electrodes, even if they showed a small variation, have only 9 mV drift. Interestingly, it was observed that when applying a silver paint (LCNF+Ag) and (LIG+Ag), the drift worsens compared to using bare carbon (LCNF and LIG). The silver paint is probably not stable enough and gets modified during the long measurement. The pristine LCNFs showed a potential drift of about 12 mV, similar to the Dropsens electrodes, representing the golden standard for a pseudo-reference electrode for miniaturized systems. Moreover, most experiments using voltammetric methods last even less than 500s, so the time frame was chosen longer to examine the electrode's behavior.

These results show that LCNF electrodes can be used in an electrochemical cell for measurements lasting until 3000s. Moreover, if the LCNFs are painted with silver paint, the potential difference is improved, but the potential drift increases.

IV. Laser-induced carbon nanofibers for redox cycling

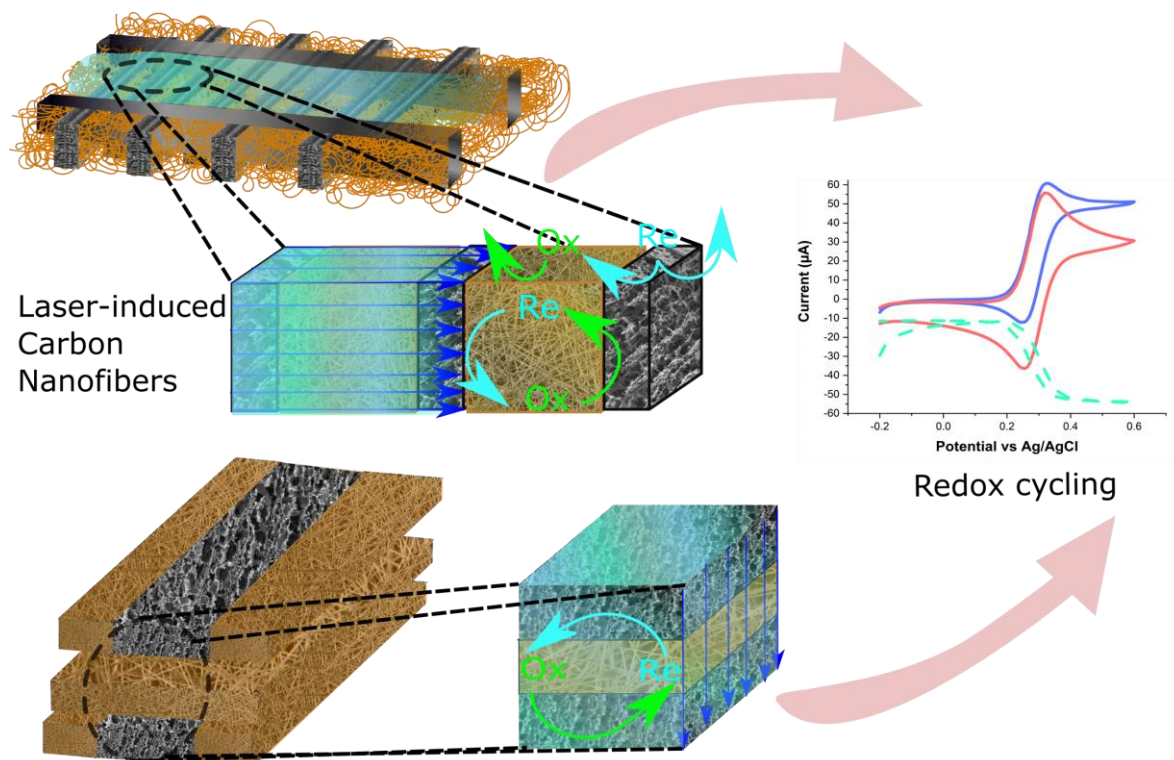


Figure 4.1. Laser-induced carbon nanofibers (LCNF) as interdigitated electrodes (IDEs) and stacked electrodes for redox cycling.

4.1 Abstract

Redox cycling is an amplification strategy used to enhance an electrode response by repetitive oxidation and reduction reactions of an electrochemical active molecule. We studied the possibility of generating systems for redox cycling as three-dimensional (3D) electrodes from carbon nanofibers as their inherent porosity should further enhance electrochemical performance. Here, we generated interdigitated – and stacked electrodes in a 3D nanofiber mat via CO₂ laser carbonization as a substrate-free system. Through the laser scribing process, quick prototyping of the electrodes is possible, enabling the fabrication of a large variety of designs, electrode finger widths, and gaps with great ease. The obtained electrodes were characterized with respect to collection efficiency and signal amplification relative to single-mode setup – without redox cycling. It was found that thicker mats result in higher electrodes with larger active surface area. In the end, a typical 3D IDE with 400 μm wide fingers and 40 μm gaps yielded a 95% collection efficiency and a signal enhancement of >4 compared to the single-mode set-up. Moreover, a similar redox cycling system is obtained by stacking two electrodes with a non-carbonized mat to separate the electrodes vertically. The systems with a vertical redox cycling strategy had similar results

as the IDE concerning the amplification factor and collection efficiency. However, IDEs are easier to handle and to fabricate compared to the stacked electrodes. The proposed fabrication strategy enables flexible and porous 3D electrodes for redox cycling with excellent electroanalytical performance that can easily be integrated into microfluidics or lab-on-a-chip systems.

This chapter will be further used as a manuscript that is intended to be submitted to Advanced Materials Technologies as an original research article.

4.2 Author contributions

The author and Dr. Nongnoot Wongkaew contributed equally to designing the experiments. The author and Prof. Dr. Antje J. Baeumner contributed equally to evaluating the data. The author and Dr. Nongnoot Wongkaew wrote the manuscript draft. Prof. Dr. Antje J. Baeumner led the project administration and promoted manuscript preparation.

4.3 Introduction

In recent decades electrochemical sensors have gained considerable attention as they have no waste generation, are fast, inexpensive, easy to operate, and portable. Their miniaturization has enabled even more precise, selective, specific, and highly sensitive sensors to achieve successful integration within micro total analysis systems (μ -TAS) or Lab-on-a-chip systems.^[189] The linear dependency of the faradaic current to the electroactive electrode area makes the electrode's surface area significantly impact the measured current.^[190] Furthermore, the mass transport of the redox species to and from the electrode surface and bulk solution is highly dependent on the size of the electrodes, influencing the electrochemical response.^[191]

Interdigitated electrodes (IDEs) have several advantages such as better sensitivity, faster response time, lower capacitive current, and higher signal-to-noise ratio compared to macroscale electrodes.^[192] If electrode arrays are in close proximity to their twin system and are being controlled separately, the redox species can quickly diffuse to the other side and be re-oxidized/reduced, resulting in a steady state by redox cycling.^[193] Furthermore, the downsizing of the electrodes results in enhanced diffusion of the analytes.^[194] Such systems with a small enough gap between the two electrodes have been studied as effective redox amplification systems.^[195] Redox cycling involves one electrode, called the generator, used to oxidize or reduce an analyte of interest. The analyte diffuses to the second electrode, called the collector, which converts the generated species back to its initial state.^[196] (Figure 4.2) The regeneration is caused by the overlap of the gradients of the diffusion layers around the generator and collector electrodes.^[197] Thus, the current is amplified by the number of recycled redox events. The geometry of the electrodes has a significant influence on the redox cycling efficiency; a better performance is achieved for smaller inter-electrode gaps.^[198–200] In addition, developing 3D IDEs has shown a significant improvement in their performance because of the trapping of the molecules between the electrodes.^[201–203]

Honda et al fabricated a highly efficient immunosensor based on 3D IDEs via photolithography. The microfabricated 3D electrodes have shown an increase in the current signal due to the increase in the surface area and also due to the increase in the trap ratio of redox species.^[204] Because of the smaller background currents and larger potential windows, carbon IDEs are more favorable than metal IDEs.^[168] Carbon 3D IDEs were developed by Kamath & Madou via UV photolithography and used for redox amplification. They showed how increasing the electrode height can overcome the limitations in reducing the gap size of their fabrication techniques.^[201] Micron-scale carbon IDEs were fabricated by Parkinson et al via controlled pyrolysis of patterned photoresists. They achieved a collection efficiency of up to 98% for 1.25 μm fingers with a 1.7 μm gap.^[205] Photolithography is the most popular method for fabricating such small electrodes.^[204–212] However, the adhesion of the carbon layer to the substrate was indicated to be weak and the carbon films suffer from poor conductivity resulting in a large iR

drop.^[205] Moreover, photolithography is a complex procedure that requires the use of high temperatures and complex instrumentation. At last, the methods based on photolithography require expensive equipment and sometimes also expensive masks, which makes them inappropriate for mass-production of inexpensive disposable devices.

The redox cycling performance for IDEs depends on the lateral resolution of the fabrication techniques. Therefore, electrodes have been stacked to achieve a small gap on the vertical axis between the electrodes. In this case, redox processes depend on the thickness of the insulating layer in between the electrodes. The first system with vertically separated electrodes array by a SiO₂ layer was created by Niwa et al.^[213] The same strategy has also been employed by separating a planar film electrode from a microdisk array.^[214] Such vertically separated electrodes have also been used in enzymatic biosensors, implementing alkaline phosphatase and horseradish peroxidase.^[215] A very efficient redox cycling was achieved by implementing dual ring arrays fabricated by focused ion beam milling, amplifying the current by a factor of 65.^[216] Furthermore, multilayer inkjet printing was also used for creating electrodes separated by polystyrene nanospheres, resulting in an amplification of 30-fold.^[217] However, even in this case, the fabrication techniques used to achieve a thin layer between the electrodes are complicated and unsuitable for point-of-care devices.

Carbon nanofibers (CNFs) have a large surface-to-volume ratio and porosity, assuring an efficient internal mass transfer. They also possess good electrical conductivity, low material cost, and chemical inertness, making them a great candidate for transducer material in miniaturized electrochemical sensors. An effective fabrication technique is electrospinning, one of the most used methods to fabricate nanofibers, due to its advantages like low cost, simplicity, and possibility for mass production.^[218] A novel method for the fabrication of CNF was developed in our group by integrating iron salt in a polyimide precursor solution yielding nanofibers, which could be efficiently carbonized in highly conductive nanofibers.^[14] The morphology of such porous structures enhances their reactivity towards electrochemical reactions, which can be further exploited in reaching lower detection limits for analytes of interest.

This study reports an inexpensive and easy fabrication technique of porous 3D Laser-induced Carbon Nanofibers (LCNFs) implemented in both separated lateral IDEs and vertically separated electrodes for redox cycling. Due to the expansion of the fibers upon laser irradiation, the size of the patterned fingers is increased, creating narrow gaps. The porous IDEs proved to be suitable for redox cycling amplification. Furthermore, the study of the scan rate revealed that a slow scan rate is necessary for reaching a steady state assuring redox amplification. Additionally, the influence of the collection time was investigated, suggesting that the performance could be further improved by increasing collection time. A non-carbonized mat vertically separates the electrodes as an insulating layer. The stacked electrodes are investigated as a possible redox cycling system, even if the electrodes are wide in contrast to the IDEs. Both systems amplified the faradaic current and achieved high collection efficiency. We

report flexible, free-standing 3D porous electrodes based on LCNF with both a lateral and vertical separation with enhanced sensitivity due to redox amplification and the possibility of integration into microfluidics and lab-on-a-chip systems.

4.4 Material and Methods

4.4.1 Fabrication of LCNF electrodes

Nanofiber mats were prepared by electrospinning of a solution containing 15 wt % Matrimid 5218 (Huntsman Advanced Materials BVBA, Belgium) and iron (III) acetylacetonate (≥ 99.9 % trace metals basis, Sigma-Aldrich, Germany) dissolved in N, N-dimethylacetamide (Merck, Germany). The polymer solution is ultrasonicated for 30 minutes and afterward stirred overnight. The mats are collected for 90 minutes, unless stated otherwise, at a flow rate of $10 \mu\text{l min}^{-1}$ with a 15 cm tip-to-collector distance on filter paper (MN 616, Carl Roth, Germany). Depending on the environmental conditions the voltage was adjusted from 13-17 kV.

After electrospinning, conductive electrodes with desired patterns of carbon nanofibers were generated by a CO₂ laser (10.6 μm , Universal Laser Systems, Polytech Systeme GmbH, Germany). The electrodes are treated with oxygen plasma for 3 minutes, to increase their hydrophilicity. To confine the area of the electrodes, a wax channel is created via wax printing on a plastic sheet and melted on the mat. The LCNFs are lifted from the paper and put on double-adhesive tape. The array is connected via a silver painting on both sides.

4.4.2 Electrochemical characterization

The electrochemical measurements were performed using a $\mu\text{Stat 400 BiPotenstiotat}$ (DropSens S.L., Spain). As a redox species potassium ferrocyanide ($\text{K}_4[\text{Fe}(\text{CN})_6]$) with 1 M potassium chloride (KCl) in 0.1 M K-phosphate buffered saline (pH 7) was used. All reported potentials are measured versus an Ag/AgCl reference electrode with a Pt wire as an auxiliary electrode. For obtaining information about electron transfer during the redox cycling, cyclic voltammograms were measured in dual mode, one working electrode being connected as a generator and a second one as a collector. The generator is swept from -0.2 to 0.6 V, while the generator is held constant at -0.25 V. For the chronoamperometric measurements one of the working electrodes was held at the oxidation potential and the other one at the reduction potential. The oxidation potential was fixed at 0.4 V and the reduction at -0.25 V, after measuring CV in a single mode.

4.4.3 Morphology characterization

The nanofibers were imaged using scanning electron microscopy (Zeiss/LEO 1530, Germany) at 5 kV. After the cutting of the samples, they were sputtered with gold for 30 s (≈ 7 nm layer thickness) and placed on specimen stubs.

A light microscope from KERN Optics Germany was used to determining the gap width and finger width.

4.5 Results and Discussions

4.5.1 Interdigitated electrodes fabrication

Most electrode systems implemented for redox cycling are fabricated via complicated and expensive methods. We propose a simple and inexpensive fabrication method for porous substrate-free electrodes based on nanofibers. For the successful implementation of redox cycling, a narrow gap between two adjacent electrodes is required so that the redox species is oxidized/reduced at the generator and the analyte is directly collected by the collector and reduced/oxidized back, creating a cycling effect. If the twin system is not connected, i.e., no collector, the analytes are oxidized and diffuse back into the bulk solution (Figure 4.2a-i). However, if both electrodes are connected and controlled separately, the oxidized/reduced analyte's regeneration enables signal amplification (Figure 4.2a-ii). Two strategies for creating redox cycling from LCNF electrodes were investigated: interdigitated electrodes (IDEs) (Figure 4.2b) and stacked electrodes (Figure 4.2c). If redox cycling is achieved, it creates the hysteresis shape due to limiting current plateau of the voltammogram in dual mode, where an amplification can be observed compared to the signal in single mode (Figure 4.2d-i), having the shape of regular CV (Figure 4.2d-ii). Then the dual mode and single mode signals overlap perfectly.

The sigmoidal shape displays the plateau of the steady state, indicating that the diffusion layer does not expand anymore but remains constant, an indication of redox cycling. Compared to the wider gap, the plateau is replaced by the peak of a usual CV, meaning that the diffusion layer keeps expanding, and the analyte does not reach the collector. The quality of the redox cycling can be assessed through the amplification factor and collection efficiency. The AF is defined as the ratio between the current in dual (collector on – during redox cycling) and in single mode (collector off – no redox cycling), while CE is the ratio between the current of the generator and the collector. Since CE describes the diffusion of one molecule after being oxidized/reduced from one electrode to another electrode, high CE is not directly correlated with high AF. This behavior of low Afs and very good Ces is common.^[219]

The writing process of the electrodes includes carbonization of the nanofiber mat by a CO₂ laser, creating very focused energy, causing heating of the material, and triggering temperature-dependent processes. The high temperatures can produce sintering and densification of the materials, which can further expand of the carbonized material.^[220] This expansion can also be seen when the LCNF is scribed on the PI NF.

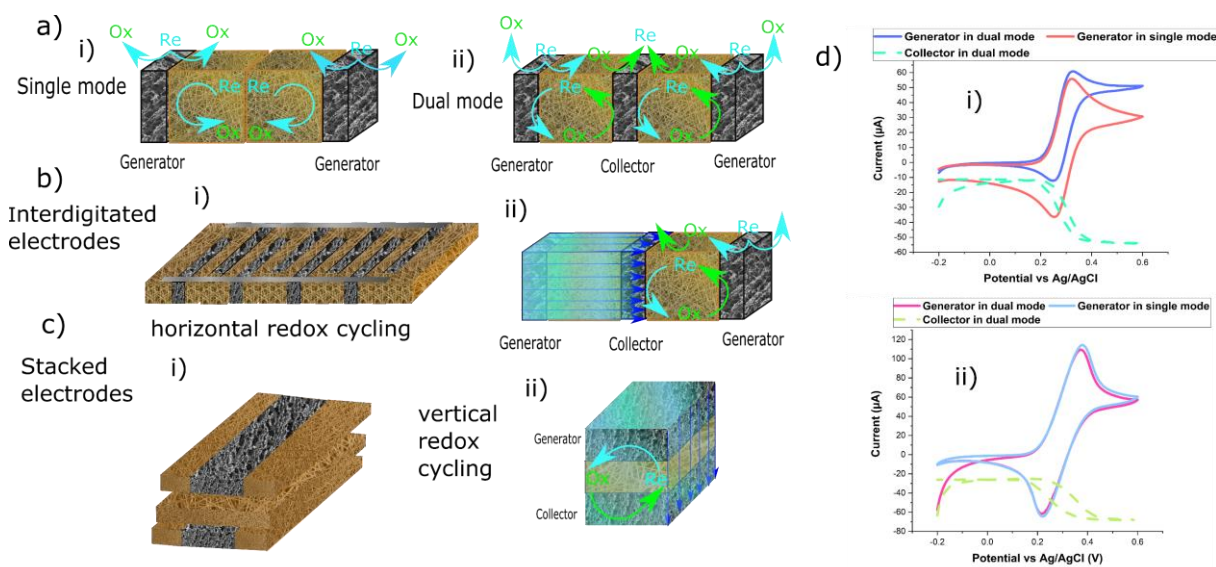


Figure 4.2. a) Scheme for redox cycling strategy in a 3D LCNF based IDE set-up: single mode (i) vs. dual mode (ii). b) IDE made from LCNF as a flow-through system with a respective redox cycling scheme. c) Stacked electrodes (i) and the vertical scheme for redox cycling (ii). d) Dual cyclic voltammetry in dual-mode and single-mode measured with 1 mM $K_4[Fe(CN)_6]$ in 0.1 M K-PBS (pH 7) with 1 M KCl for electrodes with narrow gaps (i) and wider gaps, which don't enable redox cycling (ii).

The main challenge in fabricating carbon IDEs is to achieve micrometer-sized electrodes. Therefore, the expansion of the material is an essential factor to be addressed. The studies on the expansion (Figure 4.3a) revealed that the fingers with a size close to the limit of the laser beam (around 50 μm) expand by 400%, having an actual size of 200 μm . As the width of the designed fingers increases to 100 μm , the expansion reaches 100% and remains the same for even wider fingers (Figure 4.3a). The expansion must be considered when designing the gaps because the expansion could cause a connection between fingers leading to short circuits. The expansion of the material represents a drawback of the scribing technique, which hinders the production of even smaller gaps. However, this could be solved by using a pulsed laser, which enables faster cooling (lower heat dissipation) and more precise processing.^[220]

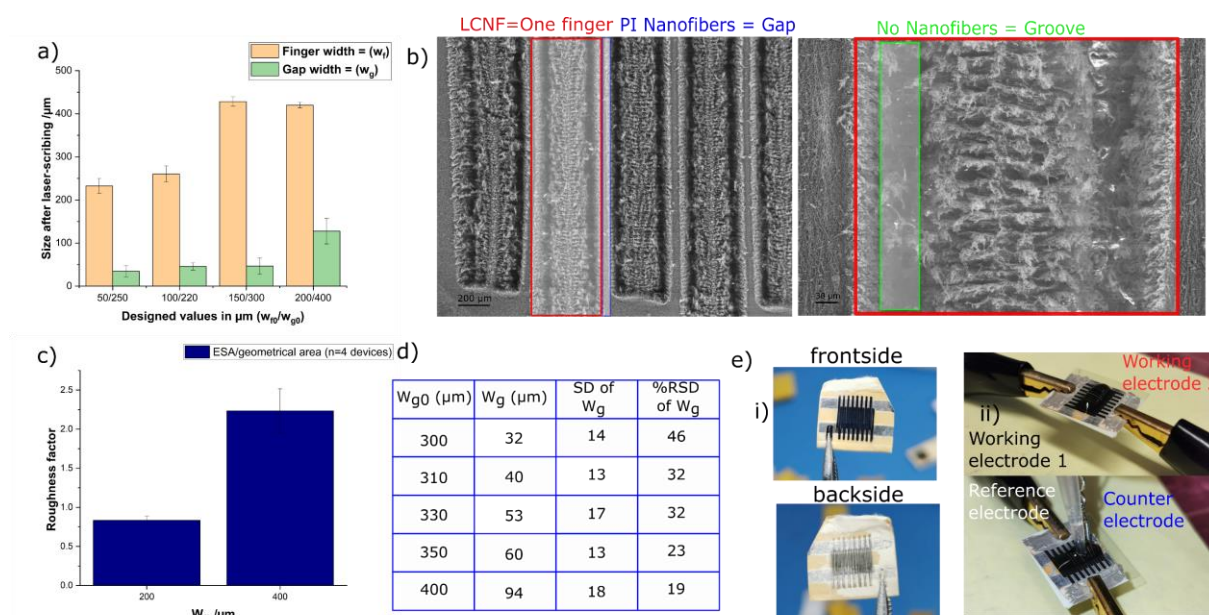


Figure 4.3. Fabrication of IDEA: a) Real size of the fingers and gap versus the designed value $n \geq 15$, b) SEM of 400 μm fingers with different magnifications, c) Roughness factor calculated for thin and thick fingers, d) Table of designed gap widths and achieved gap widths for wider fingers (400 μm), e) pictures of the IDE system for electrochemical characterization and the substrate-free IDE.

The morphology of the fingers consists of grooves between the middle and the edge of the electrodes delimited with green in Figure 4.3b. The overlapping of the laser beam's heat dissipation causes the grooves during the carbonization process. It was observed that the fingers at the edges of the array do not have these defects. The grooves are probably a consequence of the high energy density distribution of the laser beam. The energy density is unevenly distributed, disrupting the carbon material. This limitation of the laser could be facilitated by using a different laser or focusing optics to cause less overlapping or better focusing of the energy.

For the fingers designed with W_{f0} 100 and 150 μm (correlating to W_f 200 and 400 μm), the electroactive surface area (ESA) was calculated in order to find the best candidate for redox cycling (Figure 4.3c). The ESA of one array (8 fingers) was calculated with the Randles Sevcik equation. The calculated ESA was normalized by dividing it by the geometrical area of each array, resulting in the roughness factor (RF). The wider fingers have an RF twice as the thinner fingers. Moreover, these are also easier to handle and more reproducible; therefore, they were studied further. To achieve the narrowest gap for the wider fingers (W_f 400 μm), the expansion of the fingers had to be considered (Figure 4.3d). The designed gaps were around W_{g0} 300-400 μm , but the expansion decreased the gaps to a W_g of about 30 μm . Therefore, the narrowest gap had about 32 μm , but the standard deviation was high. Therefore, for studying the performance regarding redox cycling, the gaps with W_{g0} 310 to 400 μm , corresponding to W_g 40 to 94 μm , were considered. The obtained IDE system is substrate-free (Figure 4.3e-i), and can be integrated with various applications. A wax barrier is also melted into the fibers to confine the contact area between the 200 nm nanofiber and the electrodes. However, a simple system was fabricated to study its performance, by

adding a plastic sheet together with double adhesive tape for robustness. The system was studied in an electrochemical cell formed by the two IDEs as two working electrodes, a standard Ag/AgCl reference electrode, and a Pt wire as the auxiliary electrode (Figure 4.3e-ii).

4.5.2 Characterization of IDE

In order to maximize the electroactive surface area (ESA) of the finger-like electrodes, the geometrical area can be enlarged, or the height of the electrodes can be increased. The latter will also benefit the trapping of the molecules between the adjacent fingers, making redox cycling more efficient than small electrodes. Since our developed method for the fabrication of LCNFs implies collecting nanofibers, the height of the electrodes can be easily adjusted by varying the collection time. The SEM images of the IDEs collected for different times (Figure S4.1) were used to determine the height of the corresponding fingers.

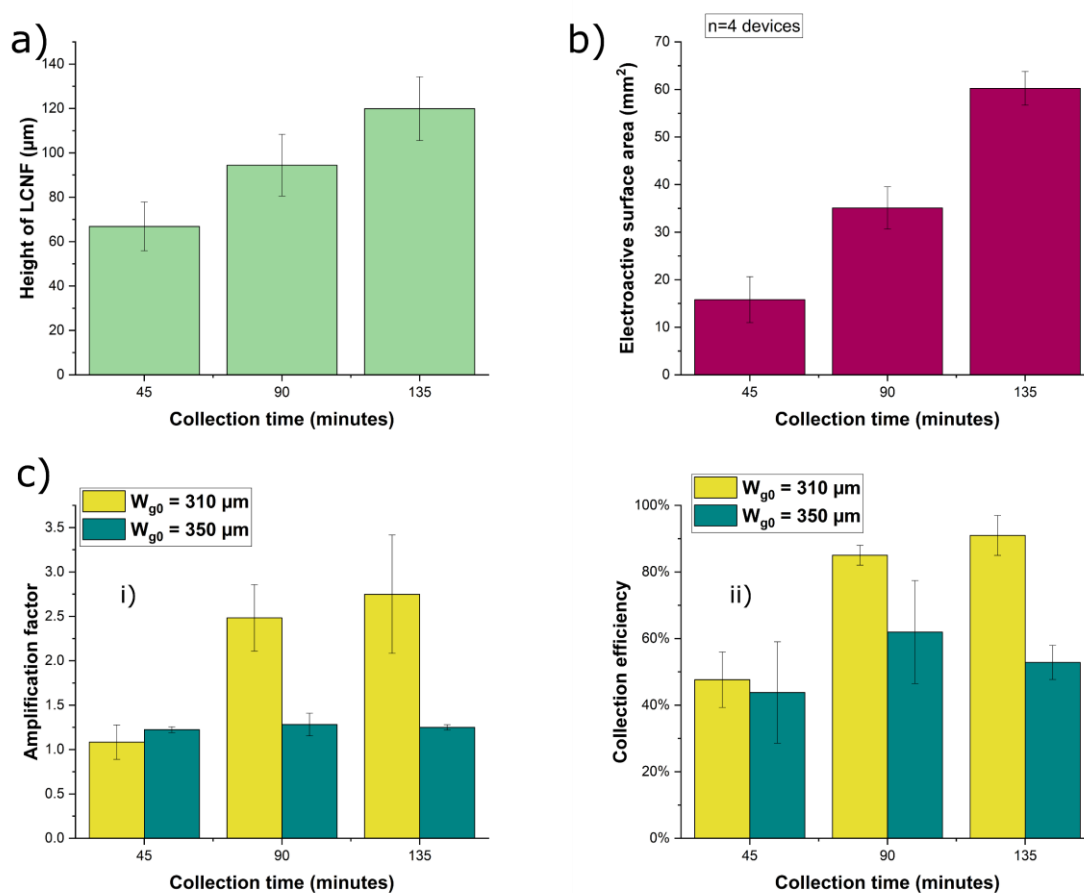


Figure 4.4. Influence of the collection time: a) Height of the LCNF determined from SEM images, b) Electroactive surface area calculated for the different LCNFs, b) Characterization of the LCNF-IDE via dual CV concerning the i) Amplification factor and ii) Collection efficiency. For all investigations $n \geq 3$ different devices. For 45 min collected mat the scribing conditions are 1% power and 60% speed, for 90 and 135 minutes collected mat: 4% power and 40% speed.

The collection time of the nanofibers directly influences the electrode height and, implicitly, their performance. For this type of polymer (Matrimid), it was found that with increasing the collection time, the height of the mat increases linearly (Figure 4.4a). In order to determine the oxidation and reduction potential, the system was first scanned in a single mode, and hence a reduction potential of -400 mV was used (Figure S4.2). The electrodes from the thicker mat have a higher ESA, which is beneficial for the electrochemical performance of these devices, showing a good correlation between the height of the electrode and the ESA (Figure 4.4b). The dual cyclic voltammograms (CVs) (Figure 4.4c) for the narrower gaps (W_{g0} 310 μm and W_g 40 μm) demonstrate that the amplification factor (AF) (Figure 2c-i) increases from 45 minutes to 90 minutes collection time. However, for higher collection time, it remains constant. The same behavior can be observed for the collection efficiency (Figure 4.4c-ii). The increase in AF is probably due to the increase in the height of the electrode, which causes the efficient trapping of the redox analyte.^[204] The broader gaps show no redox cycling as the gap is much larger than the diffusion length of the individual fingers. Regarding the redox amplification, the narrowest gap and the collection time of 90 minutes are the most beneficial ones. However, higher collection time could also be implemented to improve redox cycling. However, the scribing conditions must be studied and adjusted to carbonize the full height of the nanofiber mat without burning the material.

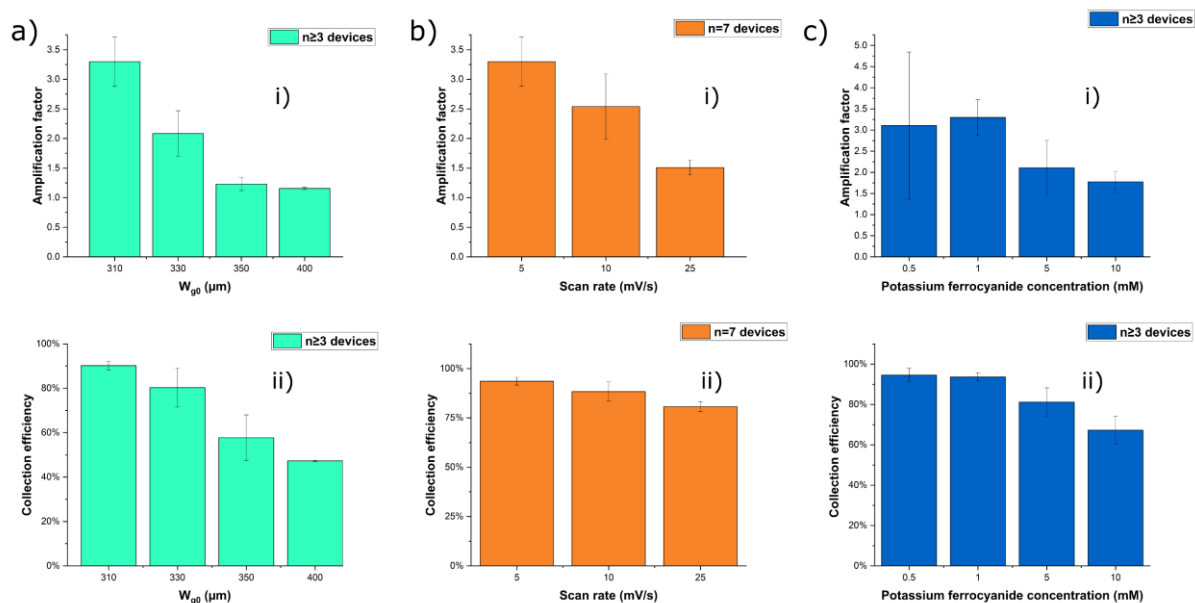


Figure 4.5. Optimization of parameters to maximize amplification factor and collection efficiency of IDEs: a) Gap width variation, b) Scan rate variation and c) Concentration variation of ferri/ferrohexacyanide. Unless stated otherwise, the scan rate 5 mV/s was applied.

One of the most important parameters influencing redox cycling is the distance between the adjacent fingers. Therefore, the gap widths were varied, and the respective AF and CE were determined (Figure 4.5a). In this case, both the AF and CE decrease with increasing the gap width. This behavior is predictable, as the higher gaps hinder the diffusion layers from overlapping. Therefore, the best

performance was achieved for the W_{g0} of 310 μm (W_g of 40 μm). The performance is highly efficient considering the gap, which is larger than the ones reported in the literature for the IDEs fabricated via photolithography.^[221] The current has been amplified by 3.5 times for this condition, and CE is 95%. This result is outstanding, considering the gap- and fingers- size, and that the device is fabricated in a couple of minutes with costs < 0.02€.

The investigation of the scan rate reveals a decrease in the AF and CE with faster scanning (Figure 4.5b). The peak current is known to be proportional to the square root of the scan rate from the Randles Sevcik equation.^[222] At higher scan rates, the redox species are consumed faster, and the diffusion cannot provide enough mass transport to reach a steady state. When the scan rate is slow, the redox species' consumption rate is slower, and diffusion is fast enough to produce a steady state. Thus, a diffusion plateau is formed. In this case, the limiting current only depends on the electrode's geometry.^[223] Because, the peak depends directly on the scan rate in the single mode, the AF (the ratio between single and dual-mode current) decreases more strongly with increasing the scan rate. As the CE is calculated exclusively from the currents in dual mode, the performance decreases more slowly. However, in both cases, a slower scan rate yields better performance because the time for redox cycling is longer, causing more cycling events. Moreover, the gap consists of NFs, which can cause molecules to get scattered away from the collector. So, with the gap increase more species could get lost to the surrounding.

The concentration variation displays a decrease in the AF and CE, when increasing the concentration from 1 to 10 mM (Figure 4.5c). The decrease in the effectiveness of the redox cycling is because the analyte is already in excess, and amplification is no longer necessary.

The fingers designed with W_{f0} 100 μm were also investigated regarding redox cycling (Figure S4.3). As the outcome of the redox cycling depends on the geometry of the finger, a better performance was expected for thinner fingers. However, the best AF is similar to the wider fingers (Figure S4.3a). The performance of the IDEs for redox cycling with respect to the scan rate (Figure S4.3b), concentration variation (Figure S4.3c), and height dependency (Figure S4.3d) resulted in the same behavior as the thick fingers. Due to the limitation of the laser used in this study, the fingers are fragile, and they easily break.

Since chronoamperometry is also a known technique to study redox cycling, the performance was also characterized with respect to dual chronoamperograms (Figure S4.4). When the collector is disconnected (single mode), the signal decreases significantly (Figure S4.4a). The AF and CE (data not shown) measured with CA correlate well with the results from CV. With increasing the gap width, the amplification factor decreases exponentially with an R^2 of 0.99. The well-known exponential behavior^[200,224,225] is observed, which is caused by the shortening of the diffusion length with decreasing the gap width.

The time constant is an essential parameter for characterizing IDEs, as it reflects how fast the two pairs of electrodes reach the steady state without being connected as two working electrodes (here, one array is the auxiliary electrode) (Figure S4.5a). The time constant increases as the gap increases because diffusion between the adjacent electrodes requires longer time. For the best condition, the steady state is reached within 5 seconds (Figure S4.5 b and c).

Laser-induced graphene (LIG) is comparable to LCNF, as both are fabricated via CO₂ laser-carbonization and are porous.^[226] In contrast to the NF, the polyimide foil (Kapton), from which LIG is fabricated, has a more planar structure. Therefore, the NFs, which have a rougher surface, lead to multiple scattering and reflecting events of the light inside the material producing a higher absorption of the energy.^[220] Higher energy dissipation causes a more extensive expansion of the LCNF compared to the LIG (Figure S4.6). If IDEs are scribed on Kapton foil with the same conditions used for PI NFs, no redox cycling can be achieved because the fingers do not expand, and the gaps are too wide for redox cycling (Figure S4.6 b and c). However, if the fingers are scribed to have the exact sizes as the ones achieved by LCNF IDEs (Figure S4.7), the fingers of the arrays are short-circuited. Therefore, the PI NFs are more beneficial to creating IDEs for redox cycling.

4.5.3 Stacked electrodes

As described before, the efficiency of redox cycling depends on the distance molecules have to travel between the electrodes. In the case of IDEs, the molecules travel horizontally between two adjacent electrodes. Therefore, the main limitation of the IDEs is the lateral resolution of the fabrication methods. For high lateral resolution, the fabrication methods require technologies such as the electron beam, which is complicated, expensive, and has low-throughput.^[227] The alternative is to deposit electrodes on top of each other, avoiding the need for high-resolution lateral fabrication. So, the spacer between the electrodes is tuned by the thickness of the insulating layer.

The vertically separated electrodes, namely stacked electrodes, are wide electrodes peeled off from the filter paper and transferred onto another. They are separated by another layer of a non-carbonized nanofiber mat, which acts as an insulating layer. Two strategies were investigated for creating the gap between the electrodes: spinning nanofibers directly onto the electrodes or spinning separately and transferring the mat afterward.

The first strategy was to create a nanofiber mat for 90 minutes, scribe the electrodes (same as our current strategy), and spin for a couple of minutes on the electrodes to create a gap between the two electrodes. In order to achieve reproducible thin mats on the electrodes, the spinning time was varied (Figure 4.7a). Interestingly, for this type of polymer (polyimide) to achieve a homogenous mat, it is necessary to spin for 5 minutes or longer. An indication of redox amplification is the obtained plateau of the steady state (Figure 4.7b). The AF and CE decrease with increasing the collection time for the good reproducible

mats (Figure 4.7c). The decrease is expected, as with higher collection time, the mat thickness is increasing, and therefore, the gap between the electrodes is wider, hindering redox cycling. The scan rate and concentration variation (Figure S4.8) showed no trend. The scan rate is related to the time available for molecule to diffuse between electrodes, so the lack of dependence could indicate a small gap, for which 10 mV/s is already enough for the molecules to diffuse.

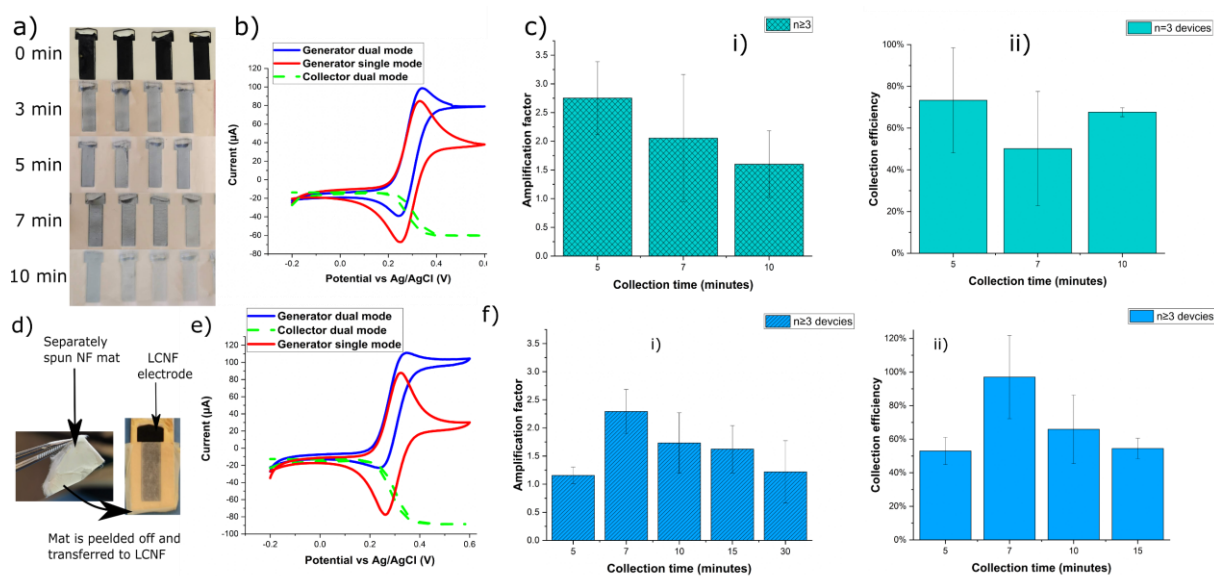


Figure 4.6. Comparison between fabrication of stacked electrodes. a) Pictures of the LCNF with collected nanofibers on top. b) Dual cyclic voltammograms of optimized system. c) Collection efficiency determined for the stacked electrodes with different collected nanofiber mats (5,7,10 minutes) on top of the electrodes. d) Pictures of the separately spun mat and the electrode covered with the mat. e) Dual CV from the optimized system. f) AM and CE determined for mats spun separately for different amount of time (5, 7, 10, 15 minutes).

Stacked electrodes, fabricated by spinning a different mat as an insulating layer between the electrodes (Figure 4.6d), display the typical current plateau (Figure 4.6e), indicating successful redox cycling. After electrospinning, the second mat is peeled off from the filter paper and transferred to the electrodes (Figure 4.6d). The voltammogram from the dual mode displays a more constant plateau than the one for the stacked electrodes with spinning on the electrodes, indicating a smaller gap between the electrodes (Figure 4.6e). The small gap is either because some NFs remain on the substrate after peeling off or get compressed when transferred. The AF and CE decrease with increasing collection time for longer than seven minutes (Figure 4.6f). For five minutes, the nanofibers are not dense enough, and peeling off hinders a reproducible, and reliable mat transfer. The best performance was achieved for seven minutes. The scan rate and concentration of ferrihexacyanide were also varied to optimize the redox cycling (Figure S4.9 a and b). The scan rate does not influence the efficiency of the redox cycling as with the IDEs, which is the same as with the other stacked electrodes. As mentioned, the gap is probably smaller for the stacked electrodes compared to the IDEs, so no difference was observed between 5 and 10 mV/s. This could indicate that even a faster scan rate could be used for this configuration. The variation of

concentration follows the pattern of the IDEs for the five minutes collected mat in between, for which the 10 mM has a significantly lower signal than 1 mM ferrihexacyanide.

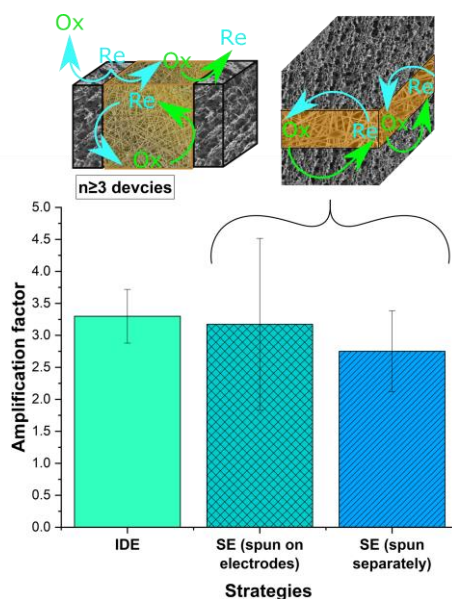


Figure 4.7. Comparison of amplification factor between IDE and stacked electrodes. Measurements were performed with 1 mM ferri/ferrohexacyanide and 5 mV/s.

The LCNFs have been demonstrated to produce redox cycling in all three studied cases. The IDEs proved to be better reproducible than the strategy where two wide electrodes are used for stacking (Figure 4.7). For the fabrication of stacked electrodes, the strategy to spin a separate mat produces more reliable gaps between the electrodes than spinning directly onto the LCNF. The performance of the stacked electrodes is not as efficient as expected, probably because the molecules are scattered away when diffusing through the middle NF mat, and can also diffuse through the second electrode, increasing the diffusional loss of the molecules. Therefore, even though the stacked electrodes probably have a narrower gap, the amplification is not very efficient. For the IDEs, peeling off the insulating NFs could be beneficial to improve the diffusion of the molecules and create a more efficient regeneration of the oxidized/reduced molecules.

The achieved AFs prove the possibility of enhancing the electrochemical signals for the improvement of sensitivity in electrochemical sensors. The significant advantages of these configurations are the simplicity, versatility, and inexpensiveness of the fabrication. The IDEs can be implemented into microfluidic chips or lateral flow assays, while the stacked electrodes are suitable for vertical flow applications. These flow-through transducers are especially beneficial for the development of electrochemical POC devices.

4.6 Conclusion

Nanofibers have been demonstrated as particular nanomaterials for POC and wearable devices since their porosity and flexibility can be used for mixing, wicking, and as breathable membranes. In this paper, electrodes made of carbonized nanofibers have been demonstrated as interdigitated or stacked electrodes to efficiently implement redox amplification for a highly sensitive strategy toward detecting electrochemically active molecules. Moreover, the as-described electrodes are not only fast, easy, and inexpensive to fabricate but also highly versatile, as their size, shape, and height are easily adjustable. Furthermore, the strategy to electrospin nanofibers onto electrodes can be exploited in terms of filtering, mixing, or capturing specific molecules which can be later detected at the electrode. The electrospun nanofibers on the electrodes could be adapted by choice of polymer to create gradients for wettability or design for repelling unwanted molecules. The as-described method is a significant development since most electrodes implemented in redox cycling schemes are expensive, and complicated to fabricate. The substrate-free electrodes can be implemented in more complex detection strategies as lateral or vertical flow assays in combination with other nanofibers or porous membranes.

4.7 Supplementary Information

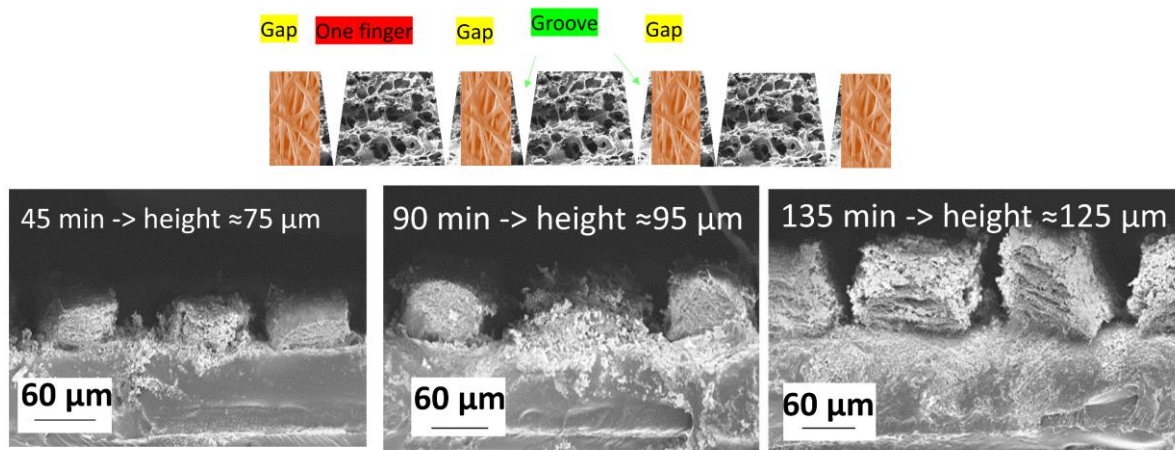


Figure S4.1. SEM images of interdigitated electrodes (IDE) made from LCNF. For 45 min collected mat the scribing conditions are 1% power and 60% speed, for 90 and 135 minutes collected mat: 4% power and 40% speed.

The nanofibers were collected for different times to adjust the height of the electrodes. In the side views of the SEM images, the following structures are displayed: not-carbonized nanofibers, a groove, a functional part-middle part, a second groove, and the next part of insulating nanofibers which represents the gap between finger electrodes. The height increases with collection time, as expected. Moreover, it can be observed how the 45 minutes mat was stronger carbonized than the longer collected mats because the laser beam's energy does not penetrate the whole depth of the mat. For the 135 minutes mat, it is also observable that the electrode is not fully carbonized, which is also reflected in its performance.

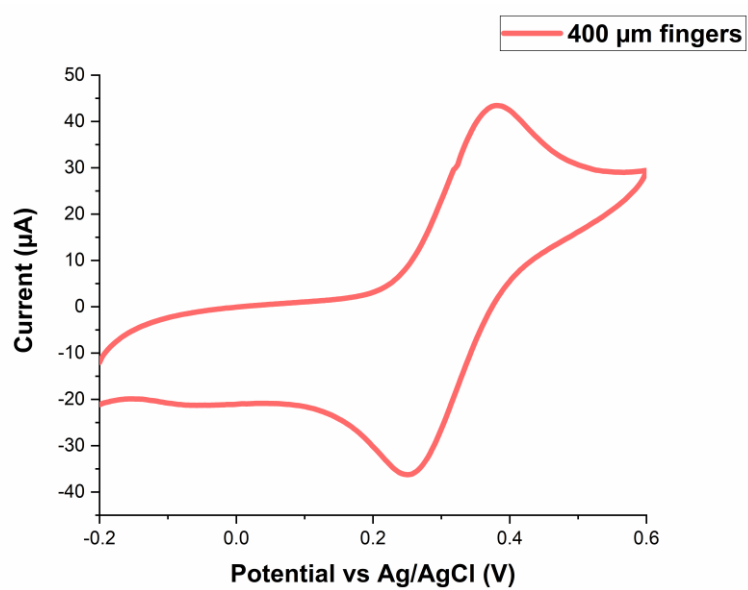


Figure S4.2. Single CV measurements of one array of 400 μm fingers. In order to determine the oxidation and reduction potential of the array system, cyclic voltammogram was measured with 1 mM $\text{K}_4[\text{Fe}(\text{CN})_6]$ in 0.1 M K-PBS (pH 7) with 1 M KCl.

The oxidation potential was further used as 400 mV.

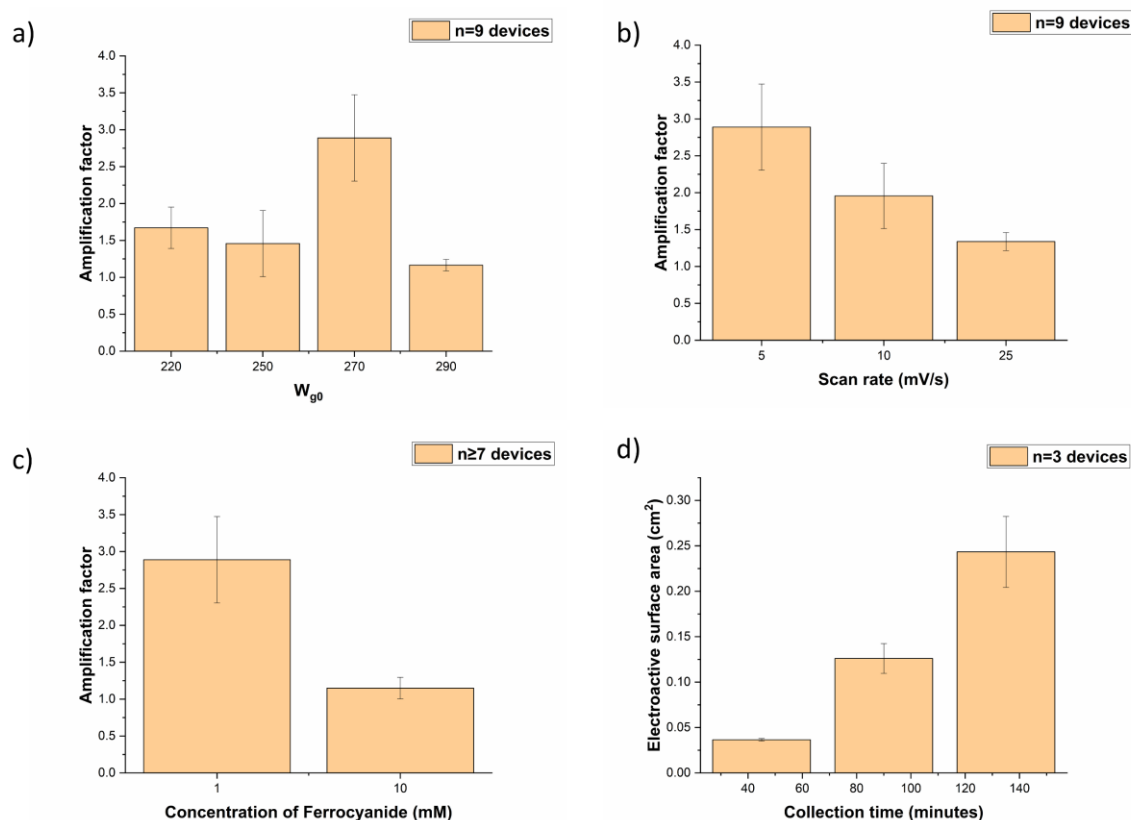


Figure S4.3. Redox cycling was measured with thinner fingers (200 μm). a) Amplification factor determined for different gap sizes. b) Amplification variation with scan rate for a 270 μm gap. c) Amplification factor dependence on the concentration of Ferrocyanide for devices with 270 μm gaps. d) Electroactive surface area for different collection times (45, 90, and 135 minutes).

No dependency can be observed for the AF with increasing the gap width (Figure S4.3a). The non-consistent Afs might be due the thinner fingers are scribed too close together; therefore, they are fragile and break. So, for 220 and 250 μm, the AF does not reflect the actual gap. When the designed gap width is increased to 270 μm, a gap of about 50 μm is realized, and the electrode can be carbonized reliably. The best amplification was determined to be 3× for the thinner fingers with a gap width of 50 μm. This condition was used to study of the different scan rates, concentrations, and collection times. The AF decreases with increasing the scan rate (Figure S4.3b). This behavior is similar with the wider fingers. Even for the thinner fingers, the higher concentration – 10 mM results in a lower signal than 1 mM, showing that the redox cycling is not as efficient for higher concentrated analytes than for lower concentrated analytes (Figure S4.3c). The collection time was varied to observe the electroactive surface area of the finger-like electrodes. It was found that the height can be increased to improve the performance of the electrodes (Figure S4.3d).

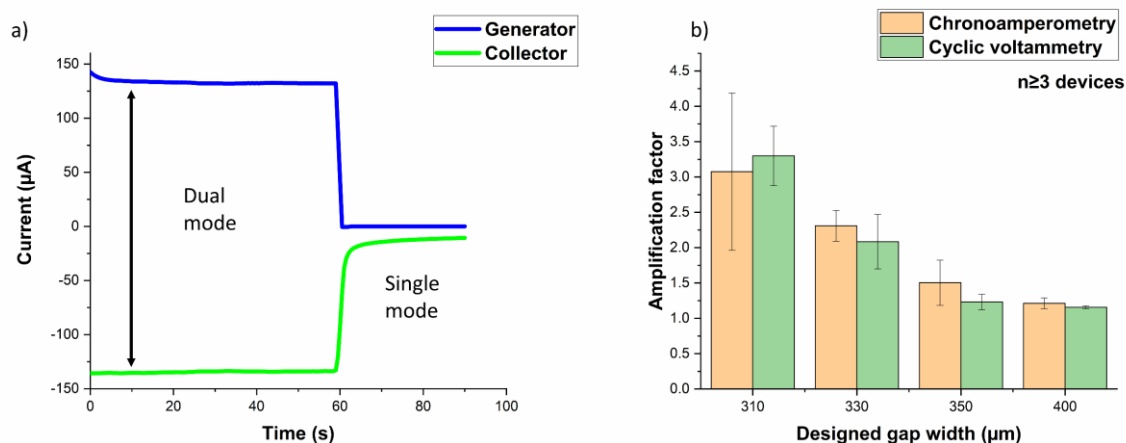


Figure S4.4. a) Dual Chronoamperogram of one device with 400 µm fingers and ~30 µm gap measured with 1 mM ferrocyanide. b) Comparison between amplification factors determined by dual Chronoamperometry and Cyclic Voltammetry. For the chronoamperometric measurements the generator was kept at 400 mV and the collector at -250 mV.

In order to display the dual and single modes, the generator was disconnected after 60 seconds to simulate the single mode. However, for the determination of the Afs two separate measurements were done, one in dual mode and one in single mode. The Afs are calculated as the ratio between the current of the collector in dual and single mode, and the Ces as the ratio between the current of the generator and the collector. In this case, it can be seen how the current is significantly enhanced when both working electrodes (arrays) are connected (Figure S4.4a). However, once the collector is disconnected, there is no more redox cycling happening, and the current of the collector drops. The results are very similar for both techniques, suggesting that both methods can be used to advantage the enhancement obtained due to redox cycling (Figure S4.4b).

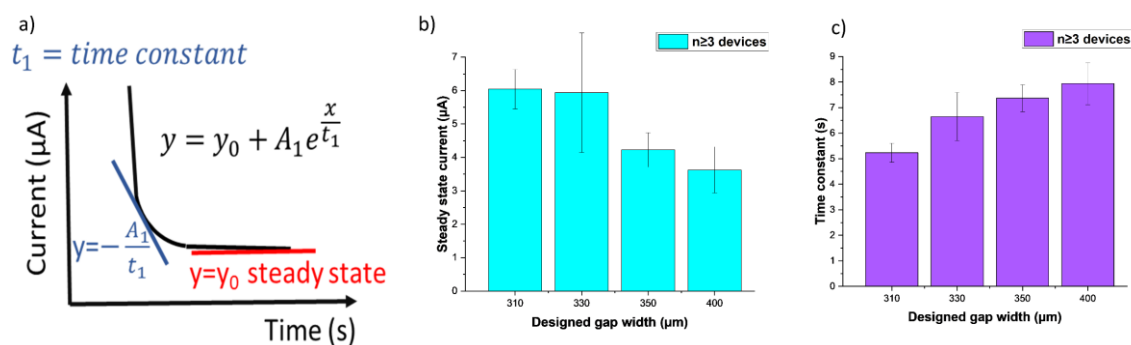


Figure S4.5. a) Scheme for determination of the time constant and steady state current from chronoamperometry. b) Steady state variation with gap width increase. c) Dependency of time constant on gap width.

The time constant is an important parameter for characterizing IDEA, as it reflects how fast the two pairs of electrodes reach the steady state. The time constant increases as the gap increases, because the diffusion between the adjacent electrodes requires a longer time.

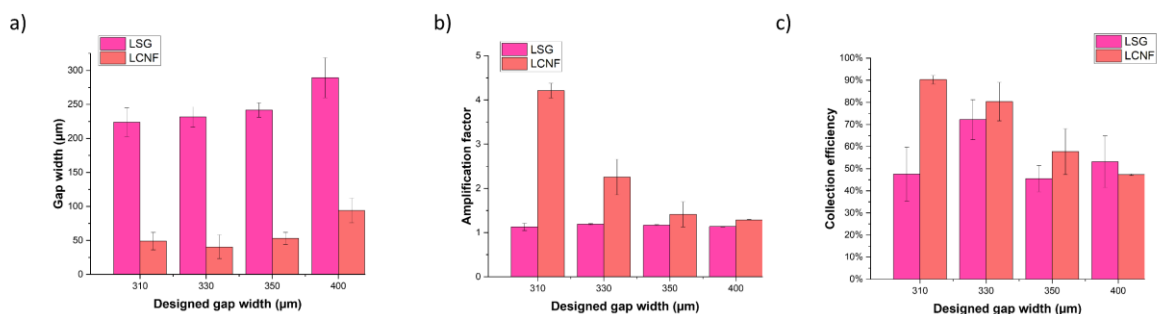


Figure S4.6. a) Size comparison between LIG and LCNF scribed with the same conditions b) Comparison of the amplification factor determined for the LIG electrodes and LCNF IDEs. C) Comparison of collection efficiency between LIG and LCNF IDEs.

Laser-induced graphene (LIG) is comparable to LCNF, as both are fabricated via CO₂ laser-carbonization on polyimide nanofibers and polyimide foil and have a graphene-like structure. In contrast to the NF, the polyimide foil, used for LSG fabrication, has a planar structure. Therefore, the nanofibers, which have a rougher surface, lead to multiple scattering and reflecting events of the light inside the material producing a higher absorption of the energy. The scattering effect causes a more significant expansion of the LCNF compared to the LSG, the LSG gap is significantly larger than for LCNF (Figure S4.6a). However, because of the lack of expansion, regardless of the width of the fingers or the gaps no amplification could be obtained (Figure S4.6b). This shows that no redox cycling takes place in the case of LSG-IDEAs. In contrast, it is shown how the LCNFs not only have higher AF (Figure S4.6b) but also vary with the finger and gap width. For both types of fingers, the AF decreases as the gap increases, and the 400 µm gap, becomes similar to the LSG, showing no redox cycling. Unlike the AF, the collection efficiency also varies for LSG, being much lower compared to the CE of the LCNF-IDEs (Figure S4.6c). The CEs describe the diffusion of the molecules between electrodes, not the regeneration of the molecules. Hence, LSG-IDEs have acceptable CE, but the molecules don't get cycled between the IDEs.

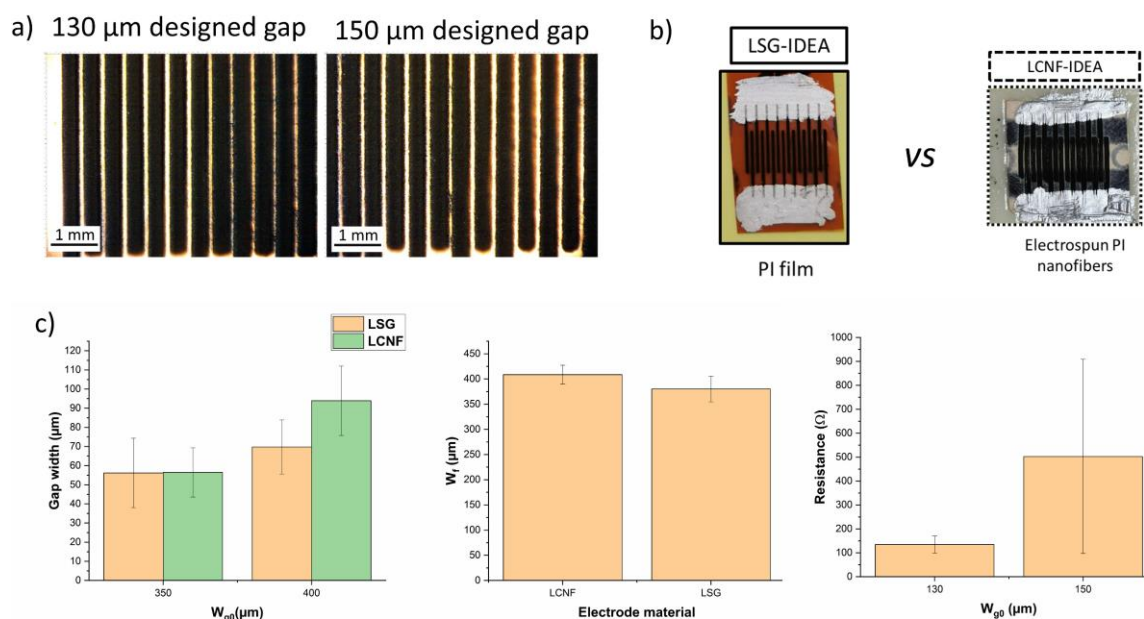


Figure S4.7. a) Microscope pictures of the Kapton foil IDE with 130 and 150 μm gap widths. B) Pictures of the devices made from Kapton foil (polyimide foil) and polyimide nanofibers. c) The difference between the gap width designed and the gap measured for LCNF and LSG. Comparison between the designed finger width and the measured finger widths. The resistance measured for LSG IDEs.

The polyimide foil was scribed with the same conditions as the NFs, resulting in very different arrays regarding gap and finger width, even if the arrays were scribed on polyimide foil having the same size as the LCNF IDE (Figure S4.7a and b). Wax was added to the LCNFs to keep the flow of the solution on the designed area, whereas the electrodes made from Kapton foil are hydrophobic, and the solution stayed on top (Figure S4.7b). The gap width and the finger width for both types of electrodes were similar (Figure S4.7c). However, in the case of the Kapton IDEs, no redox cycling could be achieved because all the devices were short-circuited. While the resistance for the LCNF is in high $\text{k}\Omega$ or $\text{M}\Omega$, for the planar LSG electrodes, they were hundreds of Ω . The resistance is higher probably due to the LCNF electrodes' porosity which insulate the adjacent fingers better.

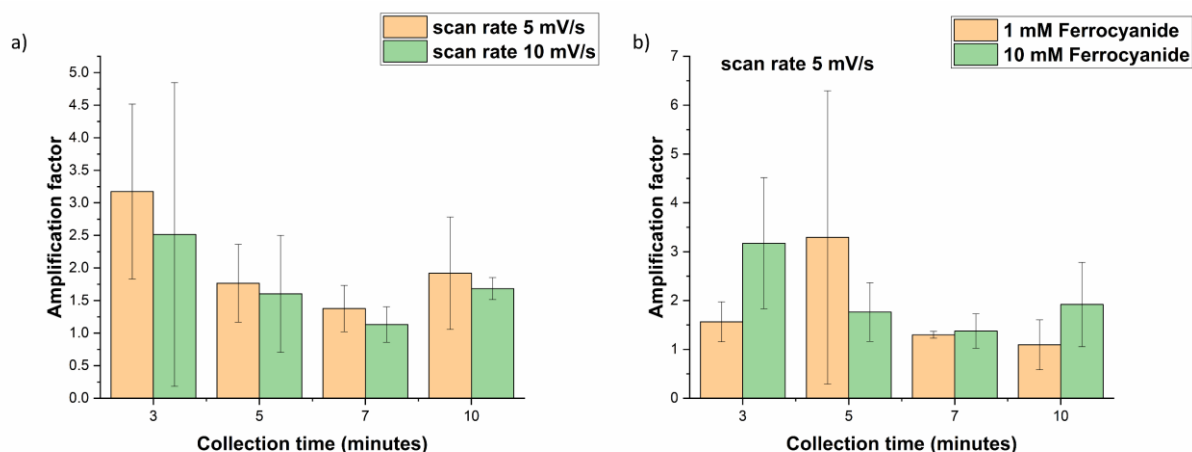


Figure S4.8. a) Amplification factor determined for 10 mM ferrocyanide and 10 mV/s with two different scan rates for different collection time of the nanofibers. b) Amplification factor determined with two different ferrocyanide concentrations for different collection times of the nanofibers.

Redox cycling was investigated for stacked electrodes fabricated by electrospinning on the electrodes. The amplification factor was determined for the different thicknesses of the insulating fiber mats and two different scan rates (Figure S4.8a). Contrary to the IDEs, the scan rate does not influence redox cycling. The lack of dependency is probably correlated with a narrower gap, as the nanofibers get pressed between the electrodes, and the analytes do not need a slower scan rate to reach the other electrode for redox cycling. So, amplification can be achieved even at faster scan rates. The behavior regarding the different concentrations of ferrohexascyanide showed no trend and high standard deviations. (Figure S4.8b) The standard deviations are caused by an inhomogeneous collection of the insulating nanofibers on the electrodes. Due to the inconsistency of the mats collected for 3 minutes no AF could be determined with 1 mM ferrocyanide.

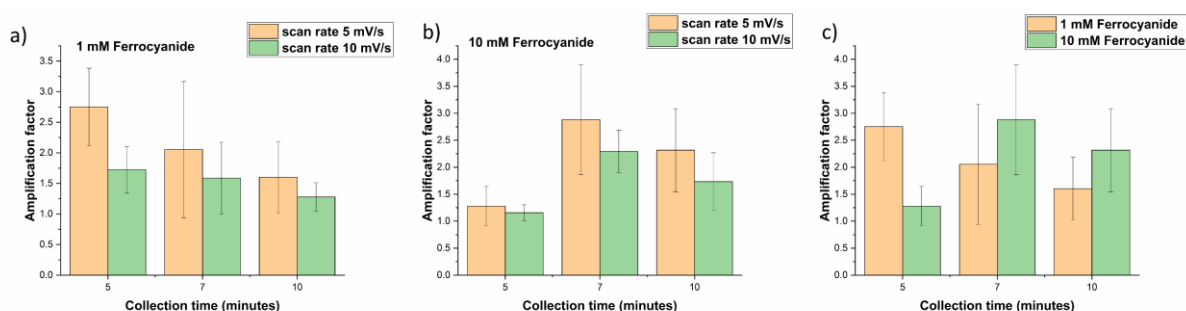


Figure S4.9. a) Dependence of the amplification factor measured with 1 mM Ferrocyanide of the scan rates for three different collection times. b) Variation of the collection time for different scan rates measured with 10 mM Ferrocyanide. c) Comparison between different concentration of Ferrocyanide for different collection times measured with 5 mV/s.

The collection time of the separately spun mat as the insulating layer was varied, and the amplification factors were determined for two scan rates, namely 5 and 10 mV/s. For 1 mM ferrocyanide, the 10 mV/s scan rate does not show any variation of the amplification factor with collection time (Figure S4.9a). The constant AF could indicate no redox cycling, or the mats do not vary enough to see a difference between five, seven, and ten minutes. However, the amplification rate decreases with increasing collection time for the lower scan rate (5 mV/s) because the mat gets thicker and redox cycling gets less efficient. For high concentrations of ferrohexacyanide (10 mM), there is a variation for both scan rates, which also shows the same trend (Figure S4.9b). Seven minutes collection time is the most efficient in this case, and then decreases when the collection time increases. The comparison between the two concentrations of ferrohexacyanide (1 and 10 mM), indicates that the thin mat shows a decrease in amplification for increasing the concentration (Figure S4.9c). The decrease in amplification is similar to the IDEs, which means that again the solution is too concentrated for efficient redox cycling.

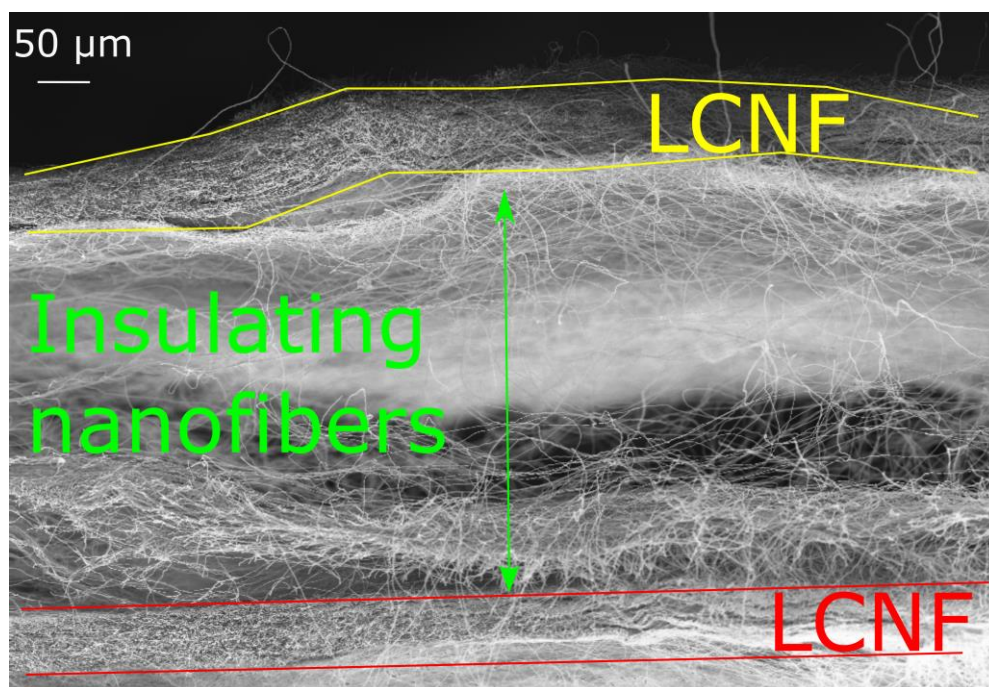


Figure S4.10. SEM image of stacked electrodes.

The mats, both the not-carbonized ones and the mats with electrodes, are very fluffy and electrostatic. Therefore, the preparation of the samples for SEM is not ideal. When the device is cut in the middle to see both electrodes and the insulating mat, the different layers move apart, as seen in the image above. However, regardless of this artifact, the two electrodes made from LCNF can be differentiated from the insulating nanofibers.

4.8 Interdigitated electrodes for point-of-care

This chapter has not been published and is not intended for publishing. All experiments were conducted by the author.

Interdigitated electrodes were fabricated via a simple and inexpensive technique, which enables their potential use for a POC device. All studies showed previously were measured with an external auxiliary electrode (platinum wire) and standard Ag/AgCl electrode. In order to be able to implement the IDEs in a POC, dual CV was measured with CE and RE made from LCNF.

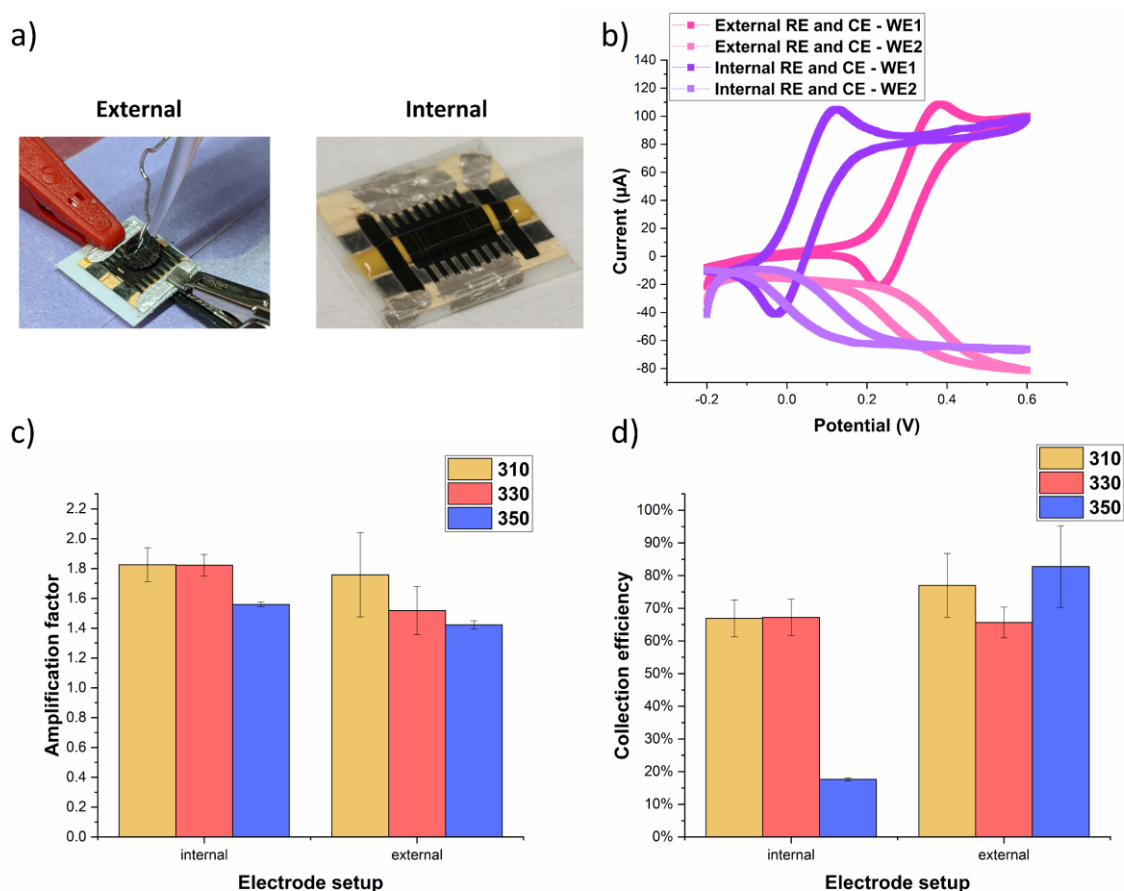


Figure 4.8. a) Pictures of LCNF IDE with external CE and RE – namely platinum wire and Ag/AgCl electrodes – external and with wide LCNF CE and RE – internal. b) Comparison between dual CVs of IDEs with internal CE and RE and with external CE and RE. c) Amplification factor determined for different gaps (310, 350 and 330 μm – designed gap width) between IDEs with internal- and external electrodes. d) Collection efficiency of IDEs with different gaps (310, 330, and 350 μm) width for internal and external electrodes. $n \geq 3$ devices

The LCNF systems with external and internal AE and CE are shown in Figure 4.8a. The dual CVs of the two electrodes setup have a similar shape, but the oxidation and reduction potentials shift when using the internal LCNF electrodes (Figure 4.8b). This shift has been seen when comparing the wide three-electrode LCNF system with LCNF with standard Ag/AgCl electrodes. The AF has a similar value for

both systems (Figure 4.8c). However, for the external RE and AE electrode system, the decrease of the AF with increasing gap size is more pronounced. The slight difference between the 310 μm and 330 μm gap sizes can be attributed to the inhomogeneous expansion of the electrodes, making the gap size the same. The collection efficiencies differed between the internal and external electrode setups, showing slightly better results for external auxiliary and reference electrodes (Figure 4.8d). The difference between the two systems can also be seen in the dual CVs, where the plateau for the limiting current is more evident and constant in the case of the external setup.

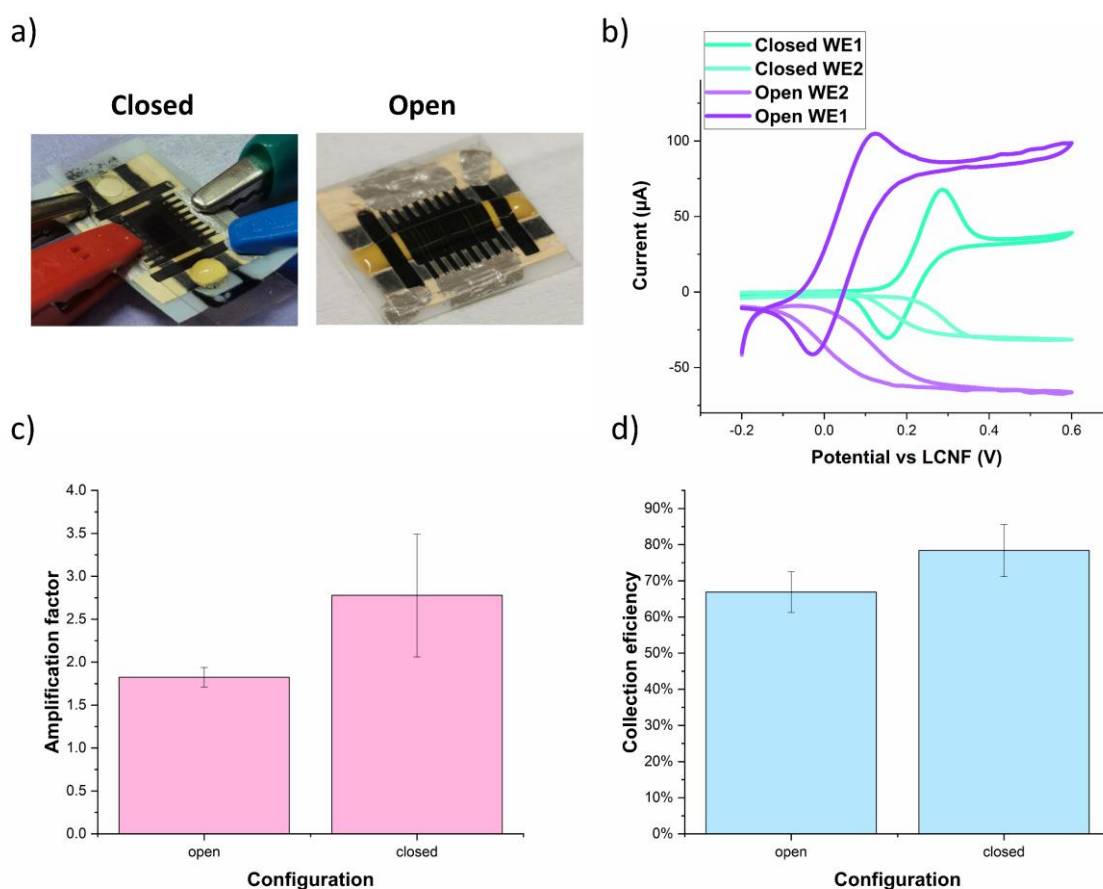


Figure 4.9. a) Pictures of a 4-electrode system with internal auxiliary and reference electrodes outside a channel (without plastic foil) and inside a microfluidic channel (with plastic foil). b) Dual CVs for the open and closed devices measured with LCNF CE and RE. c) Amplification factor for the open and closed system. d) Collection efficiencies determined for the open and closed system. $n \geq 3$ devices

As the electrochemical performance might benefit from integrating the electrodes inside a microchannel for the confinement of the analytes, the LCNF-IDE system was integrated inside a mimicking microfluidic channel (Figure 4.9a). The microfluidic channel is simulated by keeping the plastic foil from the wax printing on the electrodes and sealing the solution inside. The plastic foil consists of two holes, representing the inlet and outlet. When closing the electrodes inside the channel, the potential shifted again towards the potential seen for using an external auxiliary and reference electrodes (Figure

4.9b). The same observation was made for the wide LCNF inside and outside the channel. This consistency is proof that the electrodes and the measurements are reliable. The intensities are higher for the open configuration. The amplification factor revealed that the closed system improved the redox cycling efficiency (Figure 4.9c). This improvement results from the molecules trapping between the electrodes inside the channel compared to the open configuration, where the molecules can easily diffuse away into the bulk. Moreover, a slight increase could also be observed for the collection efficiency (Figure 4.9d).

Even though the observations confirmed the amplification of the signal for the use of LCNF-IDEs in a 4-electrode system, there could be some hidden problems in using a fully carbon-based 4-electrode system, which might not be observed with the current system. Due to the lack of confidence in the dual mode benefitting the integration of IDEs into POC devices, further experiments were carried out with single CVs (only one WE).

As highlighted in the introduction, LFA would be a perfect candidate for developing a new electrochemical POC device based on LCNF electrodes. Therefore, the following efforts focused on integrating the nanofiber mat together and scribed electrodes onto a lateral-flow strip. For all preliminary studies of the LFA, only a nitrocellulose membrane is used in the beginning, and the waste pad is added after the nanofiber mat.

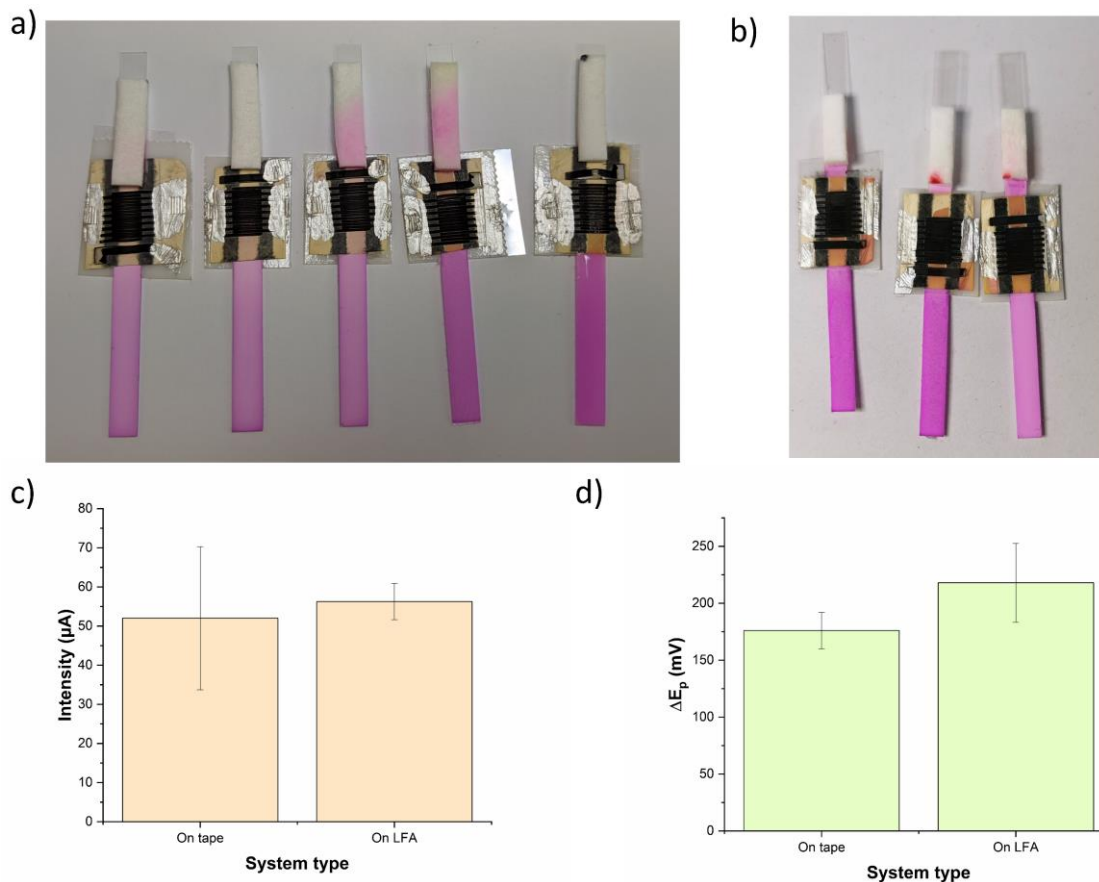


Figure 4.10. a) Pictures of LFA with nitrocellulose, PI NF incorporating 3-electrode system LCNF, and the waste pad added on top of the nanofibers. Solution containing SRB (pink dye) was used for visualization of the solution flow. b) LFA strips with LCNF, with an additional small nitrocellulose membrane and the waste pad afterwards. c) Comparison between the intensities of the oxidation peak of normal CVs measured with 1 mM ferri/ferrohexacyanide with 3-electrode system (internal LCNF CE and RE – a IDE is the AE, and the wide electrode is the RE) on tape and on LFA. d) Peak separation difference between the 3-electrode system of LCNF on tape and on LFA. $n \geq 3$ devices

Preliminary studies focused on possible integration strategies for the nanofiber mat. First, the nanofibers were added after the nitrocellulose, and the waste pad was on top of the nanofibers. As can be observed, only two devices have a proper flow of the solution till the end of the strip (Figure 4.10a). In a different strategy, another small piece of nitrocellulose was added after the nanofibers and only afterward the waste pad, so that the nanofibers would overlap on both ends the nitrocellulose membrane (Figure 4.10b). This strategy showed promising results.

Normal CVs were measured with a working electrode as one of the IDEs, and the AE as the other IDE and the RE being connected as the wide LCNF. The intensity for the oxidation potential when comparing this system on tape and LFA was similar (Figure 4.10c). The peak separations for these two systems were very similar (Figure 4.10d). The similarities show that the IDEs were successfully integrated into LFA, with the possibility to use standard CV reliably.

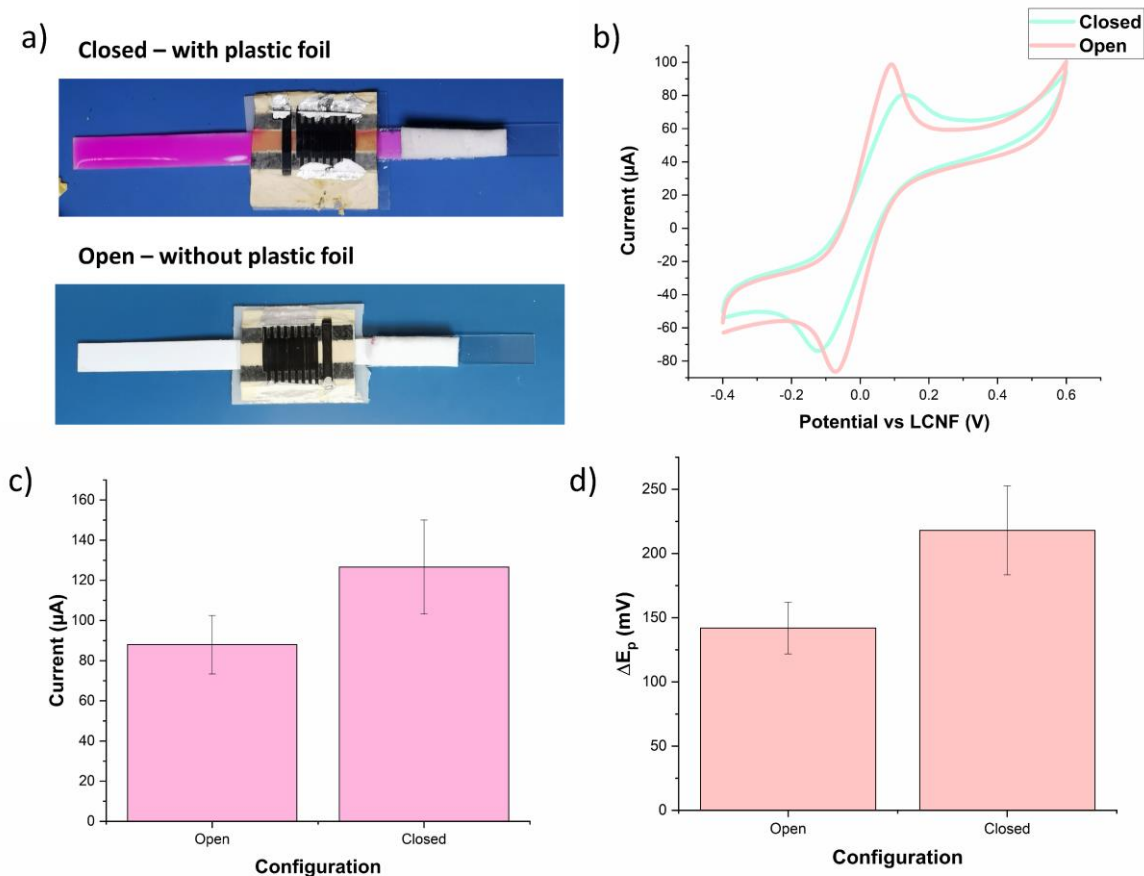


Figure 4.11. a) Pictures of LA with LCNF IDE with plastic foil from the wax channel – closed system and without the plastic foil – open system. b) CVs measured with 1 mM ferri/ferrohexacyanide of the 3-electrode setup as an open and as a closed system. c) Intensity of the oxidation peak compared between the open and the closed device. d) Peak separation between the oxidation and the reduction peak for the closed and open system. $n \geq 3$ devices

As mentioned earlier, it has been observed that the LCNFs showed better performance when being enclosed in a system where the solution is confined to flow through the electrodes. Therefore, a comparison with regular CVs between an open and a closed system was made (Figure 4.11a). The CVs look similar (Figure 4.11b), while the oxidation peak intensity is slightly increased for the closed system compared to the open one (Figure 4.11c). The electron transfer is faster in an open device than in the closed one (Figure 4.11d). However, their performance is still very similar, and no system significantly improves over the other, such as the typical wide LCNF electrodes.

Since the aim is to have a simple LFA system incorporating LCNF IDEs, two different electrode systems were studied, namely having three electrodes or just only two. As shown before, the versatility of the fabrication techniques allows the designing of different electrodes configuration (2-, 3-, and 4-electrode setup) (Figure 4.12a). In this case, the AE and RE were connected to one of the IDEs, while WE was connected to the other IDE.

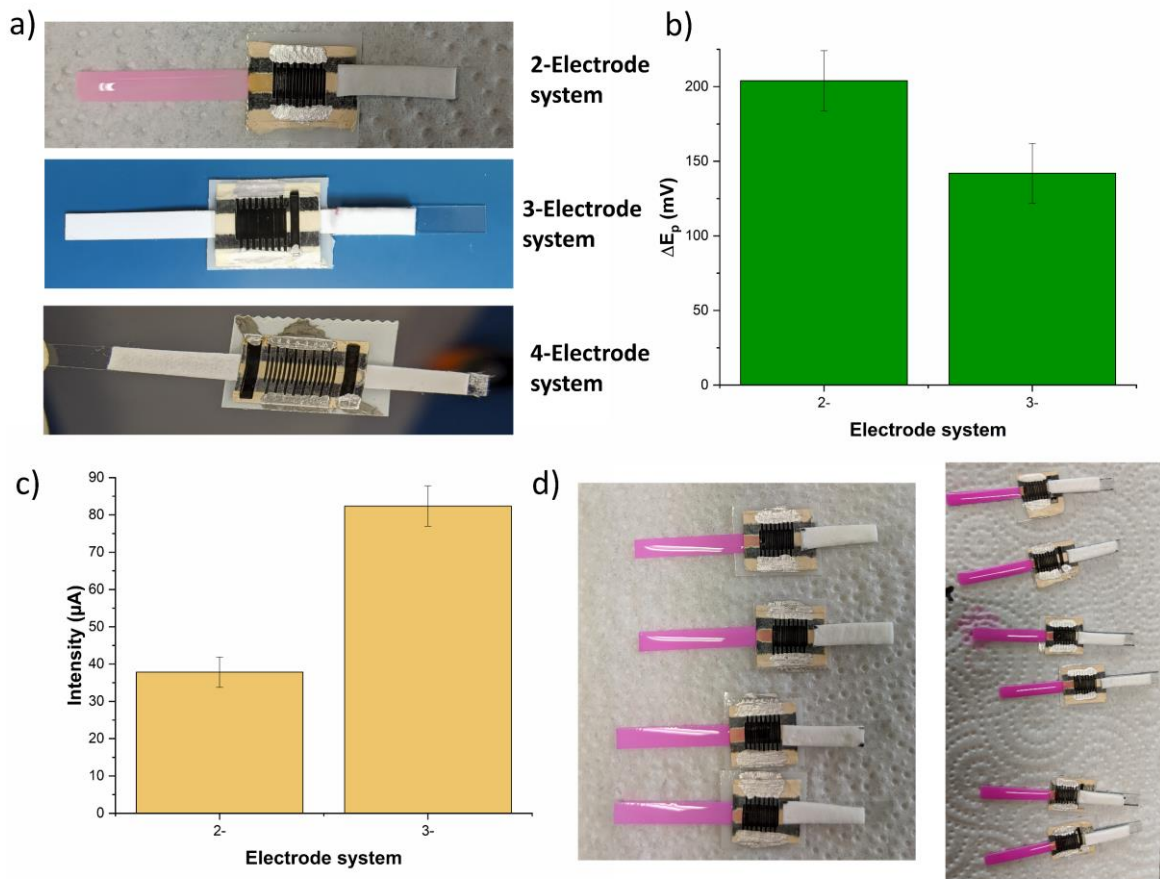


Figure 4.12. a) Pictures of different electrode systems: having 2-, 3- and 4- electrodes. b) Peak separation comparison between 2- and 3- electrode systems measured with normal CV of 1 mM ferri/ferrohexacyanide. c) Intensity of the oxidation peak for the 2- and 3-electrode system. $n \geq 3$ devices. d) Pictures of LFA incorporating LCNF IDEs.

In order to investigate the possibility of using only the two IDEs as a 2-electrode system, CVs were recorded for 2- and 3- electrode systems. The higher peak separation (Figure 4.12b) and the decreased intensity (Figure 4.12c) of the two-electrode system showed a worse overall performance for the two-electrode system.

Even though the IDEs were successfully integrated into LFA, many devices showed discontinuous flow, shown in Figure 4.12d. Moreover, optimizing the integration for the waste pads and different membrane geometries did not help tackle this problem. The problems with the solution flow are probably caused by the grooves seen in the structure of the IDE fingers. However, with a wider finger width, the groove would be significantly decreased, and the flow of the solution would improve. This system was not further studied in this project.

V. Flow-through Carbon Nanofiber-based Transducer for in-line Electrochemical Detection in Paper-based Analytical Devices

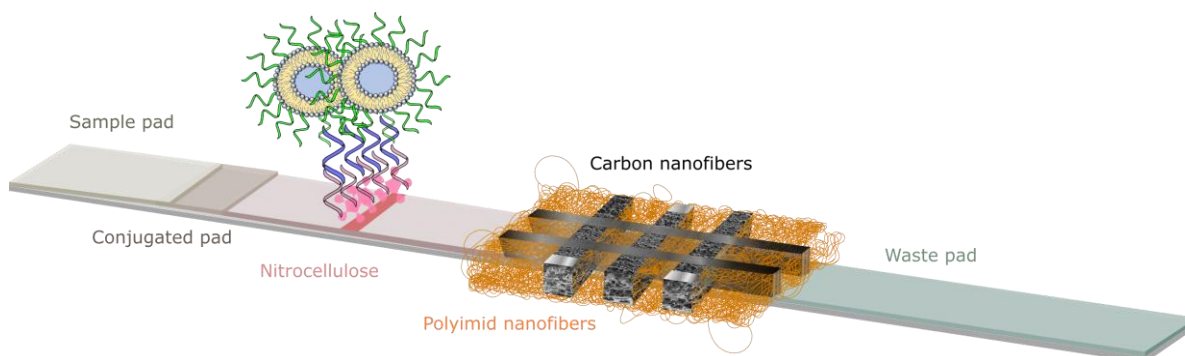


Figure 5.1. Electrochemical lateral-flow assay incorporating a three-electrode system made from LCNF with sandwich hybridized DNA sequence labelled with liposomes.

5.1 Abstract

Point-of-care (POC) devices are rapid, simple, portable, inexpensive, and convenient. On-site POC is dominated by lateral flow assays (LFAs) with optical detection delivering qualitative or semi-quantitative results. Electrochemical detection has the potential to improve their sensitivity and ensure quantitative detection, however a breakthrough in material-based technology is needed for LFAs to benefit from such integration. We demonstrate such a new concept in which the electrochemical transducer is directly embedded within the lateral-flow, enabling flow through and hence interaction with the entire sample. This is accomplished through support-free laser-induced carbon nanofibers (LCNFs). They are made by electrospinning Matrimid into nanofiber mats with subsequent pyrolyzing of electrode structures through a CO₂ laser. Their highly porous 3D structure and superior graphene-like electrochemical properties are ideally suited for the flow-through electrochemical LFA (EC-LFA), where the LCNFs are simply added in between the nitrocellulose membrane with its test line and the waste pad. LCNFs were plasma treated to enhance their hydrophilicity, wax borders were used to create a channel flow through the electrodes while keeping the contact pads isolated, and fluid flow could easily be controlled through the waste pad pulling force. With this unique set-up biological binding assays typical for LFA diagnostics were successfully implemented enabling the highly sensitive and quantitative detection of 137 pM DNA target sequences of a pathogenic organism that rivals the performance of pump-controlled microfluidic bioassays. This paves the way toward a robust integration

of highly porous carbon nanofibers-based electrochemical detection with lateral flow strategies for the detection of important biomarkers.

This chapter has been submitted as an original research article in Advanced Functional Material Journal.

5.2 Author contributions

The author, Dr. Nongnoot Wongkaew and Prof. Dr. Antje J. Baeumner contributed equally in designing, conducting the experiments, evaluating the data and wrote the manuscript draft. Prof. Dr. Antje J. Baumner and Dr. Nongnoot Wongkaew led the project administration. Anna Maria Lauerer and Ferdinand Holzhausen supported experiment implementation and validation.

5.3 Introduction

Characteristics like robustness, inexpensiveness, simplicity and the lack for large laboratory equipment or trained personnel, define point-of-care (POC) devices. The aim of these technologies is to offer people fast and direct diagnostic possibilities at their point-of-need without large expenses. Most popular POC devices are the glucometer, and the rapid Covid-19 test as well as the pregnancy test. The last two are lateral flow assays (LFAs), which typically consist of four membranes: 1) a sample pad, located at the beginning onto which the liquid sample is loaded; 2) a conjugate pad storing necessary (bio)reagents; 3) nitrocellulose hosting specific interactions between the target analytes and the reporter elements, enabling both reaction and detection during the assay; and 4) an adsorbent/waste pad, located at the end for promoting the migration of solution along the entire LFA strip.

These membranes consist of fibers made from different materials, like cotton or glass fibers, while nitrocellulose is made by partial nitration of cellulose. The porosity and surface chemistry of the fibers significantly influence the molecule immobilization, non-specific adsorption and fluid flow inside the network.^[228] The difference in the fibers' morphology renders the specific functionality of each membrane, e.g. fibers in sample pads filter unwanted molecules out, while fibers in the adsorbent pad control the flow.^[78] On the nitrocellulose membrane biorecognition elements conjugated with labeling molecules are employed to generate a detectable signal being read either by naked eyes or readout systems. Although various detection techniques have been used in LFAs^[78,229], colorimetric readout is most popular owing to its simplicity and no cost of the signal reader. Nevertheless, the colorimetric readout possesses some drawbacks such as poor sensitivity, low specificity, and lack of quantification, which highlight the need of development of a better readout system.

Electrochemical detection, used in commercially available glucometers, is considered a superior option due to its excellent sensitivity, offering quantifiable signals in a straightforward manner and simplicity of instrumentation with relatively low cost. In all currently suggested electrochemical LFAs the electrode is commonly placed or printed underneath or above the nitrocellulose membrane.^[125,126,230] Various labeling molecules, e.g., electroactive species, redox enzyme, liposome-encapsulated electroactive species, and nanoparticles have been employed to generate readable electrochemical signals. Upon the capture of analyte-labeling probe at the test zone, the label can be detected directly at the working electrode (WE).^[230] In case an electroactive marker is released from the test zone, e.g., enzyme label-generated products, and liposome- or mesoporous silica-encapsulated redox marker, the electrode is placed downstream allowing more flexibility and simplicity in electrode design and device assembly.^[128] Alternatively, the detection zone can be cut and immersed in an electrolyte solution for electrochemical measurements off-LFA strip,^[127] which is a difficult option for POC applications.

Albeit their success shown in previous works^[231] the fact, that only electroactive labels in close contact with the electrode surface can undergo electrochemical reactions inadvertently prevents these

electrochemical designs to live up to their full potential. In particular, for electrochemical label-free LFA which have the WE placed underneath the nitrocellulose,^[232] the binding between analyte and capture probe immobilized on the WE could be inefficient. Moreover, the alignment and tightness between the WE and the membrane, especially at the test zone, have to be very precise and well-controlled to avoid poor reproducibility. It is therefore suggested that flow-through electrodes, in which all of the sample naturally comes in direct contact with the electrode surface, provide an ideal solution to this challenge. Highly porous, electrochemically superior and inexpensive electrode materials must therefore be developed. Such characteristics can be offered by nanofiber-based electrochemical transducers.

Nanofibers are fibers in the nanometer scale, which can be exploited either as paper-like membranes, offering power-free fluid transport, flexibility and porosity or in modern face masks providing superior filtration compared to microfibers due to their superior surface to volume ratios.^[233] The size and density of nanofibers can be controlled during the spinning process resulting in micrometer pores, which facilitates fluid flow. The electrical conductivity of the nanofibers can be controlled either by choosing a conducting precursor material or by using laser carbonization, where the latter provides the additional advantage that conductive structures can be created within non-conductive, porous membrane material.^[234] Such 3D-porous electrodes enable flow of electroactive species accessing virtually the entire available electrode surface area, facilitating highly sensitive detection. Similar to traditional LFAs, the nanofibrous membrane is overlapped with the adjacent components to coordinate the flow. Moreover, the fibrous network facilitates wax patterning, mimicking microfluidic channels. The fabrication method not only is cost-effective but also lends itself well for large-scale production and integration into LFA strips.

In this work, we used the strategy of freestanding-LCNFs to generate high-performing electrochemical transducers in LFAs, which serves as a proof-of-principle for any other paper-based analytical device. To achieve optimal flow patterns, we investigated the design of LFAs including integration strategies for the nanofiber's membrane as well as buffer compositions. Nanovesicles in the form of liposomes were used as electrochemical labels in a biological binding assay. While the simple binding of biotin on liposome surfaces and streptavidin on the LFA test line was used for the initial proof-of-principle, the hybridization of DNA sequences for the detection of a specific target sequences of *Cryptosporidium parvum* (*C. parvum*) could then demonstrate that highly sensitive, quantitative and reproducible EC-LFAs are easily realized. The proposed device can expand its utility to any bioassays with similar detection platforms, e.g., using enzyme tags. Furthermore, it is highly suitable for electrochemical label-free based detection systems where the cost of expensive reagents can be reduced.

5.4 Materials and Methods

5.4.1 Chemicals and Reagents

A solvent-soluble polyimide (Matrimid 5218) was purchased from Huntsman Advanced Materials (Europe) BVBA Belgium. Iron (III) acetylacetonate ($\text{Fe}(\text{acac})_3$), Sephadex G-50 medium, cholesterol, potassium hexacyanoferrate(II) tetrahydrate (ferrocyanide), Triton X 100, Tween 20, Sodium dodecyl sulfate (SDS), Cetrimonium bromide (CTAB), disodium ethylenediaminetetraacetic acid (EDTA), D-(+)-Trehalose dihydrate, bovine serum albumin (BSA), and casein were purchased from Sigma Aldrich, Germany. *N,N*-Dimethylacetamide (DMAc), Disodium hydrogen phosphate dihydrate, potassium dihydrogen phosphate, hydrochloric acid, sodium azide, and formamide were purchased from Merck, Darmstadt, Germany. 1,2-Dipalmitoyl-sn-glycero-3-phosphocholine (DPPC), 1,2-dipalmitoyl-sn-glycero-3-phospho-(1'-rac-glycerol) sodium salt (DPPG), the extrusion kit and membranes were purchased from Avanti Polar Lipids (Alabaster, USA). Silver paint was purchased from DODUCO Contacts and Refining Pforzheim, Germany. Filter paper MN616 with 90 mm in diameter and 200 μm in thickness (Ref. 432009) was purchased from Machery-Nagel Düren, Germany. Double-sided adhesive tape was purchased from tesa. Plastic sheets in A4 form were purchased from Exponent as Laser Films. 2-[4-(2-hydroxyethyl)piperazin-1-yl]ethanesulfonic acid (HEPES), chloroform and methanol were purchased from VWR, Darmstadt, Germany. Synthetic *C. parvum* DNA probes and target sequences were obtained from metabion Planegg, Germany. Polystreptavidin (pStAv) was purchased from BioTeZ Berlin-Buch GmbH. Dropsens electrodes were purchased from Metrohm, Germany. Nitrocellulose and waste pads membranes were purchased from Ahlstrom-Munksjö. Octyl-beta-Glucoside (OG), Ficoll 400, sodium hydroxide, $\text{D}(+)$ -sucrose were purchased from Carl Roth.

5.4.2 Fabrication of f-LCNFs

The polymer solution contains 15% (w/v) Matrimid 5218 (750 mg) and 5% $\text{Fe}(\text{acac})_3$ (37.5 mg) in 5 mL DMAc, which is spun to form nanofibers. For the electrospinning setup a voltage supplier (Spraybase®) and a pump (kd Scientific) were used. The flowing rate was set at 10 $\mu\text{L}/\text{min}$, working distance 15 cm and a 21G needle were used. The voltage was set to 14-17 kV, depending on surrounding conditions. The nanofibers were collected for 90 min on an oxygen plasma treated filter paper fixed on a metal collector. The electrodes were designed using a vector graphic editor, CorelDRAW, and a CO_2 laser (10.6 μm) from Universal Laser Systems, Polytech System GmbH was used to carbonize the nanofibers with 1.2 W, 1016 mm/s, 1000 DPI, and 500 PPI. The electrodes are treated with oxygen plasma to increase their wettability. Wax channels are used to create hydrophobic barriers, in order to confine the flow of the solution through the nanofibers. For this, two parallel lines are printed on a plastic sheet with a wax printer. Afterwards the pattern is cut from the plastic sheet and placed on top of the

electrodes. The electrodes with the plastic containing the wax line are placed between to metal plates in a heat press at 100°C for one minute.^[234] The press used is a manual hydraulic press from Specac.

5.4.3 Assembly of LFA strip and modification with biotinylated DNA capture probes

The backside of the LFA strips is made by placing double-adhesive tape on laminated plastic sheets. Afterwards 20 mm nitrocellulose and a 35 mm piece of waste pad are aligned on the prepared plastic with tape having a gap in between. The big piece of plastic with the membranes is cut in 70 mm × 3 mm strips. On the nitrocellulose membrane polystreptavidin (pStAv) (2 mg/mL, unless stated otherwise) in 0.05 M PBS (with 0.05% NaN₃, 1 wt% Trehalose, pH = 7.4) was spotted (7.5 cm away from the end of the strip) with sciFlexarrayer from Scienion AG with 20% pressure, 350 μs pulse and 5 Hz. The membranes were dried for 90 min at 30 °C. Afterwards 1 μM (unless stated otherwise) 5'-biotinylated capture probe (cDNA) in hybridization buffer (9× sodium saline citrate (SSC) pH 7.0; 0.135 mol L⁻¹ sodium citrate, 1.35 mol L⁻¹ NaCl, 30% formamide, 0.2% ficoll 400, 0.01% NaN₃) was spotted on the same line to bind irreversibly to the pStAv. The strips were again dried for 90 minutes at 30°C in the oven. To block the nitrocellulose membrane, the blocking solution is added in a glass vial and the as-prepared strips are immersed for 30 minutes on a shaker (230 rpm). The blocking solution contains either 1% (w/v) BSA or 0.015% (w/v) casein with 2.5% polyvinylpyrrolidone (PVP) in Tris-buffered saline with NaN₃ (TBS w/ NaN₃) (1x TBS, pH = 7.4, 0.2 M Tris(hydroxymethyl)aminomethane, 1.5 M NaCl, 0.1% (w/v) sodium azide). Afterwards, the electrodes are assembled onto the strip between the nitrocellulose and the waste pad with the plastic sheet facing upwards (Figure 5.2a). To facilitate a constant sample flow, the nanofiber membrane should overlap with both pads. On the backside, the electrodes were supported by a square plastic using double-sided adhesive tape (assembled device in Figure 5.2b-vi). To enable a good electrical connection, the contact sites of the electrodes are painted with conducting silver paint.

5.4.4 Synthesis of liposomes

A protocol by K. A. Edwards et al^[55] was followed for the synthesis of liposomes using reverse-phase evaporation. DPPC (30 mg, 37.1 mol%), DPPG (15 mg, 18.2 mol%), and cholesterol (19 mg, 44.6 mol%) are dissolved in a mixture of 3 mL chloroform and 0.5 mL methanol. Then, 50 μL of a 300 μmol L⁻¹ (0.14 mol%) 3'-cholesteryl-TEG modified DNA reporter probe was added and the mixture was sonicated for 1 min at 50 °C. Afterwards, 2 mL of encapsulant solution, 200 mM ferrocyanide in 0.02 M HEPES pH 7.5, was added and sonicated for 5 min. The organic solvents were evaporated with a rotary evaporator at 55 °C and pressures of 600 mbar (10 min), 500 mbar (10 min) and 400 mbar (20 min). This was followed by another injection of encapsulant and vortexing for 5 min (the solution is reheated to maintain the lipid dispersion above the phase transition temperature). A second rotary

evaporation cycle was done with 20 min at 380 mbar and 20 min at 280 mbar. The dispersion was extruded 21 times through polycarbonate membranes (1 μm , 0.4 μm and 0.2 μm) at 55°C. Via size extrusion chromatography the liposomes are purified with a Sephadex G-50 medium column and dialysis in a Spectrum Labs Spectra/Por standard tubing dialysis membrane (molecular cut-off 12–14 kDa) against HEPES-saline–sucrose (HSS) buffer (10 mM HEPES, 200 mM NaCl, 250 mM sucrose, 0.01% NaN_3 , pH 7.5) overnight.

5.4.5 DNA sandwich hybridization assay

Liposomes in HSS buffer are mixed with target DNA (tDNA) (unless stated otherwise) in hybridization buffer (9 \times sodium saline citrate (SSC) pH 7.0; 0.135 M sodium citrate, 1.35 M NaCl, 30% formamide, 0.2% ficoll 400, 0.01% NaN_3) and incubated for 90 min on the shaker at 430 rpm at room temperature. A 10 μL volume of the tDNA-hybridized liposomes is added to the strip. After the solution has fully passed through the electrodes, 10 μL (unless stated otherwise) of washing buffer (0.05 % (v/v) Tween 20, 0.01 % BSA in PBS) is added to the strip. This should remove the nonspecifically bound liposomes from both the nitrocellulose and the nanofiber membrane. Lastly, 10 μL of the lysing buffer (100 μM Triton X in HSS buffer) is pipetted on the strip, so the lipid bilayer is destroyed, and the redox molecules can be detected at the electrodes.

5.4.6 Electrochemical measurements

A multi-channel potentiostat (MultiPalmSens4 by PalmSens BV) is used for the electrochemical detection. Chronoamperometry is employed with a set potential of 0.4 V and a time-interval of 0.5 s. The peak area is used for the quantification of the signal.

5.4.7 Characterizations

The size distributions and zeta potentials for the liposomes are determined by dynamic light scattering (DLS) and zeta potential measurements with a Malvern Zetasizer Nano-ZS (Nanoseries, Malvern Instruments). For these measurements, the liposomes are diluted 1:100 in HSS buffer. In order to determine the phospholipid concentration ICP-OES is measured with a SpectroBlue FMX36 TI/EOP (SPECTRO Analytical Instruments, Kleve, Germany). In this case, the liposomes are diluted 1:150 in 0.5 M HNO_3 . The calibration was generated with phosphorus standards in 0.5 M HNO_3 . The phospholipid concentration is calculated into a total lipid (tL) concentration. To determine the encapsulant concentration square wave voltammetry is employed on commercially available DropSens electrodes for generating calibration curves for lysed and non-lysed liposomes. (Table S5.2)

5.5 Results and discussions

5.5.1 Development of the EC-LFA assembly

Nanofiber mats are generated by the application of high voltage on a constant flowing polymer solution, containing Matrimid and iron salt. Thick nanofiber mats collected on filter paper obtained by long collection times were proven to be essential for transforming the electrical resistant fibers into highly conducting electrodes patterned with a CO₂ laser within the nanofiber mats. This process yields porous and flexible transducers for electrochemical measurements. Their characterization including SEM^[234] and Raman analysis^[235] was published earlier. To tailor the wettability of the LCNF electrodes oxygen plasma is applied for 3 minutes. The fibrous network facilitates the use of wax patterning for the fabrication of microfluidic channels by creating wax filled hydrophobic barriers guiding the liquid. We postulate here, that placing the 3D electrodes into a flow-through assay will minimize diffusion limitations of the electrochemical reaction and hence take full advantage of porous electrode structures and hence also advance their use from prior work (also see Figure 5.3d-ii).

Based on this general technology, two- and three-electrode systems were initially investigated (Figure S5.1) with respect to their electrochemical performance using chronoamperometry (Figure S1 a and b) and cyclic voltammetry (Figure S5.1 c and d). Interestingly, the two-electrode systems provided acceptable electrochemical performance and was by far superior with respect to supporting reliable flow through its electrode structures. In the case of the three-electrode system slower and less reproducible liquid flow typically resulted in lower reliability of the measurements. The two-electrode system was therefore further studied to be integrated into the LFA strip.

For a typical lateral flow strip, the colorimetric signal is observed directly on the test line, representing the spatial location of the hybridization interaction between the capture biomolecule and target analyte. In contrast, it was decided here to place the LCNF downstream of the test line, as this allows to take advantage of the well-established immobilization strategies of biorecognition molecules on nitrocellulose membranes. Furthermore, to improve LFA's sensitivity such an EC-LFA can take advantage of enzyme or nanovesicle labels which generate or release their markers and require detection downstream of the test line. (Figure 5.2a). Here, the redox-active molecules, which are either directly added to the LFA or are released by the disruption of the liposomes captured in the test line, flow through the nanofibrous membrane and later oxidize at the electrodes, enabling a quantification of the target molecules. Hence, the major optimization parameter that ensure reliable detection by the EC-LFA lies in the reliable connection between the membrane parts and a reliable, continuous fluid flow through all LFA segments. Furthermore, the contact pads of the LCNFs must be isolated from the active electrode areas. The latter is achieved by two simple wax channels guiding the liquid through the electrodes. Specifically, the wax channels are printed on a plastic sheet, placed on top of the as-prepared LCNF electrode and allowed to penetrate into the nanofiber mats through melting (Figure 5.2b-i). Prior to

assembling with nitrocellulose membrane and waste pad, the filter paper is removed from the LCNF electrode (Figure 5.2b-iii and iv). The nanofiber membrane is assembled on the strip (Figure 1b-v) and double adhesive tape with plastic backing is added underneath the nanofibers and strip to increase robustness just like in a normal colorimetric LFA (Figure 5.2b-vi). Thus, the liquid flows from the nitrocellulose, through the nanofibers further to the electrodes, wetting the conducting carbon nanofibers (Figure 5.2b-vi) and is absorbed by the waste pad.

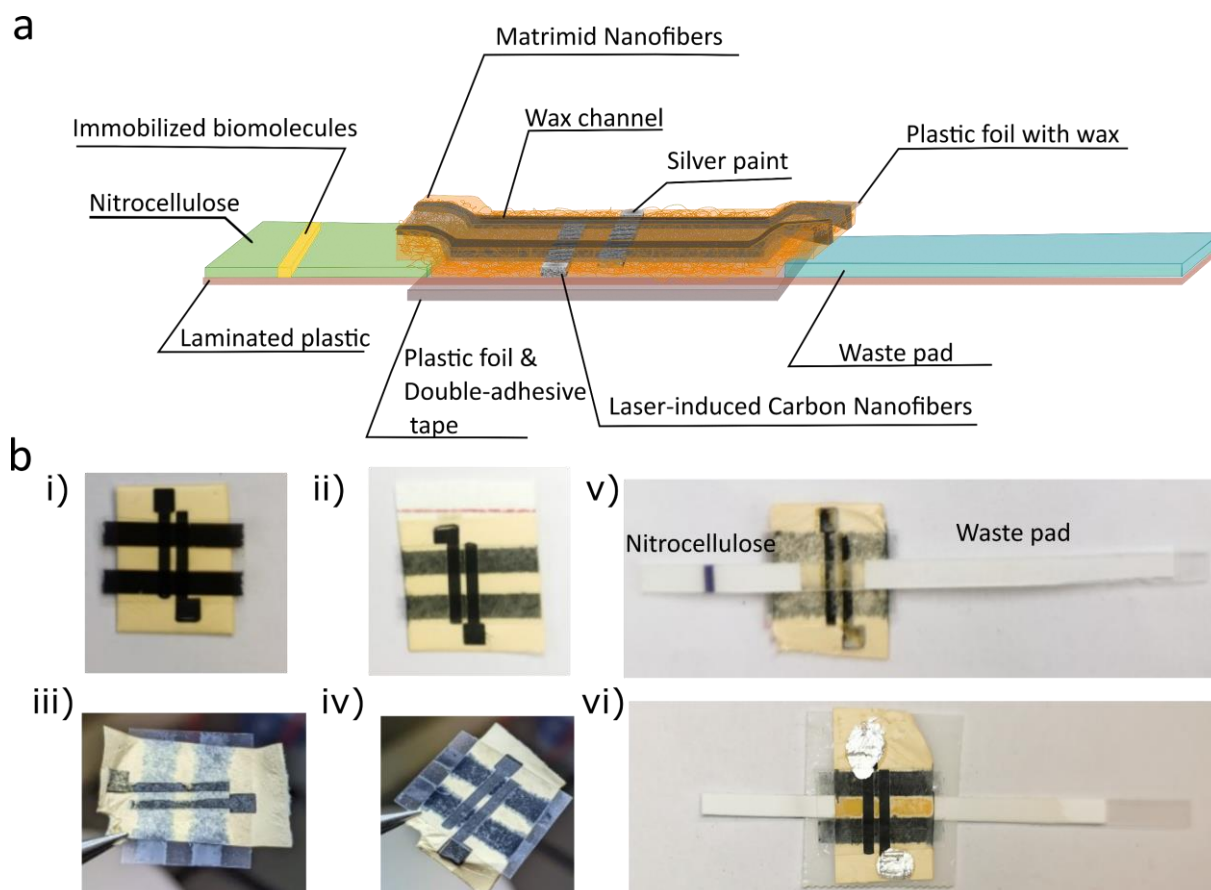


Figure 5.2. Schematics and pictures of the device. a. Schematics of the EC-LFA strip with integrated non-conducting polyimide nanofibers and conducting carbon nanofibers. b. Pictures of the carbon nanofibers electrodes with the printed wax channel before (i) and after wax melting (ii), and the assembled electrodes after peeling off the filter paper support seen from bottom (iii) and top (iv) sides, respectively. Pictures of bottom (v) side of the of the LCNFs integrated EC-LFA strip before adding the double adhesive tape backing. And final picture of assembled device (vi) with plastic foil and double adhesive tape underneath the mat and with silver painted contact sites of the electrodes, after the solution flowed through.

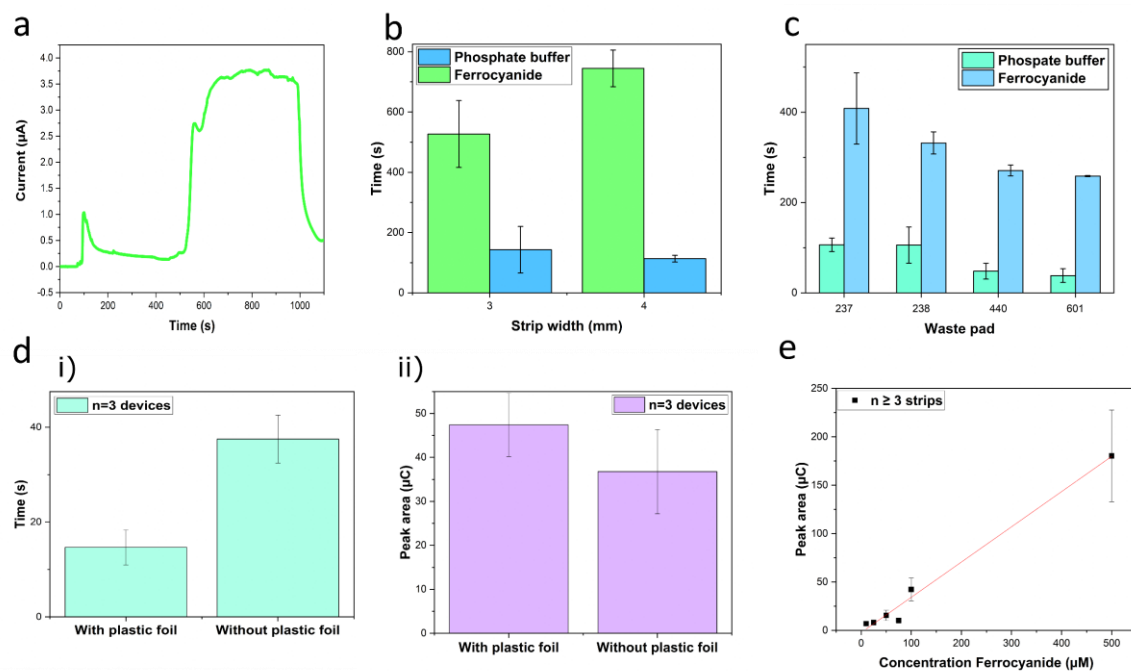


Figure 5.3. Optimization of flow in LFA strip. a. Chronoamperogram of addition of PBS (from 75-400 s) and 1 mM ferrocyanide (from 450-1100 s). b. Comparison of the time necessary for PBS and 1mM ferrocyanide to flow through the electrodes for a thinner (3 mm) and a wider (4 mm) strip width. C. Study for different waste pads regarding the time needed to complete the flow, measured with 1 mM ferrocyanide (i) and effect of plastic foil cover on time needed to complete the flow (ii). e. Dose-response curve of ferrocyanide with one concentration/strip. $n \geq 3$

The liquid flow through the EC-LFA and the resulting signal response within LFA strip was monitored using chronoamperometry with PBS buffer or ferroxhexacyanide solutions, respectively. A typical chronoamperogram (Figure 5.3a) of the signal measured on the LCNF-electrodes yielded a first peak represented by the addition of the buffer, i.e. the electrodes are wetted, followed by a high and broad peak due to the addition and oxidation of ferroxhexacyanide. The decrease of the peak signal illustrates the consumption of the redox active molecules in the solution as it passes through the electrodes until the background value is reached again. This chronoamperogram demonstrates that the effect of the fluid flow through the electrochemical LFA can easily be characterized, quantified and hence used for the optimization of the flow pattern.

In general, bioanalytical binding events are influenced by the flow rate in an LFA, where slower flow rates both improve binding signals but also increase non-specific binding events. In case of an EC-LFA the flow rate may have additional effects on the electrochemical reaction per se. Hence, parameters studied were the waste pad material, strip width and buffer additives, as these influence the capillary force and hence the capillary flow through the EC-LFA. First, traditional LFA optimization resulting from (i) strip dimensions, (ii) waste pad material and (iii) overlap design was carried out. Studying different widths revealed that a thinner strip (3 mm width) yields a faster flow (Figure 5.3b), while a wider strip demonstrated a better reproducible flow. Since the assay time should be kept short, the

reliability of the thinner strip design was improved through a careful selection of the waste pad. The overall capillary force is influenced by the waste pad characteristics including absorption capacity, i.e., volume that can be absorbed, and the wicking rate, i.e., speed of the solution flow. In colorimetric LFAs, this capillary force typically influences washing and non-specific binding events. In case of the EC-LFA it also influences signal generation. Thus, four prototypical different waste pads (Table S5.1), were investigated for the flow of the solutions (Figure 5.3c). The thick membranes (grade 237 and 238), provide a slower flow (400s until stable signals are achieved) and cause loose contact at the interface between nanofibers and the waste pad. A more flexible and thinner pad (grade 601) provides better contact, resulting in continuous flow and stable signals in little more than half the time (250s). Interestingly, the stiffness and density of the waste pad in contrast to the nanofiber mat makes a difference in location of the nanofiber mat in the overlap region. Here, the lower position results in better contact formation and generates a more robust set-up (Figure S5.2 and S3).

Secondly, the effect of plastic foil covering the electrode area was investigated. Prior work suggested that covered electrodes provide improved electrochemical signals as it better confined the solution within the electrode area^[234]. In contrast, we found here that the flow through the electrodes is faster with foil coverage (Figure 5.3d), but the signal intensities are comparable for both setups (Figure 5.3d-ii). This implies that not only diffusion as in our prior work, but also active molecule transport contributes to the electrochemical detection. Since the assembly is easier with plastic foil cover and since it decreases the assay time, it was continued to be used in the further studies. This overall design enables the detection of electrochemical markers such as ferrihexacyanide (Figure 5.3e and Figure S5.4) with a wide linear range, with high precision (0 – 500 μM , $R^2 = 0.993$) and favorable detection limits (25 μM) proving the reliability of the as-developed EC-LFA for the quantification of a redox-active analyte. The obtained LOD is in line with our prior research when electrodes are used traditionally in a three-electrode setup. In the future DPV or SWV can be implied to improve the sensitivity and thus lower the detection limit.

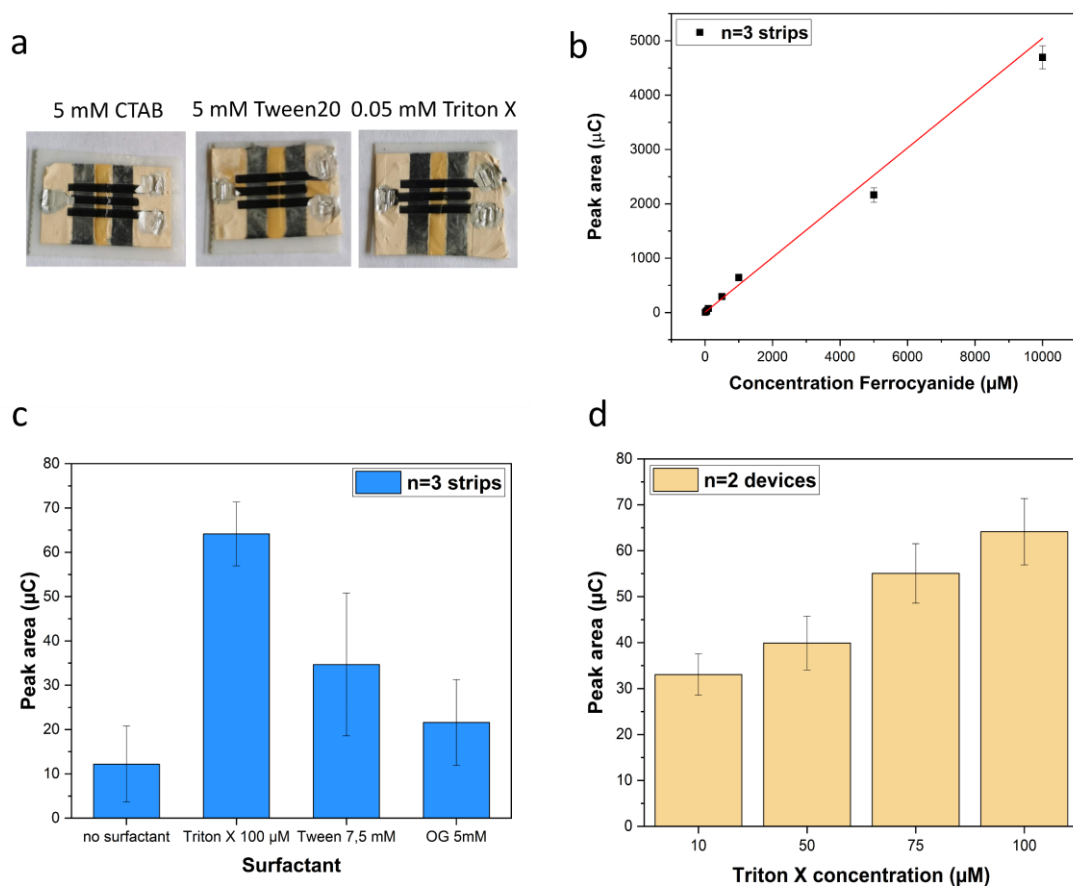


Figure 5.4. Effect of surfactants. A. Examples of LCNF on double-sided adhesive tape with different surfactants (CTAB, Tween20, and Triton X). b. Dose-response curve of ferrocyanide with surfactant (0.05 v% Triton X) was generated when different concentrations were injected on the same strip. c. Study of lysing efficiency of biotinylated liposomes (1 mM tL) on LCNF-LFA. d. Concentration variation of Triton X effect on lysing liposomes.

Thirdly, the effect of additives was studied as these may be needed for membrane manufacturing or the biological assay itself and would influence the fluid-flow through the EC-LFA. Surfactants can be found as a typical reagent to modify fiber properties, for example nitrocellulose' hydrophobicity is improved by adding surfactant during manufacturing process.^[236] They are also employed in many protein assays to avoid protein aggregation^[237] and in cell assays to lyse the cells prior to analysis^[238]. In addition, for our bioassay a surfactant will be used for the release of the encapsulated electroactive marker upon lysis of the liposomes. The choice of surfactant implies considering multiple key points, such as its impact on capillary flow, on protein adsorption, and reagent stripping. Additionally, the surface tension created by the wax barriers in the LCNF can be overcome by detergents^[239], which would adversely cause leaking of the solution to the electrical contact of the electrodes, causing short circuits. Therefore, surfactants including SDS, Triton X, Tween 20, OG, and CTAB at various concentrations were tested. It was found that reasonably high concentrations could be used without causing leakage (Figure S5.5, Figure 5.4a) and furthermore, these surfactants decreased detection times and improved detection limits

due to the improved wettability of the LCNFs. (Figure S5.4, Figure 5.4b) In case of the liposome-based assay (see also further below) the detergents' ability to effectively lyse the liposomes and release the entrapped ferrihexacyanide was also studied. (Figure 5.4c) The lysing efficiencies of surfactants were initially assessed on commercial screen-printed electrodes, calculated relative to 30 mM OG (100%), CTAB and SDS showed low signals (4% and 48% lysing efficiency), while Triton X had a slightly higher signal than OG (Table S5.3). Since Triton X performed better also on the LCNF, (Figure 5.4) the EC-LFA was therefore further optimized for Triton X. As expected, the presence of surfactants as additive increases the fluid flow rate on the EC-LFA and decreases the time needed for a stable signal to occur. (Figure S5.6) Balancing it with the concentration of Triton X needed to effectively lyse the liposomes, (Figure 5.4d) a compromise of a high signal response and non-leaking wax channel was found to be 100 μ M. In the case of other biological assays, the high concentration of surfactants tolerated in this EC-LFA will be advantageous.

5.5.2 Development of a proof-of-principle EC-LFA

Assays aiming to detect biomarkers that are not optically or electrochemically active are typically realized using signal labels. Examples of popular labels are nanoparticles, enzymes, or liposomes. Liposomes are lipid bilayers that can encapsulate a variety of signal molecules, such as dyes^[240], electrochemiluminescence molecules^[241], or electrochemically active molecules^[242]. The main advantages of using liposomes as signaling reagents are their lack of time dependency, relatively large internal volume, and the ease of their surface modification with biorecognition elements. Here, we used biotinylated liposomes encapsulating ferrihexacyanide (Figure 5.5a-I). The strong binding of biotin and streptavidin was utilized for the immobilization of biotinylated liposomes in the test line (Figure 5.5a-II). The EC marker can be released by a surfactant (figure 5.5a-IV) and later oxidized at an electrode placed downstream. For the development of the proof-of-principle EC-LFA, EC measurements were taken throughout the entire assay. Hence, the addition of liposomes, washing buffer and liposome-lysis buffer is traced (Figure 5.5b), where the first signal increase (100-250 s) correlates with the liposome solution reaching and wetting the electrodes. Once the solution flows through the membranes the signal stabilizes, and the washing buffer is added (700-1200 s) to remove nonspecifically bound liposomes. By the last injection the liposomes are lysed, and a peak-shape signal is developed (1300-1750 s), correlating to the number of liposomes captured in the test line. It should be noted that the long waiting periods and hence long assay times seen here, are artificial and only used to best understand flow and reaction patterns during the development of the assay. The ultimate test in the end will follow a normal LFA timeline of 10 – 15 minutes and only require measurement after detergent addition. Non-biotinylated liposomes were used as a negative control, demonstrating that no specific signal is recorded after the addition of the lysis reagent. (Figure 5.5c) Finally, the liposome concentration is varied, and a highly quantitative, reliable dose-response curve is recorded (Figure 5.5d) with a limit of detection

(LOD) of 12.5 μM tL. Interestingly, this correlates directly to the detection of pure liposomes on non-assembled LCNFs (Figure 5.5e) and suggests a very high efficiency in binding and lysing of biotinylated liposomes on the strip.

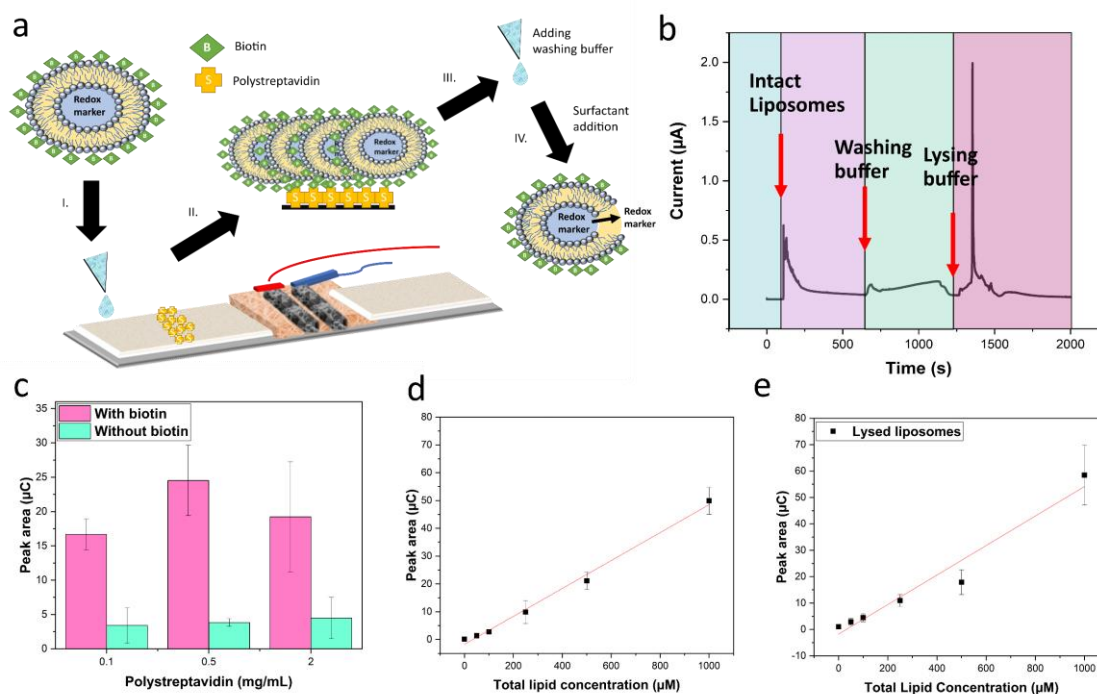


Figure 5.5. Biotinylated liposomes as labeling probes. a. Schematics of the assay: addition of biotinylated liposomes (I), binding events between polystreptavidin and biotinylated liposomes (II), addition of washing buffer (III), and addition of lysing buffer (IV) while current is being monitored throughout the assay process. B. A typical chronoamperogram of the assay, with the correlated additions. c. Comparison between liposomes modified with biotin and bare liposomes for varying concentrations of polystreptavidin. d. Dose-response curve of bound liposomes generated on LCNF-LFA with $n \geq 3$. E. Dose-response curve of lysed liposomes performed on LCNF electrode. $n \geq 3$

5.5.3 Detection of pathogenic target DNA using the EC-LFA

Cryptosporidium parvum belongs to some of the most severe waterborne pathogens around the world, where chlorination used for drinking water treatment is inefficient in inactivating *C. parvum* oocysts. It causes infection of the mammalian intestinal tract and can lead to death in immune-compromised patients. Its specific detection through a DNA sandwich assay using capture probes immobilized in the streptavidin test line and liposome-bound reporter probes was hence used as a relevant model analyte here.^[243] For the assay, liposomes and target sequence are mixed (Figure 5.6a-I), added to the strip so that a hybridization complex is formed (Figure 5.6a-II) and captured on the test line (Figure 5.6a-III). Non-hybridized target DNA and non-bound liposomes are washed off (Figure 5.6a-IV) prior to introducing the lysis buffer (Figure 5.6a-V). Upon lysis, the released ferrohexacyanide flows to the electrode generating oxidative current signal correlated to the respective target DNA concentration.

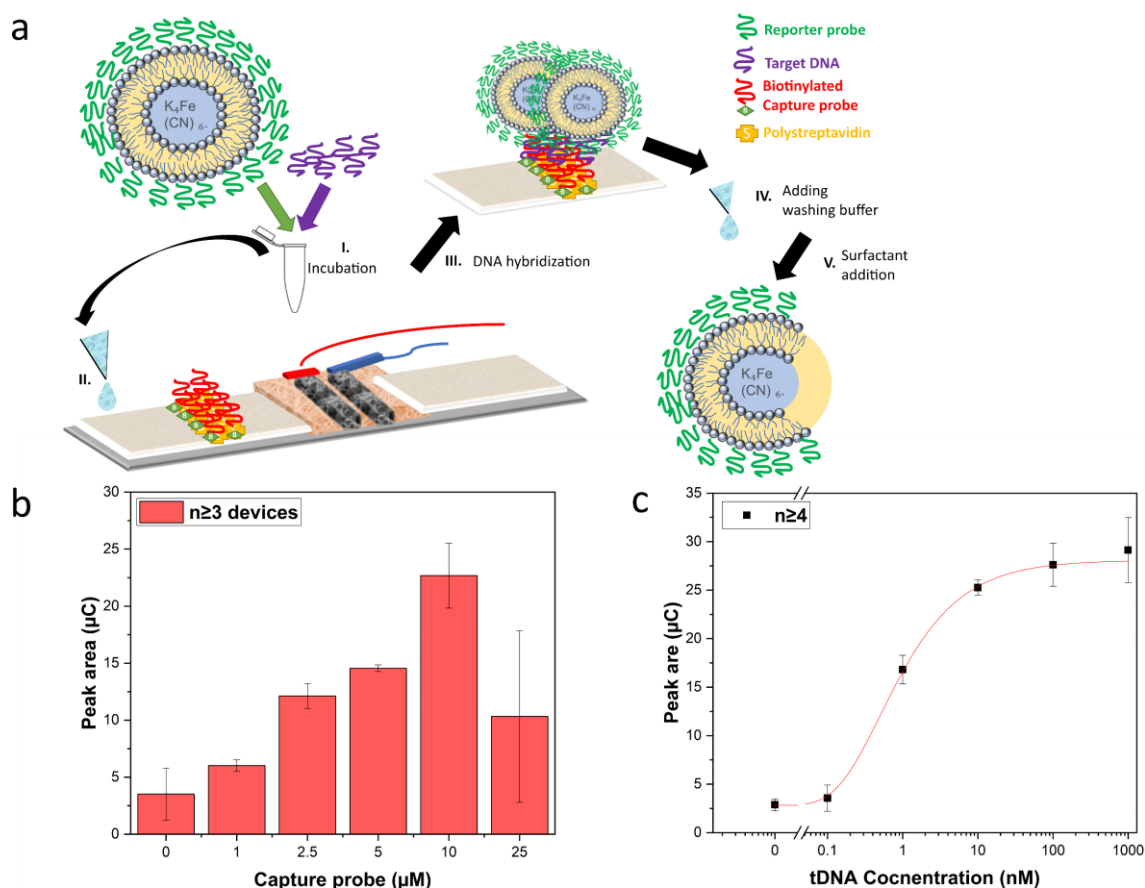


Figure 5.6. Detection of *C. parvum* target DNA with liposomes. a. Assay for the detection of *C. parvum*: Incubation of target DNA with liposomes (I), addition to the strip (II), hybridization to capture probe on the strip (III), addition of washing buffer (IV) and addition of lysing buffer (V). b. Concentration variation of the capture probe. c. Dose-response curve of target DNA (using 20 µL of washing buffer).

General LFA development and optimization such as immobilization of the capture probe and blocking reagent conditions were carried out initially (Figure S5.7), the exquisite storage stability of liposomes as signaling reagent was demonstrated (Figure S5.8a) and improvements through varying the washing buffer volume were obtained (Figure S5.8b). Furthermore, the capture probe concentration was optimized (Figure 5.6b), where it was found that concentrations above 10 µM likely lead to crowding and hence unreliable results. Finally, the overall performance of the newly developed EC-LFA was demonstrated through a calibration curve for the target DNA of *C. parvum*. A typical sigmoidal curve was obtained (Figure 5.6c). The detection limit was determined to be 137 pM. This LOD is similar to those generated in significantly more sophisticated microfluidic liposome-based systems, in which active pumping of the solution and more complex assay conditions are required.^[241] Considering the simplicity and low cost of LCNF fabrication (0.01 €/electrode set)^[234] and the purposely simple integration of the electrode integration into an existing LFA system, we could thus demonstrate the immense possibility LCNFs offer in EC-LFAs to provide quantitative, sensitive and still highly simple POC tests. Furthermore, the time required for detection on EC-LFA is currently 20-25 minutes. The time of a typical colorimetric LFA is hence increased by ~10 minutes required for the detergent addition

and EC detection. Similarly, for enzyme labels it is assumed that also 3 – 5 minutes are required for substrate addition and EC signal recording. Therefore, a simple, qualitative or semi-quantitative visual detection LFA can be transformed into a highly sensitive and quantitative EC-LFA for the cost of ~10 minutes only.

5.6 Conclusion

In this study a radically new design for simple, reliable and quantitative POC devices was accomplished through a novel nanomaterial. Laser-induced carbon nanofibers (LCNFs) were integrated into a traditional lateral flow assay (LFA) as an electrochemical transducer and placed directly in-flow. Thus, in contrast to concepts suggested to-date in which electrodes are placed on top or beneath the active membrane of an LFA, here, the entire sample flows via capillary forces through the transducer and contributes therefore fully to the overall signal. Thus, rather than only detecting on an LFA surface, LCNFs measure throughout the entire material. The highly porous nature of the 3D carbon nanofiber electrodes, their electrochemical superior performance in contrast to screen-printed carbon electrodes, their low cost and simple fabrication in contrast to previous metal electrodes makes them thus an ideal new material to realize electrochemical LFAs (EC-LFAs). Furthermore, we could demonstrate that LCNFs can simply be integrated into traditional LFAs which is an important feature for manufacturing strategies. We also demonstrated the performance of such EC-LFAs using liposomes entrapping electrochemical markers as labels and the detection of pathogenic DNA via a typical DNA hybridization reaction. The obtained limit of detection rivals those obtained in microfluidic, pump-driven bioassays using the same liposomes published earlier and hence demonstrate the immense capability LCNFs offer for EC-LFAs. Furthermore, this concept can be further exploited with the use of different labels, such as metal nanoparticles or enzymes, LCNFs can be integrated into more sophisticated paper-based assays and hence add a highly practical and yet superiorly performing electrochemical detection strategy to the POC with the prospect of enabling inexpensive, reliable, quantitative and sensitive detection at the point-of-need.

5.7 Supplementary information

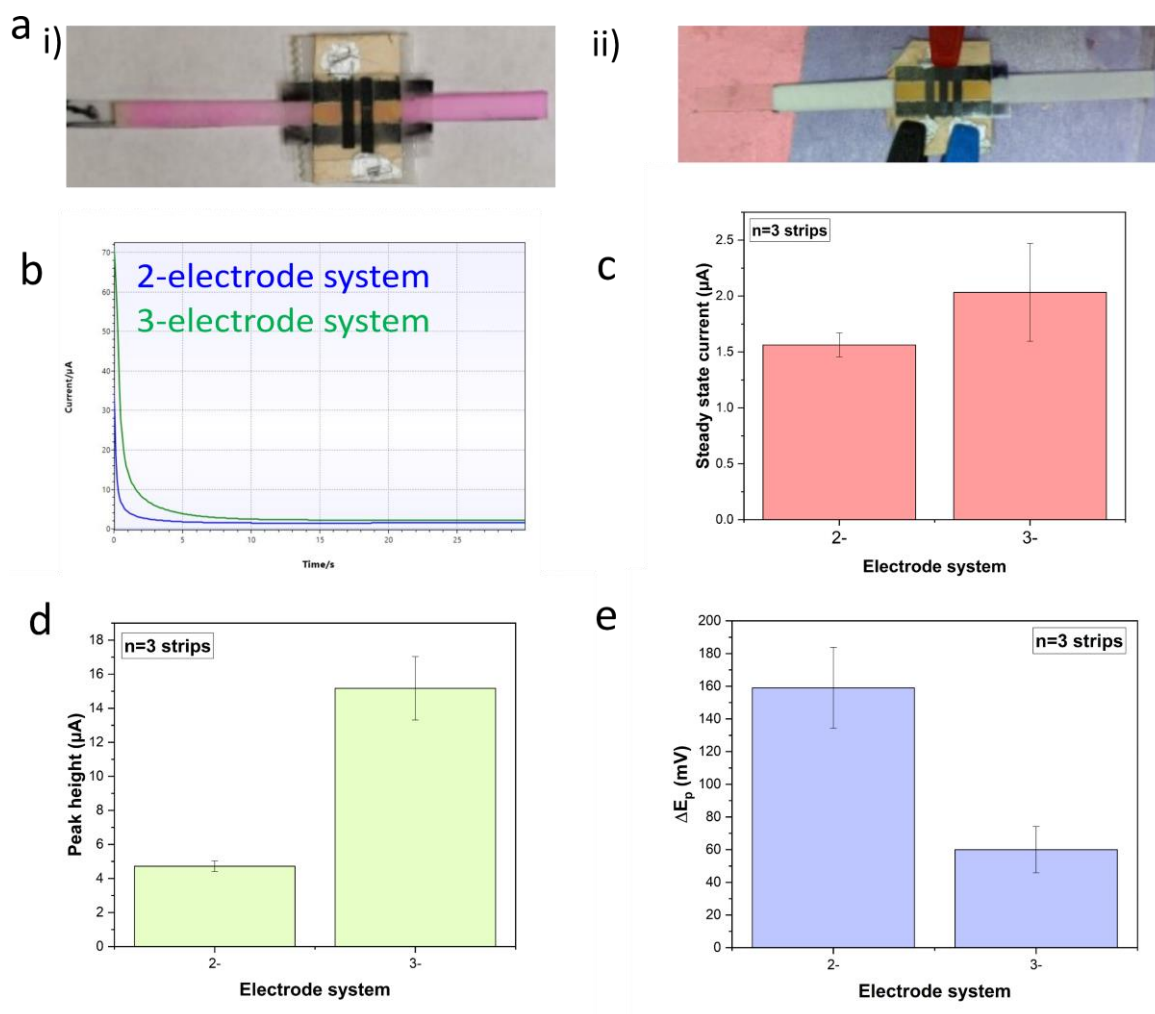


Figure S5.1. Electrochemical setup: 2- vs. 3- electrode system. a. Pictures of a strip consisting of 2-electrode setup (i) and 3-electrode setup (ii). b. Chronoamperogram measured of 1 mM Ferrihexacyanide of 2- and 3-electrode setup. c. Steady state current for 2- and 3-electrode setup. d. Peak height determined from cyclic voltammetry for the two electrode systems. e. Peak-to-peak separation determined from cyclic voltammetry for the two electrode systems.

To simplify the design of the electrochemical lateral flow strip, a study to compare the performance of using a 2-electrode or a 3-electrode setup was done (Figure S5.1a). By fitting the chronoamperogram, the steady state can be calculated (Figure S5.1b). The steady state is reached very similarly for both setups, with the 3-electrode setup having larger standard deviations (Figure S5.1c). Moreover, cyclic voltammograms of 1 mM ferri/ferrohexacyanide were recorded for both setups (data not shown). These were investigated in terms of peak intensity of the oxidation peak (Figure S5.1d) and the difference between the oxidation and the reduction peaks – the ΔE_p (Figure S5.1e). The 3-electrode setup showed higher peak and lower peak-to-peak separation, having overall better performance. However, as the 2-

electrode setup still have an acceptable performance, which is supported by easier assembling and faster flow, this was further used.

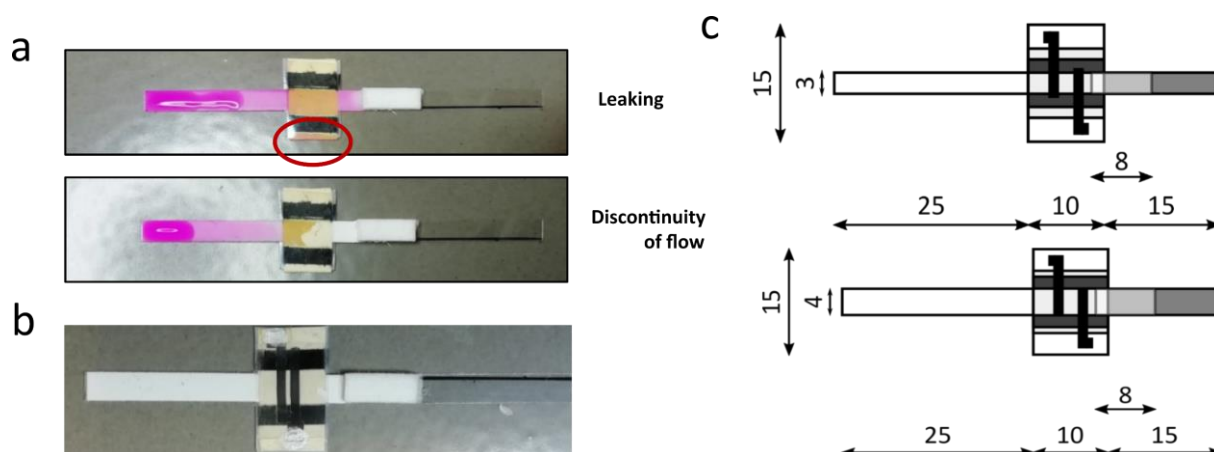


Figure S5.2. Development of the Lateral flow strip. a. Pictures of preliminary devices incorporating nanofibers without carbonized nanofibers as electrodes. b. Prototype with two nitrocellulose membranes in front and after the electrodes for using a thick waste pad. c. Schematics showing the different membranes and their size.

Different strategies were tested for the alignment of the membranes. In the first phase, the nanofibers overlapped two nitrocellulose membranes on both ends. In order to use a well-known waste pad, which is very thick, a small (8 mm) nitrocellulose piece was added before the waste pad and after the nanofibers. It was observed that the membranes' points of contact and overlapping have the highest impact on the flow of the solution through the nanofibers. This can be seen in the two extreme cases, wherein in the first case, the solution leaks out of the wax channel, probably because of misalignment (Figure S5.2). The second case shows a slow flow through the membranes, which is probably because the overlapping of the nanofibers with the nitrocellulose is not enough to ensure the capillary flow.

Table S5.1

Grade	Basis Weight	Caliper	Wicking Rate	Water Absorption	Composition
	g/m^2	mm	s/4cm	mg/cm^2	
237	183	0.42	86	38	High Purity Cotton Fibers
238	186	0.34	150	33	High Purity Cotton Fibers
440	435	1.44	33	130	Cotton/Glass Blend
601	88	0.19	120	25	High Purity Cotton Fibers

Table S5.1. Characteristics of different waste pads.

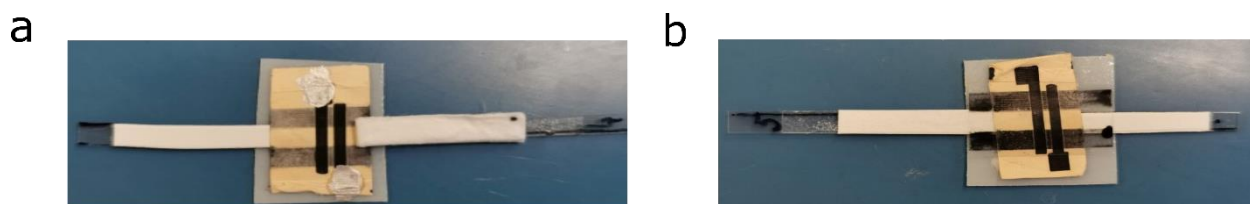


Figure S5.3. Comparison of a strip with a thick waste pad without plastic foil and a strip with a thin waste pad and plastic foil.

The waste pad is the membrane that ensures a proper capillary flow, therefore different waste pads were investigated (table S5.1). The most important factors are the wicking rate and water absorption. The waste pad used in the first studies (Figures S5.1 & S5.2) is 440, which is very thick and has a high-water absorption possibility, but the flow of the solution is slow. When using thinner waste pads (237 & 238) the flow rate improved, but lower sample volumes must be used, as the water absorption is lower. The thinnest waste pad (601) showed the fastest flow rate and very good reproducibility. It can be also seen in the pictures above, that the thicker waste pad is easier to implement with electrodes without any plastic sheet above, with having the nanofibers underneath the waste pad directly. In comparison, the thinner waste pad can be implemented in both ways, above or underneath the nanofibers, and has no drawbacks if the nanofibers contain a plastic sheet. Moreover, during these studies, it was observed that the flow is better reproducible with less point of contact between membranes: if the flow is compared with the strip having an additional nitrocellulose piece with strips having direct contact with the waste pad.

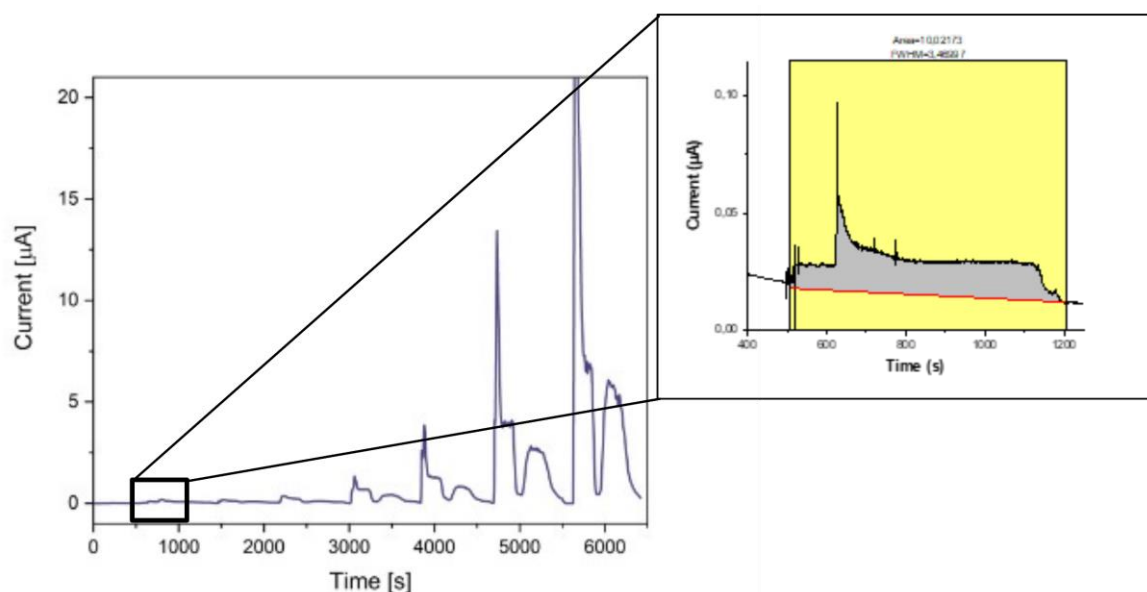


Figure S5.4. Chronoamperogram of sequential injections of ferrocyanide solution at various concentrations (10 μM , 50 μM , 100 μM , 500 μM , 1 mM, 5 mM, and 10 mM) on the same LCNF-LFA strip. The signal is analyzed by integrating the area under the peak.

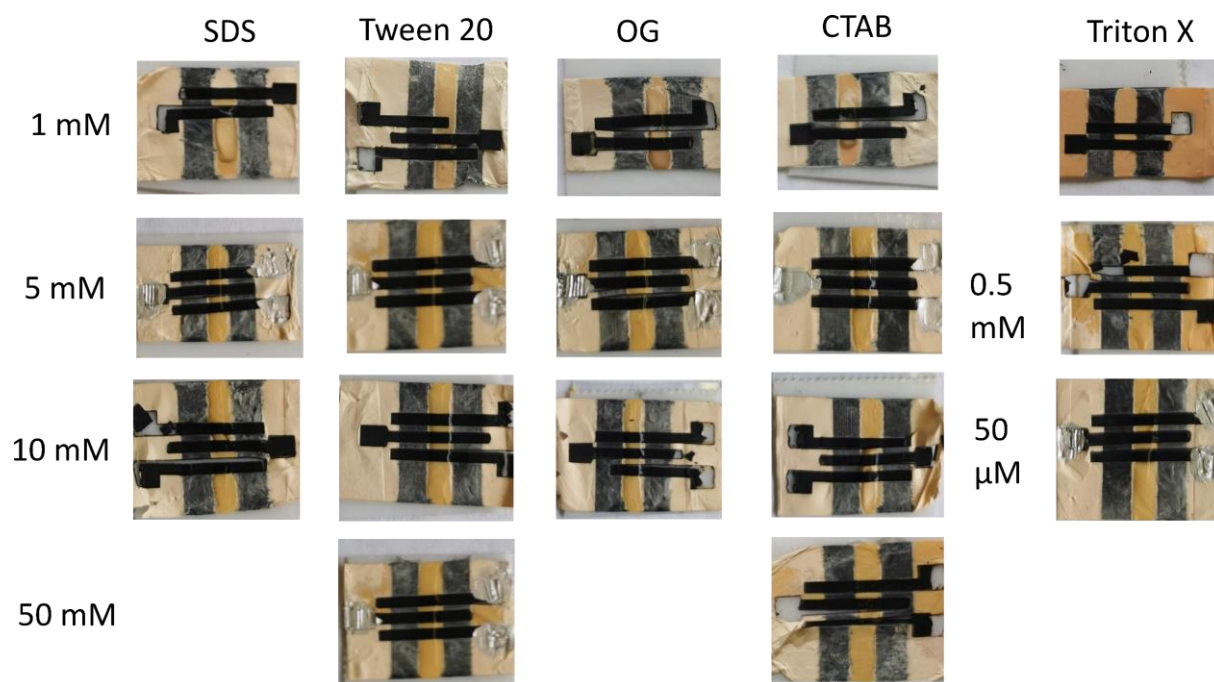


Figure S5.5. Surfactant concentration study.

To disrupt the liposomes membrane, a surfactant is added to the lysing buffer. The confinement of the electrode area is made by wax, meaning the hydrophobic barrier created by wax can be destroyed by the surfactants and cause leaking of the solution to the contact sites of the electrodes. While SDS and OG leaked at slightly higher concentrations than 10 mM (after some time – data not shown), Tween 20 and CTAB only leaked at 50 mM. Triton X proved to be the strongest affecting one, as it leaks already at 0.5 mM.

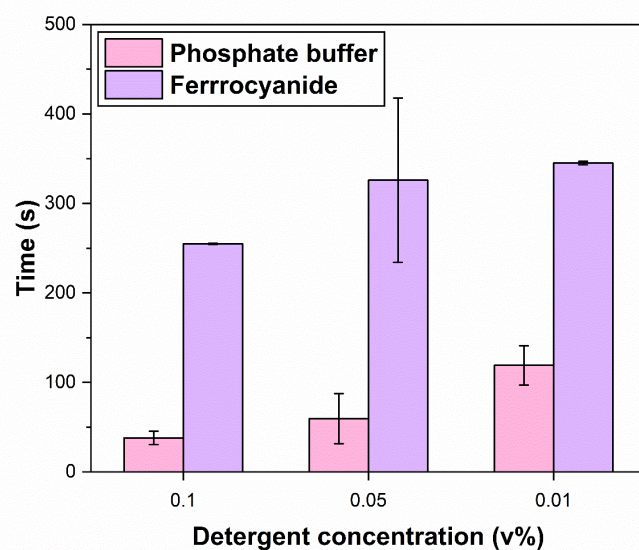


Figure S5.6. Time measured for the flow of phosphate buffer and ferrocyanide with different concentrations of Triton X.

Table S5.2. Liposome's properties.

Biotinylated Liposomes	z average / nm	Pdl	zeta potential /mV	total lipid concentration / mM	Encapsulant total ($\mu\text{M}/\text{mM tL}$)	Encapsulant outside ($\mu\text{M}/\text{mM tL}$)
AB201009	382	0.07	-24.9	8.40	ND	ND
AB210509	155	0.09	-26.6	15.70	ND	ND
C. Parvum tagged Liposomes						
AP190721	168 \pm 3	0.09 \pm 0.01	-17 \pm 2	15.5 \pm 0.2	403 \pm 44	6.2 \pm 0.9

Table S5.3.

Surfactant	OG	CTAB	Tween 20	Triton X
Concentration	30 mM	20 mM	10 mM	100 μM
Peak intensity (μA)	1.5 \pm 0.4	0.06 \pm 0.03	0.72 \pm 0.02	1.7 \pm 0.2
Lysing efficiency (%)	100%	4%	48	113%

Table S5.3. Lysing efficiencies of surfactants with different concentrations measured with 1 mM tL of biotinylated liposomes on Dropsens screen-printed electrodes.

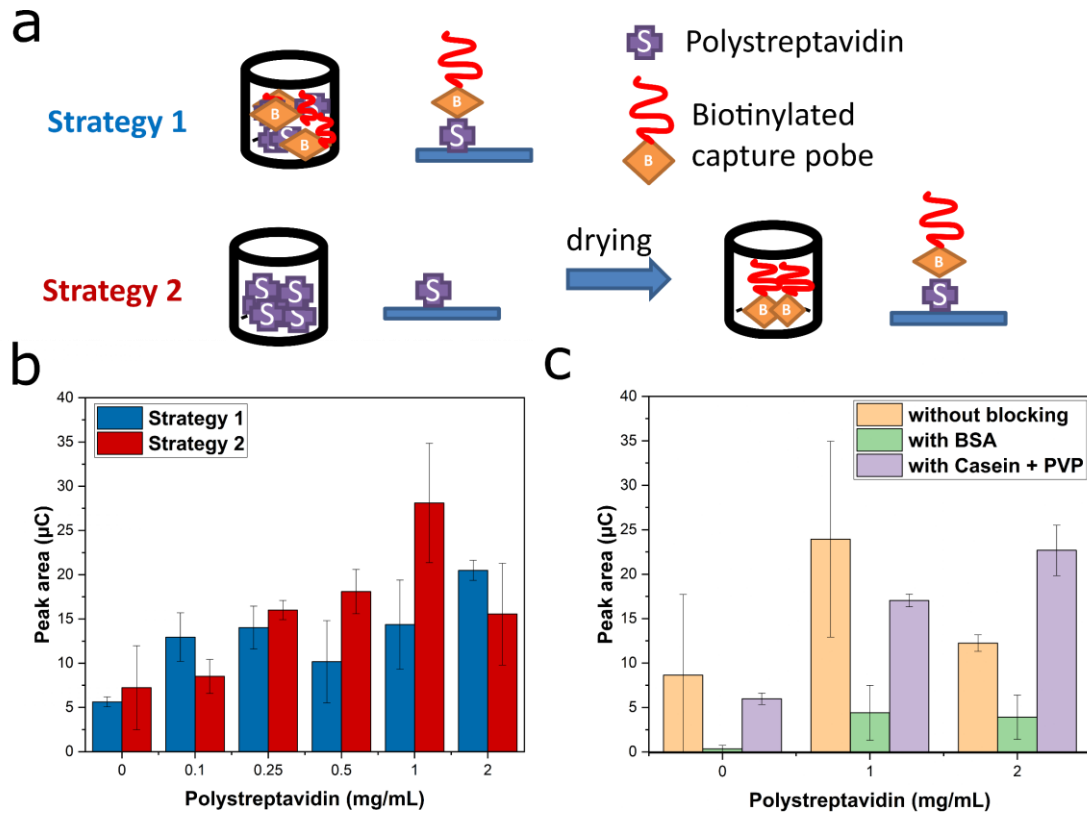


Figure S5.7. Optimization of the assay. a. Schematics of different incubation strategies. b. Peak area of the two different strategies was measured with different polystreptavidin concentrations. c. Variation of blocking solution.

For the optimization of the bioassay, two different strategies for the immobilization of the biotinylated capture probes were investigated (Figure S5.7a). It was found that the addition of pStAv to the strip with a drying step in between, followed by the addition of the biotinylated capture probe yields a better result in terms of reproducibility and signal intensity, in comparison to the addition of premixed capture DNA and pStAv (Figure S5.7b). Moreover, in order to minimize the nonspecific signal caused by binding events of the target-reporter probe-liposomes complex on the strip, different blocking solutions were considered (Figure S5.7c). While BSA efficiently blocks the strip, it also interferes with the specific binding events, decreasing the overall performance of the device. Therefore, a mixture of casein and PVP were used as blocking reagents.

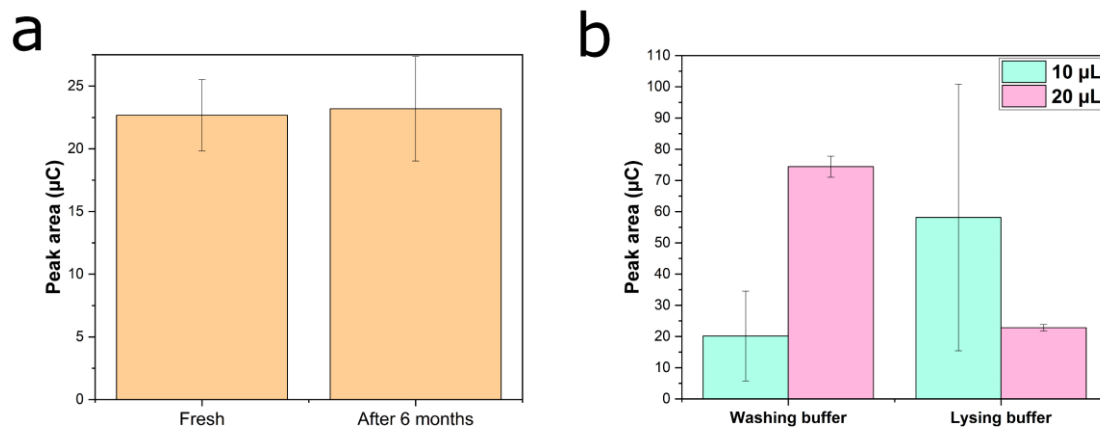


Figure S5.8. Further study and optimization of the assay. a. Comparison of the signal of freshly synthesized liposomes with 6-month-old liposomes. b. Variation of the volume used for washing buffer.

VI. Conclusion and Future Perspectives

Electrochemical sensors have an extensive palette of advantages that can be designed, and tailored to detect and monitor important analytes or biomarkers, even without being electrochemically active. Suitable materials for electrochemical detection have been extensively researched, characterized, and demonstrated for proof of principles systems. However, their implementation in products towards commercialization or implementation into real-life devices, such as point-of-care (POC) applications, is limited. These challenges come from their complicated and expensive fabrication techniques, problems with reproducibility, the ability to work in rough conditions, and the need for multiple steps.

The need for more POC devices was evident during the pandemic, where LFAs, which were in the past commonly used as pregnancy tests, were quickly adapted for detecting the antigen related to the Covid19 virus. This adaptation demonstrated the versatility of the LFAs in being modified for different analytes or biomarkers. This achievement strongly emphasizes how new biorecognition elements and new materials can be exploited towards the expansion of the LFAs for the detection of common flu viruses or other infections that can often be treated from home with some mild medical treatments. Early detection would benefit the health care systems, where doctor offices would be less crowded, and patient care could be more efficiently organized and managed. Another advantage would be to receive medical care based on POC tests, which can be done directly at the pharmacy, and drugs can be administered depending on the outcome. Quantifying the analyte of interest could make a big difference for certain diseases, where the adjustment of the drug's concentration is made based on the biomarker used to screen the infection or disease.

A different approach would be to accurately check the possible infection sites to prevent the need for health care. Such an example would be food monitoring, where detecting contaminants or bacteria could prevent their consumption and further spread diseases. Another important cause of infection and disease spreading is water, which could also be examined to hinder the spread of pathogens efficiently.

Even though nanofibers have already been implemented in clinical trials, such as the Rivelin patch with PVP electrospun nanofibers for oral ulcers treatment^[244], cellulose nanofibers as a dressing material for burn patients^[245], and polyurethane nanofiber for wound dressing, PVA nanofibers for treatment of herpes^[246], and chitosan nanofibers for different medical applications^[247], the possibilities for carbon nanofibers are still not exploited towards commercialization.

A new technology was implemented to laser-scribe nanofibers, which addressed some of the challenges enumerated for available electrochemical transducers and their fabrication. Two of the most critical limitations of CNFs are the fabrication cost and poor controllability over their microstructure. Therefore, the cost is reduced by electrospinning nanofibers, and it allows easy control of their structure. This technique is highly advantageous because it offers mass production possibilities. The mass production

could be achieved by multiple needles, multiple collectors, size of collectors, and highly controlled spinning conditions. Moreover, the scribing procedure to carbonize the electrospun nanofibers is already widely used in the industry for engraving, fine cutting, cleaning, and measuring. Laser writing is also easy to implement because it is fast, easily maneuverable, and different designs can be implemented.

The first prototype for the LCNF-based electrodes suffers from the limitation of the conducting surface. The conductivity of the substrate material was thought to be necessary for a homogenous collection of the nanofibers onto the collector. Nevertheless, this would hinder the fabrication of multiple electrodes being used together, and limit their use as porous materials since the ITO substrate is similar to a plastic foil with no pores. In this project, substrate-free LCNFs electrodes were achieved by exchanging the ITO substrate with filter paper. The filter paper has an immense porosity, presumably allowing the electrical field to pass through and enabling a homogenous collection of the nanofibers. To efficiently carbonize the non-conducting nanofibers, the collection time was proved to be one of the most significant factors. By increasing the collection time from 15 to at least 45 minutes, it was demonstrated that conducting carbon nanofibers can be achieved. However, for a proper electrode structure, a 90 minutes collection time was used to fabricate the LCNFs.

The three-electrode system was used in an open hydrophobic configuration for silver ions detection as a first proof of principle. Silver was deposited onto the working electrode and detected using linear sweep voltammetry down to nM. The substrate-free electrodes were then treated with oxygen plasma, which allowed an enormous change in wettability, making them hydrophilic. Their porosity and similarity to cellulose fibers used in paper enabled wax printing to create hydrophobic channels among the hydrophilic nanofibers, and confine the liquid flow among the nanofibrous network. The wax channels enable the development of two other configurations, such as hydrophilic open and closed devices. Three different redox markers were used to characterize these three configurations with respect to oxidation peak intensity and electroactive surface area. The results showed a superior performance of the closed device towards the redox marker dopamine.

Dopamine is an electrochemically active molecule, and a vital neurotransmitter whose concentration variation from the normal range can indicate certain brain-related diseases. A sensitive dopamine detection was demonstrated in a mixture with common interferences like ascorbic acid and uric acid. The aging behavior was evaluated for the three configurations. The storage was assessed by peak intensity and separation, which showed that the hydrophobic electrodes became more hydrophilic and remained the same over four months. The hydrophilic ones behave differently depending if they are enclosed or left in an open configuration. The closed devices, even though they perform the best overall, have limited storage possibilities because the nanofibers inside the channel are becoming more hydrophobic. The storage limitation for the closed device is a problem, which should be addressed in the future. The most stable configuration was the open one containing hydrophilic electrodes. The performance remained stable for up to 5 months.

In order to exploit the amplification strategy for cyclic voltammetry, we investigated the possibility of generating IDEs from LCNF. The scribing process proved to be more challenging for nanofibers than a flat surface, such as a Kapton foil. The energy dissipation is not as efficient, and the nanofibers expand, so the designed electrode widths are larger. However, by using this expansion, narrow gaps between finger-like IDEs could be achieved for the LCNFs with gaps of about $\sim 50 \mu\text{m}$. The smallest gap was achieved by using a different lens for the laser and optimizing the finger and gap size. The porous IDEs were implemented for redox cycling amplification. The porosity of the LCNFs is emphasized by placing LCNF electrodes on top of each other, having in between a non-carbonized NF mat. Therefore, the gap between the two electrodes would be represented by the thickness of the insulating NF mat. This hypothesis was tested for redox cycling by varying the thickness of the insulating NF mat. It was proved suitable for redox cycling, and the amplification factor decreased with increasing mat thickness. The variation of the AF with the gap size proves the suitability of the stacked electrodes for redox cycling.

For the application of LCNF IDEs into a POC device, the IDEs were investigated as redox cycling systems without external AE and RE. Additionally, the IDEs were tested in a closed and open configuration for redox cycling. Their implementation into an LFA system was further studied with normal single CVs, demonstrating the possibility of using them in a 2-, 3- and 4- electrode setup. However, even if the electrodes function properly when integrated with the other membranes, the flow is sometimes hindered by the groove caused by the expansion of the CNFs. To be further employed, the fabrication of the IDEs should be further optimized with different laser types (pulsed laser would decrease the amount of heat), variation of pixels-per-inch (PPI) and dots-per-inch (DPI) (in all the studies, 500 PPI and 1000 DPI was used), or by just using wider fingers-like electrodes.

In the last part of this thesis, it was demonstrated that not only a successful integration of the LCNF electrodes into a POC device was achieved, but also its use for detecting a waterborne pathogen. The wide LCNF electrodes are easier to handle; therefore, their implementation into an LFA was more reproducible. The studies revealed that the characteristics of the used membranes - nitrocellulose width and wicking rate of waste pads - significantly influence the flow rate, and implicitly, the sensor's performance. Furthermore, lipid vesicles were exploited for the encapsulation of electrochemically active molecules. The liposomes were proven first with the typical interaction between streptavidin immobilized on the strip and biotin from the surface of the liposomes. With the successful implementation of the liposomes and the developed electrochemical LCNF-based LFA, the detection of target DNA from *Cryptosporidium parvum* was further explored. The dose-response curve of target DNA was achieved with the described biosensor developed from LCNF.

This project highlights the achievement of a substrate-free electrochemical cell made entirely from nanofibers, both conductive and insulating. This accomplishment enables a wide range of possibilities for applications. The first studies showed a sensitive detection of silver, which can be further employed for using metal nanoparticles as labels. Besides silver, preliminary studies were also done with gold

(data not shown), proving that various metals could be used. However, studies showed that only an open system could be used for these analytes. Moreover, studies should be conducted to prove that the acids used do not cause leakage or interaction with the iron (or any other metal salt) present in the nanofibers. The use of NPs would be useful to be used in LFA systems, where a colorimetric qualitative detection could be implied as a first assessment followed by quantifying the metal concentration correlated with the concentration of the analyte of interest.

The porosity of the electrodes offers breathability, which is uncommon for electrodes. The breathability facilitates the use of these electrodes for wearable devices. Moreover, their tensile strength emphasizes the opportunity to develop a stretchable wearable electrochemical sensor for detecting biomarkers in sweat, such as Na, Cl, K ions, lactate, ethanol, nicotine, and ascorbic acid. Nonetheless, hydrogels can be applied to the electrodes for sweat sampling and as reservoirs. Preliminary studies were conducted where D4 hydrogels were coated with a knife-coater on LCNF electrodes (data not shown). The electrodes gain hydrophilicity from the hydrogel, which could mean there is no additional treatment required to make the electrodes hydrophilic. Additional studies can be made to optimize the application of the hydrogel. Furthermore, the hydrogel can also be used to incorporate an enzyme onto the electrodes to detect glucose or lactate. The LCNF maintained proper functioning after coating with the hydrogel and had similar peak intensities but higher peak separations, probably due to the diffusion through the hydrogel.

The development of the stacked electrodes, which consisted of a non-insulating mat between two wide LCNF electrodes demonstrated the possibility of using insulating nanofibers on top of the nanofiber-based electrodes. Different nanofibers containing biomolecules, such as biotin or enzymes, could be employed on top of the electrodes to act as a biorecognition element instead of modifying the electrode. Other functionalities, such as filtering unwanted molecules by implying positive or negative nanofibers, can be further exploited. A device where a sample could flow directly through different nanofiber-based membranes with different functions, where the LCNF are situated latest, can be developed.

The breathability of the LCNFs can also be exploited for breath analysis. Preliminary experiments were conducted during a research stay at Cornell University in Ithaca, USA (data not shown). The insulating nanofibers and the LCNF have been tested for filtration efficiency for particles with large diameters (1 μm) and smaller diameters (0.3 and 0.5 μm). The results are auspicious, as the efficiency for 0.3 μm particles was determined to be 83%. This filtration efficiency proved superior to standard textiles (915 material) and filter paper. The substrate-free LCNFs yielded a low and constant pressure that could be measured for 15 minutes compared to the nanofibers on filter paper, which showed pressure buildup due to moisture and swelling of the fibers. EDS measurements confirmed capturing of fine particles of the aerosols. LCNFs proved good air permeability, had outstanding filtration efficiency and showed constant pressure. The electrodes can be further employed for gas sensing via monitoring the change in electrical conductivity of the CNFs. Such monitoring has been done with CNTs and graphene to detect

ammonia, NO_x , and acetone. A different strategy is to use electrochemical sensing of the gas, which passes through a permeable membrane and gets oxidized or reduced at the electrode surface. The nanofiber membrane can act as both the permeable membrane and reduce or oxidize the analyte of interest.

The developed CNFs have also been patterned in such a way as to form very thin finger-like electrodes in the form of IDEs. The array structure of the electrodes allows modifying each finger from the array with a different biorecognition element for multiplex sensing. Multiplexing is advantageous to implement, for example, labels with different electrochemically active molecules, such as liposomes encapsulating ferri/ferrohexacyanide and ruthenium hexamine. These two analytes show signals at different potentials, allowing a simultaneous measurement of two different analytes. Such studies can also be made with nanoparticles consisting of different metals.

Even though the developed technology offers many benefits to fabricating porous freestanding electrodes, there are also drawbacks. These are caused mainly by the reproducibility issues of the electrospinning process on a stationary collector in uncontrolled conditions. These can induce differences in the electrodes scribed on different areas of the mat or variations between mats. The discrepancy between the mats mainly originates from the variation in humidity and temperature. A higher humidity results in a thicker mat, so a significant thickness difference results in a different electroactive surface area and implicitly in the variation of the measured intensity. A rotatory collector should be used to address the variation between electrodes on the same mat. The rotation of the collector should result in a more homogenous mat collection. However, the rotation could impact the density of the nanofibers and the dependency between collection time and thickness of the mat. Furthermore, the variation between the mats can be resolved by controlling the humidity and temperature inside the spinning chamber. These two parameters would lead to better reproducibility of the mat thickness and the scribed electrodes.

To conclude, CNFs are fabricated by electrospinning and laser carbonization into porous 3D freestanding electrodes. Different strategies have been implemented, yielding (bio)sensors with many possibilities for further applications, explicitly for developing POC devices.

Summary

Nanofibers offer many possibilities as nanomaterials because of their versatility and ease of handling, and this facilitates their constant development and implementation in a growing number of applications. Their nanometer diameter can be of interest, especially for interaction with molecules and biomolecules, which can be continuously monitored. In this project, nanofibers were electrospun as nonconductive nanofibers, followed by a controlled carbonization. The resulting electrodes are highly porous, have a three-dimensional structure, can be easily handled as freestanding objects, and can be modified with simple methods, such as drop-casting of Nafion or plasma treatment, to enhance their wettability.

In this thesis, a sensor for the detection of dopamine was developed using LCNFs. The three-electrode electrochemical cell was patterned on PI nanofibers. After the carbonization of the nanofibers, the system is subjected to oxygen plasma treatment to transform them into hydrophilic electrodes. Wax is printed onto a plastic foil, and heating the wax fills the nanofibers' pores, creating hydrophobic barriers to confine the solution flow. The wax also acts as a glue between the plastic foil and the nanofibers sealing the nanofibers inside a channel mimicking a microfluidic channel filled with nanofibers. To hinder the interference caused by ascorbic and uric acid in common body fluids, Nafion is applied onto the working electrode. Sensitive detection of dopamine in a mixture with the two interfering molecules is demonstrated on a closed device made from LCNFs.

The second project focused on employing LCNFs electrodes for redox cycling. Redox cycling is used here to exploit the possibility of creating very small features of the electrodes created by laser carbonization. Therefore, the limits of the laser were studied concerning scribing very thin finger-like structures on nanofibers. Interdigitated electrodes were designed and investigated for redox cycling. An amplification of the signal could be achieved. Additionally, stacked electrodes were established from wide electrodes with an insulating nanofiber mat. Herein, it was demonstrated that nanofibers could be spun directly onto the electrodes, and the nanofiber mat thickness can be varied to render different gaps between the electrodes. The second strategy was also demonstrated for redox cycling.

Lastly, the freestanding LCNFs were employed together with liposomes encapsulating electrochemically active molecules in an LFA to detect a waterborne pathogen. Target DNA was used as a biorecognition element on the nitrocellulose membrane. The detection was done on the same strip with the LCNFs membrane, which enabled constant monitoring of the flow of the solution. This experiment demonstrates that the structure of the electrode can be reliably used in a flow-through system.

The developed systems integrating LCNFs open the field to many possibilities for applications enumerated in the conclusion section.

Zusammenfassung

Nanofasern bieten als Nanomaterialien eine Vielzahl von Möglichkeiten, weil sie vielfältig und einfach zu handhaben sind. Dies fördert ihre ständige Weiterentwicklung und den Einsatz in einer wachsenden Zahl von Anwendungen. Ihr Nanometer-Durchmesser kann vor allem für die Interaktion mit Molekülen von Interesse sein. In diesem Projekt wurden nichtleitende Nanofasern aus Polyimid (PI) elektrogewoben und anschließend mit einem Laserstrahl karbonisiert. Das entstandene leitfähige Material nannten wir Laser-Karbonisierte Nanofasern (engl. LCNF). LCNFs sind hochporös, haben eine dreidimensionale Struktur, lassen sich leicht handhaben und können mit sehr einfachen Methoden modifiziert werden, wie z. B. einer Beschichtung mit Nafion oder mit einer Plasmabehandlung.

In dieser Arbeit wurde ein elektrochemischer Sensor für die quantitative Messung von Dopamin unter Verwendung von LCNF hergestellt. Durch örtlich begrenzte Karbonisierung der PI-Nanofasern entstehen drei nebeneinanderliegende Elektroden aus LCNF, wonach das System einer Sauerstoffplasmabehandlung unterzogen wird, um die Elektroden hydrophiler zu machen. Wachs wird auf eine Kunststoffolie gedruckt, mit der Fasermatte kontaktiert und erhitzt. Flüssiges Wachs füllt die Poren der Nanofasern und verfestigt nach Abkühlung, wodurch hydrophobe Barrieren entstehen, die den Fluss der Lösung einschränken. Das Wachs wirkt auch als Klebstoff zwischen der Kunststoffolie und den Nanofasern und versiegelt die Nanofasern in einem Kanal. Um die Interferenz durch Ascorbinsäure und Harnsäure in gängigen Körperflüssigkeiten zu verhindern, wird Nafion auf die Arbeitselektrode aufgebracht. In einer geschlossenen Vorrichtung aus LCNFs wird ein empfindlicher Nachweis von Dopamin in einer Mischung mit den beiden störenden Molekülen demonstriert.

Das zweite Projekt konzentrierte sich auf den Einsatz von LCNF-Elektroden für Redox cycling. Da durch Laserkarbonisierung sehr feine Elektrodenstrukturen erzeugt werden können, bietet sich die Technik des Redox cycling auf LCNFs an. So wurde untersucht, unter welchen Bedingungen der Laser kleinstmögliche fingerartige Strukturen auf Nanofasern einbrennen kann. Interdigitale Elektroden (IDE) wurden entworfen und auf das Signal durch Redox cycling hin untersucht. Eine Verstärkung des Signals konnte mit IDE aus LCNF erreicht werden. Außerdem wurden Stapel aus breiten Elektroden mit einer isolierenden Nanofasermatte hergestellt. Dabei wurde gezeigt, dass Nanofasern direkt auf die Elektroden gesponnen werden können und die Dicke der Nanofasermatte variiert werden kann, um unterschiedliche Abstände zwischen den Elektroden zu erzeugen. Die zweite Strategie wurde auch auf ihre Eignung für Redox cycling hin untersucht.

Schließlich wurden die freistehenden LCNF zusammen mit Liposomen, die elektrochemisch aktiven Moleküle einkapseln, in einem Lateral-Flow-Test zur Detektion von *Cryptosporidium parvum* DNA in Wasser eingesetzt. Die DNA wurde als biologisches Erkennungselement auf der Nitrocellulosemembran verwendet. Der Nachweis erfolgte auf demselben Streifen mit der LCNF-Membran, was die Kontrolle der Lösungsfließgeschwindigkeit ermöglichte. Dies zeigt, dass die vorteilhafte Struktur der Elektrode zuverlässig in Durchflusssystemen eingesetzt werden kann.

Die entwickelten Systeme, in die LCNFs integriert sind, eröffnen zahlreiche Möglichkeiten für Anwendungen, die im Abschnitt "Schlussfolgerungen" aufgeführt sind.

References

- [1] N. Baig, I. Kammakakam, W. Falath, I. Kammakakam, *Mater. Adv.* **2021**, 2, 1821.
- [2] L. Matlock-Colangelo, A. J. Baeumner, *Lab Chip* **2012**, 12, 2612.
- [3] M. Holzinger, A. Le Goff, S. Cosnier, *Front. Chem.* **2014**, 2, 1.
- [4] N. Wongkaew, M. Simsek, C. Griesche, A. J. Baeumner, *Chem. Rev.* **2019**, 119, 120.
- [5] D. Gugulothu, A. Barhoum, R. Nerella, R. Ajmer, M. Bechelany, *Fabrication of Nanofibers: Electrospinning and Non-electrospinning Techniques*, **2019**.
- [6] D. Cho, L. Matlock-Colangelo, C. Xiang, P. J. Asiello, A. J. Baeumner, M. W. Frey, *Polymer (Guildf)*. **2011**, 52, 3413.
- [7] A. Moradzadegan, S. O. Ranaei-Siadat, A. Ebrahim-Habibi, M. Barshan-Tashnizi, R. Jalili, S. F. Torabi, K. Khajeh, *Eng. Life Sci.* **2010**, 10, 57.
- [8] J. Yu, S. Liu, H. Ju, *Biosens. Bioelectron.* **2003**, 19, 401.
- [9] S. Piperno, B. Tse Sum Bui, K. Haupt, L. A. Gheber, *Langmuir* **2011**, 27, 1547.
- [10] L. Matlock-Colangelo, D. Cho, C. L. Pitner, M. W. Frey, A. J. Baeumner, *Lab Chip* **2012**, 12, 1696.
- [11] S. Chuangchote, A. Sirivat, P. Supaphol, *Nanotechnology* **2007**, 18.
- [12] R. Bagherzadeh, M. Gorji, M. S. Sorayani Bafgi, N. Saveh-Shemshaki, *Electrospun conductive nanofibers for electronics*, Elsevier Ltd., **2017**.
- [13] L. Zhang, A. Aboagye, A. Kelkar, C. Lai, H. Fong, *J. Mater. Sci.* **2014**, 49, 463.
- [14] N. Wongkaew, M. Simsek, P. Arumugam, A. Behrent, S. Berchmans, A. J. Baeumner, *Nanoscale* **2019**.
- [15] N. Kurra, Q. Jiang, P. Nayak, H. N. Alshareef, *Laser-derived graphene: A three-dimensional printed graphene electrode and its emerging applications*, **2019**.
- [16] C. Gao, L. Zhang, J. Wang, M. Jin, Q. Tang, Z. Chen, Y. Cheng, R. Yang, G. Zhao, *J. Mater. Chem. B* **2021**, 9, 3106.
- [17] S. Nemati, S. Jeong Kim, Y. M. Shin, H. Shin, *Nano Converg.* **2019**, 6.
- [18] S. Han, K. Nie, J. Li, Q. Sun, X. Wang, X. Li, Q. Li, *Stem Cells Int.* **2021**, 2021.
- [19] M. O. Guerrero-Pérez, *Catalysts* **2022**, 12.
- [20] L. T. H. Nguyen, S. Chen, N. K. Elumalai, M. P. Prabhakaran, Y. Zong, C. Vijila, S. I. Allakhverdiev, S. Ramakrishna, *Macromol. Mater. Eng.* **2013**, 298, 822.
- [21] Y. Li, J. Yu, B. Ding, *Facile and ultrasensitive sensors based on electrospinning–netting nanofibers/nets*, Vol. 96, **2015**.
- [22] E. Schoolaert, R. Hoogenboom, K. De Clerck, *Adv. Funct. Mater.* **2017**, 27, 1.
- [23] A. Camposeo, M. Moffa, L. Persano, *Nanosci. Technol.* **2015**, 96, 129.
- [24] T. Zhang, H. Chen, X. Zheng, *Thermoelectric Fibers*, **2020**.
- [25] J. Horne, L. McLoughlin, B. Bridgers, E. K. Wujcik, *Sensors and Actuators Reports* **2020**, 2, 100005.
- [26] R. Vajtai, *Springer Handb. Nanomater.* **2013**, 1.

- [27] A. Kundu, N. P. Shetti, S. Basu, K. Mondal, A. Sharma, T. M. Aminabhavi, *ACS Appl. Bio Mater.* **2022**.
- [28] J. Huang, Y. Liu, T. You, *Anal. Methods* **2010**.
- [29] M. Simsek, N. Wongkaew, *Anal. Bioanal. Chem.* **2021**, *413*, 6079.
- [30] X. Zhou, Y. Wang, C. Gong, B. Liu, G. Wei, *Chem. Eng. J.* **2020**, *402*, 126189.
- [31] S. Wang, Y. Liu, A. Zhu, Y. Tian, *Anal. Chem.* **2023**, *95*, 388.
- [32] Y. Wang, H. Xu, J. Zhang, G. Li, *Sensors* **2008**, *8*, 2043.
- [33] D. W. Kimmel, G. Leblanc, M. E. Meschievitz, D. E. Cliffel, *Anal. Chem.* **2012**, *84*, 685.
- [34] K. Idegami, M. Chikae, N. Nagatani, E. Tamiya, Y. Takamura, *Jpn. J. Appl. Phys.* **2010**, *49*, 1.
- [35] D. G. Rackus, M. H. Shamsi, A. R. Wheeler, *Chem. Soc. Rev.* **2015**, *44*, 5320.
- [36] J. Huang, D. Wang, H. Hou, T. You, *Adv. Funct. Mater.* **2008**, *18*, 441.
- [37] Y. Liu, H. Teng, H. Hou, T. You, *Biosens. Bioelectron.* **2009**, *24*, 3329.
- [38] H. Zhu, M. Du, M. Zhang, M. Zou, T. Yang, L. Wang, J. Yao, B. Guo, *J. Mater. Chem. A* **2014**, *2*, 11728.
- [39] V. Vamvakaki, K. Tsagaraki, N. Chaniotakis, *Anal. Chem.* **2006**.
- [40] L. Wu, X. Zhang, H. Ju, *Anal. Chem.* **2007**.
- [41] M. Hatzimarinaki, V. Vamvakaki, N. Chaniotakis, *J. Mater. Chem.* **2009**, *19*, 428.
- [42] M. Simsek, K. Hoecherl, M. Schlosser, A. J. Baeumner, N. Wongkaew, *ACS Appl. Mater. Interfaces* **2020**, *12*, 39533.
- [43] E. T. S. G. da Silva, D. E. P. Souto, J. T. C. Barragan, J. de F. Giarola, A. C. M. de Moraes, L. T. Kubota, *ChemElectroChem* **2017**, *4*, 778.
- [44] C. M. Pandey, S. Augustine, S. Kumar, S. Kumar, S. Nara, S. Srivastava, B. D. Malhotra, *Microfluidics Based Point-of-Care Diagnostics*, **2018**.
- [45] Y. Hou, C. Cong, L. Yan, L. Guo, X. Hu, M. Wei, L. Yan, J. Bao, X. Li, M. Yang, S. Yin, *J. Anal. Test.* **2022**, *6*, 247.
- [46] T. Review, **2013**, 450.
- [47] G. A. Posthuma-Trumpie, J. Korf, A. Van Amerongen, *Anal. Bioanal. Chem.* **2009**, *393*, 569.
- [48] M. M. Crane, *Organon MV*, **1969**, 3.
- [49] T. Mahmoudi, M. de la Guardia, B. Baradaran, *TrAC - Trends Anal. Chem.* **2020**, *125*, 115842.
- [50] I. R. L. Campbell, O. Connell, C. Hill, N. C., **1987**.
- [51] R. W. Rosenstein, T. G. Bloomster, **1989**.
- [52] J. K. Horton, S. Swinburne, M. J. O'Sullivan, *J. Immunol. Methods* **1991**, *140*, 131.
- [53] K. S. Lee, T. H. Kim, M. C. Shin, W. Y. Lee, J. K. Park, *Anal. Chim. Acta* **1999**.
- [54] M. Lönnberg, J. Carlsson, *Anal. Biochem.* **2001**, *293*, 224.
- [55] K. A. Edwards, A. J. Baeumner, *Anal. Bioanal. Chem.* **2006**, *386*, 1335.
- [56] J. Liu, D. Mazumdar, Y. Lu, *Angew. Chemie* **2006**, *118*, 8123.
- [57] X. Mao, Y. Ma, A. Zhang, L. Zhang, L. Zeng, G. Liu, *Anal. Chem.* **2009**, *81*, 1660.

- [58] Z. Fang, J. Huang, P. Lie, Z. Xiao, C. Ouyang, Q. Wu, Y. Wu, G. Liu, L. Zeng, *Chem. Commun.* **2010**.
- [59] A. Abera, J. W. Choi, *Anal. Methods* **2010**, 2, 1819.
- [60] Z. Li, Y. Wang, J. Wang, Z. Tang, J. G. Pounds, Y. Lin, *Anal. Chem.* **2010**, 82, 7008.
- [61] C. Liu, Q. Jia, C. Yang, R. Qiao, L. Jing, L. Wang, C. Xu, M. Gao, *Anal. Chem.* **2011**, 83, 6778.
- [62] D. S. Elenis, P. C. Ioannou, T. K. Christopoulos, *Nanotechnology* **2011**, 22.
- [63] A. M. López Marzo, J. Pons, D. A. Blake, A. Merkoçi, *Anal. Chem.* **2013**, 85, 3532.
- [64] A. Sakurai, K. Takayama, N. Nomura, N. Yamamoto, Y. Sakoda, Y. Kobayashi, H. Kida, F. Shibasaki, *J. Virol. Methods* **2014**, 209, 62.
- [65] S. Choi, S. Kim, J. S. Yang, J. H. Lee, C. Joo, H. Il Jung, *Sens. Bio-Sensing Res.* **2014**, 2, 8.
- [66] J. M. Park, H. W. Jung, Y. W. Chang, H. S. Kim, M. J. Kang, J. C. Pyun, *Anal. Chim. Acta* **2015**, 853, 360.
- [67] M. O. Rodríguez, L. B. Covián, A. C. García, M. C. Blanco-López, *Talanta* **2016**, 148, 272.
- [68] X. Fu, Z. Cheng, J. Yu, P. Choo, L. Chen, J. Choo, *Biosens. Bioelectron.* **2016**, 78, 530.
- [69] W. Kim, S. Lee, S. Jeon, *Sensors Actuators, B Chem.* **2018**, 273, 1323.
- [70] K. Serebrennikova, J. Samsonova, A. Osipov, *Nano-Micro Lett.* **2018**.
- [71] D. Quesada-González, A. Sena-Torralba, W. P. Wicaksono, A. de la Escosura-Muñiz, T. A. Ivandini, A. Merkoçi, *Biosens. Bioelectron.* **2019**.
- [72] Z. Yang, C. Yi, S. Lv, Y. Sheng, W. Wen, X. Zhang, S. Wang, *Sensors Actuators, B Chem.* **2019**.
- [73] D. Hong, E. J. Jo, K. Kim, M. B. Song, M. G. Kim, *Small* **2020**, 16, 1.
- [74] A. E. Urusov, A. V. Zherdev, B. B. Dzantiev, *Biosensors* **2019**, 9.
- [75] V. Gubala, L. F. Harris, A. J. Ricco, M. X. Tan, D. E. Williams, *Point of care diagnostics: Status and future*, **2012**.
- [76] F. S. Felix, L. Angnes, *Electrochemical immunosensors – A powerful tool for analytical applications*, **2018**.
- [77] N. Wongkaew, M. Simsek, C. Griesche, A. J. Baeumner, *Functional Nanomaterials and Nanostructures Enhancing Electrochemical Biosensors and Lab-on-a-Chip Performances: Recent Progress, Applications, and Future Perspective*, **2019**.
- [78] V. T. Nguyen, S. Song, S. Park, C. Joo, *Biosens. Bioelectron.* **2020**, 152, 112015.
- [79] E. B. Bahadır, M. K. Sezgintürk, *TrAC - Trends Anal. Chem.* **2016**, 82, 286.
- [80] C. Carrell, A. Kava, M. Nguyen, R. Menger, Z. Munshi, Z. Call, M. Nussbaum, C. Henry, *Microelectron. Eng.* **2019**, 206, 45.
- [81] K. M. Koczula, A. Gallotta, *Essays Biochem.* **2016**, 60, 111.
- [82] M. Sajid, A. N. Kawde, M. Daud, *J. Saudi Chem. Soc.* **2015**, 19, 689.
- [83] M. J. Raeisossadati, N. M. Danesh, F. Borna, M. Gholamzad, M. Ramezani, K. Abnous, S. M. Taghdisi, *Biosens. Bioelectron.* **2016**, 86, 235.
- [84] D. Quesada-González, A. Merkoçi, *Biosens. Bioelectron.* **2015**, 73, 47.

- [85] A. Chen, S. Yang, *Replacing antibodies with aptamers in lateral flow immunoassay*, **2015**.
- [86] S. Dalirirad, A. J. Steckl, *Sensors Actuators, B Chem.* **2019**, 283, 79.
- [87] R. Reid, B. Chatterjee, S. J. Das, S. Ghosh, T. K. Sharma, *Anal. Biochem.* **2020**, 593, 113574.
- [88] G. Liang, Y. Man, X. Jin, L. Pan, X. Liu, *Aptamer-based biosensor for label-free detection of ethanolamine by electrochemical impedance spectroscopy*, Vol. 936, Elsevier Ltd, **2016**.
- [89] B. H. Lee, S. H. Kim, Y. Ko, J. C. Park, S. Ji, M. B. Gu, *Biosens. Bioelectron.* **2019**.
- [90] S. H. Kim, J. Lee, B. H. Lee, C. S. Song, M. B. Gu, *Biosens. Bioelectron.* **2019**.
- [91] M. Jauset-Rubio, M. Svobodová, T. Mairal, C. McNeil, N. Keegan, A. Saeed, M. N. Abbas, M. S. El-Shahawi, A. S. Bashammakh, A. O. Alyoubi, C. K. O'Sullivan, *Sci. Rep.* **2016**.
- [92] N. Kaur, B. J. Toley, *Analyst* **2018**, 143, 2213.
- [93] J. R. Choi, J. Hu, Y. Gong, S. Feng, W. A. B. Wan Abas, B. Pingguan-Murphy, F. Xu, *Analyst* **2016**, 141, 2930.
- [94] B. Cai, S. Wang, L. Huang, Y. Ning, Z. Zhang, G. J. Zhang, *ACS Nano* **2014**, 8, 2632.
- [95] E. Cadoni, A. Manicardi, A. Madder, *PNA-based microRNA detection methodologies*, **2020**.
- [96] S. Reisberg, L. A. Dang, Q. A. Nguyen, B. Piro, V. Noel, P. E. Nielsen, L. A. Le, M. C. Pham, *Talanta* **2008**, 76, 206.
- [97] J. Liu, S. Tian, P. E. Nielsen, W. Knoll, *Chem. Commun.* **2005**, 2969.
- [98] S. Pavagada, R. B. Channon, J. Y. H. Chang, S. H. Kim, D. MacIntyre, P. R. Bennett, V. Terzidou, S. Ladame, *Chem. Commun.* **2019**.
- [99] D. Mazumdar, T. Lan, Y. Lu, In *Methods in Molecular Biology*, **2017**.
- [100] T. Lan, K. Furuya, Y. Lu, *Chem. Commun.* **2010**, 46, 3896.
- [101] Y. Xiang, P. Wu, L. H. Tan, Y. Lu, *Adv. Biochem. Eng. Biotechnol.* **2014**, 140, 93.
- [102] P. K. Kulabhusan, J. M. Rajwade, A. S. Sahul Hameed, K. M. Paknikar, *Appl. Microbiol. Biotechnol.* **2017**.
- [103] Q. Liu, J. Wang, B. J. Boyd, *Talanta* **2015**, 136, 114.
- [104] H. Huang, *Sensors (Switzerland)* **2018**, 18, 5.
- [105] C. Parolo, A. Sena-Torralba, J. F. Bergua, E. Calucho, C. Fuentes-Chust, L. Hu, L. Rivas, R. Álvarez-Diduk, E. P. Nguyen, S. Cinti, D. Quesada-González, A. Merkoçi, *Tutorial: design and fabrication of nanoparticle-based lateral-flow immunoassays*, **2020**.
- [106] B. Zhao, Q. Huang, L. Dou, T. Bu, K. Chen, Q. Yang, L. Yan, J. Wang, D. Zhang, *Sensors Actuators, B Chem.* **2018**, 275, 223.
- [107] P. Noguera, G. A. Posthuma-Trumpie, M. Van Tuil, F. J. Van Der Wal, A. De Boer, A. P. H. A. Moers, A. Van Amerongen, *Anal. Bioanal. Chem.* **2011**.
- [108] A. Moyano, M. Salvador, J. C. Martínez-García, V. Socoliuc, L. Vékás, D. Peddis, M. A. Alvarez, M. Fernández, M. Rivas, M. C. Blanco-López, *Anal. Bioanal. Chem.* **2019**.
- [109] H. Ye, X. Xia, *J. Mater. Chem. B* **2018**, 6, 7102.
- [110] K. K. Fung, C. P. Y. Chan, R. Renneberg, *Anal. Chim. Acta* **2009**.
- [111] J. Deng, M. Yang, J. Wu, W. Zhang, X. Jiang, *Anal. Chem.* **2018**, 90, 9132.
- [112] G. R. Han, M. G. Kim, *Sensors (Switzerland)* **2020**, 20, 1.

- [113] Z. Chen, R. Liang, X. Guo, J. Liang, Q. Deng, M. Li, T. An, T. Liu, Y. Wu, *Biosens. Bioelectron.* **2017**.
- [114] N. A. Taranova, A. N. Berlina, A. V. Zherdev, B. B. Dzantiev, *Biosens. Bioelectron.* **2015**.
- [115] M. Zhu, Y. Jia, L. Peng, J. Ma, X. Li, F. Shi, *Anal. Methods* **2019**.
- [116] M. Hasanzadeh, N. Shadjou, *Microchim. Acta* **2017**, *184*, 389.
- [117] M. Li, Y. T. Li, D. W. Li, Y. T. Long, *Anal. Chim. Acta* **2012**, *734*, 31.
- [118] Z. Shi, Y. Tian, X. Wu, C. Li, L. Yu, *Anal. Methods* **2015**, *7*, 4957.
- [119] D. Du, J. Wang, L. Wang, D. Lu, Y. Lin, *Anal. Chem.* **2012**, *84*, 1380.
- [120] L. Cao, C. Fang, Y. Liang, X. Zhao, Y. Jiang, Z. Chen, *J. Nanosci. Nanotechnol.* **2016**, *16*, 12187.
- [121] Y. Y. Lin, J. Wang, G. Liu, H. Wu, C. M. Wai, Y. Lin, *Biosens. Bioelectron.* **2008**, *23*, 1659.
- [122] F. Lu, K. H. Wang, Y. Lin, *Analyst* **2005**, *130*, 1513.
- [123] M. Medina-Sánchez, M. Cadevall, J. Ros, A. Merkoçi, *Anal. Bioanal. Chem.* **2015**, *407*, 8445.
- [124] L. Wang, D. Lu, J. Wang, D. Du, Z. Zou, H. Wang, J. N. Smith, C. Timchalk, F. Liu, Y. Lin, *Biosens. Bioelectron.* **2011**, *26*, 2835.
- [125] X. Zhu, P. Shah, S. Stoff, H. Liu, C. Z. Li, *Analyst* **2014**, *139*, 2850.
- [126] G. Ruiz-Vega, M. Kitsara, M. A. Pellitero, E. Baldrich, F. J. del Campo, *ChemElectroChem* **2017**, *4*, 880.
- [127] K. Inoue, P. Ferrante, Y. Hirano, T. Yasukawa, H. Shiku, T. Matsue, *Talanta* **2007**, *73*, 886.
- [128] K. Tominaga, S. Arimoto, K. Shimono, T. Yoshioka, F. Mizutani, T. Yasukawa, *Anal. Sci.* **2017**, *33*, 531.
- [129] M. R. Akanda, H. A. Joung, V. Tamilavan, S. Park, S. Kim, M. H. Hyun, M. G. Kim, H. Yang, *Analyst* **2014**, *139*, 1420.
- [130] C. Fernández-Sánchez, C. J. McNeil, K. Rawson, *TrAC - Trends Anal. Chem.* **2005**, *24*, 37.
- [131] P. D. Sinawang, V. Rai, R. E. Ionescu, R. S. Marks, *Biosens. Bioelectron.* **2016**, *77*, 400.
- [132] C. Fernández-Sánchez, A. M. Gallardo-Soto, K. Rawson, O. Nilsson, C. J. McNeil, *Electrochem. commun.* **2004**, *6*, 138.
- [133] G. Liu, Y. Y. Lin, J. Wang, H. Wu, C. M. Wai, Y. Lin, *Anal. Chem.* **2007**, *79*, 7644.
- [134] E. Dempsey, D. Rathod, *IEEE Sens. J.* **2018**, *18*, 1828.
- [135] P. D. Sinawang, L. Fajs, K. Elouarzaki, J. Nugraha, R. S. Marks, *Sensors Actuators, B Chem.* **2018**, *259*, 354.
- [136] V. Mirceski, S. Skrzypek, L. Stojanov, *ChemTexts* **2018**.
- [137] X. Zhu, M. Sarwar, J. J. Zhu, C. Zhang, A. Kaushik, C. Z. Li, *Biosens. Bioelectron.* **2019**, *126*, 690.
- [138] Y. Wang, L. Wang, S. Wang, M. Yang, J. Cai, F. Liu, *Microchim. Acta* **2016**, *183*, 2509.
- [139] A. J. Bäumner, R. D. Schmid, *Biosens. Bioelectron.* **1998**.
- [140] J. M. Olivares-Ramírez, V. M. Ovando-Medina, A. Ortíz-Verdín, D. M. Amaya-Cruz, J. Coronel-Hernandez, A. Marroquín, A. Dector, *J. Phys. Conf. Ser.* **2018**, *1119*.

- [141] S. Yamamoto, S. Uno, *Sensors (Switzerland)* **2018**, *18*.
- [142] Y. Zhao, X. Chen, S. Lin, D. Du, Y. Lin, *Anal. Chim. Acta* **2017**, *964*, 1.
- [143] N. Baig, T. A. Saleh, *Microchim. Acta* **2018**, *185*.
- [144] C. Jiang, B. Zhao, J. Cheng, J. Li, H. Zhang, Z. Tang, J. Yang, *Electrochim. Acta* **2015**, *173*, 399.
- [145] T. Thomas, A. Agarwal, *Materials (Basel)*. **2021**, *14*, 1.
- [146] Z. Zhang, F. Xiao, L. Qian, J. Xiao, S. Wang, Y. Liu, *Adv. Energy Mater.* **2014**, *4*.
- [147] M. P. Browne, F. Novotný, Z. Sofer, M. Pumera, *ACS Appl. Mater. Interfaces* **2018**, *10*, 40294.
- [148] M. A. Ali, K. Mondal, Y. Jiao, S. Oren, Z. Xu, A. Sharma, L. Dong, *ACS Appl. Mater. Interfaces* **2016**, *8*, 20570.
- [149] M. A. Ali, K. Mondal, Y. Wang, H. Jiang, N. K. Mahal, M. J. Castellano, A. Sharma, L. Dong, *Lab Chip* **2017**, *17*, 274.
- [150] Z. Chen, S. B. Cheng, P. Cao, Q. F. Qiu, Y. Chen, M. Xie, Y. Xu, W. H. Huang, *Biosens. Bioelectron.* **2018**, *122*, 211.
- [151] A. G. M. Ferrari, C. W. Foster, P. J. Kelly, D. A. C. Brownson, C. E. Banks, *Biosensors* **2018**, *8*, 1.
- [152] A. Calvimontes, P. Mauersberger, M. Nitschke, V. Dutschk, F. Simon, *Cellulose* **2011**, *18*, 803.
- [153] M. Inagaki, Y. Yang, F. Kang, *Adv. Mater.* **2012**, *24*, 2547.
- [154] H. Zhao, R. Su, L. Teng, Q. Tian, F. Han, H. Li, Z. Cao, R. Xie, G. Li, X. Liu, Z. Liu, *Nanoscale* **2022**, *14*, 1653.
- [155] V. Y. Maldonado, P. J. Espinoza-Montero, C. A. Rusinek, G. M. Swain, *Anal. Chem.* **2018**, *90*, 6477.
- [156] N. Wongkaew, S. E. K. Kirschbaum, W. Surareungchai, R. A. Durst, A. J. Baeumner, *Electroanalysis* **2012**, *24*, 1903.
- [157] G. Hinds, J. M. D. Coey, M. E. G. Lyons, *Electrochem. commun.* **2001**, *3*, 215.
- [158] L. Matlock-Colangelo, N. W. Colangelo, C. Fenzl, M. Frey, A. J. Baeumner, *Sensors (Switzerland)* **2016**, *16*, 1.
- [159] X. Chu, X. Fu, K. Chen, G. L. Shen, R. Q. Yu, *Biosens. Bioelectron.* **2005**.
- [160] H. Cai, Y. Xu, N. Zhu, P. He, Y. Fang, *Analyst* **2002**, *127*, 803.
- [161] T. J. Davies, *Analyst* **2016**, *141*, 4742.
- [162] M. B. Gholivand, M. H. Parvin, *Electroanalysis* **2010**, *22*, 2291.
- [163] S. Jahandari, M. A. Taher, H. Fazelirad, I. Sheikhshoai, *Microchim. Acta* **2013**, *180*, 347.
- [164] Y. Fu, Y. Yang, T. Tuersun, Y. Yu, J. Zhi, *Analyst* **2018**, *143*, 2076.
- [165] A. W. Martinez, S. T. Phillips, G. M. Whitesides, E. Carrilho, *Anal. Chem.* **2010**.
- [166] X. Mao, F. Simeon, G. C. Rutledge, T. A. Hatton, *Adv. Mater.* **2013**, *25*, 1309.
- [167] T. R. L. C. Paixão, *ChemElectroChem* **2020**, *7*, 3414.
- [168] R. L. McCreery, *Chem. Rev.* **2008**.

- [169] J. F. Hernández-Rodríguez, D. Rojas, A. Escarpa, *Sensors Actuators, B Chem.* **2020**, 324.
- [170] M. Waleed Shinwari, D. Zhitomirsky, I. A. Deen, P. R. Selvaganapathy, M. Jamal Deen, D. Landheer, *Sensors* **2010**, 10, 1679.
- [171] R. P. Bacil, L. Chen, S. H. P. Serrano, R. G. Compton, *Phys. Chem. Chem. Phys.* **2020**, 22, 607.
- [172] M. Labib, E. H. Sargent, S. O. Kelley, *Chem. Rev.* **2016**, 116, 9001.
- [173] H. Jeong, S. Jeon, *Sensors* **2008**, 8, 6924.
- [174] N. F. Atta, A. Galal, D. M. El-Said, *ACS Omega* **2019**, 4, 17947.
- [175] X. Dong, X. Wang, L. Wang, H. Song, H. Zhang, W. Huang, P. Chen, *ACS Appl. Mater. Interfaces* **2012**.
- [176] L. Jiang, G. W. Nelson, J. Abda, J. S. Foord, *ACS Appl. Mater. Interfaces* **2016**, 8, 28338.
- [177] J. Cheng, X. Wang, T. Nie, L. Yin, S. Wang, Y. Zhao, H. Wu, H. Mei, *Anal. Bioanal. Chem.* **2020**, 412, 2433.
- [178] E. Peltola, J. J. Heikkinen, K. Sovanto, S. Sainio, A. Aarva, S. Franssila, V. Jokinen, T. Laurila, *J. Mater. Chem. B* **2017**, 5, 9033.
- [179] H. Y. Yue, P. F. Wu, S. Huang, Z. Z. Wang, X. Gao, S. S. Song, W. Q. Wang, H. J. Zhang, X. R. Guo, *Microchim. Acta* **2019**, 186.
- [180] C. Zhang, J. Ren, J. Zhou, M. Cui, N. Li, B. Han, Q. Chen, *Analyst* **2018**, 143, 3075.
- [181] Z. Wang, H. Y. Yue, Z. M. Yu, S. Huang, X. Gao, B. Wang, S. S. Song, E. H. Guan, W. Q. Wang, H. J. Zhang, *Ionics (Kiel)*. **2019**, 25, 1813.
- [182] S. Huang, S. Song, H. Yue, X. Gao, B. Wang, E. Guo, *Sensors Actuators, B Chem.* **2018**, 277, 381.
- [183] H. Y. Yue, H. J. Zhang, S. Huang, X. X. Lu, X. Gao, S. S. Song, Z. Wang, W. Q. Wang, E. H. Guan, *Mater. Sci. Eng. C* **2020**, 108, 110490.
- [184] B. Huang, J. Liu, L. Lai, F. Yu, X. Ying, B. C. Ye, Y. Li, *J. Electroanal. Chem.* **2017**, 801, 129.
- [185] F. Beck, C. Horn, A. J. Baeumner, *Anal. Bioanal. Chem.* **2022**, 414, 475.
- [186] F. Beck, C. Horn, A. J. Baeumner, *Anal. Chim. Acta* **2022**, 1191, 339375.
- [187] H. Lee, D. Kharaghani, I. S. Kim, In *Novel Aspects of Nanofibers* (Ed.: Lin, T.), IntechOpen, Rijeka, **2018**.
- [188] L. Y. Wan, H. Wang, W. Gao, F. Ko, *Polymer (Guildf)*. **2015**, 73, 62.
- [189] C. Zhu, G. Yang, H. Li, D. Du, Y. Lin, *Electrochemical sensors and biosensors based on nanomaterials and nanostructures*, **2015**.
- [190] S. D. Minteer, In *Encyclopedia of Microfluidics and Nanofluidics* (Ed.: Li, D.), Springer US, Boston, MA, **2008**, pp. 2079–2083.
- [191] X. J. Huang, A. M. O'Mahony, R. G. Compton, *Microelectrode arrays for electrochemistry: Approaches to fabrication*, **2009**.
- [192] V. Matylitskaya, S. Kasemann, G. Urban, C. Dincer, S. Partel, *J. Electrochem. Soc.* **2018**.
- [193] L. B. Anderson, C. N. Reilley, *J. Electroanal. Chem.* **1965**.
- [194] M. A. Dayton, J. C. Brown, K. J. Stutts, R. M. Wightman, *Anal. Chem.* **1980**.

- [195] K. Aoki, M. Morita, O. Niwa, H. Tabei, *J. Electroanal. Chem.* **1988**.
- [196] E. O. Barnes, G. E. M. Lewis, S. E. C. Dale, F. Marken, R. G. Compton, *Generator-collector double electrode systems: A review*, **2012**.
- [197] E. O. Barnes, G. E. M. Lewis, S. E. C. Dale, F. Marken, R. G. Compton, *Generator-collector double electrode systems: A review*, **2012**.
- [198] E. D. Goluch, B. Wolfrum, P. S. Singh, M. A. G. Zevenbergen, S. G. Lemay, *Anal. Bioanal. Chem.* **2009**.
- [199] M. Morita, O. Niwa, T. Horiuchi, *Electrochim. Acta* **1997**.
- [200] K. Aoki, M. Morita, O. Niwa, H. Tabei, *J. Electroanal. Chem.* **1988**.
- [201] R. R. Kamath, M. J. Madou, *Anal. Chem.* **2014**.
- [202] N. Honda, M. Inaba, T. Katagiri, S. Shoji, H. Sato, T. Homma, T. Osaka, M. Saito, J. Mizuno, Y. Wada, In *Biosensors and Bioelectronics*, **2005**.
- [203] F. Liu, G. Kolesov, B. A. Parkinson, *Anal. Chem.* **2014**.
- [204] N. Honda, M. Inaba, T. Katagiri, S. Shoji, H. Sato, T. Homma, T. Osaka, M. Saito, J. Mizuno, Y. Wada, In *Biosensors and Bioelectronics*, **2005**.
- [205] F. Liu, G. Kolesov, B. A. Parkinson, *Anal. Chem.* **2014**.
- [206] S. Partel, C. Dincer, S. Kasemann, J. Kieninger, J. Edlinger, G. Urban, *ACS Nano* **2016**.
- [207] A. E. Cohen, R. R. Kunz, *Sensors Actuators, B Chem.* **2000**.
- [208] K. Ueno, M. Hayashida, J. Y. Ye, H. Misawa, *Electrochem. commun.* **2005**.
- [209] L. H. D. Skjolding, C. Spegel, A. Ribayrol, J. Emnéus, L. Montelius, In *Journal of Physics: Conference Series*, **2008**.
- [210] J. Il Heo, Y. Lim, H. Shin, *Analyst* **2013**.
- [211] H. Sugime, T. Ushiyama, K. Nishimura, Y. Ohno, S. Noda, *Analyst* **2018**.
- [212] E. D. Goluch, B. Wolfrum, P. S. Singh, M. A. G. Zevenbergen, S. G. Lemay, *Anal. Bioanal. Chem.* **2009**.
- [213] O. Niwa, M. Morita, H. Tabei, *J. Electroanal. Chem.* **1989**, 267, 291.
- [214] F. Zhu, J. Yan, M. Lu, Y. Zhou, Y. Yang, B. Mao, *Electrochim. Acta* **2011**, 56, 8101.
- [215] K. Ino, Y. Kanno, T. Nishijo, H. Komaki, Y. Yamada, S. Yoshida, Y. Takahashi, H. Shiku, T. Matsue, *Anal. Chem.* **2014**, 86, 4016.
- [216] D. Han, L. P. Zaino, K. Fu, P. W. Bohn, *J. Phys. Chem. C* **2016**, 120, 20634.
- [217] N. Y. Adly, B. Bachmann, K. J. Krause, A. Offenhäusser, B. Wolfrum, A. Yakushenko, *RSC Adv.* **2017**, 7, 5473.
- [218] M. Inagaki, Y. Yang, F. Kang, *Carbon nanofibers prepared via electrospinning*, **2012**.
- [219] P. M. Lewis, L. B. Sheridan, R. E. Gawley, I. Fritsch, *Anal. Chem.* **2010**, 82, 1659.
- [220] H. Palneedi, J. H. Park, D. Maurya, M. Peddigari, G. T. Hwang, V. Annapureddy, J. W. Kim, J. J. Choi, B. D. Hahn, S. Priya, K. J. Lee, J. Ryu, *Laser Irradiation of Metal Oxide Films and Nanostructures: Applications and Advances*, **2018**.
- [221] R. R. Kamath, M. J. Madou, *Anal. Chem.* **2014**, 86, 2963.
- [222] P. Zanello, *Inorganic Electrochemistry*, The Royal Society of Chemistry, **2003**.

- [223] A. J. Bard, L. R. Faulkner, *John Wiley&Sons, New Jersey, USA* **2001**.
- [224] O. Niwa, M. Morita, H. Tabei, *Anal. Chem.* **1990**.
- [225] S. Partel, C. Dincer, S. Kasemann, J. Kieninger, J. Edlinger, G. Urban, *ACS Nano* **2016**.
- [226] J. Lin, Z. Peng, Y. Liu, F. Ruiz-Zepeda, R. Ye, E. L. G. Samuel, M. J. Yacaman, B. I. Yakobson, J. M. Tour, *Nat. Commun.* **2014**.
- [227] B. Wolfrum, E. Kätelhön, A. Yakushenko, K. J. Krause, N. Adly, M. Hüske, P. Rinklin, *Acc. Chem. Res.* **2016**, *49*, 2031.
- [228] J. Hu, S. Q. Wang, L. Wang, F. Li, B. Pingguan-Murphy, T. J. Lu, F. Xu, *Biosens. Bioelectron.* **2014**, *54*, 585.
- [229] W. C. Mak, V. Beni, A. P. F. Turner, *TrAC - Trends Anal. Chem.* **2016**, *79*, 297.
- [230] W. Deenin, A. Yakoh, C. Kreangkaiwal, O. Chailapakul, K. Patarakul, S. Chaiyo, *Anal. Chem.* **2022**, *94*, 2554.
- [231] A. Perju, N. Wongkaew, *Anal. Bioanal. Chem.* **2021**.
- [232] Z. Shi, Y. Tian, X. Wu, C. Li, L. Yu, *Anal. Methods* **2015**, *7*, 4957.
- [233] M. Tebyetekerwa, Z. Xu, S. Yang, S. Ramakrishna, *Adv. Fiber Mater.* **2020**, *2*, 161.
- [234] A. Perju, A. J. Baeumner, N. Wongkaew, *Microchim. Acta* **2022**, *189*, 1.
- [235] N. Wongkaew, M. Simsek, P. Arumugam, A. Behrent, S. Berchmans, A. J. Baeumner, *Nanoscale* **2019**, *11*, 3674.
- [236] M. A. Mansfield, *Lateral Flow Immunoass.* **2009**, 95.
- [237] K. B. Vargo, P. Stahl, B. Hwang, E. Hwang, D. Giordano, P. Randolph, C. Celentano, R. Hepler, K. Amin, *Mol. Pharm.* **2021**, *18*, 148.
- [238] M. Manaargadoo-Catin, A. Ali-Cherif, J. L. Pougna, C. Perrin, *Adv. Colloid Interface Sci.* **2016**, *228*, 1.
- [239] J. Wang, M. R. N. Monton, X. Zhang, C. D. M. Filipe, R. Pelton, J. D. Brennan, *Lab Chip* **2014**, *14*, 691.
- [240] S. Rink, B. Kaiser, M. S. Steiner, A. Duerkop, A. J. Baeumner, *Anal. Bioanal. Chem.* **2022**, *414*, 3231.
- [241] F. Gerstl, U. Pongkitdachoti, F. Unob, A. J. Baeumner, *Lab Chip* **2022**, *22*, 3721.
- [242] N. Wongkaew, P. He, V. Kurth, W. Surareungchai, A. J. Baeumner, *Anal. Bioanal. Chem.* **2013**, *405*, 5965.
- [243] M. B. Esch, A. J. Baeumner, R. A. Durst, *Anal. Chem.* **2001**, *73*, 3162.
- [244] Y. Zhou, M. Wang, C. Yan, H. Liu, D. Yu, **2022**.
- [245] A. Pandey, *Environ. Chem. Lett.* **2021**, *19*, 2043.
- [246] Z. Golestannejad, F. Khozeimeh, S. Mirzaeei, D. Sarfaraz, **2022**, 184.
- [247] M. A. Sylvester, F. Amini, T. C. Keat, *Mater. Today Proc.* **2020**.

Curriculum Vitae

Personal Data

Name	Antonia-Teodora Perju
Address	Gertrud-von-le-Fort-Street Nr. 18, 93051 Regensburg
Mobile	+49-(0)1628590915
E-Mail	antonia-teodora.perju@chemie.uni-regensburg.de antoniaperju@yahoo.com ap2242@cornell.edu
Place of birth	Cisnadia, Romania
Date of birth	11.03.1996
Nationality	Romanian
Languages	Romanian (native), German (C2), English (C1)

Professional experience

01.2019-08.2019	Graduate assistant Regensburg University, Supervision of Bioanalytical lab course
07.2021-06.2022	Co-Chair for Gordon Research Seminar: <i>Nanoscale Science and Engineering for Agriculture and Food Systems</i>
06.2022-10.2022	Visitor Researcher at Cornell University, Department of Fiber Science, Group of Prof. Margaret Frey

Education

09.2010-06.2014	Baccalaureate Degree, Samuel von Brukenthal High School, Sibiu, Romania <i>Natural sciences program</i>
10.2014-07.2017	Diplom degree, Educational teaching program for physics teachers, Faculty of Psychology and Educational Sciences, Babes-Bolyai University Cluj-Napoca, Romania <i>Including active teaching at Tiberiu Popoviciu High School of Computer Science</i>

- 10.2014–07.2017 Bachelor of Science in Medical Physics, Babes-Bolyai University, Cluj-Napoca, Romania
Bachelor thesis: *Laser induced active compound release by Gold Nanoparticles modified Microcapsules*
- 10.2017–09.2019 Master of Science in Nanoscience, Universität Regensburg, Germany
Master thesis – *Integration of laser-induced carbon nanofibers into miniaturized analytical systems for development of point-of-care devices*
- 12.2019- present PhD degree program in Chemistry
Institute of Analytical Chemistry, Universität Regensburg
Project title: Development of nanofiber-based biosensors

Scholarships and international research stays

- 03.2016–07.2016 Erasmus Scholarship Friedrich-Alexander-University, Nuremberg-Erlangen, Germany
- 20.02-24.02.2017 Research stay at Biological Research Centre of the Hungarian Academy of sciences in Szeged, Hungary – AFM measurements on Gold Nanoparticles
- 04.2019-09.2019 Deutschlandstipendium: Scholarship awarded to promising and best performing students
- 06.2022-10.2022 Research Fellowship for PhD Students from German Academic Exchange Service (Deutscher Akademischer Austauschdienst – DAAD)

Poster and oral presentations:

- 21.09-22.09.2020 German Chemical Society (GDCh)– Section of Process Analytics: Graduate student symposium (digital) – Poster
'Laser-induced porous carbon nanofibers interdigitated electrode array (LCNFs-IDEA): Fabrication and Electrochemical Characterization of a High Performing Novel Transducer'
- 20.10-23.10.2020 Sensors in Medicine (digital) – Poster
'Laser-induced porous carbon nanofibers interdigitated electrode array: Fabrication and electrochemical characterization'

- 08.03-12.03-2021 PITTCON2021 (digital) – Oral presentation
‘Investigating 3D Freestanding Laser-Induced Carbon Nanofibers Electrodes for Efficient Redox cycling’
- 15.04.2021 Annual PhD colloquium of the graduate school ChemPharm (digital) – Oral presentation
‘New generation of carbon nanofibers for point-of-care testing’
- 08.11-12.11.2021 Sensors in Medicine (digital) – Poster
‘Lateral flow biosensor based electrochemical flow-through transducer’

Publications (peer-reviewed)

Perju, A., Wongkaew, N. Integrating high-performance electrochemical transducers in lateral flow assay. *Anal Bioanal chem* (2021). <https://doi.org/10.1007/s00216-021-03301-y>

Graphical Abstract on issue cover of the *Analytical and Bioanalytical Chemistry* Volume 413, number 22, September 2021

Perju A., Baeumner, A.J., Wongkaew, N. Freestanding 3D-interconnected carbon nanofibers as high-performance transducers in miniaturized electrochemical sensors. *Microchimica acta* (2022) <https://doi.org/10.1007/s00604-022-05492-2>

Perju A., Wongkaew, N., Baeumner, A.J. Flow-through Carbon Nanofiber-based Transducer for in-line Electrochemical Detection in Paper-based Analytical Devices, *manuscript submitted to Advanced Functional Materials*

Patents

Carbon Nanofiber electrodes for flow-through electrochemical sensors, Perju A., Baeumner, A.J., Wongkaew, N., Submitted September 22nd, 2021

Awards

Poster Award in Sensors in Medicine - second prize for ‘Lateral flow biosensor based electrochemical flow-through transducer’

Publications

Perju, A., Wongkaew, N. Integrating high-performance electrochemical transducers in lateral flow assay. *Anal Bioanal chem* (2021). <https://doi.org/10.1007/s00216-021-03301-y>

Perju A., Baeumner, A.J., Wongkaew, N. Freestanding 3D-interconnected carbon nanofibers as high-performance transducers in miniaturized electrochemical sensors. *Microchimica acta* (2022) <https://doi.org/10.1007/s00604-022-05492-2>

Perju A., Wongkaew, N., Baeumner, A.J. Flow-through Carbon Nanofiber-based Transducer for in-line Electrochemical Detection in Paper-based Analytical Devices, *manuscript submitted to Advanced Functional Materials*

Perju A., Baeumner, A.J., Wongkaew, N. Laser-induced carbon nanofibers for redox cycling, *manuscript in preparation*

Presentations

Oral presentations

2021 Pittcon, Digital Event

“Investigating 3D Freestanding Laser-Induced Carbon Nanofibers Electrodes for Efficient Redox cycling”

2021 PhD colloquim of the graduate school ChemPharm graduate, Digital Event

“New generation of carbon nanofibers for point-of-care testing”

Poster presentations

2020 Graduate student symposium organized by German Chemical Society (GDCh), Digital event

“Laser-induced porous carbon nanofibers interdigitated electrode array (LCNFs IDEA): Fabrication and Electrochemical Characterization of a High Performing Novel Transducer”

2020 Sensors in Medicine, Digital event

“Laser-induced porous carbon nanofibers interdigitated electrode array: Fabrication and electrochemical characterization”

2021 Sensors in Medicine, Digital Event

“Lateral flow biosensor based electrochemical flow-through transducer”

Eidesstattliche Erklärung

Ich erkläre hiermit an Eides statt, dass ich die vorliegende Arbeit ohne unzulässige Hilfe Dritter und ohne Benutzung anderer als der angegebenen Hilfsmittel angefertigt habe; die aus anderen Quellen direkt oder indirekt übernommenen Daten und Konzepte sind unter Angabe des Literaturzitats gekennzeichnet.

Weitere Personen waren an der inhaltlich-materiellen Herstellung der vorliegenden Arbeit nicht beteiligt. Insbesondere habe ich hierfür nicht die entgeltliche Hilfe eines Promotionsberaters oder anderer Personen in Anspruch genommen. Niemand hat von mir weder unmittelbar noch mittelbar geldwerte Leistungen für Arbeiten erhalten, die im Zusammenhang mit dem Inhalt der vorgelegten Dissertation stehen.

Die Arbeit wurde bisher weder im In- noch im Ausland in gleicher oder ähnlicher Form einer anderen Prüfungsbehörde vorgelegt.

Ort, Datum

Unterschrift

